CRANFIELD UNIVERSITY

COLLEGE OF AERONAUTICS

TOTAL TECHNOLOGY PhD THESIS

Academic Year 1998-9

LEE AXON

THE AERODYNAMIC CHARACTERISTICS OF AUTOMOBILE WHEELS - CFD PREDICTION AND WIND TUNNEL EXPERIMENT

Supervisor: Dr. K. P. Garry

September 1999

CRANFIELD UNIVERSITY

LEE AXON

THE AERODYNAMIC CHARACTERISTICS OF AUTOMOBILE WHEELS - CFD PREDICTION AND WIND TUNNEL EXPERIMENT

COLLEGE OF AERONAUTICS

TOTAL TECHNOLOGY PhD THESIS

To My Parents

ABSTRACT

When analyzing the aerodynamic characteristics of a road vehicle, the flow around the basic body shape is complicated by the presence of the rotating wheels. Even though on most vehicles the wheels are partially shrouded their effect on the flowfield is still considerable. Despite this, very little is understood about the flow around a rotating wheel. This thesis describes the development of a validated steady state Reynolds Averaged Navier-Stokes CFD model to investigate the flow around automobile wheels.

As all the previous investigations into the aerodynamic characteristics of wheel flows had been experimental, preliminary computational studies were performed. The basis of these was the 2D circular cylinder. The effects of cylinder rotation and ground proximity were modelled, and strategies for boundary conditions and mesh topology were developed.

This work was extended into 3D with the modelling of an isolated wheel, both rotating and stationary. Using existing experimental data for validation, an extensive investigation into the effects of solver numerics, symmetry planes, turbulence models, and the method of turbulent closure was performed. An optimum solver configuration was developed which comprised of the RNG k-ϵ turbulence model with full boundary layer closure. It was accurately predicted that the rotating wheel generates less lift and drag than the equivalent stationary wheel. A number of postulated experimental flow features were captured in the final solutions.

Using a parallel experimental study to provide further validation data, the CFD model was extended to incorporate an asymmetric shroud containing a wheelhouse cavity. The influence of the rotation of the wheel, the geometry of the shroud, and the thickness of the stationary groundplane boundary layer were investigated. The rotating wheel now produced more drag than the equivalent stationary wheel. Reductions in wheel drag were found with a reduction in the ride height of the shroud, and with the addition of spoilers to the lower front edge of the shroud. Increasing the stationary groundplane boundary layer thickness also reduced the wheel drag. The effects of these changes on the wheel surface pressure distributions are presented.

Acknowledgements

Throughout this research project I have received generous help and support from many people at Cranfield University, Rover Group Ltd., and MIRA.

Special thanks go to my supervisor at Cranfield, Dr. Kevin Garry, and the head of aerodynamics at Rover, Dr. Jeff Howell, for their valuable guidance and encouragement.

Also at Cranfield I am grateful for the help of Chris Stanley for the supervision of the non technical aspects of the thesis programme. I would also like to thank Jonathon Haynes, Dr. Les Oswald, and Grahame Jones for their help with computing support.

Many thanks also go to the workshop and wind tunnel staff at MIRA and Cranfield for their help with the experimental aspects of the programme.

I have been fortunate to make many new friends during my time at Cranfield and I would like to thank all of them, and in particular Kris Petterson, for their efforts in keeping me smiling.

Finally, my thanks to Rover Group Ltd. and EPSRC who provided the financial backing for this research project.

Contents

List of Figures

List of Tables

Nomenclature

A	Frontal Area (m^2)
A_S	Frontal Area of the Wheel Shroud (m^2)
A_T	Total Frontal Area of the Model (m^2)
A_W	Frontal Area of the Wheel (m^2)
AR	Wheel Aspect Ratio (100*W/D)(%)
C_D	Drag Coefficient
C_{Ds}	Shroud Drag Coefficient
C_{Dt}	Total Shroud & Wheel Drag Coefficient
C_{Dw}	Wheel Drag Coefficient
C_L	Lift Coefficient
C_{Ls}	Shroud Lift Coefficient
C_{Lw}	Wheel Lift Coefficient
C_P	Static Pressure Coefficient
C_Z	Side Force Coefficient
C_{Zs}	Shroud Side Force Coefficient
C_{Zw}	Wheel Side Force Coefficient
D	Wheel Diameter (m)
r_w	Wheel Radius (m)
r	Radial Distance From the Wheel's Axis of Rotation (m)
R	Non-Dimensional Radial Distance From the Wheel's Axis of Rotation (r/r_w)
Re	Reynolds Number
Re_D	Reynolds Number Based on Wheel / Cylinder Diameter
θ	Angular Position on the Surface of the Wheel / Cylinder (degrees)
v	Freestream Velocity (m/s)
ω	Angular Velocity (rad/s)
w	Wheel Semi-Width (W/2) (m)
W	Wheel Width (m)

x	Distance Downstream of the Wheel's / Cylinder's Axis of Rotation (m)
X	Non-Dimensional Distance Downstream of the Wheel's / Cylinder's Axis of Rotation (x/r_w)
y	Distance From, and Normal to, the Groundplane (m)
Y	Non-Dimensional Distance From, and Normal to, the Groundplane (y/r_w)
Y_f	Non-Dimensional Distance From, and Normal to, the Groundplane to the Lower Horizontal Face at the Front of the Shroud
Y_r	Non-Dimensional Distance From, and Normal to, the Groundplane to the Lower Horizontal Face at the Rear of the Shroud
ΔY_s	Change in Non-Dimensional Ride Height of the Shroud Relative to its Baseline Position
y^+	Non-Dimensional Wall Unit
z	Distance From, and Normal to, the Plane of the Wheel Centreline (m)
Z	Non-Dimensional Distance From, and Normal to, the Plane of the Wheel Centreline (z/w)

Chapter 1

Introduction

> ... a consistent physical model for the flow around a wheel within a wheel housing does not yet exist.
>
> Wolf-Heinrich Hucho (editor)
> pp 184
> Aerodynamics of Road Vehicles
> Fourth Edition
> SAE International
> 1998

When analyzing the aerodynamic characteristics of a road vehicle the flow around the basic body shape is complicated by the presence of the rotating wheels. Even though on most vehicles the wheels are partially shrouded their effect on the flowfield can still be considerable. Therefore, it is not surprising that the issues of wheel rotation and groundplane movement remain significant ones in the field of experimental automotive aerodynamics.

1.1 Wind Tunnel Ground Plane Representation

Fixed or moving ground? This still remains one of the most important decisions in production vehicle aerodynamic testing. Whilst race car aerodynamic development almost exclusively uses a moving groundplane wind tunnel configuration, does the less ground sensitive production road car require the use of such a complex facility? What 'errors' does the lack of relative vehicle to ground movement introduce to the flowfield around that vehicle?

The research into these questions, whilst extensive and well documented, is ongoing.

A number of different types of groundplane representation have been investigated. Hucho, *Ref.[1]*, summarizes ten different configurations. The most basic form is when the vehicle, whether model or full-scale, is placed on the stationary floor of the wind tunnel's test section. Thus the presence of the boundary layer changes the profile of the upstream flowfield ahead of the test vehicle from the 'ideal' on road condition.

All other forms of representation aim to minimize the effect of this boundary layer. One way is to mount the vehicle on a secondary floor above the main wind tunnel boundary layer. To give zero local flow incidence onto the leading edge of the board a flap is usually used at its trailing edge. However, this board is stationary, thus having its own boundary layer, and has to extend far enough upstream so the flow around the nose of the vehicle is not 'contaminated' by leading edge effects.

Instead of moving the vehicle above the tunnel boundary layer, more frequently it is attempted to reduce the thickness of the boundary layer on the working section floor. The main boundary layer control techniques are:

- *Upstream Boundary Layer Suction*
  Air is sucked through a slot or a strip of porous material on the ground ahead of the test section. If the suction flow rate is correct then a new boundary layer will start to form downstream of the boundary layer control which is consequently thinner in the region of the test vehicle than would otherwise have been.

- *Distributed Suction*
  The whole floor of the working section is made of a porous material and varying suction rates are used to try to remove the boundary layer from the entire area beneath the test vehicle.

- *Tangential Blowing*
  Air is blown into the lower part of the boundary layer ahead of the test vehicle through a narrow slot. This aims to eliminate the deficit of mass and momentum that exists in the boundary layer.

Whilst all these methods aim to improve the correlation of the profile of the relative air to vehicle movement between the wind tunnel and 'on-road' conditions the rel-

ative vehicle to road movement is not reproduced. For this a moving groundplane system is required.

The essence of a moving groundplane configuration is that the fixed floor of the working section is replaced with a belt which is driven so that its velocity matches that of the freestream flow. The boundary layer upstream of the belt is removed with either suction through a porous surface or a 'scoop'. Often both systems are used in conjunction. Tangential blowing immediately in front of the belt can also be employed to reduce any momentum deficit developed downstream of the suction system or brought through into the working section from below the plattern due to the motion of the belt. Whilst boundary layers cannot be entirely removed from the surface of the belt local to freestream velocity ratios within two millimetres of the ground should ideally be no less than 99%.

However, the benefit of better wind tunnel to 'on-road' correlation brings with it penalties in both the complexity of the wind tunnel system and data acquisition. Not only are moving ground systems expensive to install but increased tunnel downtime is required for maintenance.

With a fixed ground configuration force and moment data is usually measured with an underfloor balance; the test vehicle is either mounted on balance 'pads' in the floor or is supported on a strut going through the groundplane to the balance. With a one piece full width belt both these methods are not possible and thus an internal balance and overhead strut arrangement is normally used. Alternatives include a twin belt arrangement to allow for an underfloor balance and strut, *Ref.[2]*, or a narrow belt which just spans the central area between the wheels of the test vehicle, *Ref.[3]*.

However, the use of a moving groundplane only provides the relative vehicle body to road movement. A detailed test model will also have both wheels and wheelhouses. Thus to optimize the wind tunnel to 'on-road' correlation both moving groundplane and rotating wheel systems are required.

Mercker, *Ref.[4]*, outlines a system of modifications to a full-size passenger car that were required to measure total vehicle forces with a one piece moving groundplane. These modifications make this type of testing on a regular basis impractical compared to the 'drive-in, park, and test' method of a full size fixed groundplane wind tunnel. Thus, if the effects of using a moving groundplane with rotating wheels could be understood in enough depth then would it become possible for correction

factors to be used in fixed groundplane stationary wheel testing to account for the poorer correlation to 'on-road' conditions?

1.2 Difficulties in Experimental Measurements of Wheel Aerodynamics

Published results on the basic aerodynamic changes due to introducing a moving groundplane are generally in agreement. This is despite them being heavily dependent on the geometry and ride height of the test vehicle. For example, Howell and Hickman, *Ref.[5]*, found that for a simple generic body shape without wheels its drag coefficient decreased when tested above a fixed ground, relative to when the ground was moving, whilst the lift coefficient increased. This was for a variety of combinations of underfloor roughness and engine bay cooling. These trends were also shown by Le Good, *Ref.[6]*, Mercker *et al*, *Ref.[7]*, and Mueller *et al*, *Ref.[8]*.

When wheels are added to the test vehicle the relative changes in total vehicle forces with ground condition are influenced by the interaction of the flow around the body with the wheels, suspension etc., and the aerodynamic forces produced by the wheels themselves. Experimental results have shown these changes to be significant. For example, the flow around the wheels of an Audi A3, and the interaction of this flowfield with the wheels' associated structures, accounts for approximately one third of the total drag of the vehicle, *Ref.[9]*.

Considering the possibilities for drag reduction in this area very little work has been done in understanding the flow around a rotating wheel. This is probably due to two reasons. Firstly, the design of contributory factors to the drag, for example the shape of the wheelhousing, is based more on the needs of, say, suspension design, than aerodynamic considerations. As well as requiring enough volume for the mechanical components clearance has to be provided for the desired maximum steering angle and vertical wheel travel.

Secondly, the technical problems involved in conducting experiments on rotating wheels are considerable. Even though moving groundplane facilities are now available at most scale aerodynamic facilities full scale moving belts are rare. Thus most testing has to take plane at component level, i.e. not with the whole of the test vehicle present, or at a reduced scale, which may then introduce unknown Reynolds number effects.

Obtaining meaningful data is also difficult. Isolating the wheel aerodynamic forces from the wheel-ground reaction forces is complicated. Whilst measuring wheel drag with strain-gauged axles is now frequently used issues remain regarding the tare values taken at 'belt trundle'. Systems to measure wheel lift, such as monitoring the change in load experienced by a roller placed under the belt beneath the wheels, are even more complex. Integrating the pressures on the surface of the wheel to obtain lift and drag is laborious due to it being a rotating system. Thus, only a limited number of connections can be made between the wheel and its support system through the bearing. Any pressure measuring equipment located inside the wheel would have to be calibrated for rotational effects and a method for locating the angular position of any measurement would be needed. If wheel surface pressures were to be surveyed regularly then the surface would also have to be 'mapped' in a single run to avoid a large number of runs per test vehicle configuration.

In view of such experimental difficulties would it be possible to utilize the developing field of numerical techniques for studying the flow around a wheel?

1.3 An Introduction to Numerical Techniques and their Automotive Aerodynamics Applications

Computational Fluid Dynamics, or CFD, is the generic term given to the range of techniques and procedures involved in obtaining a numerical solution for the flow of a fluid around, or through, the object of interest. As computer technology has developed over the past twenty five years so has the complexity of simulation techniques. In terms of increasing computational effort these methods can be summarized as:

1. Linear Methods: Vortex Lattice and Panel Codes
2. Non-Linear Methods:
   (a) Inviscid or Euler
   (b) Time Averaged Viscous - Steady State Reynolds Averaged Navier-Stokes Equations (RANS)
   (c) Unsteady Viscous Methods:
      i. Unsteady RANS
      ii. Large Eddy Simulation

iii. Direct Numerical Simulation

Imposing the condition of irrotational flow and neglecting the viscous terms reduces the steady Navier-Stokes equations down to the linear Laplace equation. Both vortex lattice and panel method codes are methods for solution which only involve discretization of the surfaces of interest. Whilst these methods can be coupled with corrections for both boundary layer and wake effects they are seldom used today in the field of production car aerodynamics. However, they are still used in racing car development, particularly for initial design analysis of wing sections, *Ref.[10].*

The addition of non-linear terms in the governing equations to be solved dramatically increases the complexity of the numerical method. Whilst inviscid, or Euler, methods only add first order partial differential terms the complexity of viscous interactions in the flowfields of interest means that this simplification is generally considered irrelevant in vehicle aerodynamics. Simulation of viscous flowfields means solving second order partial differential equations.

Consider a fully turbulent flowfield. The time-dependent dynamics of the fluid will be governed by the Navier-Stokes equations, for which many derivations exist in print, for example Batchelor, *Ref.[11].* The turbulence itself is characterized by fluctuations in all of the fluid variables around mean values. These small scale turbulent components are computationally very intensive to resolve and hence the classical approach is to average the instantaneous equations, in time, over these turbulent fluctuations. The fluid motion is split into two components; a mean flow upon which a second fluctuating flow is superimposed. This leads to the time-dependent Reynolds Averaged Navier-Stokes (RANS) equations. Averaging over much larger time steps typical of the mean flow components gives the steady state RANS equations.

Direct Numerical Simulation, DNS, is the term given to the solution of the complete unsteady Navier-Stokes equations. An intermediate step between DNS and RANS is Large Eddy Simulation, LES, where the larger turbulent eddy length scales are solved and the smaller eddies are modelled empirically.

Due to the computational demands of these latter two numerical methods viscous simulation of vehicle aerodynamics generally employs RANS methods, usually steady state. However, this introduces turbulence modelling. The simplifications employed in the governing equations means that products of the fluctuating terms, the so-called Reynolds Stresses, exist giving more unknowns than equations. There-

fore, to close the set of RANS equations requires the addition of further equations, the turbulence model, so that the effect of the turbulent motion on the mean flow can be modelled. This means that the realism of a flow simulation with RANS methods is highly dependent on the turbulence model employed.

For solution the continuum properties of the RANS equations have to be discretized, both in terms of the fluid volume of interest and the mathematical equations. This discretization of the space through which the fluid passes is known as mesh generation, and it is only this grid which provides the solver with geometric information. Whilst linear methods only need the body surface to be meshed all the other schemes require meshing of both the geometry of interest and the surrounding computational domain. Thus if a geometric component or flow region is not resolved adequately with the mesh it becomes impossible for the solver to give an adequate solution in this area. However, no theoretical methods are available for determining the appropriate size and detail of the mesh other than numerical experimentation.

Thus, for successful CFD simulation both the volume mesh and numerical scheme have to be appropriate for the expected flow physics of the solution. Otherwise numerical errors tend to dominate. For the complex flows found around automotive shapes minimizing the influence of the numerics requires a lot of effort and thus much of the published information still relates to numerical effects and not actual conclusions about the aerodynamics modelled. For example, Hajiloo *et al*, *Ref.[12]*, and Ramnefors *et al*, *Ref.[13]*, have looked at the effects of mesh refinement on the computed solution.

The effectiveness of a turbulence model is not only dependent on the quality of its mathematical reasoning but also the computational grid, especially in terms of its requirements for the range of permisable first cell centre y^+ values[1] next to, and cell size growth away from, wall boundaries. The many derivatives of the k-ϵ model are still the frequent choice for simulations. Comparisons of different types of model are becoming more widely published; for example Ramnefors *et al*, *Ref.[13]*, Axelsson *et al*, *Ref.[14]*, and Perzon *et al*, *Ref.[15]*. However, not one specific turbulence model shows consistently good results; the choice still seems to be dependent on the configuration of interest.

[1] A wall unit, y^+, is a characteristic non-dimensional distance from a wall which is dependent on the physical perpendicular distance from the wall boundary as well as friction velocity and viscosity

Despite these issues numerical techniques have been applied to a wide range of automotive problems. Dhaubhadel, *Ref.[16]*, provides a comprehensive review. As well as external aerodynamics, climate control, engine cylinder flows and combustion, engine cooling, exhaust systems, engine bay flows, and rotating systems such as disc brakes have all been subject to published CFD studies.

1.4 Summary of Research Objectives

The main objective of this research was to investigate the possibilities of using numerical methods to investigate the flow around an automobile wheel. In doing so, it was intended that conclusions be drawn about both the numerical methods selected for the study and the actual aerodynamics characteristics of such flows.

Once an appropriate CFD method had been selected, all the models produced were to be fully validated against experimental data. This applied to all stages of model development; from 2D simulations, through 3D isolated wheels, and to 3D shrouded wheels. From this validation work conclusions were reached concerning the influences of the turbulence model and computational mesh. Only from the 'best' of these solutions was aerodynamic data drawn.

It was intended that wherever possible validation will use existing published data. However, if this was not possible at any stage of the research an experimental programme would be developed for this purpose.

1.5 Layout of Thesis

1.5.1 Technical Research Programme

In Chapter 2 a review of the previous published work concerning the aerodynamic properties of wheel flows is presented. This will refer to both experimental and computational data. It will allow an understanding of the flow structures which have to be resolved numerically, thus guiding the choice of computational method, as well as determining whether an experimental programme is required for validation of the models produced.

The implementation of the chosen numerical scheme is described in Chapter 3.

Details of the work undertaken to achieve the research objectives are given in Chapter 4 to Chapter 9.

Chapter 4 gives details of preliminary two dimensional work concerning rotating isolated cylinders and a stationary cylinder resting on an infinite groundplane. This is to validate that the chosen numerical method could accurately apply various boundary conditions and to develop a basic mesh structure for later 3D calculations.

Chapter 5 and Chapter 6 show the results of the work relating to the extension of the 2D work to three dimensions; i.e. an isolated wheel. This gives the details of a comprehensive numerical investigation into mesh dependency and turbulence modelling. The effects of these on both surface pressures and the wake behind the wheel are considered. Finally, aerodynamic conclusions about the flowfield are given.

The final section of work on shrouded wheel aerodynamics is related in Chapter 7 through to Chapter 9. Again, details of the work completed for validation of the model is given before a discussion of the aerodynamic characteristics of the modelled flowfield.

Chapter 10 contains overall conclusions and recommendations for further work.

1.5.2 Total Technology Research Programme

This research programme was carried out, with the sponsorship and guidance of Rover Group Ltd., under the Total Technology scheme which requires the depth and specialism of a conventional PhD along with an appreciation of some of the business aspects of the research work.

Throughout its duration the availability of adequate computational resources was always an issue. Therefore, in Chapter 11, the provision and management of computer resources for CFD is investigated. The utilization of existing networked CAD resources for processing CFD calculations is discussed and comparisons made with having a dedicated CFD multi-processor machine, as well as outsourcing the work to another department or company. In particular, the effect on system administration and 'day-time' users is considered.

Chapter 2

Literature Review

As previously described the aim of the review of the published work concerning wheel aerodynamics is twofold. It will concentrate on both the suitability of data for validation of the computational models as well as guiding the development of these models through an initial understanding of the flow structures to be resolved.

It will be split into two main sections. The first will cover isolated wheels, i.e. where the whole of the wheel is exposed to the freestream flow. This will include both ways of supporting the wheel; either the wheel is studied totally in isolation with only a non-intrusive support system or, secondly, it is mounted to a simple slender body in an open-wheel race car type configuration. The second section will cover wheels that are partially shrouded from the freestream, whether in an actual vehicle wheelhouse cavity or in a simplified body.

Any published work used that relates to models produced during the initial stages of the research leading up to the first three-dimensional wheel flow model will be reviewed at the appropriate point in the text.

2.1 Isolated Wheels

Morelli, *Ref.[17]* and *Ref.[18]*, was the first to publish details of research specifically related to the flow around a rotating automobile wheel. This covered both isolated and shrouded wheel flows. In the 3m diameter closed working section wind tunnel of the University of Turin a flat plate was mounted parallel to the freestream to represent a stationary groundplane. The solitary exposed wheel, a typical 1960s

racing tyre of 0.630m diameter, entered, without any contact, into a rectangular recess in this plate in the stated attempt to represent the deflection of the wheel on the ground. Aerodynamic forces and moments were measured with a six component balance connected to the faired driveshaft of the wheel which could be yawed, together with the groundplane, upto an angle of twenty degrees.

It was found, however, that the measured isolated rotating wheel lift force was negative, i.e. a downforce, which is contrary to the accepted direction of positive lift. The results relating to wheel drag showed that the use of faired rims on the centre of the wheel reduced drag by 22% whilst wheel drag was doubled by increasing the yaw angle of the wheel from zero to twenty degrees. However, these must be viewed with caution due to the wheel lift results.

Stapleford and Carr, *Ref.[19]*, used a slender streamlined body fitted with four unenclosed wheels as a basis to study the effects of groundplane movement, wheel rotation and wheel ground clearance on vehicle wind tunnel force measurements. Both the MIRA quarter scale tunnel and the Imperial College $5' \times 4'$ tunnel were used. The circular cross-section slender body was fitted, via simple fixed suspension units, with four wheels of 0.1524m diameter, giving an approximate Reynolds number, Re_D, of 2.0×10^5. Total forces on the vehicle were measured using an underfloor balance at MIRA, and with an overhead balance at Imperial College. Wheel forces were extracted from the overall forces by subtracting tares for the strut, body, and suspension units at the corresponding ride height. Thus, the interference effects between the body and wheels were not quantified.

The lift generated by the four stationary wheels at a large ground clearance was very small. As this gap was reduced C_{Lw} increased rapidly. Wheel drag also increased with decreasing ground clearance. Rotation of the wheels caused a large negative wheel lift to be generated with a gap between the wheels and the stationary groundplane. This became positive when this gap was sealed with strips of paper. Tuft flow visualization showed the rotation of the wheels drew air through the gap to the groundplane, thus creating large local negative pressures. With zero ground clearance rotation of the wheels reduced both their lift and drag compared to when the wheels were stationary under otherwise identical test conditions.

The effect of using the moving groundplane at Imperial College on the derived wheel forces was found to be small. Most coefficients only changed by a few percent when compared to the same configuration with the belt non-operational. The only

exception was when the wheels were rotating and close to the moving belt. This was, however, without any seal between the wheels and groundplane. The optimum case of zero gap was not studied due to the wheel / groundplane contact forces not being able to be isolated from the aerodynamic forces.

Probably the most well known work concerning isolated wheel aerodynamics is that of Fackrell. This is described briefly in *Ref.[20]* and *Ref.[21]*, and in more depth in *Ref.[22]*.

Using two wheels of varying profile and tread width, and of diameter 0.415m, surface static pressure measurements and total head wake surveys were conducted at a Reynolds number, Re_D, of 5.3×10^5. The wheels, machined from light alloy, were kept in contact with the moving groundplane by a system of supports not dissimilar to a racing car suspension system, *Fig.2.1.* With the pressure transducer mounted inside the model, on the axis of rotation, its electrical output, corresponding to the cyclical pressure distribution measured with flush tapping across the semi-span of the wheel surface, was recorded outside the wheel with the use of slip rings formed of low noise silver graphite bushes.

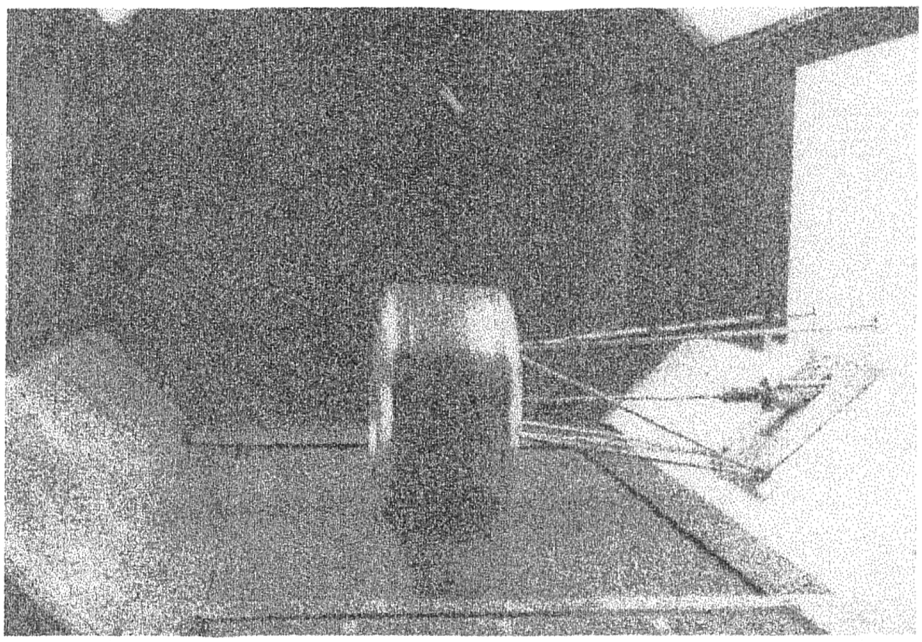

Figure 2.1: Fackrell's Experimental Configuration

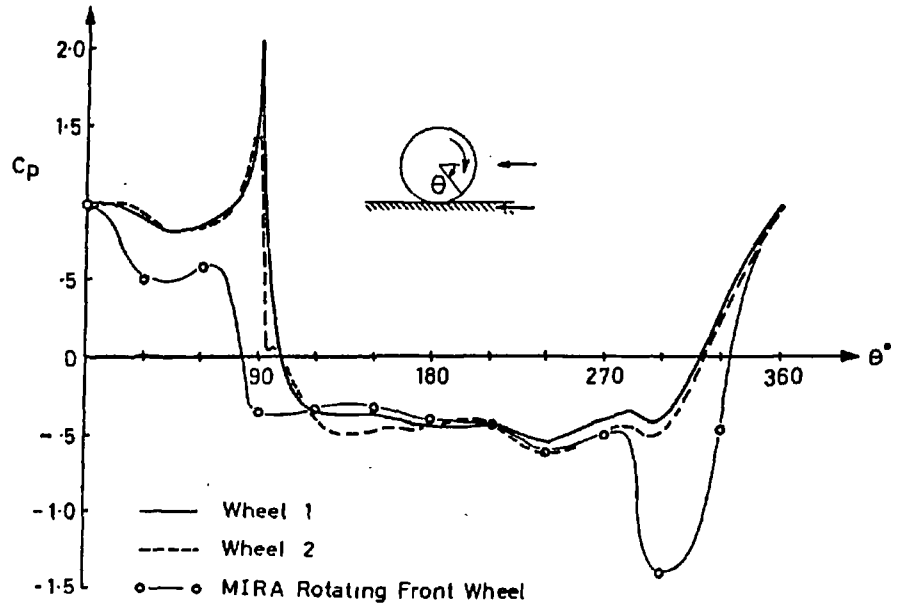

Figure 2.2: Surface Static Pressure Distribution on the Centreline of a Rotating Wheel (Fackrell)

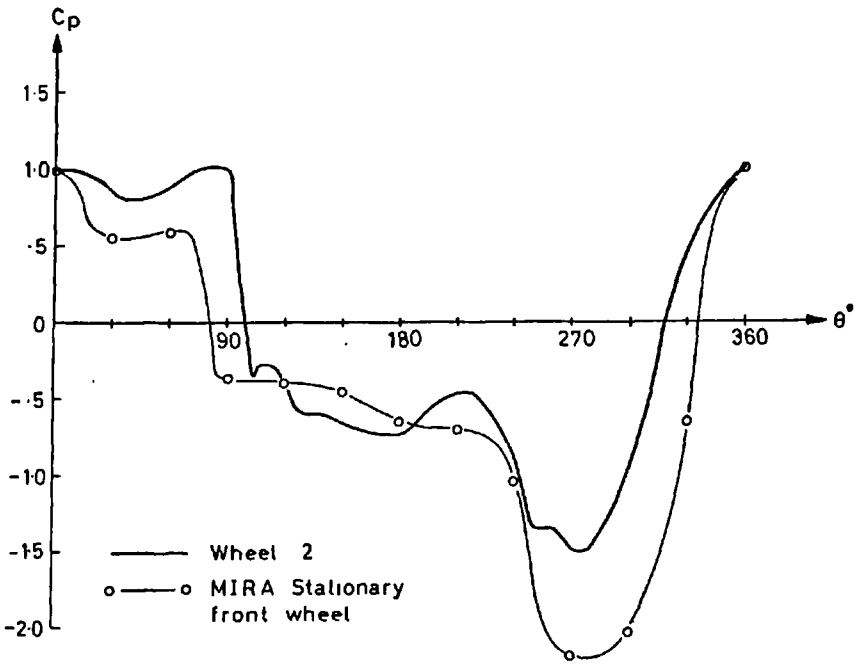

Figure 2.3: Surface Static Pressure Distribution on the Centreline of a Stationary Wheel (Fackrell)

Pressure distributions on the centreline of the wheel are shown in *Fig.2.2.* The MIRA results are those of Stapleford and Carr, *Ref.[19]*, measured with an exterior static probe. The differences between the two show the effect of tyre profile when the wheel was rotating. Wheel 2 has a more rounded profile than wheel 1 but is slightly narrower (AR=61.2% compared to AR=65.8%, equating to a 5% decrease in frontal area). The pressures on top of, and behind, wheel 2 were found to be more negative showing that the edge profile can have significant effects on the wake structure even in the plane of the centreline of the wheel. Integration of the complete set of pressure profiles measured across each wheel gave a higher lift coefficient and a lower form drag coefficient for wheel 2 compared to wheel 1, *Table 2.1.*

	C_{Lw}	C_{Dw}
Wheel 1	0.40	0.63
Wheel 2	0.44	0.58

Table 2.1: The Effect of Wheel Edge Profile on the Lift and Drag Coefficients of a Rotating Isolated Wheel (Fackrell)

	C_{Lw}	C_{Dw}
Rotating Wheel	0.44	0.58
Stationary Wheel	0.76	0.77

Table 2.2: The Effect of Ground Movement and Wheel Rotation on the Lift and Drag Coefficients of an Isolated Wheel (Fackrell)

Comparing the centreline pressure profiles recorded for a rotating wheel and moving groundplane with those of a fixed wheel and stationary groundplane, *Fig.2.3*, showed major differences. These included very high pressures at the front of the contact patch when the wheel was rotating, a lower base pressure for the stationary wheel, as well as a lower suction pressure on the top of the wheel surface due to the later flow separation, *Fig.2.4.* The effects of these were that the stationary wheel produced 73% more lift and 33% more form drag than the rotating wheel under the equivalent test conditions, *Table 2.2.*

Using the angular notation shown in *Fig.2.2*, Fackrell postulated that the boundary

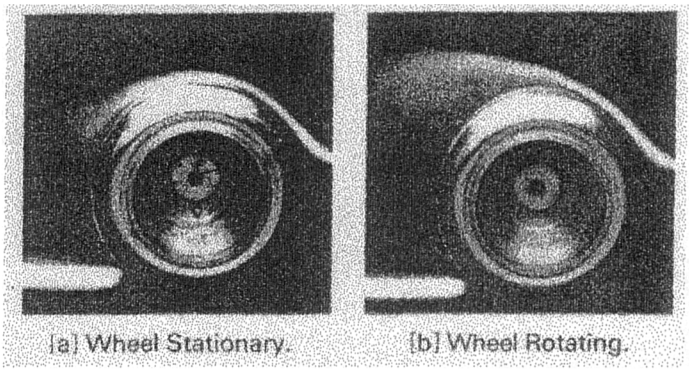

flow direction: right to left wheel rotation: clockwise

Figure 2.4: The Flow over an Isolated Wheel (Fackrell)

layer remained attached over the stationary wheel until approximately $\theta = 210^o$. On the wheel centreline the separation process was said to be similar to that of a solitary two-dimensional circular cylinder in the transcritical regime i.e. a laminar separation bubble, turbulent reattachment, and final turbulent separation. When the wheel was rotating, however, the attached wheel boundary layer meant that this type of separation could not occur. As the top part of the rotating wheel moved in the opposite direction to that of the freestream there would have existed within the boundary layer structure an iso-surface of zero velocity magnitude. Fackrell suggested that the centreline 'separation' point for a rotating wheel occurred on this zero velocity iso-surface, in a favourable pressure gradient, 70^o further forward than on the stationary wheel.

Investigations into the characteristics of the wake were made with a total head survey, in four planes perpendicular to the freestream, with a Kiel tube which was stated to be insensitive to yaw upto flow angles of $\pm 35^o$. Plots of 90% total head, intended to represent the edge of the wake, are shown in *Fig.2.5*. These support the pressure measurements by showing that the flow 'separated' earlier when the wheel was rotating, thus giving a taller wake. The bulges near to the groundplane show the presence of vortices shed from the front of the wheel. For the stationary wheel it was stated that these probably represented the formation of a horseshoe vortex due to the wheel causing upstream groundplane separation (no thickness of this boundary layer was stated).

When the wheel was rotating the surfaces of the wheel and groundplane converged towards the front of the contact patch at the freestream velocity. Fackrell postulated, *Fig.2.6*, that air was drawn into this region due to the non-slip conditions which was

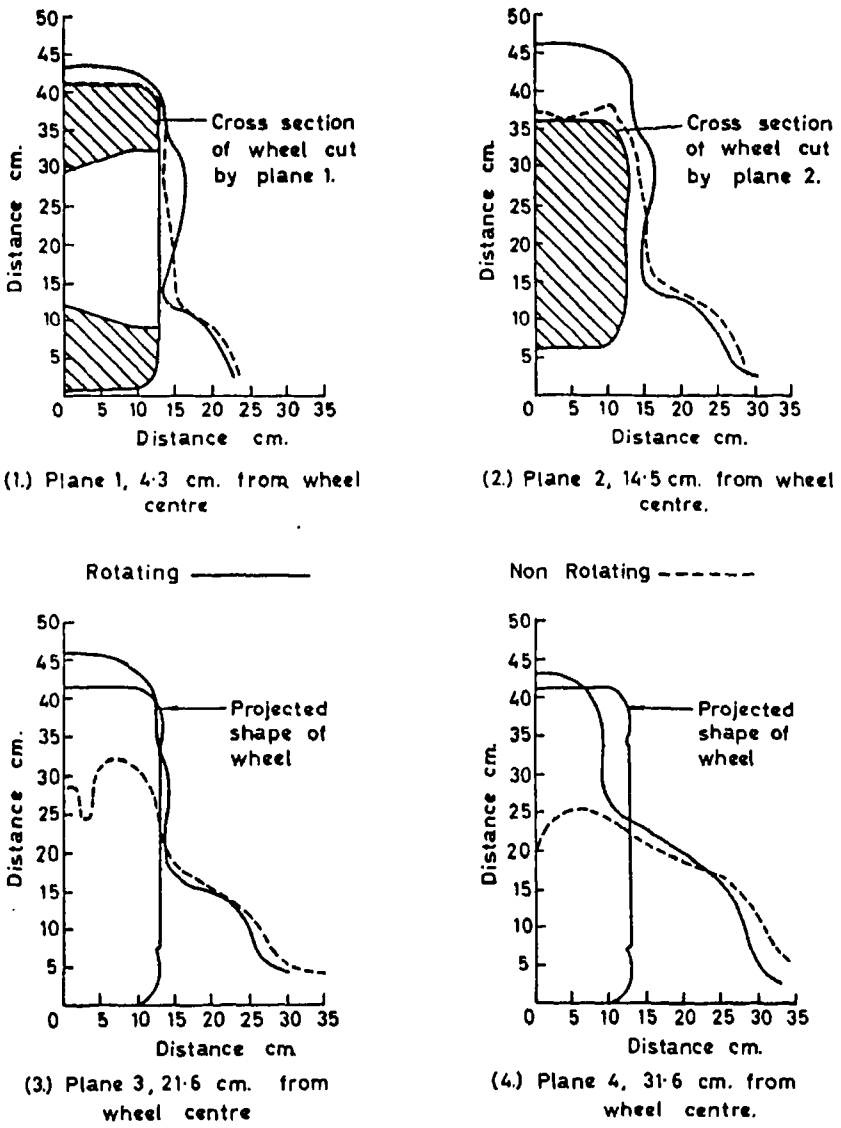

Figure 2.5: The Wake Behind Rotating and Stationary Isolated Wheels (Fackrell)

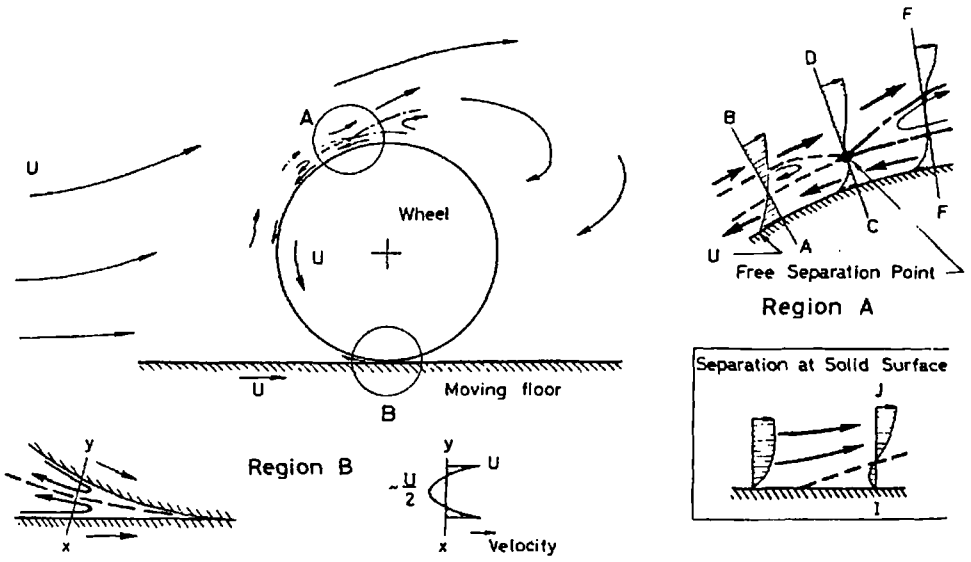

Figure 2.6: The Characteristics of the Flow Around Isolated Wheels Postulated by Fackrell

then forced out between the two attached layers. In this very small region the viscous forces dominated and it was this squeezing of the flow which resulted in pressure coefficients greater than unity. As the wheel was of finite aspect ratio this 'jet' of air was then deflected sideways by the freestream and then passed down either side of the wheel.

Limited investigations were also performed into the effect of wheel aspect ratio and grooves in the wheel surface, similar to those found on current Formula 1 cars.

As part of a study in the Pininfarina wind tunnel into wheelhouse cavity flows Cogotti, *Ref.[23]*, also documented a number of initial experiments concerning the flow about isolated wheels. However, no mention is made of the use of a moving groundplane or details given of the characteristics of the fixed groundplane boundary layer.

To emphasize the importance of sealing the gap between a rotating wheel and groundplane pressure measurements were made on the tunnel floor for a range of wheel to ground distances, *Fig.2.7.* The wheel, a Pirelli 145 SR 10 tyre filled with foam and turned on a lathe until almost slick, was of diameter 0.485m and AR=28%. It was driven by an adjacent faired motor to give matching circumferential wheel and freestream velocities and $Re_D = 1.1 \times 10^6$. It was found that when the rotating

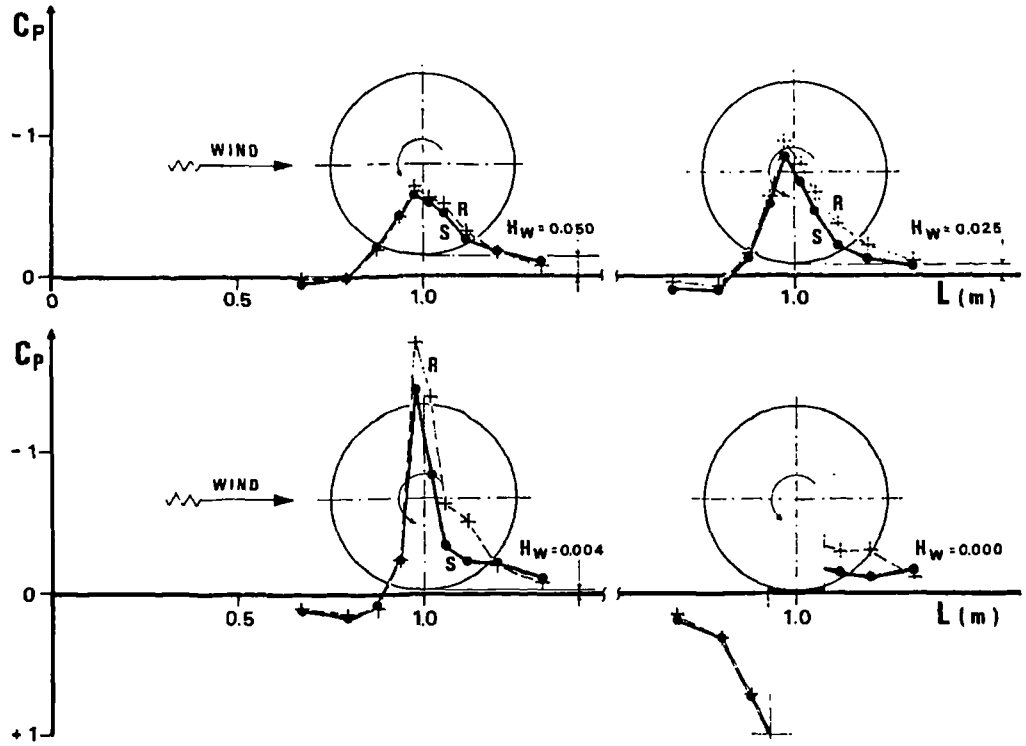

Figure 2.7: Stationary Groundplane Pressure Distributions Beneath an Isolated Rotating Wheel at Various Ride Heights (Cogotti)

wheel approached the ground the flow in the narrowing gap became increasing accelerated, and hence, more negative groundplane pressures were generated beneath the wheel. However, when the wheel to groundplane gap was sealed these pressures at the front of the 'contact' patch became positive. The magnitude of this positive pressure was stated to be dependent on the quality of this seal - a foam rubber insert, fitted under slight pressure, between the rotating wheel and tunnel floor was favoured by Cogotti.

For force measurements the wheel was mounted above a pad of the underfloor balance. Evidence was found of a critical Reynolds number for a stationary wheel which was independent of any fairing on the central hub of the wheel. How this was affected by upstream boundary layer thickness was not considered. The addition of these fairings decreased the wheel drag coefficient; the reduction was greater for a rotating wheel than for a stationary wheel. The drag coefficient for the stationary wheel in contact with the fixed groundplane was slightly greater than for the rotating wheel and, in both cases, the wheel produced positive lift. The stationary wheel generated more lift than the rotating wheel. Changing the yaw angle of the

wheel from 0^o to 15^o increased the drag coefficient of the isolated, i.e. without motor present, stationary wheel by 10% and its lift coefficient by 40%.

Other experimental studies reporting results regarding isolated wheel aerodynamics include Bearman *et al*, *Ref.[24]*, who performed further wake studies behind one of Fackrell's wheels with a nine hole pressure probe. Contour plots of both total pressure and vorticity were presented. A taller, narrower wake was found behind the rotating wheel on a moving groundplane when compared to the stationary wheel fixed groundplane case at $Re_D = 5.5 \times 10^5$. Both wakes were dominated by a vortex either side of the wheel near to the groundplane. The vortices behind the rotating wheel were found to be much weaker, and closer to the wheel, than those behind the stationary wheel.

Both Hilhorst and Giachi, *Ref.[25]*, and Schiefer *et al*, *Ref.[26]*, have reported results for isolated wheels both on their own and in an open wheel race-car configuration. It was found that a wheel placed behind another is strongly influenced by being in the wake flow for separation distances of upto ten wheel diameters. The drag of the rear wheel, in particular, was significantly reduced from its isolated value. However, for the race-car configurations, interactions between the wheel flows and the nearby bodywork surfaces were found to be considerable, and, thus, the results are not generally applicable to studies of totally isolated wheels

Computationally, apart from this study, the only published information on solutions for the flow around an isolated wheel is that of Skea *et al*, *Ref.[27]*. Published after the isolated wheel work of this research was completed the authors report the results of basic numeric and mesh studies for the CFD simulation of the flow around a finite aspect ratio square edged three-dimensional cylinder in ground effect. Comparisons were made with just the centreline pressures of Fackrell despite $Re_D = 6.9 \times 10^5$ instead of $Re_D = 5.3 \times 10^5$ and the different edge profiles.

2.2 Shrouded Wheels

The published data on the aerodynamics of wheels within wheelhouse cavities can be split into three distinct categories; track data, wind tunnel data, and computational results.

Oswald and Browne, *Ref.[28]*, made detailed measurements of the flowfield around a wheel within an actual wheelhouse cavity on the track. The vehicle velocities used were in 16km/h increments from 16 to 96km/h, and all the tests were performed with the ambient wind speed less than 5km/h for repeatability.

To study the flow direction a tuft grid was attached to the test car. This surrounded the wheel and the indicated flow direction was photographed from an adjacent vehicle, and through two windows inserted in the wheelarch using a camera mounted in the engine bay. A single hot-wire anemometer was then used to measure the local air velocity and turbulence levels; the alignment of the hot-wire used the tuft-grid results. Transient data series were recorded over a period of at least fifty seconds.

A flow model was constructed using the tuft grid results, *Fig.2.8.* This general description of the flow direction was found to be independent of the vehicle velocity over the range of speeds tested. Limited numbers of contour plots of the turbulence and velocity data obtained from the hot-wire were also presented. Very high turbulence intensities, of the order of 60%, were found in regions of the wheelhouse cavity.

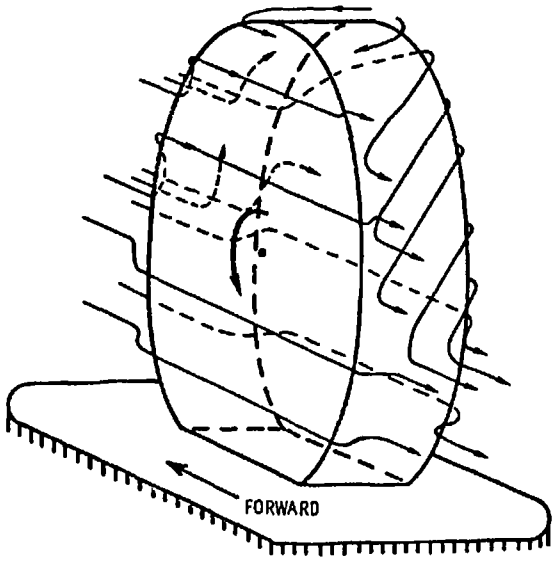

Figure 2.8: Proposed Flow Model for a Wheel Located in a Wheelhouse Cavity (Oswald and Browne)

Generally, wind tunnel studies on shrouded wheels have used a simplified wheelhouse cavity within a low drag body. Again, Morelli, *Ref.[17]* and *Ref.[18]*, reported the first study of such flows. However, as previously described, the use of a small gap

between the rotating wheel and stationary groundplane resulted in the direction of the wheel lift measured without a wheelhouse cavity present being opposite to the rest of the published literature concerning isolated wheels. Therefore, the shrouded wheel force results must also be regarded with caution, and are not considered here. No data was reported for wheel shroud forces.

Following on from his isolated wheel work, Cogotti, *Ref.[23]*, initially studied the effect of adding four wheels to a low drag passenger car. With the wheels and groundplane stationary the total drag measured was almost two and a half times that of the basic body mounted on simple cylindrical struts to the underfloor balance pads. It was found that most of this increase was from the front wheels which were subject to a highly yawed freestream flow. A similar flow pattern has been observed onto the front wheels of a Opel Calibra, *Fig.2.9.* The flow approaching the Calibra near its centreline was drawn towards the front wheel resulting in a highly yawed local freestream direction. Rotation of the four wheels, with the fixed groundplane, was found to decrease total drag but increase total lift.

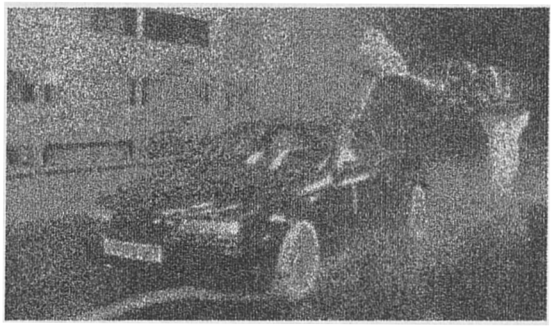

↑

smoke visualization of flow direction

Figure 2.9: The Local Flow Direction Approaching the Front Wheels of an Opel Calibra (Hucho)

To study these effects further a simple teardrop body was used. This was fitted with two wheels, one either side and approximately midway along its length, within wheelhousings of variable width and height. Forces were measured for the body only as the small gap left between the wheel, whether rotating or stationary, and the fixed groundplane, would have reduced the validity of any measured wheel forces. It was found that both the body lift and drag coefficients were reduced by keeping the wheelhouse volume as small as possible. Wheel rotation increased both the

body lift and drag coefficients compared to the comparative stationary wheel case. However, Cogotti expressed caution regarding the application of these results to a passenger car due to the local freestream incidences onto the wheels of the model having only a small yaw angle.

Fabijanic, *Ref.[29]*, and *Ref.[30]*, also used a simple body with interchangeable wheelhouse cavity sections to investigate shrouded wheel aerodynamics. Using a low noise wind tunnel of cross-section 0.75m $\times$ 0.5m at Cornell University the stated aim was to understand the basic mechanisms underlying the lift and drag changes created by the addition of wheels and simple wheelhouses to a basic automotive body. The model consisted of rear, nose, and wheelhouse cavity components. The central wheelhouse cavity section was 0.1778m in length. Two wheels, one either side and of diameter 0.0766m with aspect ratio 47.5%, were centred longitudinally in this central section in variable radius, height, and depth wheelhouse cavities. The wheels were driven from the moving groundplane system and were supported on strain gauged axles. A three-component overhead balance was used to record the wheel shroud forces. The freestream velocity of 30m/s gave a Reynolds number, Re_D, of 1.6×10^5. To try to ensure fully turbulent flow transition strips were applied to the rounded nose of the model.

Flow visualization highlighted a flowfield that was stated to be in general agreement with that of Oswald and Browne. A large degree of unsteadiness without periodicity was observed. Both yawed flow onto the wheels, although at a narrow angle, and a triangular separated region where the flow exited the wheelhouse cavity at the rear of the wheelarch were highlighted. Surface pressure coefficients measured within the cavity were between ± 0.3.

Analysis of the measured forces showed that the addition of wheels and wheelarches to the basic body increased total lift and drag significantly. Increasing the depth of the wheelhouse cavity was found to reduce the lift coefficient of the shroud whilst increasing its drag coefficient. Wheel drag was also reduced but the change in wheel lift was found to be negligible. Reducing the radius of the wheelhouse cavity had the opposite effect, i.e. it increased shroud lift coefficient and decreased shroud drag coefficient.

Imaizumi and Yoshida, *Ref.[31]*, briefly summarizes the effect of wheel rotation and ground movement on 'notchback' and open-wheeled models. No Reynolds number

was stated. The wheels were driven from motors internally mounted in the model. The wheel to groundplane clearance was approximately 0.002m. It was not stated whether or not the gap was sealed.

Rotation of the wheels was found to decrease both total lift and drag for both moving and stationary groundplanes. This effect was more pronounced for the open wheeled model than for the notch-back model. Pressure measurements in the wheelhouse cavities of the notchback model gave coefficients that were both small and negative. The minimum C_p measured was approximately -0.35.

Using a full-size Calibra fitted with a modified suspension package, to allow for wheel force measurements, and a smooth underfloor, Mercker, *Ref.[4]*, reports the results of investigations into the effects of using rolling wheels in automotive aerodynamic experiments. Comparisons were made between fixed and rotating wheels when used in conjunction with a moving groundplane. A calibration for the gap between the moving ground and the fixed wheels was made.

It was found that total vehicle lift and drag increased with a decreasing gap between the stationary wheels and moving groundplane. Mercker stated that this was due to the development of stronger horseshoe vortices in front of each wheel as the groundplane clearance was reduced. Using inserts to seal the wheelhouse cavities with the fixed wheels in place reduced the vehicle drag coefficient by approximately 0.075. Thus, wheelhouse shape and volume was stated to be a major consideration for vehicle drag optimization. Rotation of the wheels in contact with the moving groundplane reduced the total vehicle drag coefficient by 0.021. The rotating front wheels were found to produce negative lift, or a downforce, with the smooth underfloor panels fitted, which became positive when they were removed to leave the rough underfloor. Both tyre width and tread pattern were found to have minimal effects on total vehicle forces.

Wake measurements behind the front and rear wheels were made with rakes of total head probes insensitive to yaw angles upto $\pm 25^o$. The front wheel wake flows were dominated by vortices close to the moving groundplane which were stronger when the wheels were fixed. A vortex structure exiting from the rear of the wheelarch was also found, particularly for when the wheels were rotating. The width of the tyre was found to influence the strength of this vortex. Both the ride height of the vehicle and the front spoiler were also major influences and could totally suppress this vortex. Weaker vortex structures were measured behind the rear wheels, probably due to

being in the wake flow of the front wheels.

Pfadenhauer *et al*, *Ref.[32]*, and Wickern *Ref.[9]*, used a similar full-scale set-up but with an Audi A3. On comparing forces measured with both internal and external balance arrangements a wheel 'fan moment' was proposed as an extra tare measurement[1] for vehicle drag measurements with external balances. The influence of the belt speed at which the tare measurements for wheel forces were taken was also investigated.

The differences between the aerodynamic forces generated by fixed and rotating wheels on stationary and moving groundplane systems respectively were stated to be influenced by the dynamics of the tyre contact patch. A rig was used which allowed for wheel force measurements to be taken for different wheel loads, and thus tyre deformations. Using a single wheel located in a shroud with a quarter sphere outer shape, and a typical wheelhouse cavity profile for its inner shape, the influence of yaw angle was investigated. At zero yaw angle the rotating wheel produced approximately 60% of the drag of the stationary wheel. Whether or not the groundplane was moving for the two cases was not clearly stated. Increasing the yaw angle (a positive angle gave flow onto the inside of the wheel) gave drag coefficients equal to one another at 10^o, and at a yaw angle of 25^o the rotating wheel produced approximately 25% more drag than the fixed wheel. Changing the geometry of the contact patch by placing the wheel under load had only a minimal effect on the measured forces throughout the range of yaw angles tested.

Wiedemann, *Ref.[33]*, looked at the influence of ground and wheel simulation techniques on the flow around vehicles. The yaw angle onto the front wheels of a small passenger car was found to decrease for moving belt and rotating wheels compared to using a fixed groundplane and stationary wheels. Blocking the radiators reduced this flow angle onto the wheels in both cases. Thus, it was stated that improving the groundplane and wheel simulation would be significant in regards to measuring the cooling properties of a vehicle. Pressure measurements along the length of the vehicle showed that these changes affected the rest of the vehicle body. The total pressure coefficient downstream of the rotating wheels was more negative than the profile downstream of the fixed wheels. Blocking off the cooling flow also reduced the underbody total pressure distribution and seemed to increase the influence of

[1]Tare measurements are corrections that are applied to measured forces and moments to account for balance offsets and the influence of the model support system

the wheel wakes even further downstream.

Numerical simulations of shrouded wheel flows have been very limited. Full vehicle simulations tend to have either no wheels modelled, or are only modelled with a very course mesh. Piccioni *et al Ref.[34]*, looked at different fender shapes for a motorcycle wheel to try to reduce its lift. However, by its nature, this only simulated a limited enclosure of the wheel.

2.3 Summary

From this chapter it can be summarized that:

1. During wind tunnel tests there should be contact between the wheels and groundplane. A gap would have significant effects on both the aerodynamic forces produced by the wheel and the surface pressures on the groundplane.

2. For CFD modelling of isolated wheels enough validation data is provided by Fackrell, *Ref.[22]*. Both detailed geometrical information is given as well as wheel surface static pressures and wake total pressures.

3. The modelling of the viscous properties of the flowfield around a wheel will be crucial for accurate simulation. Emphasis will have to be given to both the turbulence model and boundary layer resolution.

4. An exact match of the geometrical properties of the wheel groundplane contact patch will not have to be modelled; an approximate shape should have minimal effect on the global flowfield around the wheel. However, a good quality refined mesh will be required in this area to try to capture the flowfield features proposed by Fackrell, *Ref.[22]*.

5. Whilst providing useful introductions to the subject none of the published information regarding shrouded wheel flows provide enough data for validation of a CFD model. Geometric dimensions are limited, and neither enough force or pressure data for a range of configurations is tabulated. Therefore, a specific experimental programme should be instigated for this purpose.

Chapter 3

Computational Method

3.1 Introduction

At the start of the research programme a study was made into which of the range of computational methods outlined in Chapter 1 would be most suitable for solving the type of flows that were to be modelled. This encompassed both the suitability of the numerics and the practicalities of establishing the analysis procedure at Cranfield.

With Fackrell, *Ref.[22]*, highlighting the importance of viscous effects in the flow-field around an isolated wheel both linear and Euler methods were immediately discounted. Similarly, due to the very high turbulence intensities recorded by Oswald and Browne, *Ref.[28]*, the use of laminar versions of steady state RANS codes would probably give unrealistic results. However, a laminar facility would probably be useful due to a critical Reynolds number having been observed for stationary isolated wheels on a fixed groundplane. Therefore, the main focus of attention was methods of turbulent viscous simulation.

Even during the early stages of the research it was evident that access to massive computer resources would be unlikely. Thus, only methods of solving the turbulent versions of the RANS equations were considered. However, with the emphasis of the research being using CFD as an aerodynamic tool, and not the development of numerical techniques such as RANS vorticity methods (for example, Turkiyyah *et al*, *Ref.[35]*), it was decided that an existing commercial RANS code should be used as the basis of the research.

From the main incompressible flow codes on the market at that time only the Fluent

Incorporated range of products was available at Cranfield. As experience was gained with Fluent 4.3.2 during a Master of Science degree thesis, *Ref.[36]*, it was decided to continue with this suite of products. Two solver codes were suitable. Fluent V4 was a body fitted hexahedral cell block structured code whilst FLUENT/UNS V4 was capable, through its unstructured mesh file structure, of solution with both hexahedral and tetrahedral element based meshes. To ensure that the complexity of the planned shrouded wheel geometries could be meshed for solution to a high enough quality for accurate solutions FLUENT/UNS 4.2 (hereafter referred to as just FLUENT/UNS) was chosen as the main analysis code so as to provide maximum flexibility in grid topologies.

Full details of the numerics contained within, and procedures of how to use, FLUENT/UNS can be found in *Ref.[37]*. The following sections will give a brief overview of how the code was utilized for this research, together with its associated codes, including the numerical options investigated to improve the accuracy of the simulations.

3.2 The Solution Procedure with FLUENT/UNS

The process of obtaining a CFD solution of a flowfield with FLUENT/UNS comprised of four steps:

1. Pre-processing: geometry preparation, surface mesh generation, & volume mesh generation
2. Definition of initial solution parameters for numerics and boundary conditions
3. Iteration of solution to convergence
4. Post-processing of computed flowfield

3.2.1 Pre-processing

To prepare computational meshes for FLUENT/UNS, Fluent Incorporated distributed two pre-processors; Geomesh 3.0, *Ref.[38]*, and TGrid 3.0, *Ref.[39]*. The use of either package depended on which type of mesh topology was to be generated.

Geomesh consisted of two main modules. The first, ICEM DDN, was a geometry modeller which contained many of the features found in current CAD packages. Either geometry could be imported in IGES format or created / edited with the point, curve, and surface tools.

This geometry then formed the basis on which mesh blocks were built in the grid generator P-Cube. This could generate in 2D either quadrilateral or triangular meshes, and in 3D hexahedral volume meshes or unstructured surface meshes. Only one type of element, however, could be generated in a single mesh. A user-defined structure of interconnected faces or blocks would be overlaid, and in the cases of complex surfaces mapped onto, the geometry constructed in DDN. These blocks then define the structure of the mesh around the geometry. On the edges of the faces or blocks both boundary conditions, such as wall, velocity inlet, or symmetry, and node distributions were defined. Thus the mesh could be structured so that the mesh would be concentrated in areas of any expected large gradients in the fluid properties; for example, boundary layers. Finally the mesh would be generated and smoothed.

TGrid provided the capability of generating 3D unstructured volume meshes consisting of either solely tetrahedral elements, or with a hybrid structure with tetrahedral, prismatic, and pyramidal cells. Any number of 3D hexahedral or tetrahedral volume meshes and 3D unstructured surface meshes could be simultaneously imported and merged. It could also generate 2D unstructured meshes.

Pyramidal elements were used to provide an interface between a quadrilateral face of a hexahedral mesh element and the tetrahedral mesh. A pyramidal element had the quadrilateral face as its base, and four triangular faces extending from its sides up to a single point above the base. From either quadrilateral or triangular faces prismatic volume elements could be extruded from a boundary, with various growth parameters such as constant or exponential, giving hexahedral or five sided elements. Prisms could bc used to resolve a boundary layer region in an otherwise triangular or tetrahedral mesh, to extend some portion of a domain for which a volume mesh exists (for example, increase the length of an inlet pipe), or to create a volume mesh by extrusion.

Once all the prism layers and pyramidal elements had been created then a sub-domain could be defined in which an tetrahedral volume mesh could be automatically generated. This then could be refined locally to provide extra resolution in areas

where important flow features were expected in the solution to further improve the accuracy of the simulations.

3.2.2 Definition of Initial Solution Parameters

Once the final volume mesh had been successfully generated and imported into the FLUENT/UNS solver the steps that needed to be completed before iteration of the solution could begin can be summarized as:

1. *Mesh Checking and Modification*
   To ensure that the mesh was suitable for a solution mesh checking was required to verify, for example, that there were no degenerate elements. These were most likely to occur in areas close to highly curved surfaces, or within corners. Meshes were then partitioned for use in the parallel version of the solver. Mesh zones could also be modified for extra convenience, especially in the setting of boundary conditions and post-processing, and scaled to SI units.

2. *Choice of Computational and Physical Models*
   To set-up the solver to best simulate the flowfield of interest both the reduction of numerical errors and the use of the most appropriate physical models are important. Would the solver be used to solve for an inviscid, laminar, or turbulent flow, steady state or unsteady, incompressible or mildly compressible, with or without heat transfer to surfaces etc.? What order of discretization would be used with what degree of under-relaxation, or solution acceleration? All these choices will have an influence as to how accurate a simulation would be and, therefore, require investigating.

3. *Boundary Conditions*
   The boundary conditions specify all the information on the state of the flow simulation at the boundary zones of the computational mesh. This includes setting of the material properties of the fluid or fluids of interest. For incompressible turbulent flow the main boundary conditions in FLUENT/UNS were velocity inlets where velocity and turbulence parameters are set for flow entering the computational domain, pressure outlets for flow leaving the domain, and for bounding the fluid zones walls, whether moving or stationary, and symmetry planes.

Apart from the mesh generation these three steps are all that influence whether a simulation would be successful or not.

3.2.3 Solution Iteration

Once the definition of the parameters of the flow simulation had been completed, flow variables for the solution to iterate from had to be initialized onto all the cell centres of the mesh. Only then can the discretized form of the governing equations be solved sequentially using pressure correction methods:

1. The momentum equations are each solved in turn using the current pressure values giving an updated pressure field
2. The pressure correction equation is solved, and the pressure and velocity fields corrected, so that the continuity equation is satisfied
3. For turbulent flow the discretized equations of the turbulence model are solved using the updated velocity data
4. Fluid properties are updated
5. A check on convergence is made

If the convergence criterion is satisfied the iteration procedure is completed and the final solution data is written to file. Otherwise, another loop, or iteration, of the above procedure is made. If the numerical parameters are set correctly then the amount that the solution changes per iteration should decrease until the convergence criterion is reached.

A number of methods are available to monitor convergence. The classical way is with normalized residuals. Residuals are a measure of how much the solution changes, or its error, per iteration, relative to the maximum change which normally occurs in the first few iterations. However, the maximum residual can vary in size depending on the settings of the numerical parameters, such as under-relaxation, and the solution can still be changing dramatically even if the normalized residuals have reduced by three orders, the usual measure of convergence.

Therefore, for this research, it was decided that the actual predicted force on bodies within the computational domain, for example, the wheel, should be monitored at

the end of every iteration. Only when these forces have stabilized to a value was the solution said to be converged.

3.2.4 Post-processing

Within FLUENT/UNS solutions could be examined through the use of contour plots, velocity vector, path line analysis, and x-y plots of solution variables. Both graphical hardcopy could be made and data exported to ascii files.

3.3 Turbulence Modelling

The quality of the turbulence model will be crucial if the CFD solutions are going to be within acceptable limits of experimental data. As well as being able to be configured for laminar calculations FLUENT/UNS provided two two-equation turbulence models and the Reynolds stress model. As the Reynolds stress model is more memory and CPU intensive than the two-equation models, and is also more numerically unstable, it was decided to solely concentrate on studying the effects of the two simpler models.

In two-equation turbulence models the effects of turbulence are represented by a turbulent viscosity which is derived from turbulent kinetic energy and its rate of dissipation. These two quantities, k and ϵ, are obtained from the solutions of the two transport equations of the turbulence model.

The two two-equation turbulence models provided by FLUENT/UNS are:

1. Standard k-ϵ model
2. Renormalization Group (RNG) based k-ϵ model

3.3.1 Standard k-ϵ Model

The standard k-ϵ model in FLUENT/UNS was initially proposed by Jones and Launder, *Ref.[40]*, and developed by Launder and Spalding, *Ref.[41]*. It is a semi-empirical model, and the derivation of the model equations, including the various

	$C_{1\epsilon}$	$C_{2\epsilon}$	C_μ	σ_k	σ_ϵ	α_0
k-ϵ	1.44	1.92	0.09	1.0	1.3	-
RNG k-ϵ	1.42	1.68	0.0845	-	-	1.0

Table 3.1: Turbulence Model Constants Used for the CFD Calculations

model constants, relies on phenomenological considerations and empiricism. It is only valid for fully turbulent flows.

The Reynolds stresses in the steady state RANS equations are modelled using the Boussinesq hypothesis. A consequence of this is the need for five constants in the model. The default values for these constants in FLUENT/UNS were determined from experiments with air and water in shear flows. It is stated that they were found to work for a wide range of wall-bounded and free shear flows.

Throughout this research all constants in the turbulence models were kept at their default values, *Table 3.1.*

3.3.2 RNG k-ϵ Model

Unlike the standard k-ϵ model, the RNG-based k-ϵ turbulence model, *Ref.[42]*, is derived using mathematical techniques called Renormalization Group (RNG) methods. The analytical derivation results in a model with constants different from those in the standard k-ϵ model, and additional terms and functions in the transport equations for k and ϵ. For instance, the transport equation for ϵ contains a rate-of-strain term that is important for treatment of separated flows.

It is stated that the RNG k-ϵ model provides more universality and rigour over the standard k-ϵ model, and yields improved predictions for flows with high streamline curvature and streamwise vortices, separated and recirculating flows, low Reynolds number and transitional flows with a differential viscosity option, and wall heat and mass transfer.

3.3.3 Near Wall Treatment for Wall Bounded Flows

Turbulent flows in the regions close to the wall boundaries are affected by the presence of these walls. Firstly, the mean velocity field is affected through the no-slip

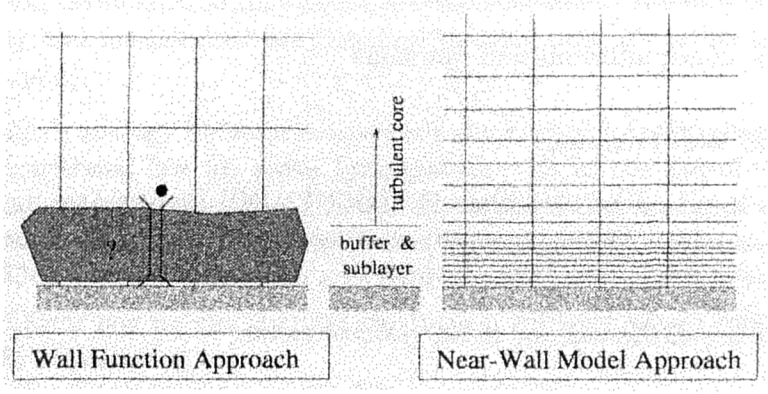

Figure 3.1: Near Wall Treatments for Fully Turbulent Flow in FLUENT/UNS

condition. Secondly, the turbulence field is also influenced by the presence of the wall. Very close to the wall, the turbulence is damped, but toward the outer part of the near-wall region of the boundary layer the turbulence intensity is increased by the production of turbulent kinetic energy due to Reynolds stresses and the large velocity gradients.

Thus, the near wall modelling significantly impacts the accuracy of the solutions. Therefore, accurate prediction of the flow in the near wall region is a large factor in the successful prediction of wall bounded turbulent flows. In FLUENT/UNS there are two approaches to modelling this near wall region; wall functions and a near wall, or two-layer, approach, *Fig.3.1.* With the wall function approach the inner regions of any boundary layer (the viscous sublayer and the buffer layer) are not resolved. Instead, semi-empirical formulas, the wall functions, are used to 'bridge' the regions between the wall and the fully-turbulent bulk flow region. This has the advantage of saving computational resources as the region with the largest gradients does not have to be resolved. However, if the assumptions made in the formulation of the wall function are not valid for a flow structure then accuracy will be compromised.

FLUENT/UNS offered two choices for the wall function approach:

1. Standard wall function
2. Non-equilibrium wall function

The standard wall function is based on the work of Launder and Spalding, *Ref.[43].* However, it is assumed that the rates of production and dissipation of turbulent kinetic energy are equal. The non-equilibrium wall function removes this constraint,

and also accounts for pressure gradient effects on mean velocity.

With the two-layer model, wall functions are completely abandoned in favour of resolving the viscosity affected near wall region of the boundary layer all the way to the viscous sublayer, i.e. the complete boundary layer is resolved numerically with the mesh. Therefore, the mesh spacing next to a wall boundary has to be suitable for the near wall treatment being used. As well as having enough mesh density to adequately resolve the gradients within the boundary layer the distance from the wall boundary to the centre of the wall adjacent cells must correspond to the part of the boundary layer that can be resolved with the near wall scheme. These distances are measured in numbers of wall units, y^+. For the wall function approach the first cell centre distance should be approximately 30 wall units from the wall boundary. However, with the two layer approach the wall adjacent cell centre distance should be of the order of a single wall unit. Also, at least ten cells should be located within the near wall region of the boundary layer - the region 'bridged' by the wall function. Therefore, a mesh for the near wall approach will have to be much larger than a mesh for the wall function approach, assuming identical meshes away from the wall boundaries.

3.4 Numerical Parameters

3.4.1 Discretization Schemes

FLUENT/UNS allowed the choice the discretization scheme for the convection terms of each governing equation. Second-order accuracy was automatically used for the viscous terms. By default, all the equations are solved using the first-order upwind discretization for convection. However, for increased accuracy, all solutions were obtained with second order upwind discretization of the convection terms.

3.4.2 Underrelaxation Values

The underrelaxation values set for the solution process control the amount a solution can vary between each iteration. Especially in the early stages of iteration, if the underrelaxation values are set too large then the solution can diverge.

Due to the complex flow structures that were being predicted it was necessary to

	Conservative Values	Aggressive Values
Pressure	0.25	0.50
Momentum	0.50	0.75
Turbulence Kinetic Energy	0.50	0.75
Turbulence Dissipation Rate	0.50	0.75
Density	0.50	0.75
Body Forces	0.50	0.75
Viscosity	0.50	0.75

Table 3.2: Underrelaxation Values Used for the CFD Calculations

change the values of the underrelaxation parameters during the iteration process. Depending on the stability of the solution the following values were determined through experience, and used for the calculations throughout the research, *Table 3.2.*

3.4.3 PRESTO

Linear interpolation is the default procedure for computing the pressure at the centre of a face of a cell from the adjoining cell centre values. These face pressures are required due to the way the momentum equations are discretized. For flows with large pressure gradients an accurate solution will, therefore, require small volume cells in these areas. PRESTO, PREssure STaggering Option, *Ref.[37]*, is an effectively higher order interpolation scheme, which reduces the number of cells required, but can only be used with quadrilateral and hexahedral mesh elements. Instead of solving both pressure and velocity at the cell centres the pressure field is calculated at a staggered control volume centred, instead, on the cell faces.

A similar procedure for a staggered grid scheme is outlined by Patanker, *Ref.[44]*.

3.4.4 SIMPLE and SIMPLEC

As previously described, the momentum and continuity equations are solved sequentially. In this sequential procedure, the continuity equation is used as an equation for pressure. However, if the assumption is made of incompressible flow, pressure does

not explicitly appear in the continuity equation. Then the SIMPLE (Semi-Implicit Method for Pressure Linked Equations) family of algorithms, *Ref.[44]*, is used for this purpose. These use a relationship between velocity and pressure corrections to enforce mass conservation and to obtain the pressure field.

In FLUENT/UNS, both the standard SIMPLE algorithm and the SIMPLEC (SIMPLE-Consistent) algorithm, *Ref.[45]*, are available. SIMPLEC is stated to give better convergence than SIMPLE because it allows higher underrelaxation values to be used as well as giving improved pressure and velocity coupling.

3.4.5 Implicit Body Forces

When large body forces exist, the body force and pressure gradient terms in the momentum equation are almost in equilibrium, with the contributions of convective and viscous terms small in comparison. The segregated algorithms, like SIMPLE and SIMPLEC, converge poorly unless partial equilibrium of pressure gradient and body forces is taken into account. This procedure is called the 'implicit body force' treatment in FLUENT/UNS. Its use adds an extra corrective term for the body forces into the SIMPLE and SIMPLEC algorithms for cell centre pressures and face flow rates.

3.5 Memory Requirements

As well as the structure of the fluid flow to be resolved influencing both the mesh size and the solver numerics, the amount of computer resources available, especially memory, will be the other main limiting factor to the complexity and size of any solution. The large number of variables to be stored for each mesh element cell centre means that memory requirements would be substantial, especially in 3D.

Geomesh, when used to create block structured hexahedral meshes, would present minimal memory problems. With its regular array based i,j,k storage 256Mb[1] would have been sufficient for generating million cell plus meshes. However, TGrid also has to store unstructured node connectivities, as well as the coordinate data, and therefore memory requirements were higher; approximately 400Mb RAM per one million cells.

[1] All references to memory usage are for 32-bit, not 64-bit, operating systems

For setting up the initial solution parameters in FLUENT/UNS extra system resources would be required; for a one million cell case approximately 750Mb RAM. To run the solution in serial mode 1Gb RAM would be required per one million cells. For processing in parallel this increases further due to having to store the partition information. These figures are for a typical incompressible flow configuration with a two-equation turbulence model.

Post-processing with FLUENT/UNS would require similar amounts of memory as running in serial, i.e. approximately 1Mb RAM for every one thousand cells in 3D.

3.6 Availability of Computational Resources

At the start of the research the main computer facility used was an SGI Indy workstation fitted with a R5000 processor and 256Mb RAM. This provided enough resources for the 2D calculations and early 3D isolated wheel models. The acquisition of a dual R10000 195MHz processor SGI Octane fitted with 1Gb RAM allowed the development of larger isolated wheel models and the initial shrouded wheel solutions.

To iterate larger models the Octane was used in parallel at Cranfield with dual processor DEC Alpha machines, along with Hewlett Packard resources at Rover Group Ltd.

3.7 Summary

From this chapter it can be summarized that:

1. A review of possible computational methods was made and FLUENT/UNS, a commercial RANS solver, was selected so that the emphasis of the research could be aerodynamics and not numerical development.

2. The solution procedure has been briefly described, from mesh generation, the definition of the problem in the solver, iteration, and through to post-processing. A number of turbulence modelling and numerical options have been highlighted that will have an influence on the solution, and therefore will require investigating.

3. A method for judging convergence based on the stability of the computed forces acting on bodies within the domain was determined to be the way of deciding when to stop iterating a solution.

4. The amount of memory required for each stage of the solution process has been identified.

Chapter 4

Preliminary Two Dimensional Studies

Before starting on the modelling of the complex three dimensional wheel flows it was deemed important to complete some preliminary two dimensional studies. The aims were to gain experience with the new code, FLUENT/UNS, to verify that the solver could predict the types of flow structure expected around a 3D wheel, and to develop mesh topologies. The basis of these studies was the 2D circular cylinder. The effects of cylinder rotation (to check the effectiveness of moving wall boundary conditions with angular velocities), and groundplane proximity (to check the interactions between adjoining boundaries), were modelled. The aim, however, was not to quantitatively validate the results but to gain confidence in the solution procedure by verifying that the predicted flowfields were qualitatively accurate.

4.1 Rotational Boundary Conditions

The study of the flow around a two dimensional cylinder is one of the most researched flowfields in aerodynamics. Zdravkovich, *Ref.[46]*, provides a very comprehensive review of the aerodynamic properties of such flows.

When a circular cylinder is rotated at an angular velocity four times that of freestream a saddle point below the cylinder has been observed. Prandtl and Tietjens, *Ref.[47]*, presented flow visualization images which showed that the location of this saddle point was slightly away from the surface of the cylinder due to the viscosity of the

fluid. No details of the freestream flow conditions, or geometric dimensions of the cylinder, were given. However, from the authors' general description of experimental techniques for flow visualization it is probable that that the Reynolds number was of the order of hundreds.

With Fackrell, *Ref.[22]*, showing the importance of viscous effects in the flowfield around a 3D isolated wheel it was decided that a structured grid topology would be used throughout the domain for resolution of the boundary layers present next to wall boundaries. An O-type topology was developed around a cylinder of diameter 0.005m with 240 cells circumferentially around the cylinder surface at an even spacing of one per every 1.5 degrees. This, together with the fine mesh in the normal direction away from the cylinder surface to resolve the saddle point area, gave a mesh of 51,200 quadrilateral elements.

The solver was used in its laminar configuration. A freestream velocity of 1m/s was defined which gave a Reynolds number, Re_D, of 342.3. A comparison of the predicted streamlines with the experimental visualization is shown in *Fig.4.1.* The comparison of the structure of the saddle point predicted below the cylinder was excellent. Given the unknown Reynolds number of the experiment the location of the saddle point was also considered good and thus it was concluded that the treatment of moving wall boundary conditions within FLUENT/UNS was good enough for modelling wheel flows.

4.2 The Geometry of the Wheel Contact Patch

Previous work by the author, *Ref.[36]*, looked at modelling the flow over a two dimensional circular cylinder resting on an infinite groundplane. It was found that it was very unlikely to be able to obtain grid-independent solutions unless some modifications to the theoretical tangential convergence of the two solid surfaces were made. Thus, instead of having a tangential contact point the cylinder surface was shortened to end at 5° and 355°, 0° being the actual contact point, *Fig.4.2*,[1] and two small verticals were used instead to represent the physical contact between the cylinder and the groundplane. The criterion used to decide the location, and thus size, of these verticals was to make them as small as possible whilst allowing for enough cells of low aspect ratio to adequately represent an important region for

[1]This angular notation differs from the one used by Fackrell, *Ref.[22]*, where 0° was at the front of the wheel and 90° at the contact patch

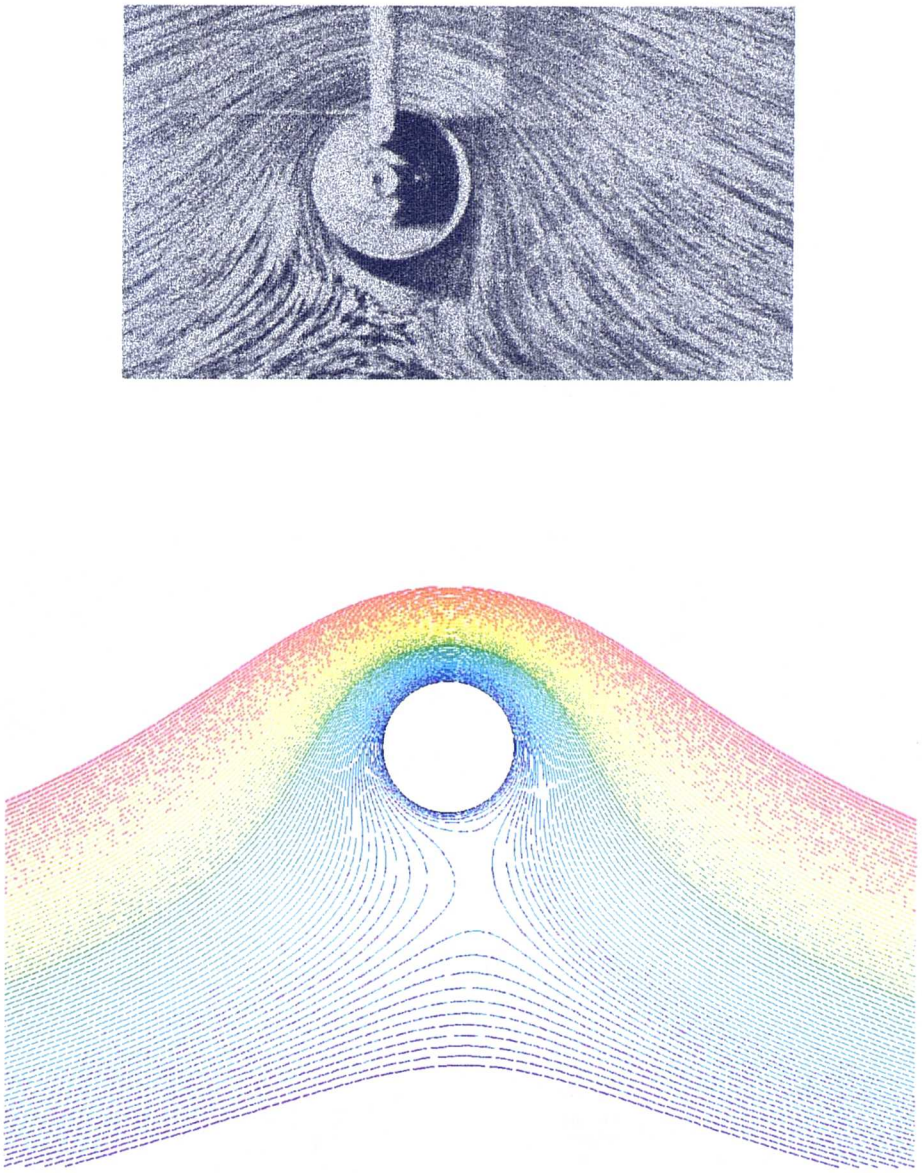

Figure 4.1: Comparison of Experimental (Prandtl & Tietjens) and Computational Results for the Flow Around a Rotating Two Dimensional Cylinder with a Circumferential to Freestream Velocity Ratio of Four at Low Reynolds Number

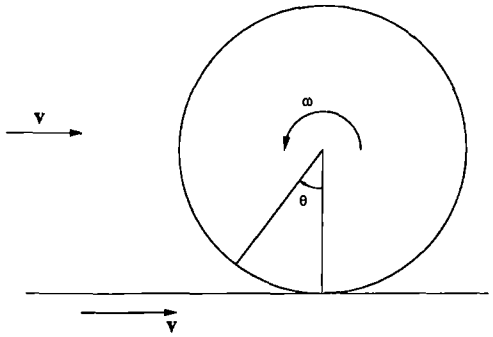

Figure 4.2: Description of Angular Position for Locations on the Surface of a Circular Cylinder / Wheel

when rotation of the cylinder along the groundplane was modelled.

However, as modelling this flowfield was going to aid the development of a mesh topology for a 3D simulation of the flow around an isolated wheel, it was thought that the angular location of these verticals should be more related to actual tyre contact patch geometry.

The deformation of a pneumatic tyre rolling on a solid surface is affected by the dimensions of the tyre, the carcass stiffness, inflation pressure, and axle load, *Ref.[48]*. Upadhyaya and Wulfsohn, *Ref.[49]*, derived mathematical expressions for the length, width, and area of the contact patch of a stationary wheel under load on a rigid surface, and verified them with experimental results. Although more related to agricultural tyres with a rounder profile than a road tyre, the results can be used to give an approximation for the length of the contact patch. From this a cut-off angle, defined as the angle around the tyre's rotational axis between the tangential contact point and its vertical ground contact approximations, and the height of these vertical edges can be derived.

The expression for contact length, l_c, was given as

$$l_c = 2\sqrt{\frac{\delta_z(2R_2 - \delta_z)(R_1 - \delta_z)}{R_2 - \delta_z}}$$

where

R_1 : tyre radius (m)
R_2 : tread envelope radius (m)
δ_z : amount of tyre deflection in the vertical plane (m)

The tread envelope radius is defined to be the approximate radius of the outside of the tread of the tyre taken in profile, *Fig.4.3*. As such a value does not apply

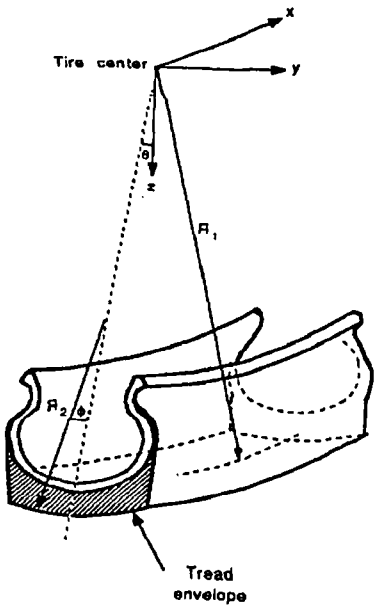

Figure 4.3: Definition of Tyre Geometry (Upadhyaya and Wulfsohn)

to a road tyre it is proposed to use for this variable the radius of the edge of the tyre. Taking the tyre radius to be 0.25m, with a tread radius of 0.02m and vertical deflection of 0.005m, gave a tyre contact length, l_c, of 0.107m, and a cut-off angle, θ, of 12.36°. The height of the verticals would then be 0.0058m, or 1.16% of the wheel diameter, D.

However, as agricultural tyres are generally inflated to a lower pressure than road tyres it would be expected that tyre contact lengths for road tyres are smaller than those for agricultural tyres. Thus, it is proposed that the cut-off angle be limited to 10°. This gives a tyre contact length of 0.084m and a vertical height of 0.0038m, or 0.76% of D. This vertical length should allow enough room for two blocks of mesh to give good boundary layer definition on both the groundplane and the wheel surface.

4.3 The Flow Over a Two Dimensional Cylinder Resting on an Infinite Groundplane

Despite the amount of knowledge about the flow around an isolated circular cylinder, when the same cylinder is placed near to, or against, a plane boundary the extent

of the published research is extremely limited.

The introduction of the plane boundary affects the flow field in two major manners. Firstly circulation around the cylinder is prohibited when there exists contact between the two surfaces. Also, the flowfield upstream of the cylinder is not uniform; the boundary layer on the surface on which the cylinder is resting results in a sheared freestream velocity profile.

The main source of previous experimental work into this flow at high Reynolds numbers was performed by Bearman and Zdravkovich, *Ref.[50]*.

Previous work by the author, *Ref.[36]*, described the results of preliminary CFD models of this type of flowfield. Due to the single block restrictions of the mesh generator used it was considered that remodelling this flowfield with FLUENT/UNS, using a multiblock structured mesh generated with Geomesh, would give an indication of the influence of the mesh on the solutions. This then could be applied to the initial 3D isolated wheel solutions through the structure of the symmetry plane located on the centreline of the wheel.

4.3.1 Bearman and Zdravkovich

The cylinder, of 0.019m diameter, spanned the test section of the 1m × 0.61m closed test section closed return wind tunnel at Imperial College, London. It was placed 36 diameters downstream of the leading edge of a full width flat plate, which was aligned parallel to the freestream and midway up the working section. This was 1m long and 0.01m thick. A small flap on its trailing edge allowed for correction of any local flow asymmetries around the rounded leading edge. Distributions of mean surface static pressure coefficient on the cylinder surface, and along the flat plate, were measured at a Reynolds number, Re_D, of 4.8×10^4 for various cylinder to flat plate distances including contact between the two surfaces. Due to the magnitude of the Reynolds number a trip wire, of diameter 0.001m, was attached across the flat plate 0.14m from its leading edge. Freestream turbulence levels were measured to be less than 0.2%. The thickness of the turbulent boundary layer on the plate at the cylinder position, but with it removed from the tunnel, was stated to be equal to 0.8 cylinder diameters.

Once initial model development had been completed, and the mesh structure of 49,876 cells, *Fig.4.4*, defined, two final simulations were run; one fully turbulent

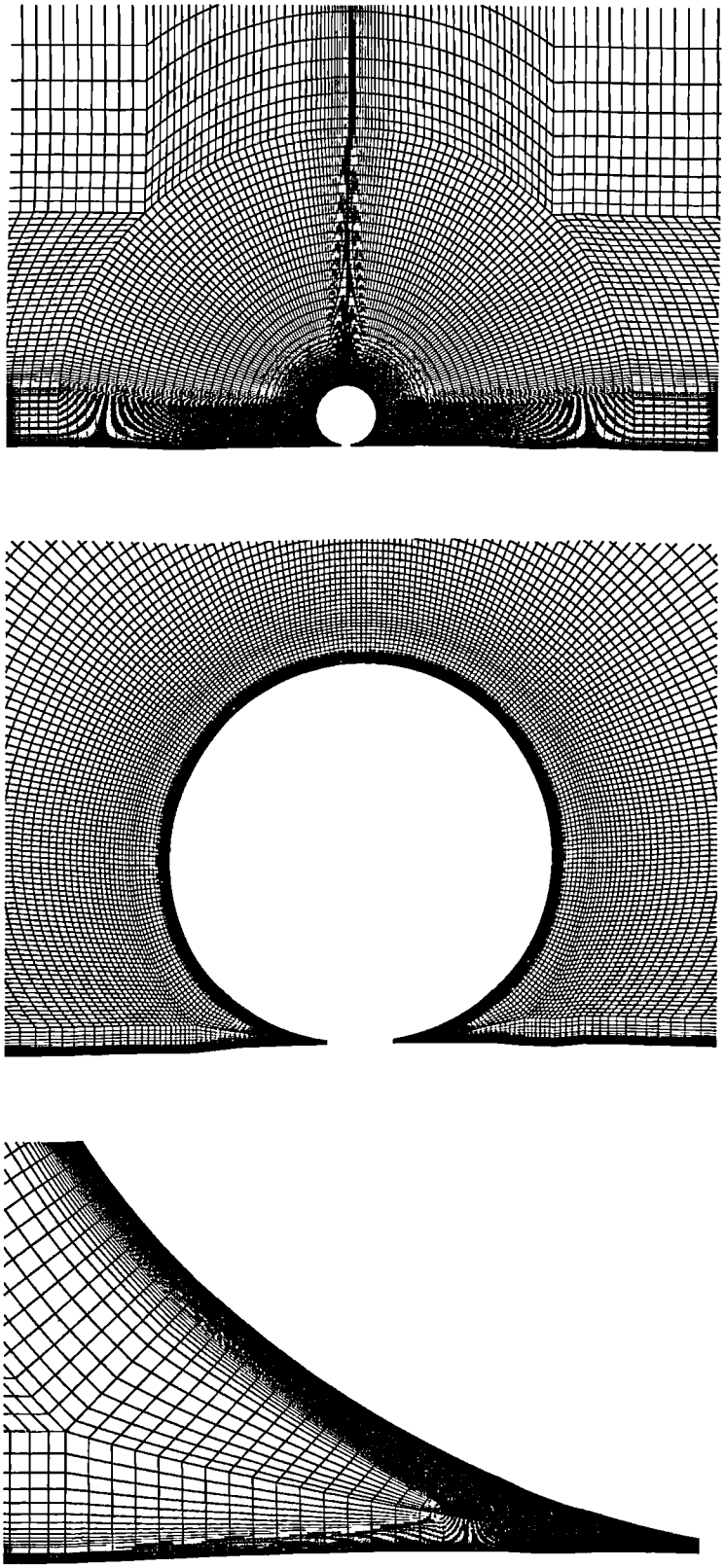

Figure 4.4: The Mesh Structure for the Flow Over a Two Dimensional Cylinder Resting on an Infinite Groundplane

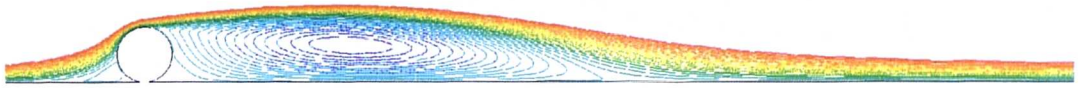

Figure 4.5: The Fully Turbulent Flow Over a Two Dimensional Cylinder Resting on an Infinite Groundplane at a Reynolds number, Re_D, of 4.8×10^4

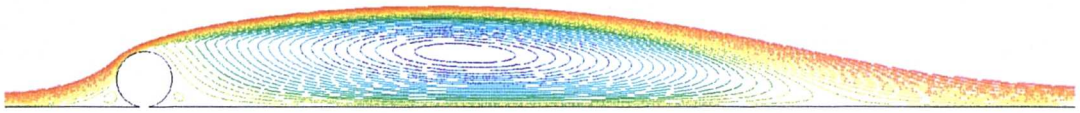

Figure 4.6: The Hybrid Laminar / Turbulent Flow Over a Two Dimensional Cylinder Resting on an Infinite Groundplane at a Reynolds number, Re_D, of 4.8×10^4

whilst the other used a hybrid laminar / turbulent calculation. Both used the RNG $k - \epsilon$ turbulence model with full two-layer closure. In the first the turbulence model was applied throughout the domain, whilst in the hybrid case two separate fluid zones were used. In this case the turbulence equations were not solved in two localized areas. One area was placed from the leading edge of the plate to the trip position, and the second was around the whole of the cylinder surface. These strips extended 0.05m away from the wall boundary surfaces; this distance being chosen due to existing domain and mesh block topology. However, in the region of the contact patch the boundary between the laminar and turbulent zones bisected the distance between the cylinder and the groundplane.

Fig.4.5 and *Fig.4.6* show the streamlines over the cylinder for the two flowfields. The use of laminar zones had a significant influence on the wake structure behind the cylinder. Earlier separation from the surface of the cylinder gave a taller and longer wake than that in the fully turbulent case. This change in separation position resulted in a much smaller suction peak on the cylinder surface, a Cp of -0.65 compared to -1.6 for the fully turbulent solution, *Fig.4.7*.

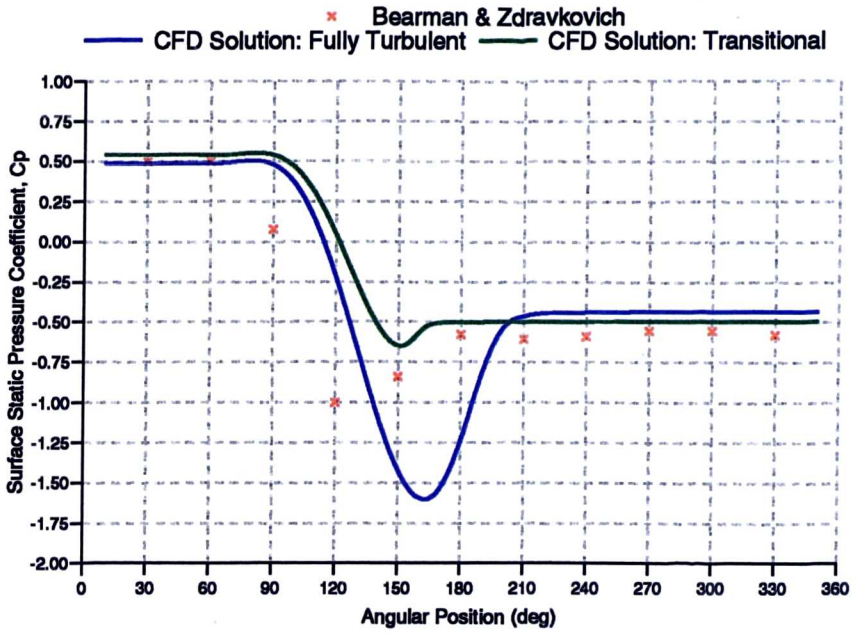

Figure 4.7: Comparison of CFD and Experimental Cylinder Surface Static Pressure Coefficient Distributions for the Flow Over a Two Dimensional Cylinder Resting on an Infinite Groundplane at a Reynolds number, Re_D, of 4.8×10^4

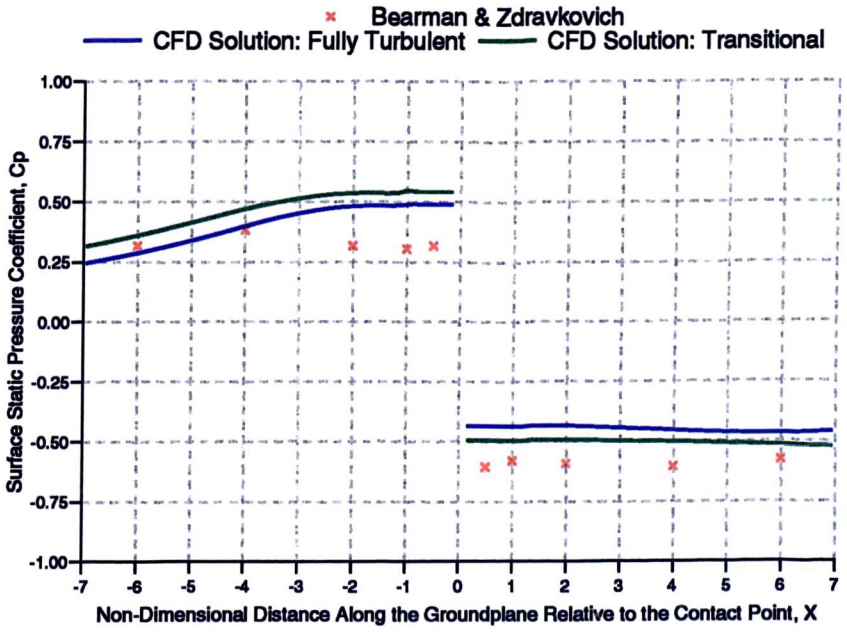

Figure 4.8: Comparison of CFD and Experimental Groundplane Surface Static Pressure Coefficient Distributions for the Flow Over a Two Dimensional Cylinder Resting on an Infinite Groundplane at a Reynolds number, Re_D, of 4.8×10^4

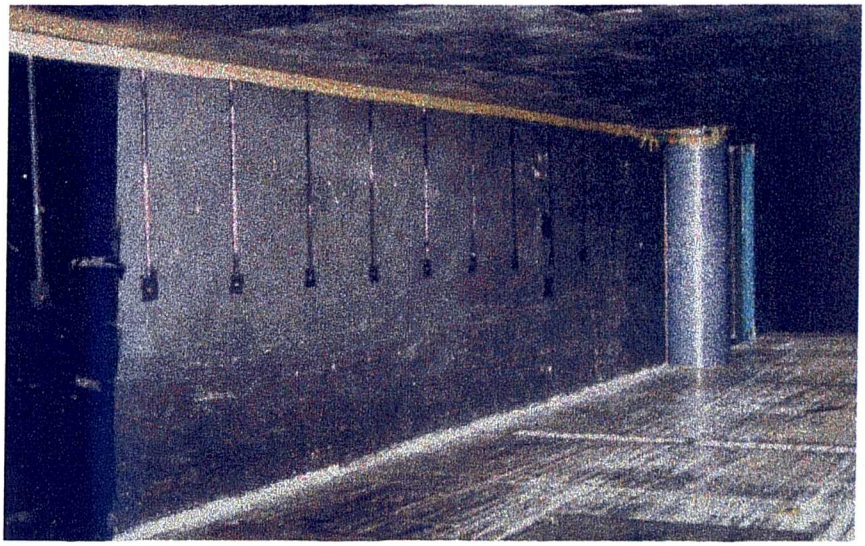

Figure 4.9: Downstream View of the Experimental Setup in the 8' × 4' tunnel at Cranfield College of Aeronautics

Comparison with the experimental data was poor. Neither solution predicted the location of the suction peak, between 120° and 150°, correctly. The hybrid solution, at 150°, was closer than the fully turbulent solution, at 165°. The interactions with the groundplane boundary layer were inadequately resolved, *Fig.4.8*. Despite this, the base pressure prediction was reasonable.

Whilst the set-up of the hybrid case is not meant to be a method for the prediction of boundary layer transition it is clear that the low Reynolds number of the experimental data made it difficult to obtain comparative surface static pressure coefficient distributions. Thus it was decided to obtain experimental data at higher Reynolds numbers.

4.3.2 Simulations at Higher Reynolds Numbers

During earlier work by the author, *Ref.[36]*, a period of experimental work to obtain surface pressure measurements was completed in the 8' wide × 4' high atmospheric boundary layer tunnel at Cranfield College of Aeronautics. Then, problems were encountered with the three piece plastic cylinder flexing away from the tunnel wall due to the aerodynamic load. Therefore, for this set of similar experiments, *Fig.4.9*, the cylinder was bolted to the tunnel sidewall at 4 spanwise locations and the contact area further sealed with aluminium tape. Pressure data, both on the cylinder surface

and the tunnel sidewall, Appendix B, was taken for Reynolds numbers of 2.0×10^5, 3.0×10^5, and 4.0×10^5 based on the cylinder diameter of 0.314m. Freestream turbulence intensity was measured to be approximately 1.0%.

Smoke flow visualization revealed flow features relating to the small aspect ratio of the cylinder. Large areas of three dimensionality, especially near to the the wind tunnel floor and roof, were found. However, in the plane of the pressure tappings the flow structure was found to be acceptable as the dominant flow component was in the freestream direction.

To minimize any transitional issues, all validation work used the pressure data at the highest Reynolds number, Re_D, 4.0×10^5. Two meshes were developed using the same basic topology as used for the Bearman and Zdravkovich calculations. One had 41,700 cells and the second 166,800 cells. This larger mesh was generated from the first by subdividing all the cells into four. This meant the first cell distance from the wall boundaries halved but as the y^+ values from the smaller mesh were in the upper part of the allowable range this was not considered a problem. The inlet to the computational domain was placed so that the experimental boundary layer thickness measured on the tunnel wall at the location of the cylinder was matched computationally. At this inlet boundary the turbulence parameters were set to a 1.0% freestream turbulence intensity and a length scale equal to the diameter of the cylinder. The inlet velocity was 18.82m/s.

At this higher Reynolds number the comparison with experimental data, *Fig.4.10* and *Fig.4.11*, was much more encouraging. The angular position of the suction peak on the cylinder surface, at 165°, was predicted to within a few degrees for both meshes. However, the prediction of the magnitude of the suction peak was influenced by the mesh. The over-prediction with the finer mesh was under 10% whilst the use of the coarser mesh resulted in a under-prediction of approximately 15%. The finer mesh also better predicted the magnitude of the base pressure. The least accurate comparison was at the front of the contact patch between the cylinder surface and the tunnel wall.

The length of the wake behind the cylinder was also better predicted by the finer mesh. Although the length of the wake was still too large the profile of the pressure recovery with non-dimensional distance downstream of the cylinder was much more accurate than with the coarse mesh.

Fig.4.11 also shows the extent of the influence of the cylinder on the upstream

groundplane static pressure gradient. Its effect can be seen upto twenty cylinder radii upstream. As the wind tunnel used was an atmospheric boundary layer tunnel the cylinder was placed only two metres downstream of the end of the contraction to try to reduce as much as possible the boundary layer thickness on the tunnel sidewall (it was still 0.1m thick at the location used for the cylinder, measured without it in place). Thus, its influence would have extended into the contraction of the tunnel and, therefore, the boundary layer thickness modelled in the calculations could have been significantly different from that in the working section of the tunnel with the cylinder in place.

Fig.4.12, and *Fig.4.13*, show the effect of the groundplane boundary layer thickness on the CFD solutions. The inlet of the domain was moved closer to the cylinder by 0.5m. The reduction in the groundplane boundary thickness did not have any significant effects on the solution. A marginally larger suction peak was predicted as well as the distance for groundplane pressure recovery to occur behind the cylinder being slightly reduced.

The influence on the groundplane pressure distribution of the reduced inlet to cylinder distance was more important though. Instead of converging to a single pressure coefficient value towards the inlet the two profiles remained slightly offset from each other. This indicated that the blockage of the cylinder in the computational domain was having an influence on the pressure distribution on the inlet boundary.

Using the coarse mesh as a basis, this effect was investigated further. *Fig.4.14* shows the pressure distribution on the inlet of the domain, with non-dimensional distance above the groundplane, for three inlet locations of -6.0m, -4.0m, and -2.0m relative to cylinder and groundplane contact point. If the cylinder was having no effect on the inlet boundary then this profile would be a vertical straight line.

It is clear that there is an influence between the cylinder and the inlet boundaries in all three cases and that moving the inlet as far away from the cylinder as possible would be advantageous in terms of solution quality. If the object of interest was located in free space this would then only impact on total volume mesh size. However, the requirement for modelling the ground effect in automotive aerodynamics brings a further complication. If the whole of the bottom of the computational domain was modelled as a stationary groundplane then a significant boundary layer would be predicted. Any comparison made with experimental data would be made more difficult due to having to compromise between the location of the farfield of the computational domain and the accuracy of the prediction of the groundplane

boundary layer thickness.

With many modern fixed groundplane automotive tunnels, such as the MIRA full scale wind tunnel, using devices to reduce the influence of the floor boundary layer, it may be impossible to replicate computationally the groundplane boundary layer thickness without adversely affecting the numerical farfield boundary conditions. Even a compromised boundary layer thickness may bring inaccurate results, especially in areas of groundplane interaction such as wheel flows. Having the first part of the floor of the computational domain as a freestream pressure boundary, equivalent to modelling the test vehicle on a raised floor in the wind tunnel, may bring numerical convergence problems with pressure gradients from the downstream test vehicle affecting the transition from the freestream to the wall boundary condition.

Thus, not only does the mesh resolution affect the quality of CFD solutions, the placement, and treatment, of farfield boundaries can also affect numerical convergence and the predicted aerodynamics properties of a flow.

4.4 Summary

From this chapter it can be summarized that:

1. Computations of the flow about a rotating cylinder at a low Reynolds number have shown that FLUENT/UNS can adequately model rotating wall boundary conditions.

2. A initial study of the tyre deformation on a solid surface has been made and, based on this, the contact between the groundplane and the wheel surface will be modelled using vertical wall boundaries located at 10^o and 350^o. This will enable a structured grid to be used to discretize this region without the use of highly skewed cells, which would adversely effect the quality of any computational solution.

3. Calculations of the flow over a 2D cylinder resting on an infinite groundplane have shown the difficulties of modelling transitional flows with CFD. At higher Reynolds numbers the solutions showed qualitatively good agreement. This together with the rotational boundary condition simulation, gave encouragement in the capabilities of CFD being able to model 3D wheel flows.

4. A quadrilateral mesh structure has been developed in 2D which then could easily be used as a basis for a symmetry plane boundary mesh for a 3D isolated wheel solution.

5. The importance of moving the computational farfield boundaries as far away from the test vehicle has been shown. However, for automotive solutions, this will conflict with the requirements for matching the thickness of stationary groundplane boundary layers.

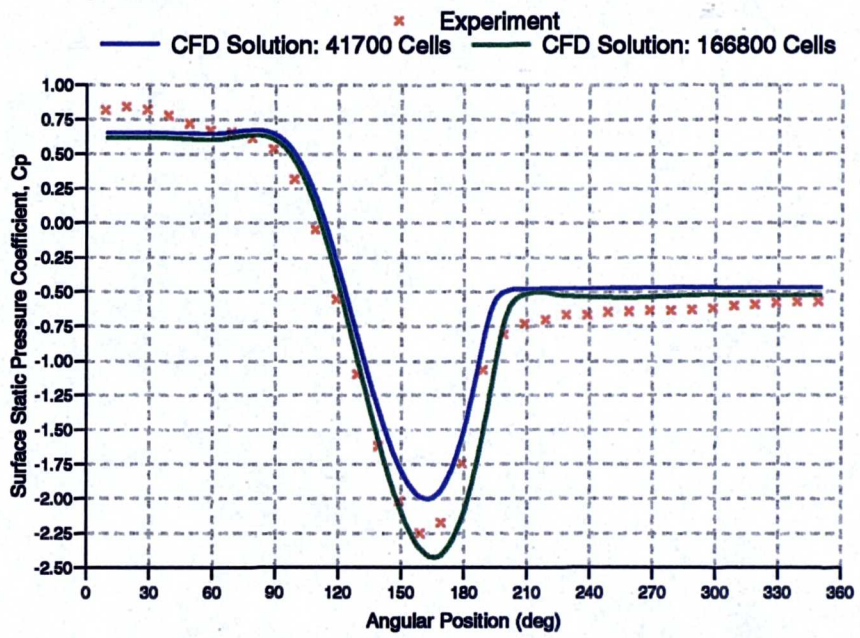

Figure 4.10: The Influence of Mesh Size on the Cylinder Surface Static Pressure Coefficient Distributions for the Flow Over a Two Dimensional Cylinder Resting on an Infinite Groundplane at a Reynolds Number, Re_D, of 4.0×10^5

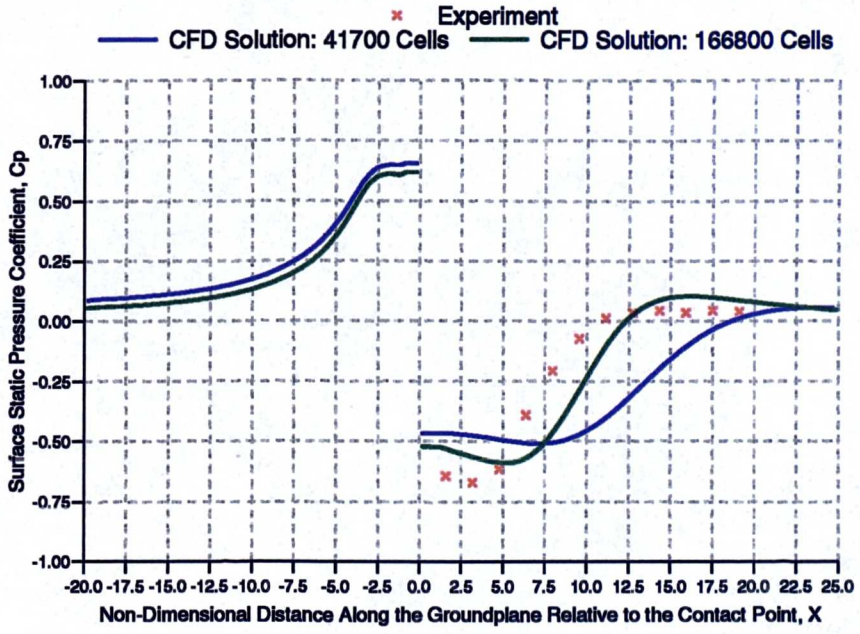

Figure 4.11: The Influence of Mesh Size on the Groundplane Surface Static Pressure Coefficient Distributions for the Flow Over a Two Dimensional Cylinder Resting on an Infinite Groundplane at a Reynolds Number, Re_D, of 4.0×10^5

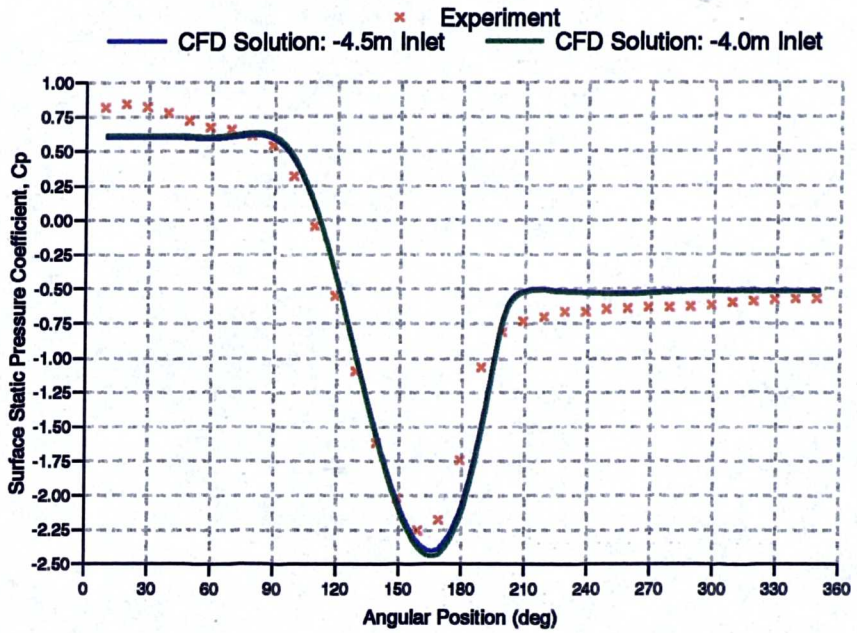

Figure 4.12: Comparison of CFD and Experimental Cylinder Surface Static Pressure Coefficient Distributions for the Flow Over a Two Dimensional Cylinder Resting on an Infinite Groundplane at a Reynolds Number, Re_D, of 4.0×10^5

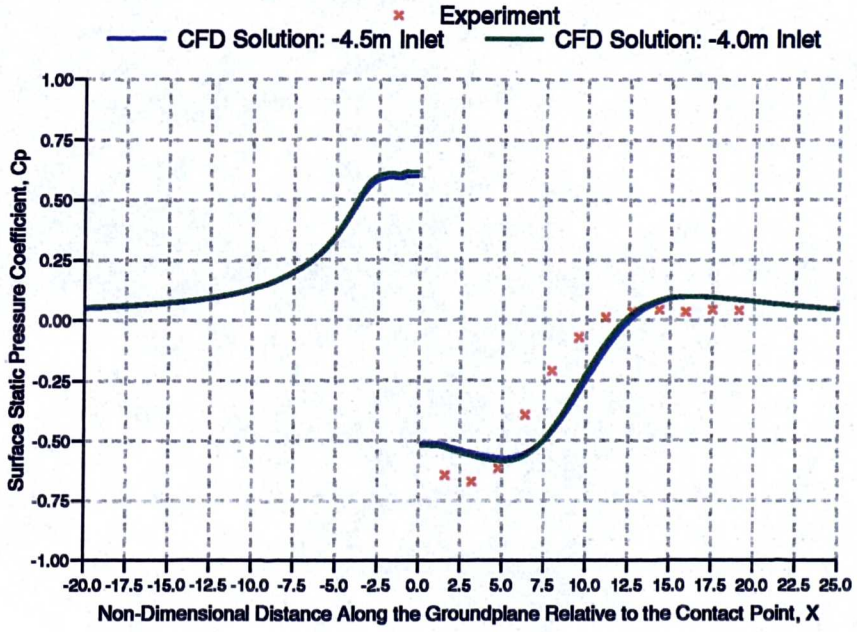

Figure 4.13: Comparison of CFD and Experimental Groundplane Surface Static Pressure Coefficient Distributions for the Flow Over a Two Dimensional Cylinder Resting on an Infinite Groundplane at a Reynolds Number, Re_D, of 4.0×10^5

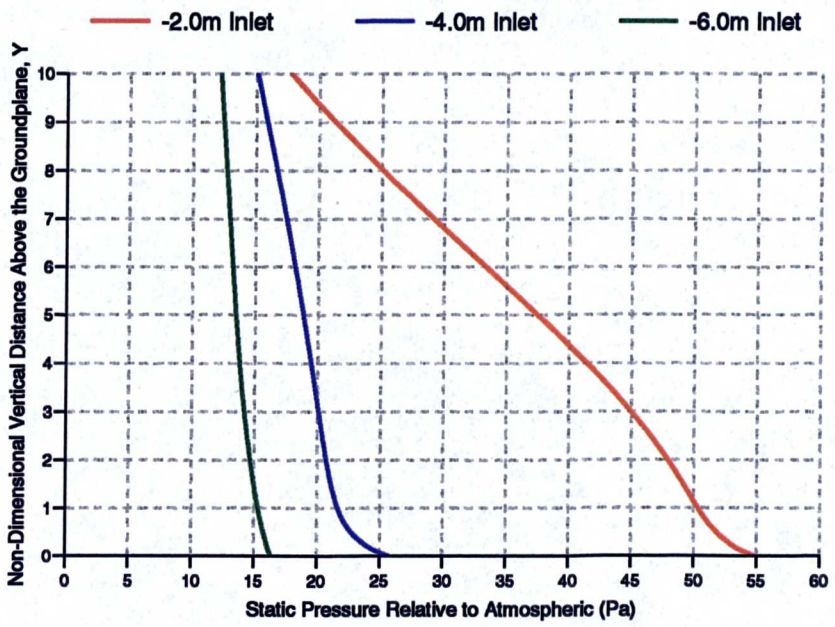

Figure 4.14: The Influence of the Distance Between the Cylinder and the Inlet to the Computational Domain on the Pressure Distribution on the Inlet Boundary

Chapter 5

The Influence of Numerics on the Isolated Wheel Solutions

The two dimensional studies of the flow over a stationary cylinder resting on an infinite groundplane have shown how much the different numerical schemes contained within the CFD solution procedure can influence the quality of a simulation. The aim of this section of the research was to find a set-up for the solver which would reduce these numerical dependencies for wheel flow solutions, and in particular, for the shrouded wheel calculations. The large volume meshes that will be required to resolve the details of the flow and geometry mean that only a limited number of shrouded wheel simulations will be able to be completed, and, therefore, confidence in the chosen solver numerics must be achieved before this final phase of the research.

With Fackrell, *Ref.[22]*, presenting both isolated wheel surface static pressure distributions and a wake profile contour (90% total head) on four planes downstream of the wheel, enough published data was available to investigate the influence of these numerical parameters through simulating the flow around an isolated wheel for both fixed and moving groundplane configurations.

5.1 Mesh Generation

Most of the experimental data presented by Fackrell, *Ref.[22]*, was for the wheel profile designated B2. This had a diameter of 0.415m with an aspect ratio, AR,

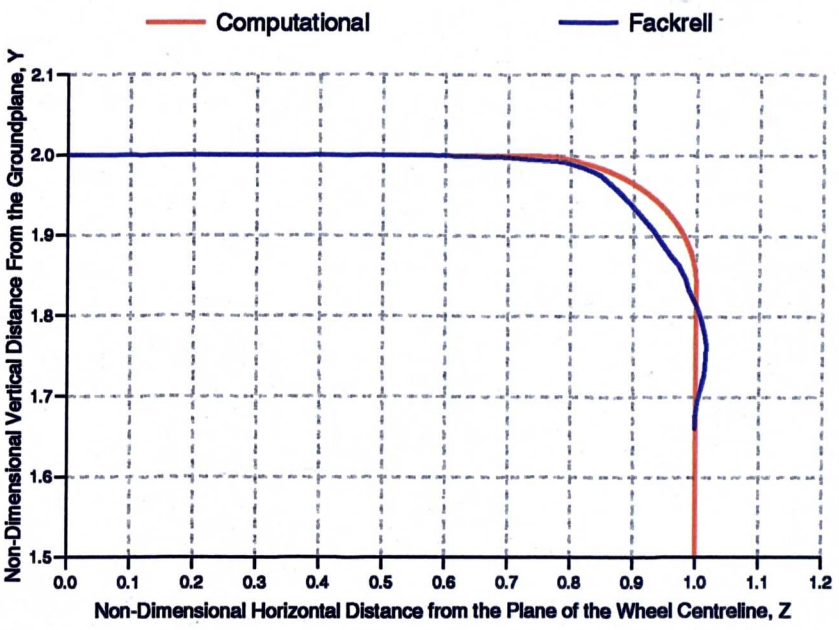

Figure 5.1: Comparison of the Computational and Experimental (Wheel B2, Fackrell) Isolated Wheel Edge Profiles

over the maximum width of the wheel of 61.2%. Over the width of the main central hub section of the wheel, however, AR=60.0%. As the aim of the initial 3D isolated wheel modelling was to look at the relative effects of numerics, which together with the limited hardware available at the time, resulted in a simplified version of the geometry being modelled. Thus, the computational wheel still retained the 0.415m diameter but had a circular edge profile and no recessed central hub, i.e. the wheel was meshed as a single solid body. Its aspect ratio was set as 60.0% to match the width of the central hub section of Fackrell's wheel. *Fig.5.1* shows a comparison of the two edge profiles.

With the two dimensional study providing a quadrilateral mesh structure suitable for a symmetry boundary through the plane of the centreline of the wheel it was decided to model just half of the wheel with a multiblock hexahedral mesh created in Geomesh. This would allow greater volume mesh density than if both sides of the wheel were modelled within the initial 250,000 cell limit. Despite this simplification significant coarsening of the mesh on this symmetry plane was required relative to the 2D cases. Also, the number of cells normal to the wheel surface was reduced to aid meshing around the side of the wheel into the contact patch.

Fig.5.2 shows the surface mesh for the wheel, contact patch, groundplane, and sym-

metry plane. The number of cells was 248,349. Circumferentially, the maximum node spacing was three degrees. The similarity in the mesh structure on the symmetry plane (yellow) with the 2D cases can clearly be seen. Maintaining orthogonality next to the wall boundaries was considered important and this determined the mesh structure in the area around the contact patch, and on the side of the wheel.

The length of the contact patch, *Fig.5.3*, was set with verticals placed at 10^o and 350^o. These extended for the full width of the 'tread' surface of the wheel, and were then connected by a third planar face. This meant that the profile of the wheel had to be modified slightly in this area, *Fig.5.4*. The mesh spacing also had to be set carefully in this area to provide the correct range of y^+ values for the closure of the turbulence model.

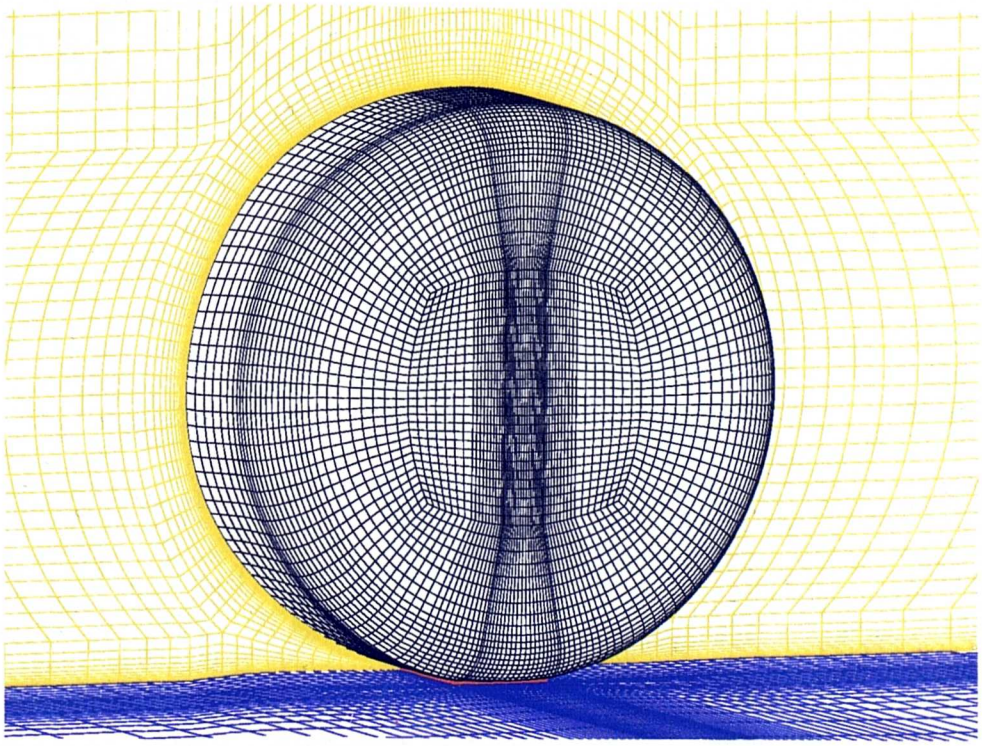

Figure 5.2: Surface Mesh for the Isolated Wheel, Contact Patch, Groundplane, and Symmetry Plane for the 248,349 Cell Volume Mesh for Turbulent Closure with Wall Functions

Referenced to the centre of the wheel, the farfields of the domain were set at ten wheel radii upstream for the inlet, thirty downstream for the outlet, with both the height and width of the domain also being set at ten wheel radii. This domain length was determined from the two dimensional model. As Fackrell, *Ref.[22]*, stated no stationary groundplane boundary layer thickness the inlet distance was a compro-

mise between setting a reasonable boundary layer thickness, approximately 0.04m at the location of the wheel without it in place in the domain, reducing the influence of the wheel on the pressure distribution on the inlet of the domain, and total mesh size. Due to the third dimension the area blockage of the wheel in the computational domain, at approximately 0.25%, was much less that the 2D cases.

Two different meshes, both with 248,349 cells, were generated to initially study numerical influences. Next to the wall boundaries different first cell centre distances, and, therefore, cell height growth rates, were set to allow for both wall functions and the two-layer approaches to turbulent closure to be used.

Subsequently three other meshes were created for the two-layer closure method. Two of these had 392,836, and 538,350 hexahedral volume cells, and were created by increasing the number of cells within the boundary layer regions next to the wall surfaces through a decreased cell height growth rate. This larger mesh was also further refined with a smaller first cell height giving a 686,870 cell volume mesh size.

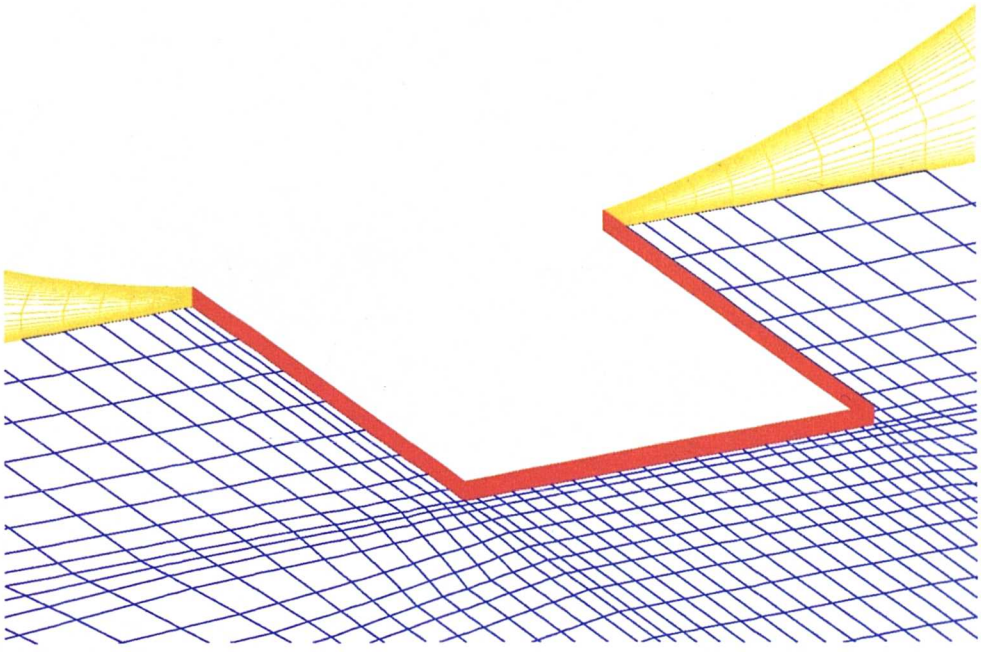

Figure 5.3: The Treatment of the Contact Patch in the Structure of the Isolated Wheel Mesh

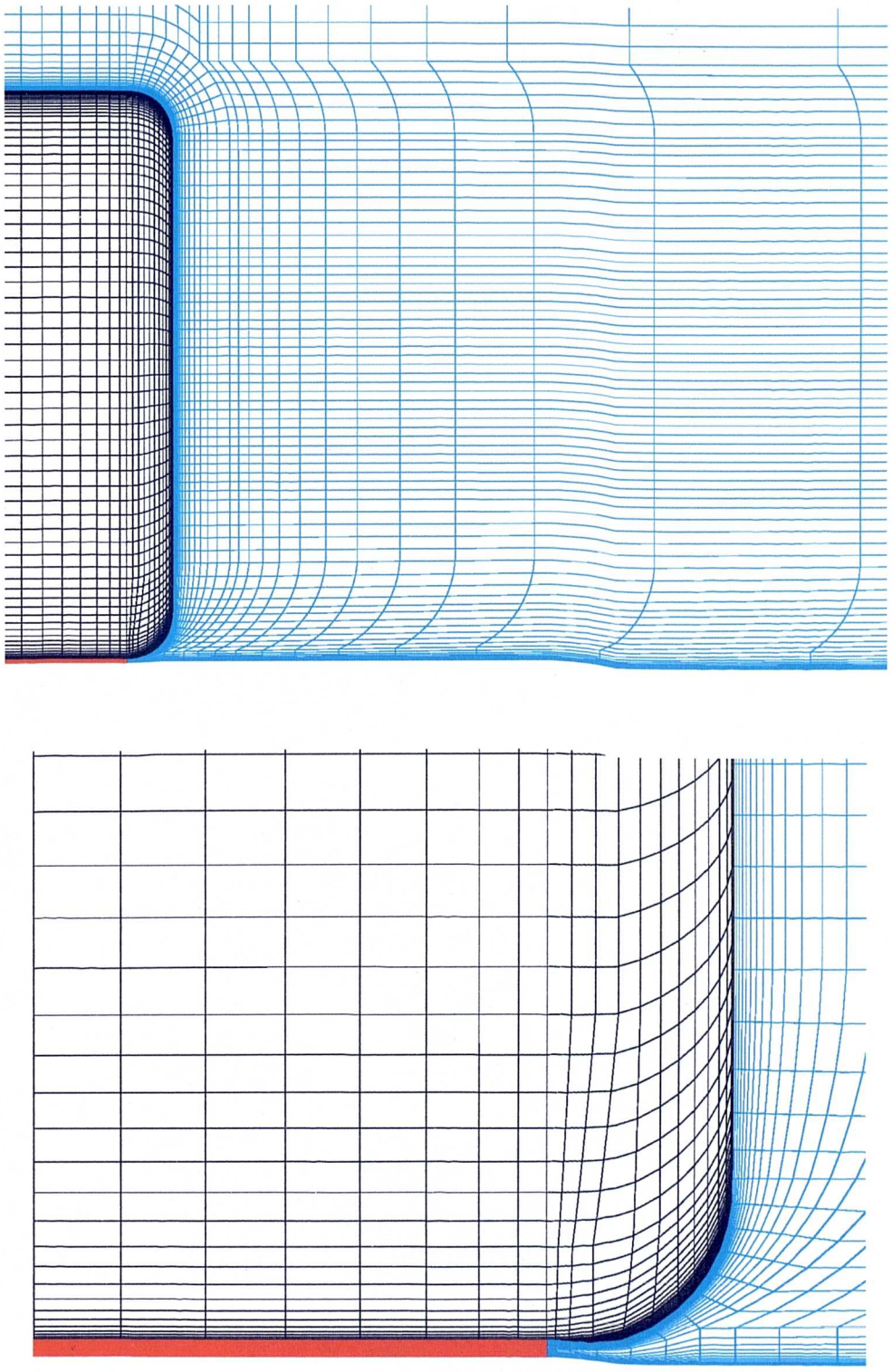

Figure 5.4: The Hexahedral Volume Mesh Structure Around the Isolated Wheel on a Vertical Plane Through the Axle Line of the Wheel

5.2 Boundary Conditions

To avoid the need for dynamically moving meshes the boundary conditions were determined to represent the wheel as if it was mounted on a rolling road. Smooth wall boundary conditions were used for the groundplane and the wheel, including tangential velocities for the moving groundplane configuration cases. On the contact patch wall velocities were set to minimize any discontinuities between those set on the wheel and groundplane. At the inlet boundary the turbulence parameters were set with a 0.25% freestream turbulence intensity and a length scale equal to the diameter of the wheel. To match the experimental Reynolds number, Re_D, of 5.3×10^5, the inlet velocity was set to be 18.6m/s.

5.3 Results

Appendix C tabulates the isolated wheel lift and drag coefficients for the investigations into numerical influences on the solutions. The remainder of this chapter will describe the findings of this study, whilst Chapter 6 will analyze the aerodynamic properties of the flow around isolated wheels from the 'best' predicted flowfields.

5.3.1 The Influence of the Numerical Schemes

Using the basic set-up of the fully turbulent 2D solutions, together with the guidelines containing within the FLUENT/UNS manuals, *Ref.[37]*, a baseline set of parameters was determined for the solver which were to be used initially with the mesh with first cell heights set for the use of wall functions. This comprised of the RNG k-ϵ turbulence model with non-equilibrium wall functions for turbulent closure, and SIMPLEC for pressure and velocity coupling. A stationary wheel and groundplane was also simulated as this eliminated the complexity of the rotating wheel flow features postulated by Fackrell, *Ref.[22]*.

From this baseline the influence of various numerical parameters were investigated individually. These were:

1. SIMPLE instead of SIMPLEC
2. SIMPLEC plus PRESTO
3. SIMPLEC plus 'implicit body forces'

The baseline case gave a predicted C_{Lw} of 0.647 and a C_{Dw} of 0.718. These compare to Fackrell's data of 0.76 and 0.77 respectively. The under-prediction in the lift coefficient was 14.9%, and for the drag coefficient it was 6.8%.

The effect of using both SIMPLE and 'implicit body forces' was negligible. The use of SIMPLE reduced the drag coefficient by 0.001, whilst leaving the lift coefficient unchanged. Also, its use potentially increased the number of iterations required for the forces to stabilize through having to use smaller under-relaxation values. The force coefficients were unchanged with the 'implicit body force' treatment. PRESTO had the one significant effect. Its use reduced C_{Lw} by 0.016, to 0.631, and C_{Dw} by 0.014, to 0.704.

Whilst these changes gave a larger discrepancy to the experimental results, this was for one turbulence model and closure method. Its use might be more beneficial with other models. Also, as it could only be used with totally hexahedral volume meshes, and not hybrid meshes, PRESTO was retained as a numerical option for further investigation and not used as a default setting for the work on turbulence modelling.

5.3.2 The Influence of the Turbulence Model

For the modelling of viscous flowfields FLUENT/UNS gave the choice of two two-equation turbulence models, k-ϵ and RNG k-ϵ, as well as a laminar option. The effects of the use of all three approaches was investigated with all the isolated wheel meshes and appropriate closure options. Both the magnitude of the predicted force coefficients, C_{Lw} and C_{Dw}, and the stability of the solutions were criteria for the choice of a final turbulence model to use for the rest of the research.

All the laminar calculations were very unstable for both moving and stationary groundplane configurations. The force coefficient histories showed large irregular oscillations, and no obvious trends were seen in their final values.

In contrast, almost all the solutions with the k-ϵ model gave stable final force coefficients for both groundplane configurations. The only exception was those run using the largest 686,870 cell mesh where, after 3000 iterations, the predicted forces were still slowly decreasing.

The k-ϵ simulations correctly predicted that the rotating wheel produced less lift and drag than the stationary wheel. Both C_{Lw} and C_{Dw} were over-predicted for the

rotating wheel. However, when the wheel was stationary C_{Lw} was under-predicted but C_{Dw} was slightly over-predicted.

Changing to the RNG k-ϵ turbulence model improved the comparison of the force coefficients with experimental data but at the cost of instability in some of the solutions due to the extra non-linearity of the model relative to the standard k-ϵ version. Relative to this standard k-ϵ model, using the RNG variant reduced both the predicted lift and drag coefficients of the rotating wheel. These became more sensitive to the closure method but most of the predicted force coefficients were within ± 0.05 of Fackrell's results. For the stationary wheel, C_{Lw} was still under-predicted, but to a lesser degree than with the standard k-ϵ model, but C_{Dw} was now also under-predicted. Again, the solutions correctly simulated less lift and drag for the rotating wheel compared to the stationary wheel.

Fig.5.5 through to *Fig.5.8* show comparisons of the k-ϵ and RNG k-ϵ solutions with the experimental pressures on the surface of the wheel, and in the wake, for both groundplane configurations. All four solutions used standard wall functions.

When the wheel was rotating the use of the RNG k-ϵ model showed large improvements in the pressure profiles over the standard k-ϵ model, *Fig.5.5*. This reflects the trends shown in the force coefficients. On the wheel centreline both models predicted pressure coefficients of approximately 1.4 at the front of the contact patch. Fackrell measured pressure coefficients greater than two in this area. Both models predicted stagnation approximately ten degrees too far around the wheel. However, the k-ϵ model over-predicted the stagnation pressure coefficient. The RNG model predicted earlier 'separation', but this was still approximately 15° too far around the wheel. Consequently, the suction peak was -0.3 too large. The k-ϵ model predicted separation a further 15° around the wheel surface. Both model slightly under-predicted base pressure as well as poorly reproduce the interactions with the groundplane in the last 30° of the wheel surface. This could be due to the poor prediction of the flow at the front of the contact patch.

A similar trend was predicted on the second plane on the main 'tread' surface of the wheel, Z=0.201.

The improvements in the accuracy of the RNG variant over the standard k-ϵ model increased closer to the edge of the wheel. The prediction in the flow around the side of the wheel was improved, with some of the discrepancies being due to the differences in edge profiles. This is clearly seen in the position of the downstream

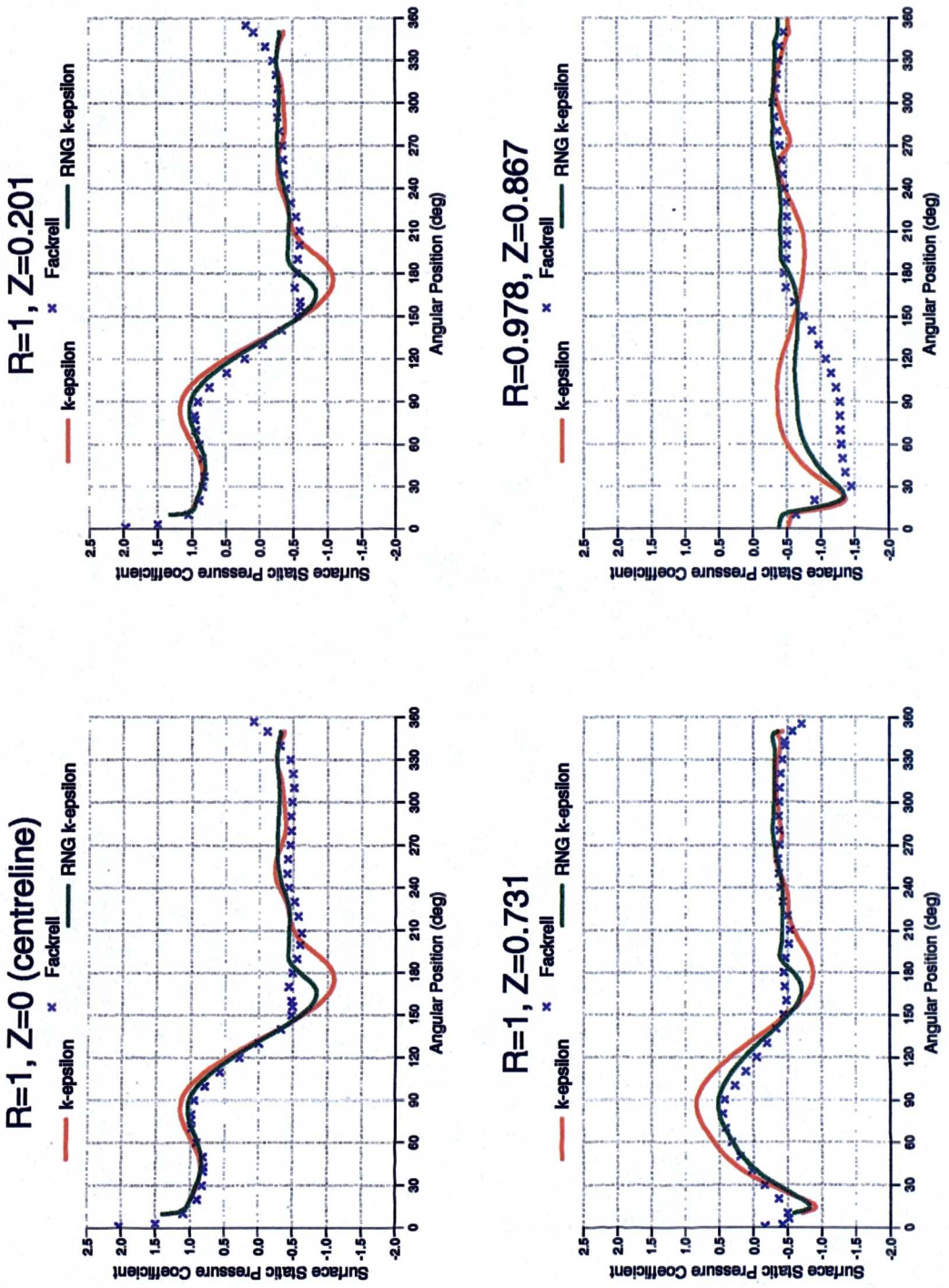

Figure 5.5: The Influence of the Turbulence Model, with Standard Wall Functions, on the Predicted Surface Static Pressure Coefficient Distributions on an Isolated Rotating Wheel

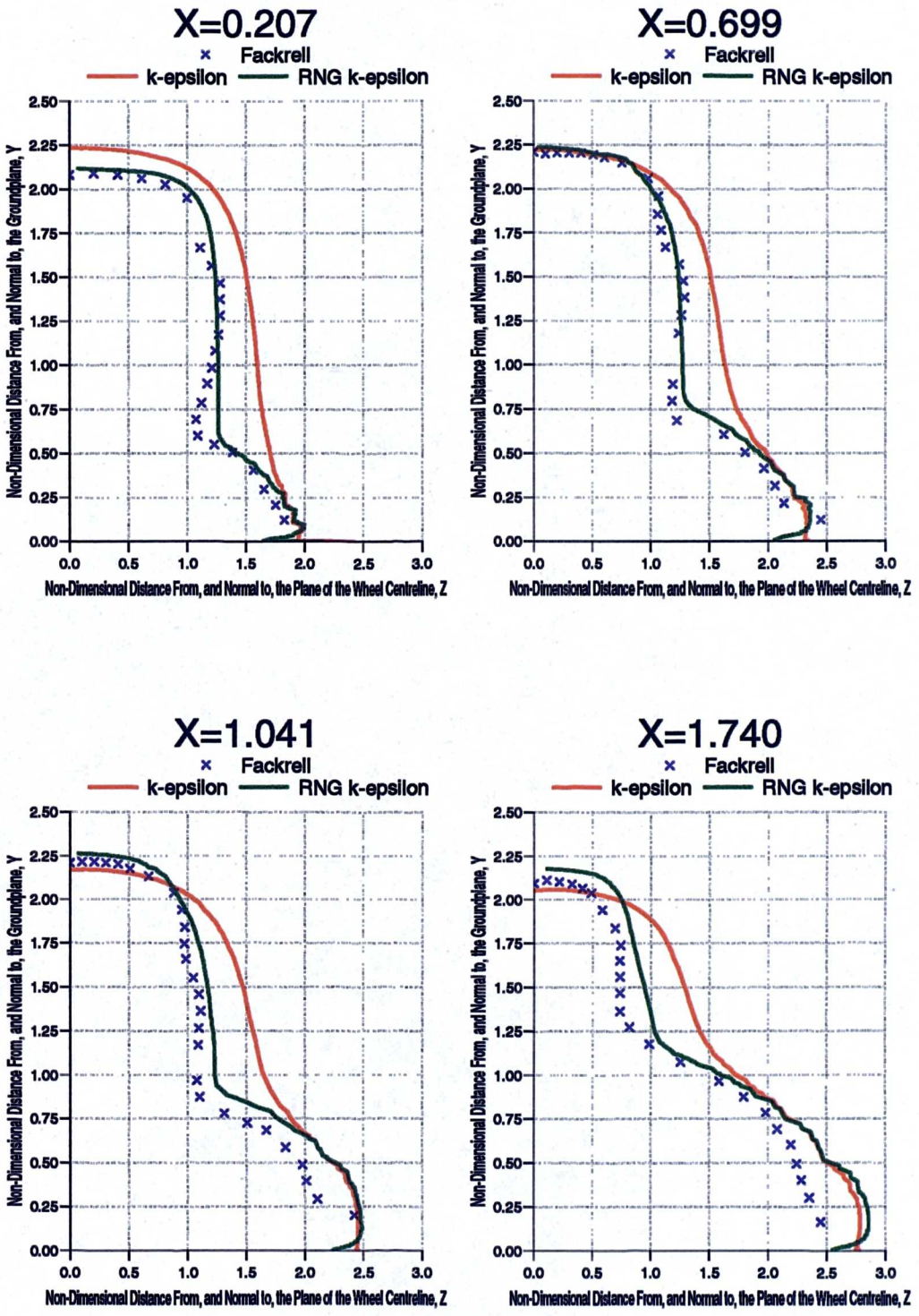

Figure 5.6: The Influence of the Turbulence Model, with Standard Wall Functions, on the Predicted Wake Structure (90% Total Head) Behind an Isolated Rotating Wheel

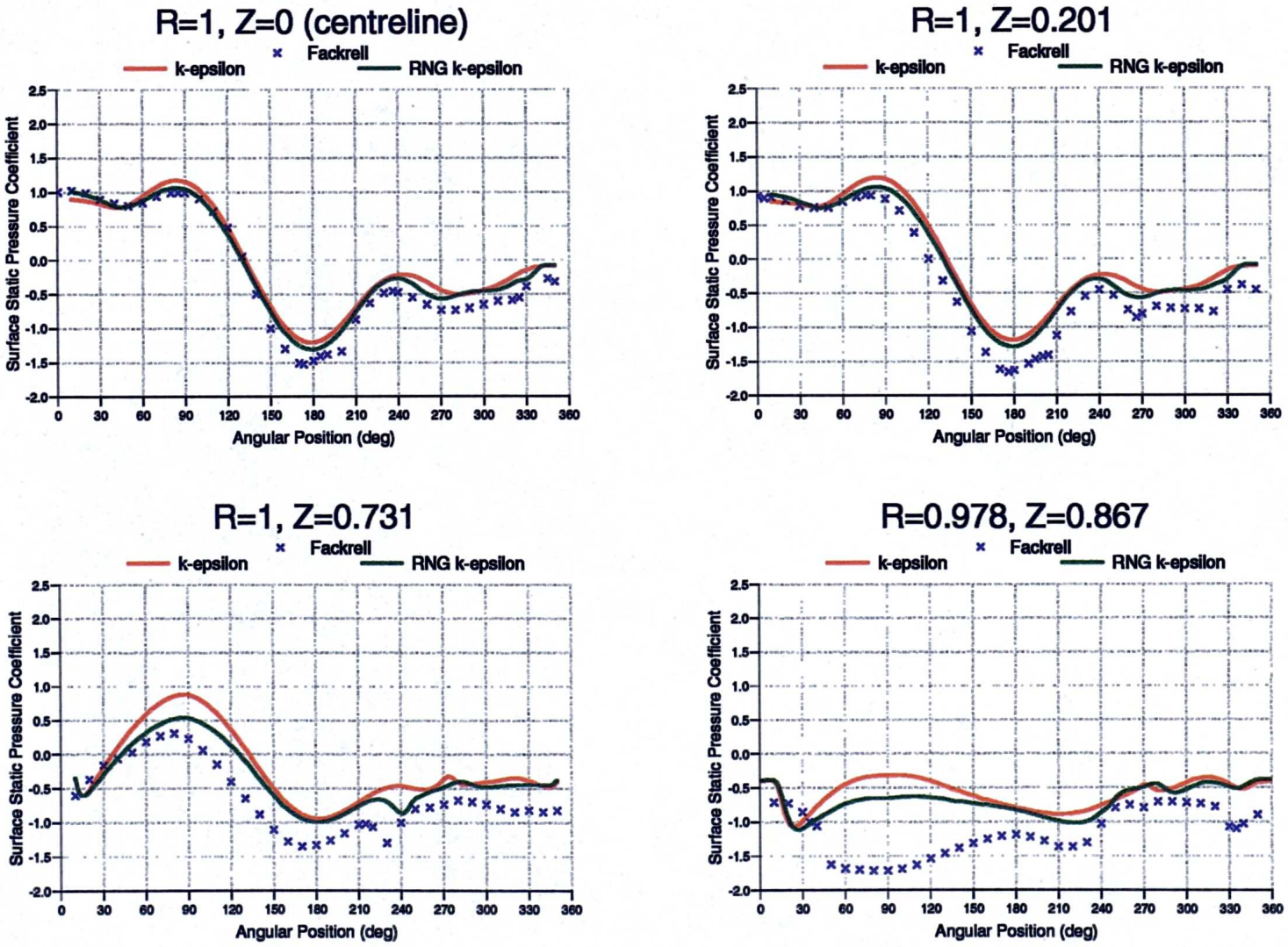

Figure 5.7: The Influence of the Turbulence Model, with Standard Wall Functions, on the Predicted Surface Static Pressure Coefficient Distributions on an Isolated Stationary Wheel

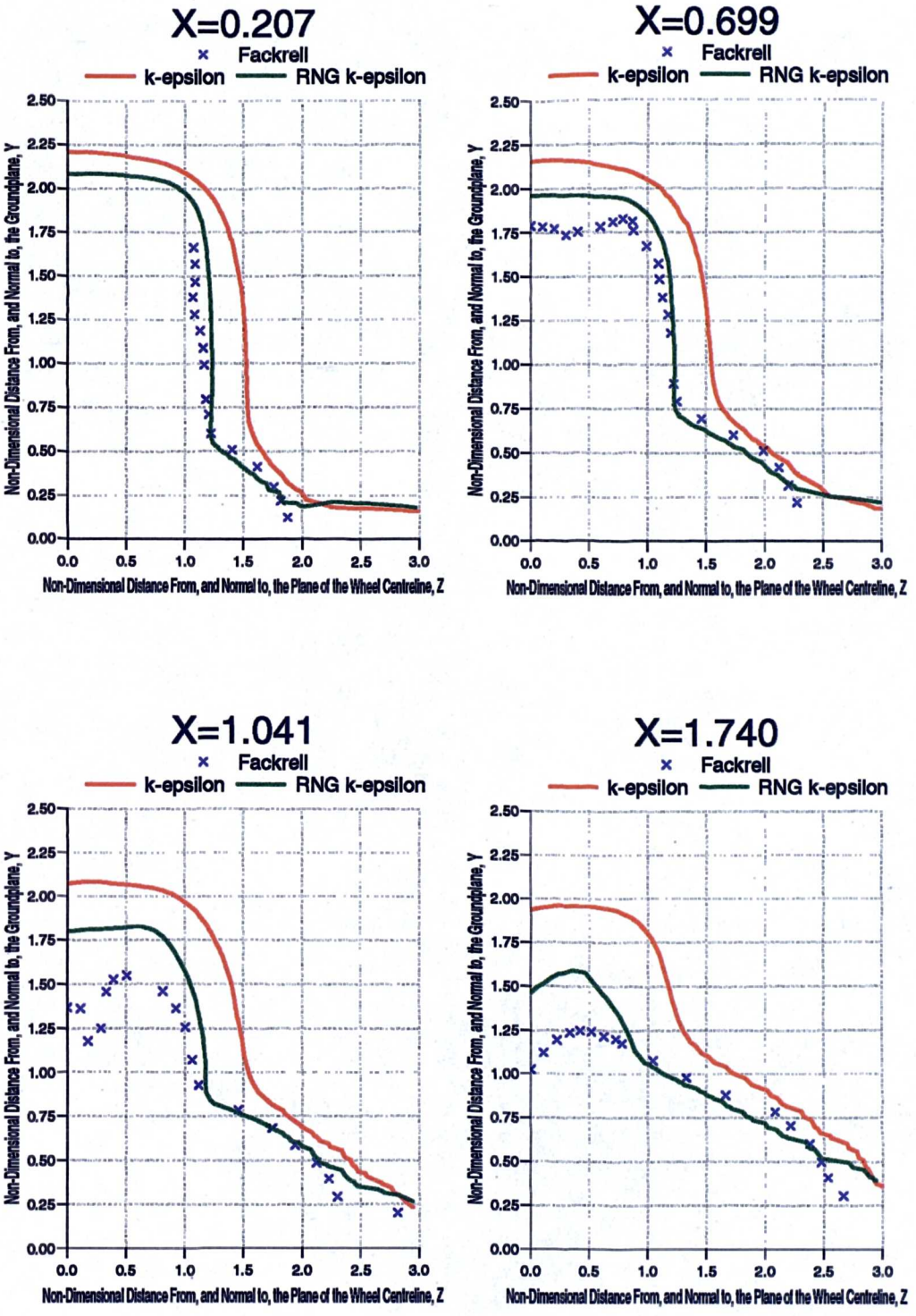

Figure 5.8: The Influence of the Turbulence Model, with Standard Wall Functions, on the Predicted Wake Structure (90% Total Head) Behind an Isolated Stationary Wheel

contours of 90% total head, *Fig.5.6.* The shape of the profiles with the RNG model was good, with the reflex due to the position of the vortex next to the groundplane clearly defined. The profiles with the standard k-ϵ model were wider and more smeared, possibly due to the inherent higher production of turbulence dissipation.

Similar trends were seen for the stationary groundplane configurations. On the centreline of the wheel, *Fig.5.7*, the pressures in the area of the front of the contact patch were more accurately predicted with the RNG k-ϵ model. The position of the stagnation point was accurately predicted with both models, but the standard k-ϵ model again over-predicted the magnitude of the stagnation pressure coefficient. Instead of over-predicting the suction peak, similar to the rotating wheel cases, both simulations under-predicted the pressures in this area. The magnitude of the peak was more accurate with the RNG model, but the coefficient was still approximately 0.2 in error. Thus, the base pressures were under-predicted in both cases, with the RNG model better predicting the profile with angular position.

For the other three surface profiles the RNG results compared better with the experimental data than the standard k-ϵ model. It was encouraging that the suction peak at 230° on the Z=0.731 profile was also seen in the RNG solution, although it was ten degrees too far around the surface of the wheel.

The better prediction of the wake edge with the RNG model was also seen in these stationary groundplane cases, *Fig.5.8.* However, the under-prediction of the suction peak is probably due to the earlier prediction of the separation point, thus increasing the height of the wake behind the stationary wheel. This could be in part due to an increase in the predicted groundplane boundary layer thickness, over the unstated experimental one, as shown by the height above the groundplane at which the total pressure contour flattens towards horizontal. The Reynolds number, Re_D, of 5.3×10^5 is also only just supercritical for a 2D circular cylinder. Thus, the transitional effects noted by Fackrell, *Ref.[22]*, and Cogotti, *Ref.[23]*, for stationary isolated wheels will make discrepancies in this area likely due to the fully turbulent assumption made in the closure of the turbulence models used.

In summary, the RNG k-ϵ turbulence model predicted more accurately the flow around an isolated wheel than the standard k-ϵ model. However, these improvements came with a penalty of decreased solution stability, together with increased memory requirements and CPU time to convergence.

5.3.3 The Influence of the Turbulent Closure Method

The complete resolution with the mesh of any boundary layer profiles predicted in the solution domain should improve the quality of the solution over one computed with the use of wall functions. However, this will be at the expense of a much larger volume mesh. Are the extra resources required worth any gains in accuracy?

The k-ϵ model was found to be much less sensitive to the method of closure than its RNG variant. Apart from the 686,870 volume cell mesh all the solutions, both rotating and stationary, were stable. For the moving groundplane configurations the variance in C_{Lw} with closure method was 0.017, and 0.026 for C_{Dw}. These reduced to 0.011 and 0.017 respectively for the stationary groundplane calculations. The almost identical force results from the 392,836 and 538,350 cell meshes showed that the solutions could be considered mesh independent in the normal direction away from wall surfaces within the boundary layer regions.

The poorer results with the largest mesh show the importance of the y^+ distribution on wall boundaries. For this mesh most of the y^+ values were between 0.25 and 0.5, which were too small. The other full boundary layer meshes gave most of the y^+ values within the range of unity to three, which were within the acceptable range stated by Fluent, *Ref.[37]*.

With the RNG k-ϵ model and volume mesh size of 248,349 cells the only solutions which gave stable solutions were for the stationary wheel with wall functions. None of the rotating wheel solutions were stable, and neither was the stationary wheel solution with two-layer closure. Only the 392,836 and 538,350 volume cell meshes gave stable solutions for both rotating and stationary wheel cases. There were slight differences in C_{Lw} and C_{Dw} from the two meshes. The largest of the two gave the better results for the rotating wheel. The lift coefficient was over-predicted by 0.022, or 5.0%, with the drag coefficient over predicted by 0.008, or 1.4%. For the stationary wheel solution with this mesh both C_{Lw} and C_{Dw} were under-predicted by 0.128 and 0.063 respectively.

Fig.5.9 through to *Fig.5.12* show the influence of the closure method with comparisons of the predicted surface and wake edge profiles for the 248,349 cell standard wall function solutions and the 538,350 cell two-layer full boundary layer closure solutions. The use of the larger mesh increased C_{Lw} and C_{Dw} of the rotating wheel by 0.059 and 0.028 respectively, and reduced C_{Lw} and C_{Dw} of the stationary wheel 0.010 and 0.028 respectively.

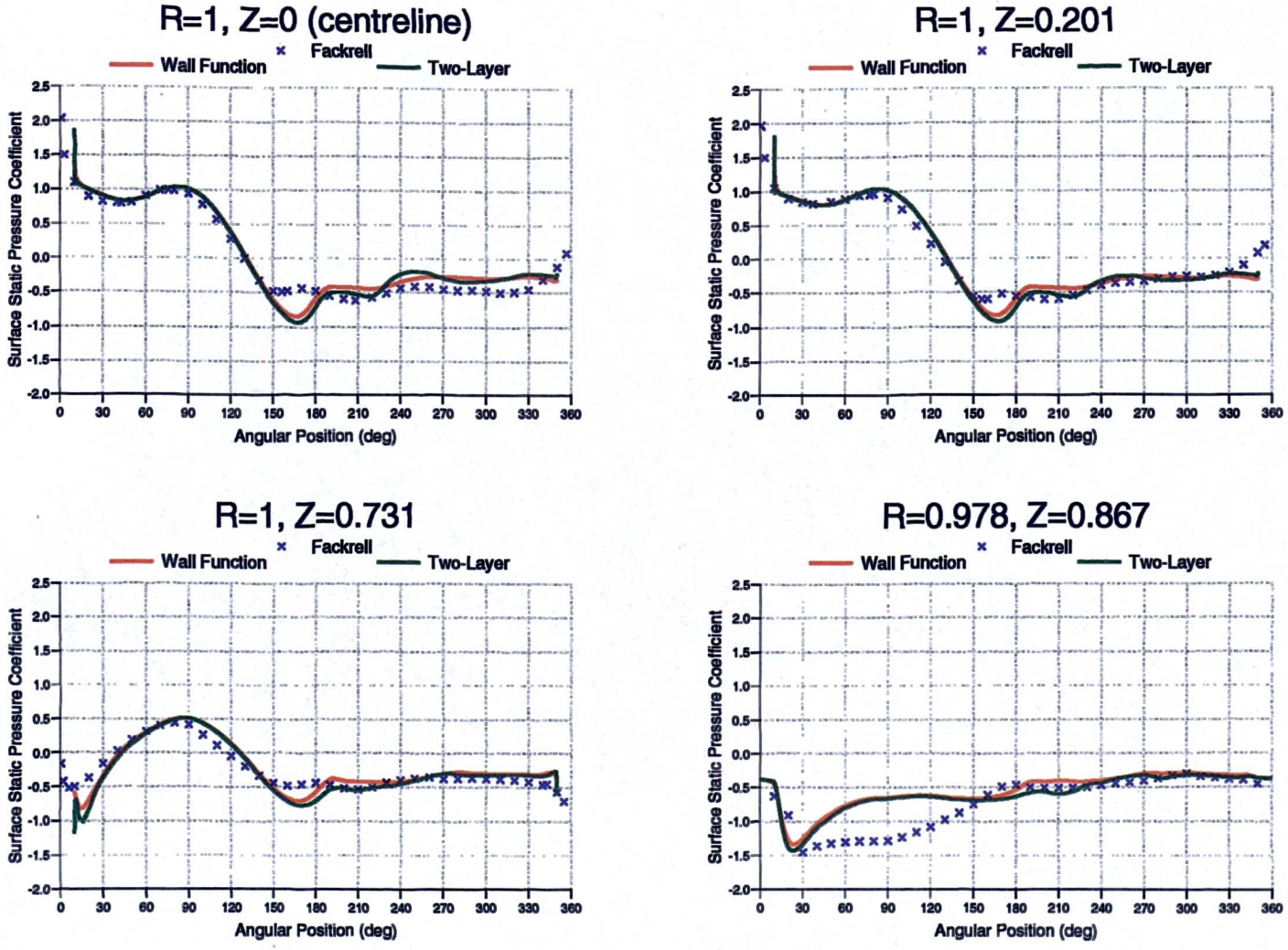

Figure 5.9: The Influence of the Closure Method on the Predicted Surface Static Pressure Coefficient Distributions on an Isolated Rotating Wheel with the RNG k-ϵ Turbulence Model

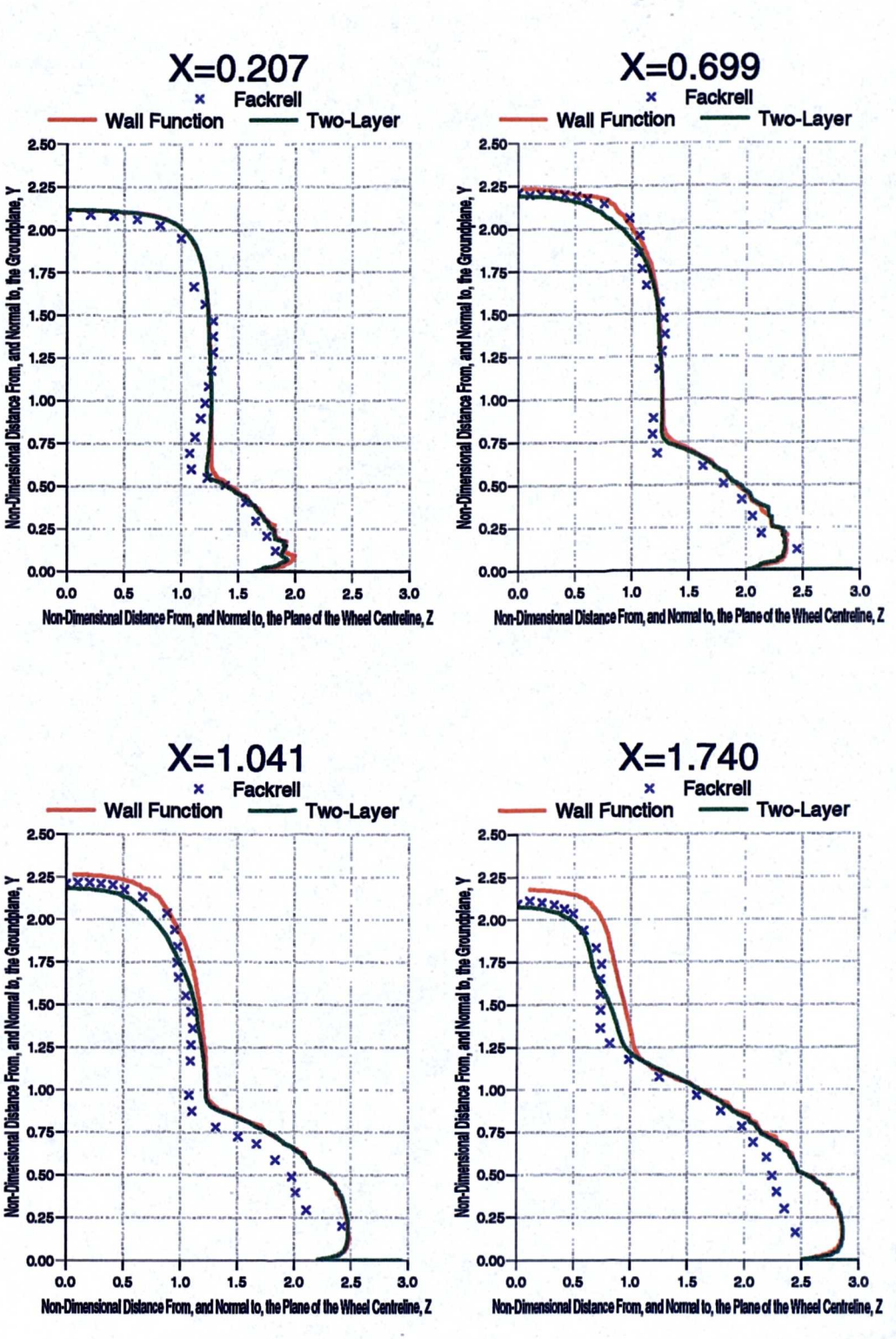

Figure 5.10: The Influence of the Closure Method on the Predicted Wake Structure (90% Total Head) Behind an Isolated Rotating Wheel with the RNG k-ϵ Turbulence Model

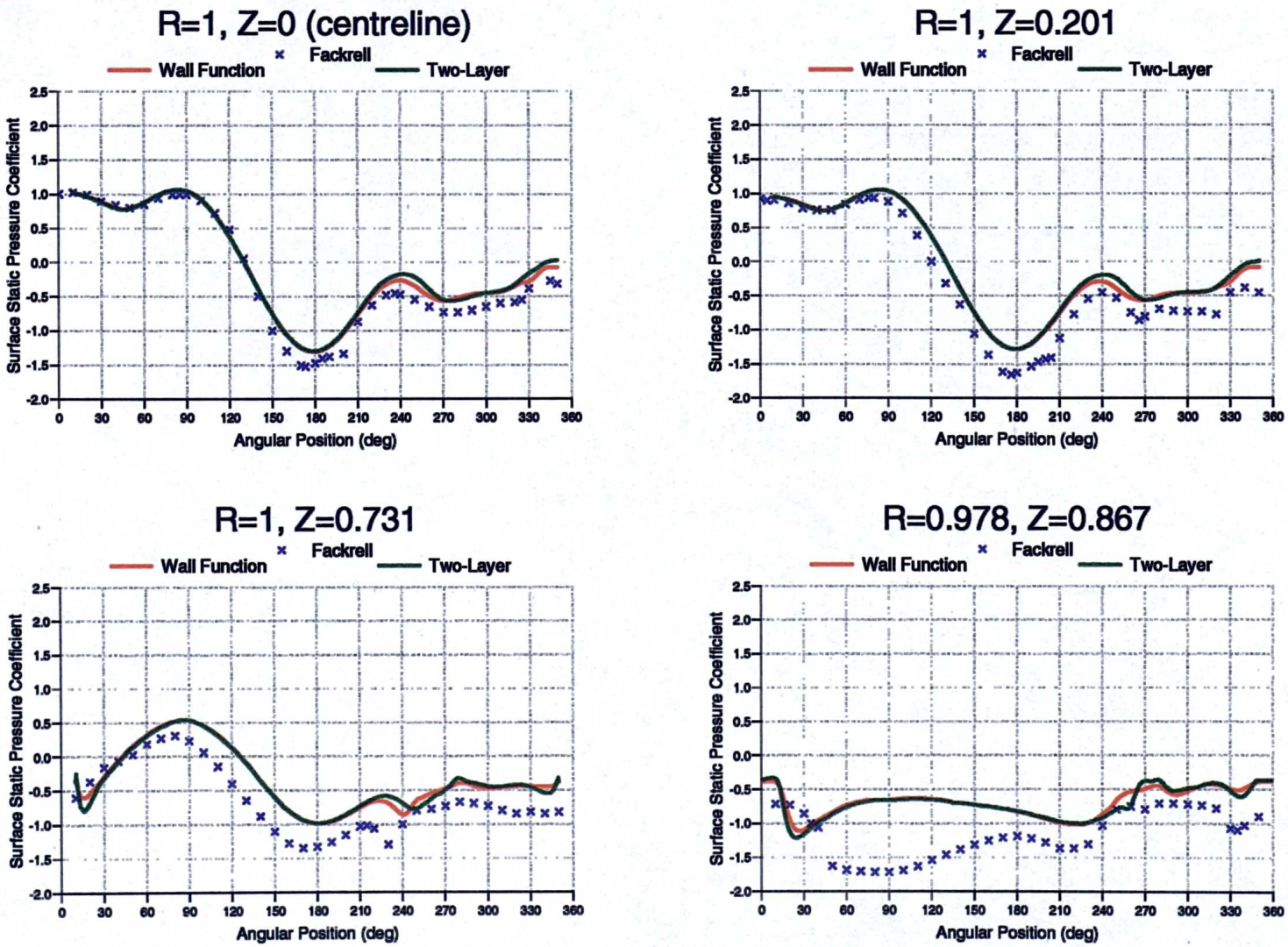

Figure 5.11: The Influence of the Closure Method on the Predicted Surface Static Pressure Coefficient Distributions on an Isolated Stationary Wheel with the RNG k-ϵ Turbulence Model

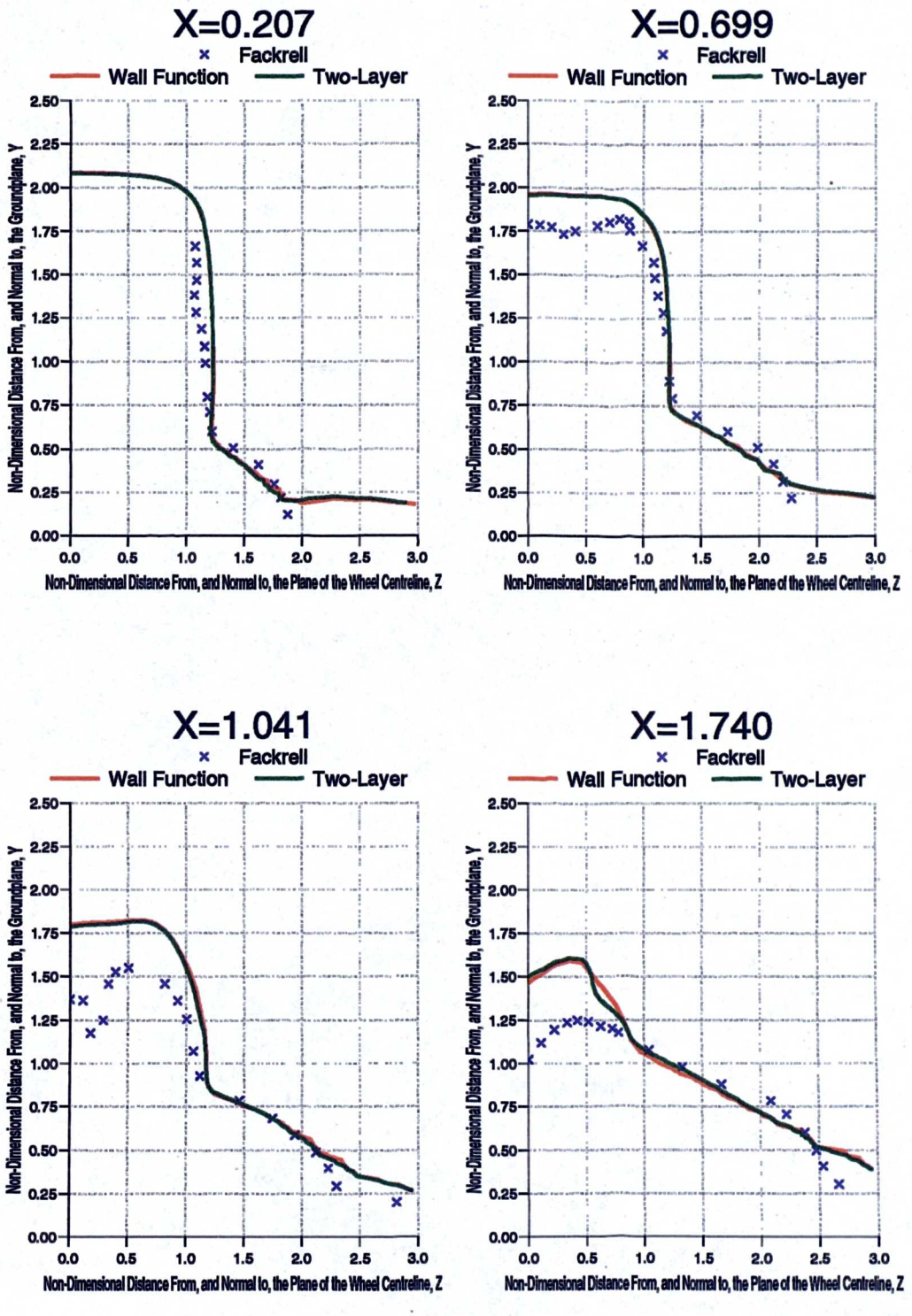

Figure 5.12: The Influence of the Closure Method on the Predicted Wake Structure (90% Total Head) Behind an Isolated Stationary Wheel with the RNG k-ϵ Turbulence Model

For the rotating wheel solution the extra boundary layer refinement increased the pressure coefficients at the front of the contact patch. Pressure coefficients upto 1.9 were predicted which were similar to those found experimentally, *Fig.5.9.* Thus, the computed flow structure in this area will be improved, and consequently, so will the flow downstream near to the groundplane. On the centreline of the wheel the accuracy of the magnitude of the predicted pressure coefficients decreased, but with an increase in the accuracy of the shape of the profile. In particular, the decrease in the surface pressures between 180^o and 210^o was computed with the full boundary layer model. A similar trend was found in the other three comparisons.

The extra resolution of the boundary layer on the upper part of the wheel surface gave an increase in the accuracy of the downstream wake profiles, *Fig.5.10.* This would be expected as the empirical wall function would not have been derived from boundary layer profiles with the flow next to the surface opposing the freestream. The two-layer closure solution gave the edge of the wake to be narrower and slightly lower in this region compared to the solution that used wall functions. No major change in the profiles of the edge of the wake near to the groundplane was predicted between the two closure methods.

For the stationary wheel and groundplane, where the boundary layer structures are likely to be less complex, there were smaller changes in the solutions with the two closure methods. On the front half of the wheel, 0^o to 180^o, *Fig.5.11*, the predicted pressure coefficients were almost identical. The only exception was where the flow around the side of the wheel interacted with the groundplane. The extra resolution with the two-layer mesh resulted in more negative pressure coefficients in this area. In the region of the wake behind the wheel the two-layer closure gave a slightly worse prediction of the magnitude of the surface pressure coefficients then the closure with wall functions. Again, more interaction around the lower rear edge of the wheel with the groundplane seemed to be predicted.

Unsurprisingly, those small changes in the structure of the surface pressure profiles resulted in very similar edges to the wake with both methods of turbulent closure, *Fig.5.12.*

In summary, the extra computational expense of the full boundary layer model gave, in particular for the rotating wheel solutions, solution stability with the RNG k-ϵ turbulence model and an overall improvement in the predicted flowfield. The improvements in the predicted pressures at the front of the contact patch should

improve the structure of the computed vortex structure next to the groundplane as well as the position of its edge. The two-layer closure also seemed to be better able to resolve the complex boundary layer structures at the top of the wheel. Therefore, it is proposed to continue with the full boundary layer resolution for the remainder of the research.

5.3.4 The Influence of the Symmetry Plane

All the isolated wheel calculations so far have used a symmetry plane to halve the size of the volume mesh. This, therefore, does not predict the interactions between the two sides of the wake which, in particular for time-dependent calculations, could reduce the accuracy of the solution. Hence, the 538,350 cell volume mesh was mirrored through the symmetry plane, and the two parts fused together, to give a 1,076,700 cell volume mesh with no symmetry plane. This would enable the implications of modelling only half the wheel to be analyzed.

Its effect was found to be small. The solution for a rotating wheel without the symmetry plane gave an increase in both the predicted lift and drag coefficients, compared to the equivalent solution with the symmetry plane, of 0.005. Such a small change in the force coefficients was reflected in only very minor changes in the wheel surface pressure coefficients and wake edge profiles, *Fig.5.13*, and *Fig.5.14*, and, thus, the use of a symmetry plane in the isolated wheel solutions would not have been an significant influence on the validity of the steady state calculations to investigate numerical influences.

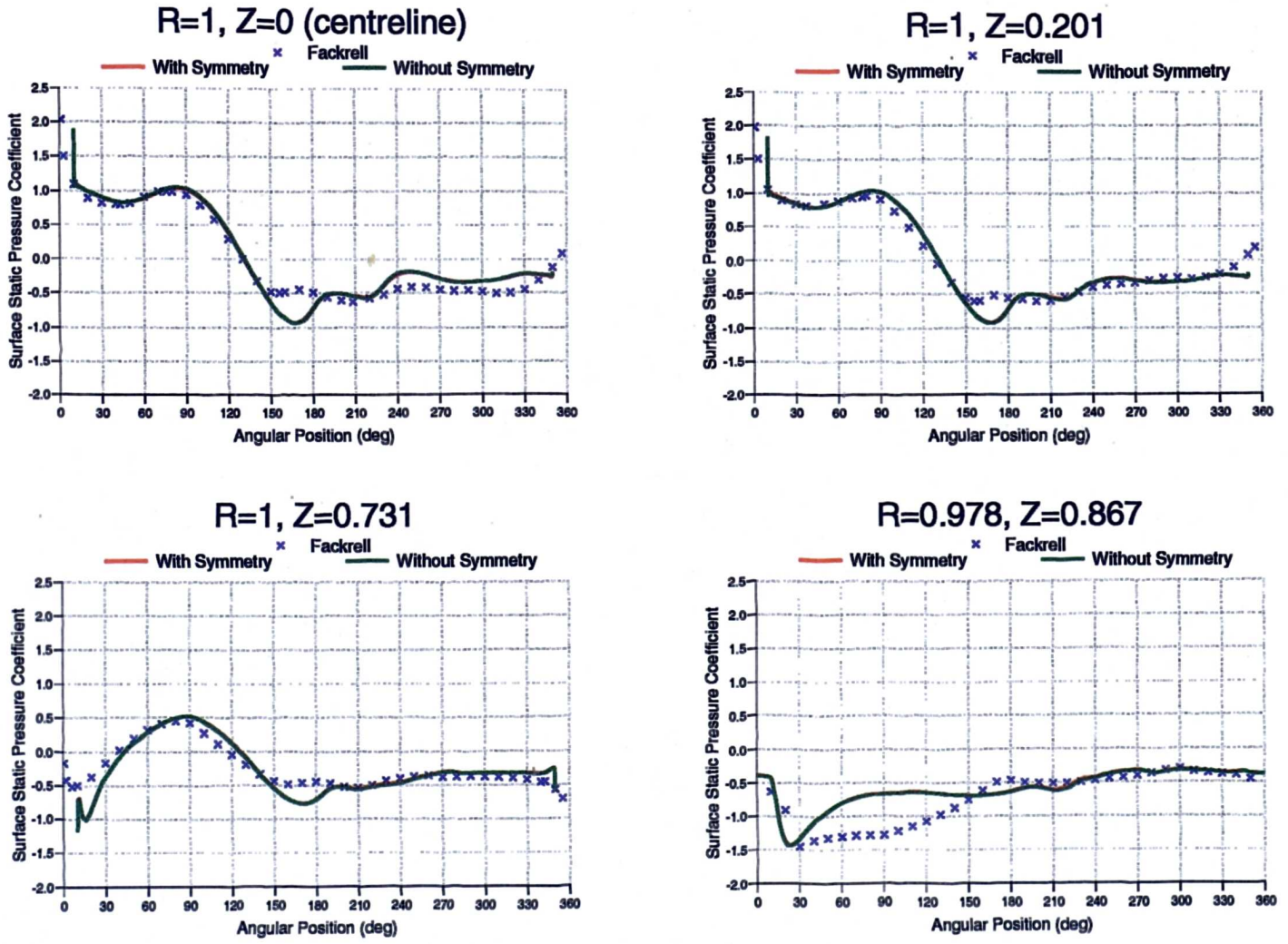

Figure 5.13: The Effect of the Use of a Symmetry Plane on the Predicted Surface Static Pressure Coefficient Distributions on an Isolated Rotating Wheel (RNG k-ϵ Turbulence Model with Two-Layer Closure)

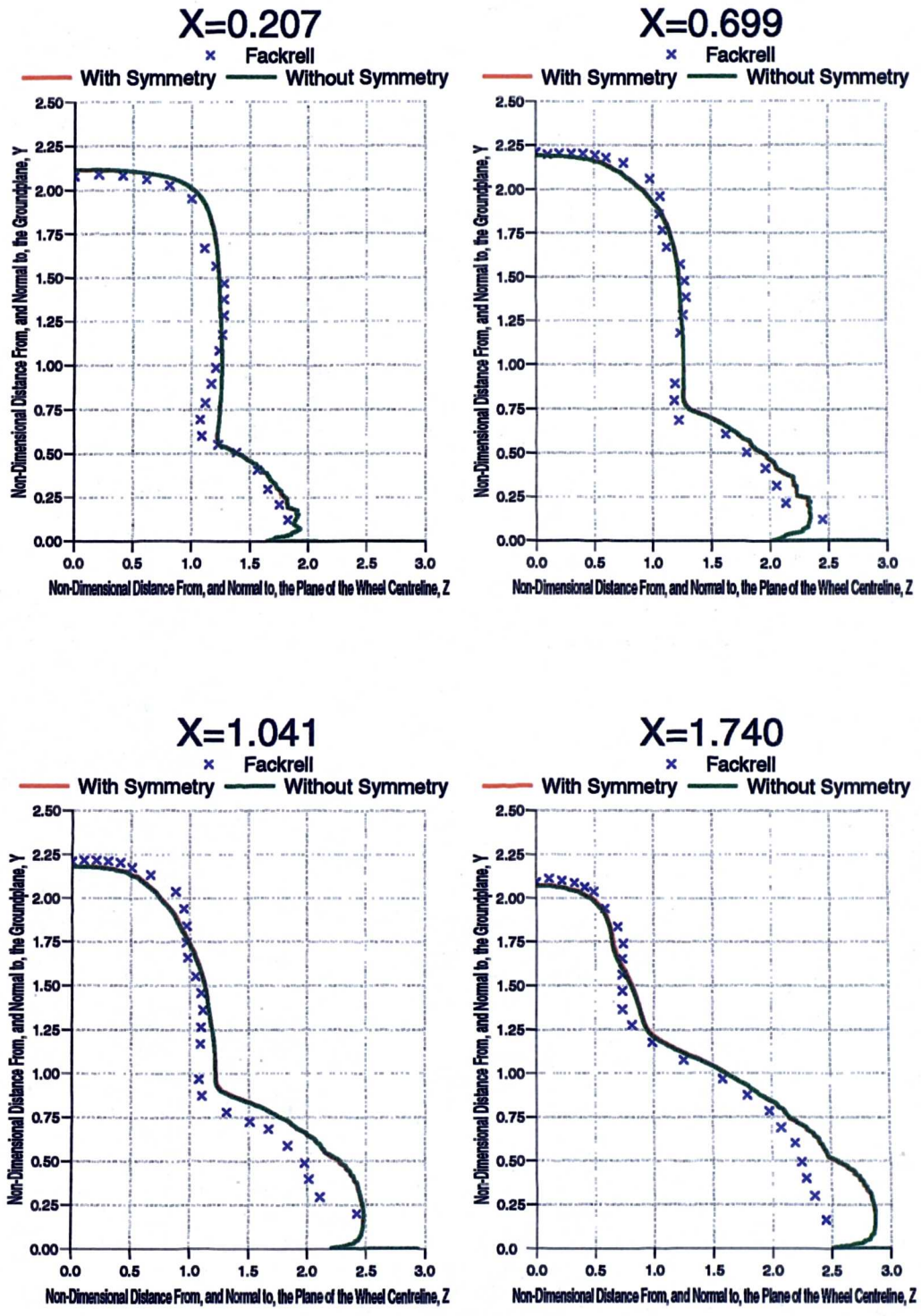

Figure 5.14: The Effect of the Use of a Symmetry Plane on the Predicted Wake Structure (90% Total Head) Behind an Isolated Rotating Wheel (RNG k-ϵ Turbulence Model with Two-Layer Closure)

5.4 Summary

From this chapter it can be summarized that:

1. Based on the mesh structure developed for the 2D calculations a number of totally hexahedral isolated wheel volume meshes have been developed. These have been used for a series of calculations which investigated the influence of solver numerics for wheel flow calculations. The predicted flowfields were compared to the experimental data of Fackrell, *Ref.[22].*

2. It was correctly predicted that a rotating isolated wheel on a moving groundplane generates less lift and drag than the equivalent stationary wheel on a stationary groundplane.

3. The use of the RNG k-ϵ turbulence model gave improved solutions compared to the equivalent ones with the k-ϵ model. However, this was at the expense of extra solution instability. The use of a full boundary layer closure, compared to using wall functions, improved, in particular, the structure of the wake behind the wheel.

4. The use of a symmetry plane was only a minor influence on the steady state solutions for the flow around an isolated rotating wheel.

5. The importance of setting the magnitude of the y^+ distributions on wall surfaces correctly has been shown. Having y^+ values too small for the two-layer closure affected both the rate of solution convergence and the predicted force coefficients.

6. A set-up for the solver for the shrouded wheel solutions was established. This comprised of the RNG k-ϵ turbulence model with two-layer closure, and SIMPLEC. This would be suitable for use with any volume mesh structure that would be developed.

Chapter 6

Analysis of the Aerodynamic Characteristics of Isolated Wheels

Whilst Chapter 5 outlined the work completed to optimize the solver set-up for the prediction of wheel flows (without any grid topology restrictions) the predicted aerodynamic characteristics of isolated wheels were not analyzed. This chapter will describe the results from the 'best' isolated wheel solutions and highlight aspects of the predicted flowfield. In particular, the flow features identified by Fackrell, *Ref.[22]*, will be considered.

6.1 The Optimum Predictions of the Flow Around an Isolated Wheel

It was found that using the RNG turbulence model, with the 538,350 cell mesh and two-layer closure, gave the most accurate comparisons with the experimental data of Fackrell, *Ref.[22]*. However, the rotating wheel solution with this set-up gave lift and drag coefficients that were over-predicted. It was also found that the use of PRESTO reduced C_{Lw} and C_{Dw}, and, thus, it was used with this optimum turbulence model configuration to give final isolated wheel simulations.

Table 6.1 shows the comparison of the computational and experimental force coefficients, whilst *Fig.6.1* and *Fig.6.2* show the optimum surface static pressure coefficient and wake profile comparisons with the experimental data. Relative to the comparable solutions without PRESTO, *Fig.5.9* and *Fig.5.10*, the major effect of

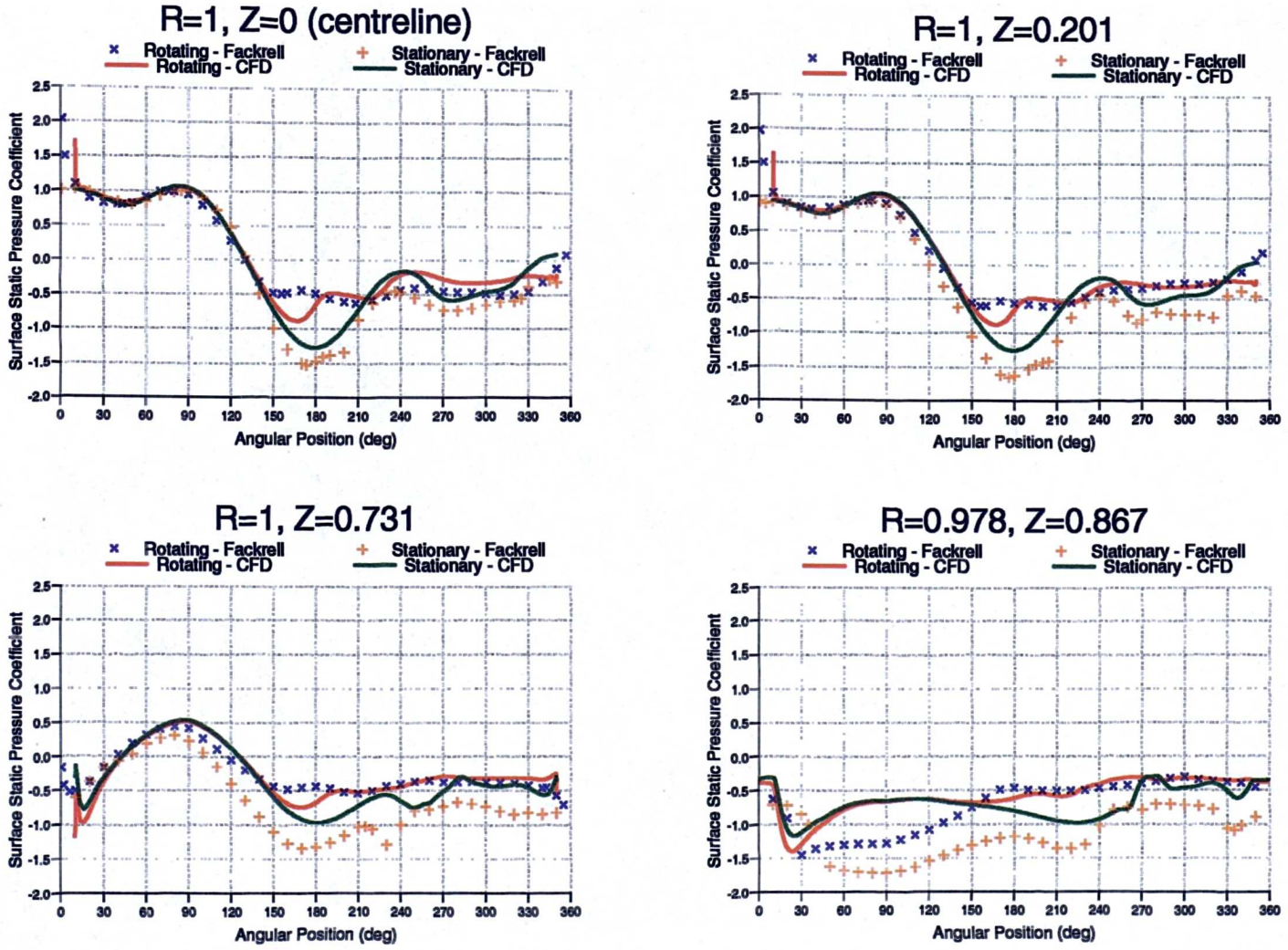

Figure 6.1: Comparison of the Final Computational Surface Static Pressure Coefficient Distributions on an Isolated Wheel with Experimental Data

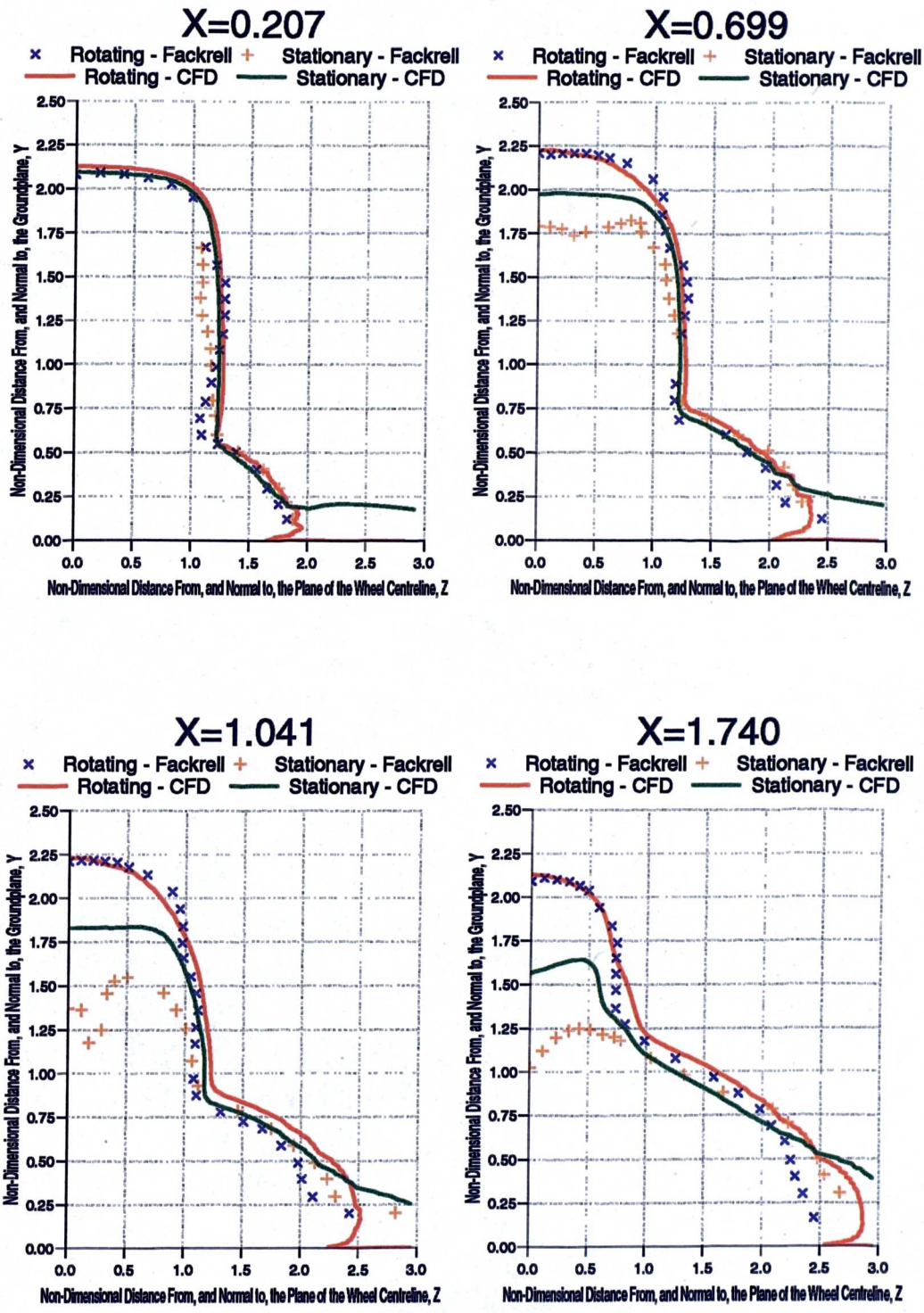

Figure 6.2: Comparison of the Final Computational Wake Edge Profiles (90% Total Head) Behind an Isolated Wheel with Experimental Data

	C_{Lw}	% Error in C_{Lw}	C_{Dw}	% Error in C_{Dw}
Rotating	0.447	1.6	0.590	1.7
Stationary	0.625	-17.8	0.709	-7.9

Table 6.1: Comparison of the Final Computational Isolated Wheel Lift and Drag Coefficients with Experimental Data

using PRESTO was a decrease in the lift coefficient for both the rotating and stationary wheels due to a reduction in the magnitude of the suction peak on the top of the wheel. This gave slightly taller wakes in both cases. The drag coefficient, in both cases, was slightly increased. The final comparison of the rotating wheel force coefficients were very good, whilst both the stationary wheel force coefficients remained under-predicted. It has already been stated that it is thought that transitional effects and the thickness of the predicted groundplane boundary layer were the main reasons for these discrepancies.

Despite the use of PRESTO the solutions can, at best, only be described as being qualitatively correct for the reasons outlined in Section 5.3. Thus, only large scale flow features can be analyzed with a degree of confidence.

6.2 The Flow at the Front Contact Patch of an Isolated Rotating Wheel

Fackrell, *Ref.[22]*, postulated a 'jetting' phenomena at the front of the contact patch of the isolated rotating wheel to account for the pressure coefficients greater than unity, *Fig.2.6*. *Fig.6.3* shows the predicted velocity vectors in this region on the symmetry plane. The reversal of the flow is clearly resolved. The moving wheel and groundplane surfaces bring attached flow into this area which is then forced upstream, away from the contact patch, at a velocity approximately half that of freestream. Thus, the CFD solutions support Fackrell's 'jetting' theory.

Fackrell, *Ref.[22]*, also postulated that this 'jet' of air was deflected downstream either side of the wheel. *Fig.6.4* shows the predicted pathlines from the front part of the contact patch boundary. The flow from this region is clearly entrained into the vortex structure at the side of the wheel and carried downstream.

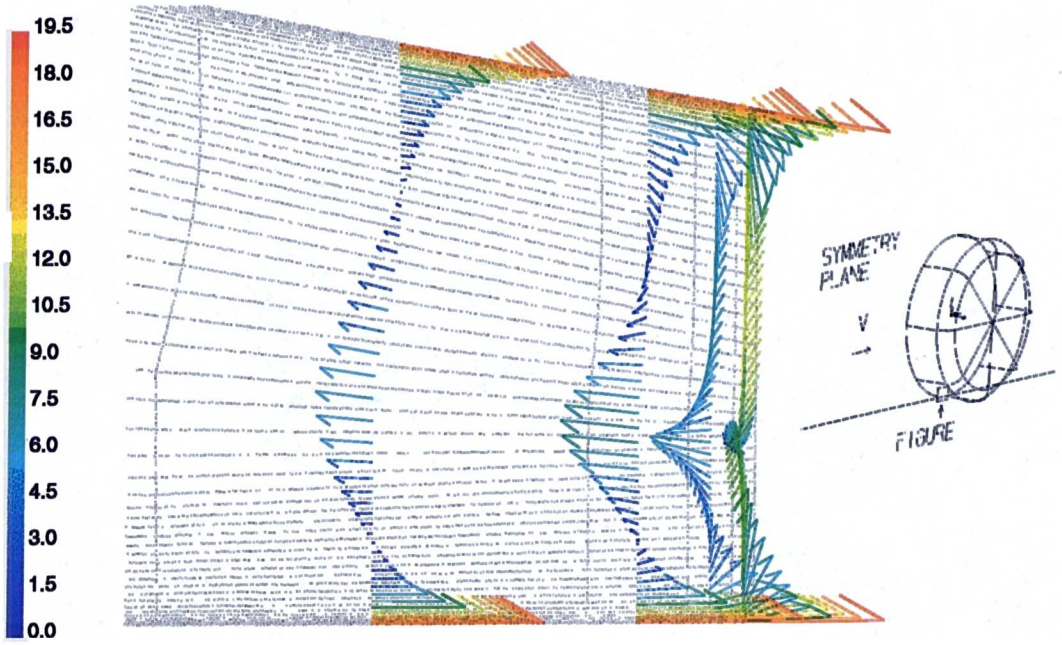

Figure 6.3: Velocity Vectors Showing the Prediction of the 'Jetting' Phenomena Postulated by Fackrell on the Symmetry Plane at the Front of the Contact Patch (Coloured by Velocity Magnitude)

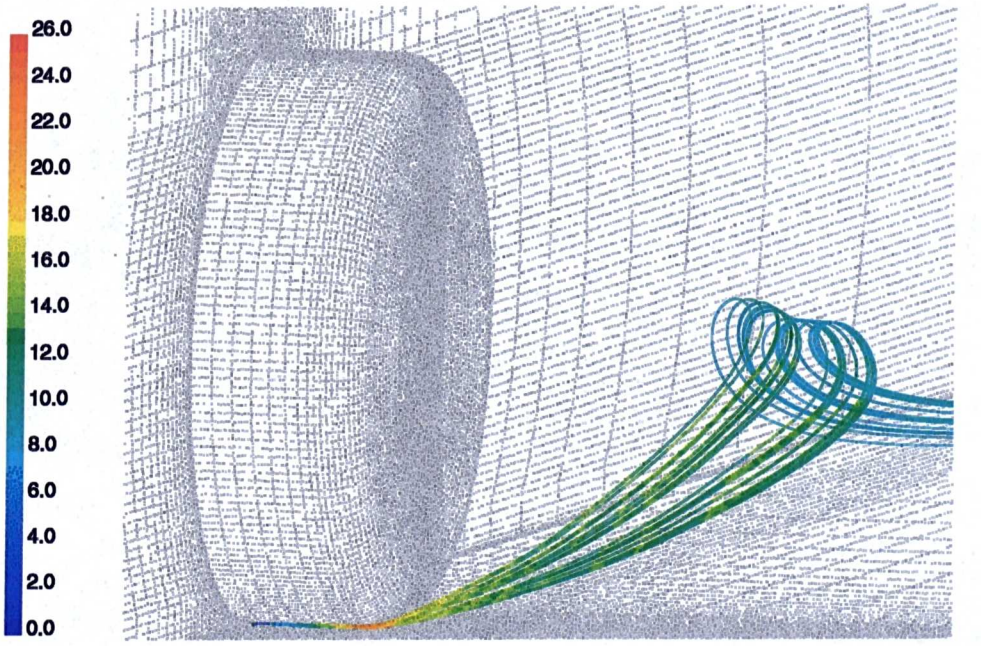

Figure 6.4: Pathlines of the Flow from the 'Jetting' Phenomena at the Front of the Contact Patch (Coloured by Velocity Magnitude)

6.3 The Structure of the Wake Behind an Isolated Wheel

Fig.6.5 and *Fig.6.6* shows the structure of the predicted wake behind the isolated wheel for both rotating and stationary cases. The contours of total pressure are relative to the atmospheric pressure set in the solver, and are plotted on the four planes used experimentally. The taller wake structure behind the rotating wheel can clearly be seen.

A number of significant differences between the rotating and stationary flowfields are apparent. Firstly, the vortex structure next to the stationary groundplane is stronger than that next to the moving groundplane. The smearing of its structure due to the non-movement of the groundplane is also predicted. Secondly, two areas of total head deficit are apparent behind the top half of the rotating wheel compared to just one behind the stationary wheel. Both wakes contain a small vortex structure arising from the flow passing over the rounded profiles of the edge of the wheel. However, the attached flow on the surface of the rotating wheel going against the direction of the freestream at the 'separation' point seemed to result in an additional area of recirculating flow.

Fackrell, *Ref.[22]*, used a Kiel tube for the total head wake surveys downstream of the wheel. This was stated to be insensitive to yaw angles upto $\pm 35°$. Whilst this tolerance would be sufficient to locate the edge of a wake structure would its use give enough accuracy inside the complex wake structure behind an isolated wheel?

Fig.6.7 and *Fig.6.8* show pathlines of the predicted flow behind the isolated wheel for the rotating and stationary cases respectively. The formation of the vortex structure at the side of the wheel is clearly seen. The flow around the front of the wheel is drawn towards the contact patch where it is deflected out towards the side of the wheel. The low pressures this produces results in a relatively weak vortex structure shed from the top edge of the wheel being drawn down towards the contact patch where it is entrained into the vortex adjacent to the groundplane.

Thus, the main component of the flow direction in this area is vertical, and the use of most total pressure probes would produce significant errors in any measured wake structures.

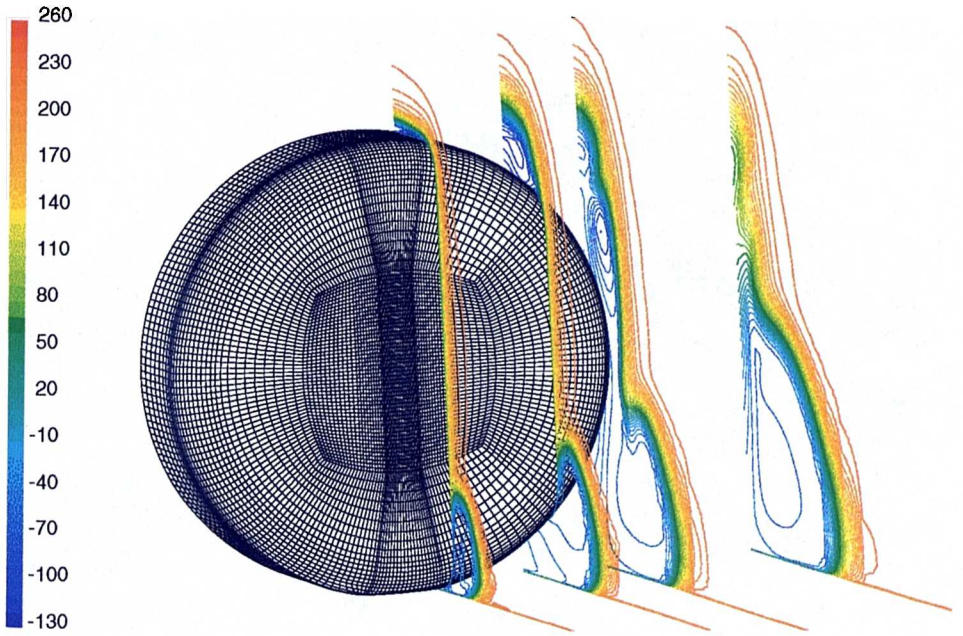

Figure 6.5: Contours of Total Pressure, Relative to the Atmospheric Pressure of 101325Pa, in the Wake Behind an Isolated Rotating Wheel

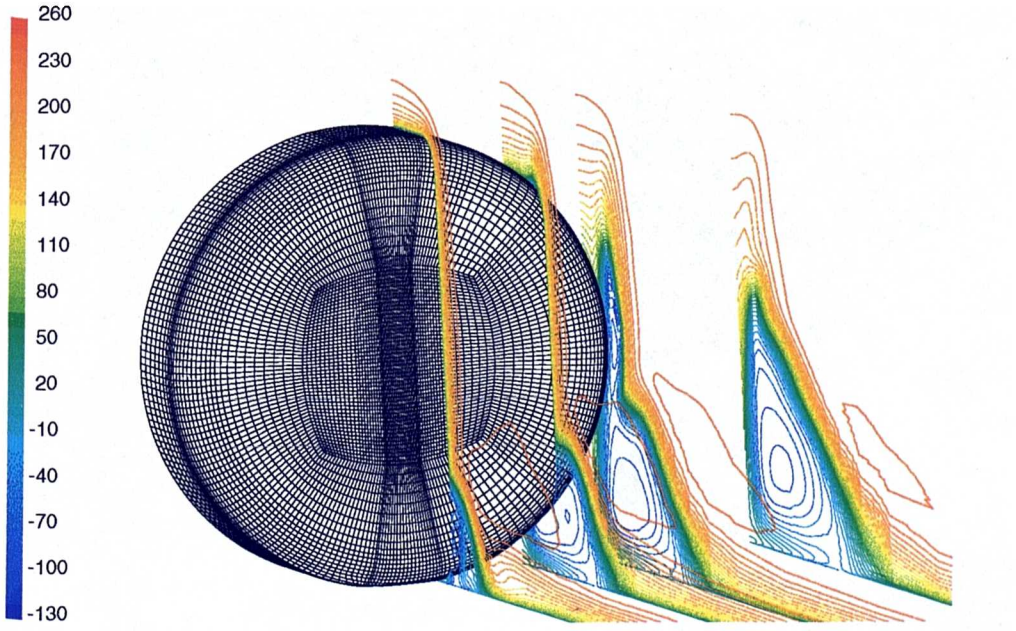

Figure 6.6: Contours of Total Pressure, Relative to the Atmospheric Pressure of 101325Pa, in the Wake Behind an Isolated Stationary Wheel

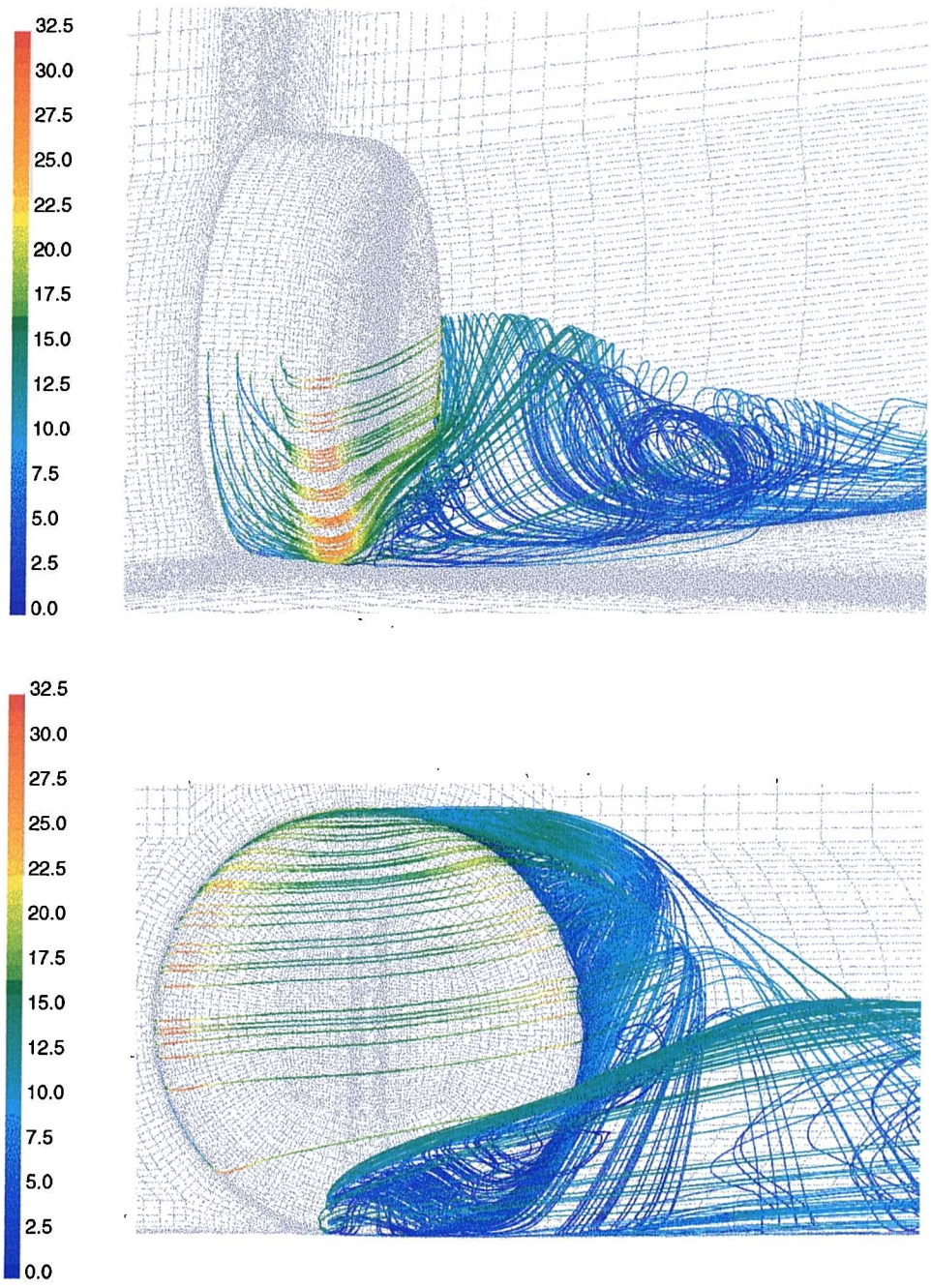

Figure 6.7: The Predicted Flow Around an Isolated Rotating Wheel (Coloured by Velocity Magnitude)

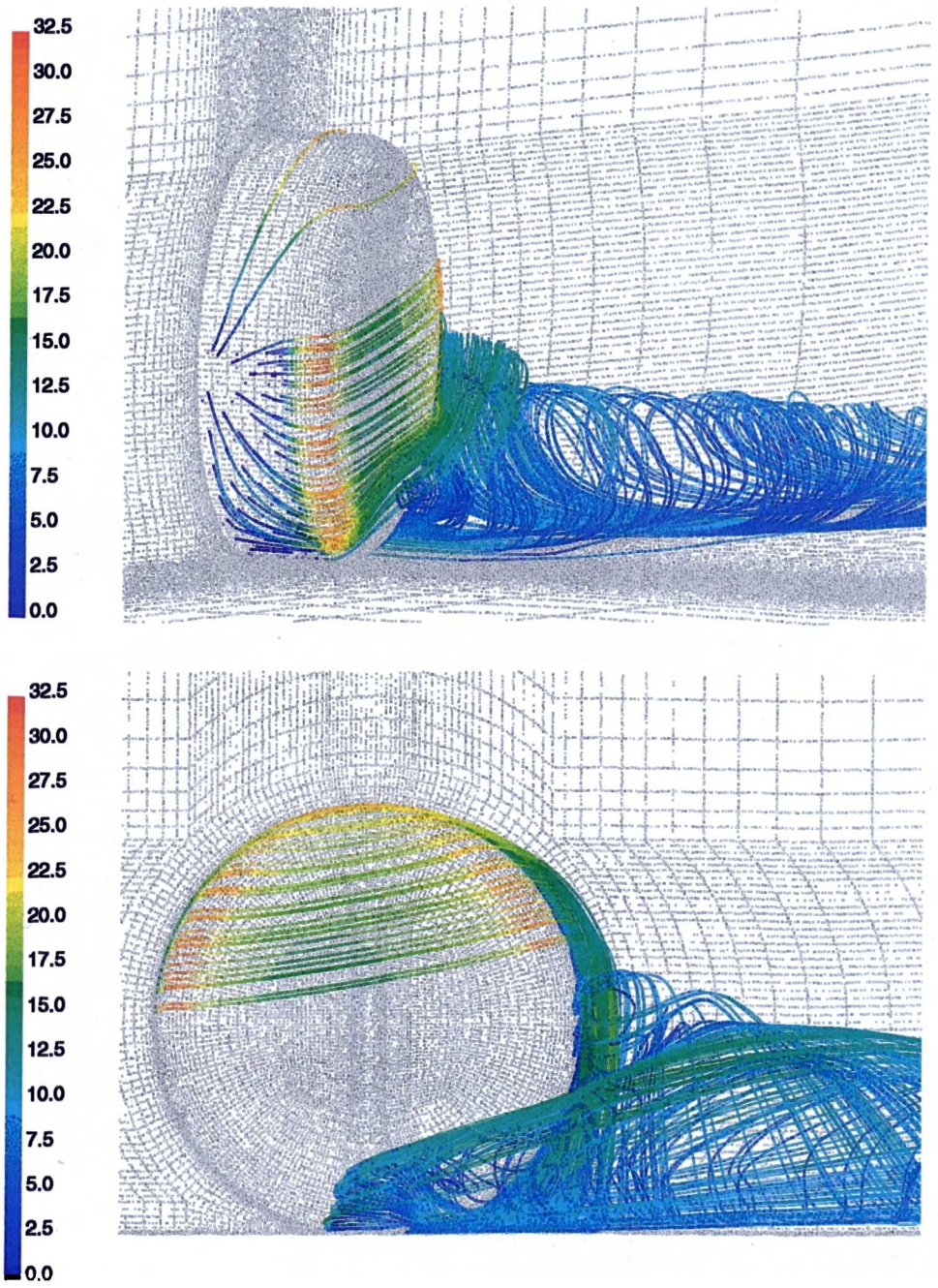

Figure 6.8: The Predicted Flow Around an Isolated Stationary Wheel (Coloured by Velocity Magnitude)

6.4 Summary

From this chapter it can be summarized that:

1. Final isolated wheel calculations using PRESTO have been described which have successfully qualitatively predicted the structure of the flow around an isolated wheel.

2. The rotating wheel solutions corroborated Fackrell's postulation of a 'jetting' phenomena at the front of the contact patch of the rotating wheel. The flow from this area was then entrained into a vortex structure going downstream adjacent to the groundplane and the side of the wheel.

3. This vortex structure next to the groundplane was found to be stronger behind the stationary wheel compared to behind the rotating wheel.

4. The solutions also provided evidence of a weak vortex shed from the top of the wheel which was entrained vertically downwards into the main groundplane vortex structure.

Chapter 7

Experimental Investigation of Shrouded Wheel Flows

Unlike for isolated wheels, none of the published studies concerning the flow around shrouded wheels was found to provide enough information, both in terms of geometric and aerodynamic data, for validation of a CFD model. Therefore, it was decided to conduct an experimental programme for this purpose. To provide a complete a picture as possible of the flowfield both force and pressure measurements would be taken as well as flow visualization.

7.1 Experimental Configuration

All the experimental testing was conducted in the MIRA Model Wind Tunnel. This is a open return open jet facility with a 6.0m long working section and a 1.0m high by 2.1m wide nozzle. A moving groundplane system, flush to the tunnel floor, was fitted throughout. Both upstream boundary layer suction and tangential blowing through the gap created between the belt on the front roller and the tunnel floor were used when the belt was moving. When the groundplane was stationary the gaps at the beginning and the end of the exposed belt surface were left open.

The model was developed by Rover Group Ltd. to specifically investigate wheel aerodynamics using the MIRA Model Wind Tunnel. The wheel, essentially a solid disc with chamfered edges, had a diameter, D, of 0.5m and an aspect ratio, AR, of 30%. The shroud represented a single wheelhouse cavity and consisted of a wooden

box with external dimensions 0.685m long by 0.275m wide. The depth of 0.325m at the front increased to 0.425m at the rear. The wall thickness was 0.0125m. The wheelhouse cavity was open on the underside and there was a part circular opening on one side with a radius of 0.3m. Adding the semi-elliptical front fairing and the tapering tail section increased the length of the model to 1.285m. A faired top section, with a 0.05m edge radius, was also added to give an overall shroud height of 0.475m. The wheel and shroud geometries were designed to give an acceptable wheelhouse size without high wind tunnel blockage. CAD plots of the shroud and wheel are shown in *Fig. 7.1.*

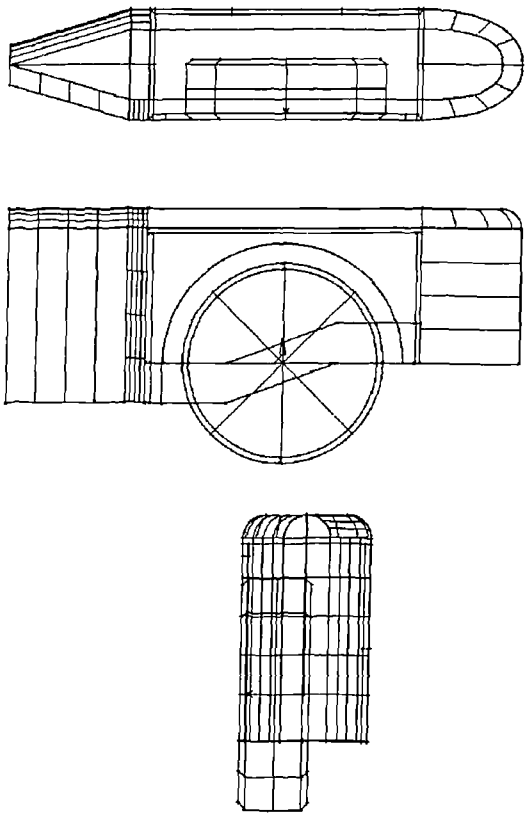

Figure 7.1: CAD plots of the Wheel and Shroud Geometry

The semi-elliptical front fairing housed a two-component strain gauge balance which, together with the tail wire (fixed to the rear of the upper surface of the wheelhouse cavity), allowed lift, drag, and pitching moment to be measured for the shroud. The wheel was independently mounted to a cantilever strut fixed to the tunnel floor by the side of the belt. This was pivoted to allow for vertical movement of the wheel. The relative position of the wheel across the wheelhouse cavity could also be varied.

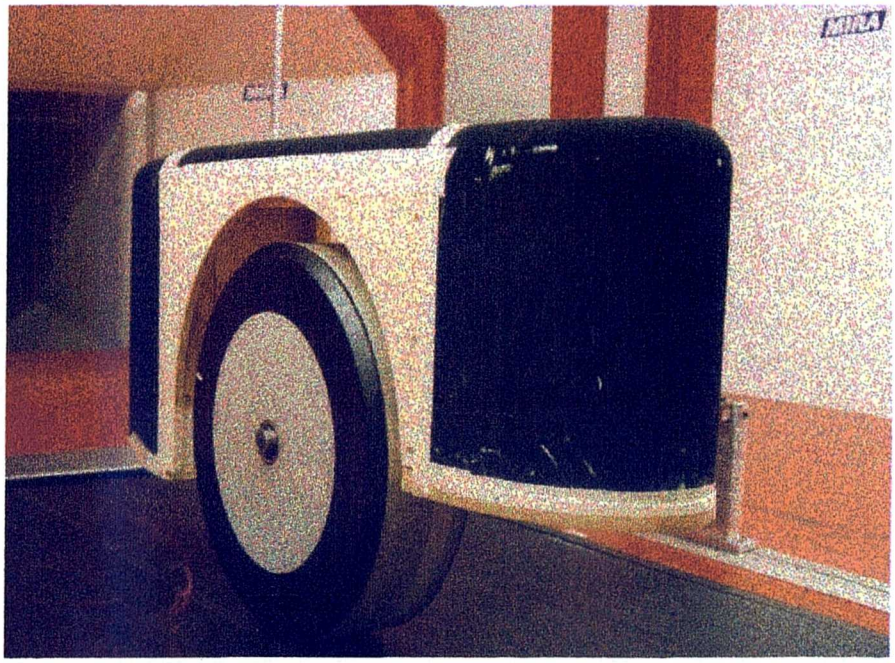

Figure 7.2: Baseline Shrouded Wheel Experimental Configuration

For this study the wheel was mounted so that the outside face of the wheel was aligned with the exterior of the wheelarch face of the shroud. Immediately inboard of the wheel the axle was strain gauged to measure wheel drag. Internal wheelhouse cavity pressure measurements were obtained with 142 'lollipop'[1] tappings attached to the walls. These were connected to a pressure scanner mounted in the rear of the shroud fairing. Due to the constraints of the system a maximum of thirty tappings could be used at once and, therefore, the pressure tubing was not too intrusive in the wheelhouse cavity. All the data was collected with a Pi data acquisition system and then exported to an Excel spreadsheet.

The force coefficients presented were taken without the pressure measuring apparatus in place, although when pressure data was being taken the forces were also measured as a check of consistency. The force coefficients were corrected for blockage using Mercker's open jet correction, *Ref.[51]*, and are based on a reference area of $A_T = 0.15526m^2$.

For the purposes of the CFD study two modifications were made to the existing

[1]The 'lollipop' pressure tappings were formed from a circular disc of metal of approximate diameter 0.01m and depth 0.0015m. One end of a thin metal tube, of an outside diameter less than the disc's thickness, was inlaid into the disc. A small hole was then drilled at the centre of the disc into the tube to form the pressure tapping

wind tunnel model. The aim of the changes was to ease potential meshing problems and increase overall mesh quality. A radius at the lower edge of the rear face of the cavity was removed to give a square corner. The radius of the wheelarch was also increased by 0.025m from the original 0.275m.

The freestream velocity used for both the experimental results and the CFD calculations was 25m/s. This gave a Reynolds number, Re_D, of approximately 850,000 for the wheel diameter of 0.5m. The baseline position for the shroud, *Fig. 7.2*, was with its flat upper surface at zero incidence to the groundplane, together with a front ride height $Y_f = 1$ and a rear ride height $Y_r = 0.6$.

As well as looking at the differences between moving groundplane and rotating wheel with stationary groundplane and stationary wheel, a number of geometric variations of the shroud were also tested. Keeping the top of the shroud parallel to the groundplane its ride height was increased in increments to a maximum of $Y_f = 1.2$ and $Y_r = 0.8$. Also 0.025m chin spoilers, *Fig. 7.3*, were added to the front lower edge of the shroud. Up to four could be fitted at once to give a maximum front spoiler depth of 0.1m. All possible combinations were tested, i.e. the combined effect of shroud ride height and front spoilers were studied.

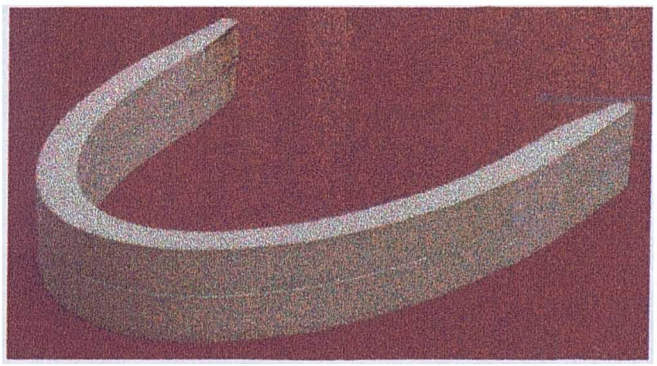

Figure 7.3: 0.050m Front Spoiler for Addition to the Front of the Shroud

Two sessions, comprising of a total of eight days, were used for the collection of data:

- *Session One*
  1. Force and pressure measurements in non-dimensional ride height increments of 0.1 and front spoiler increments of 0.05m
  2. Groundplane boundary layer thickness measurements
  3. Internal wheelhouse cavity wool tuft flow visualization

- *Session Two*
  1. Force and pressure measurements in non-dimensional ride height increments of 0.05 and front spoiler increments of 0.025m
  2. Wool tuft flow visualization of the flow near to the groundplane

7.2 Results

It is intended to briefly describe the main trends shown in the data in the remainder of this chapter, with further analysis of the flowfield, in conjunction with the results from the CFD model, in Chapter 9.

7.2.1 Groundplane Boundary Layer Thickness

A survey was made of the groundplane boundary layer when the belt was both moving and stationary. The primary reason for this was so the computational stationary groundplane boundary layer could be set to the same approximate thickness. A rake consisting of eleven pitot tubes was mounted from a frame 0.25m upstream of the nose of the shroud, *Fig.7.4*.

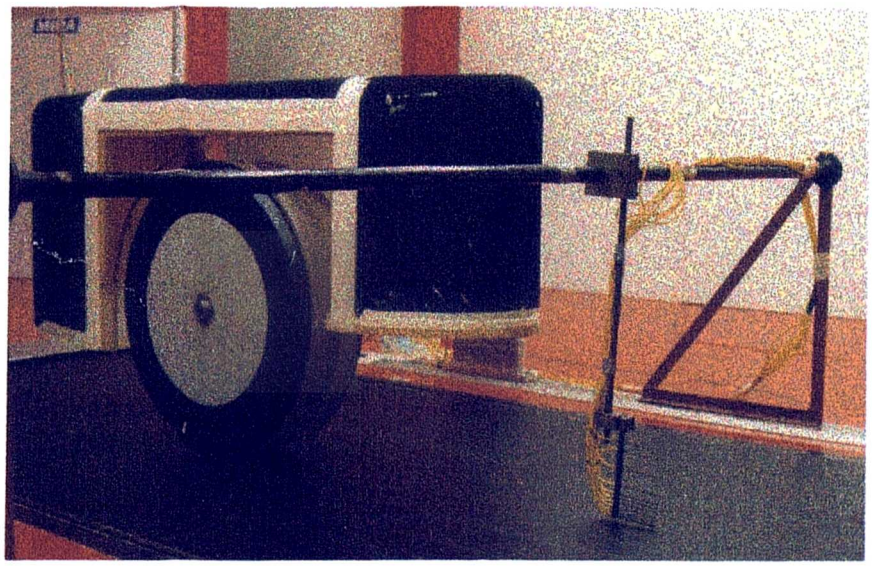

Figure 7.4: The Configuration of the Rake for Measurement of the Groundplane Boundary Layer Thickness Ahead of the Shrouded Wheel

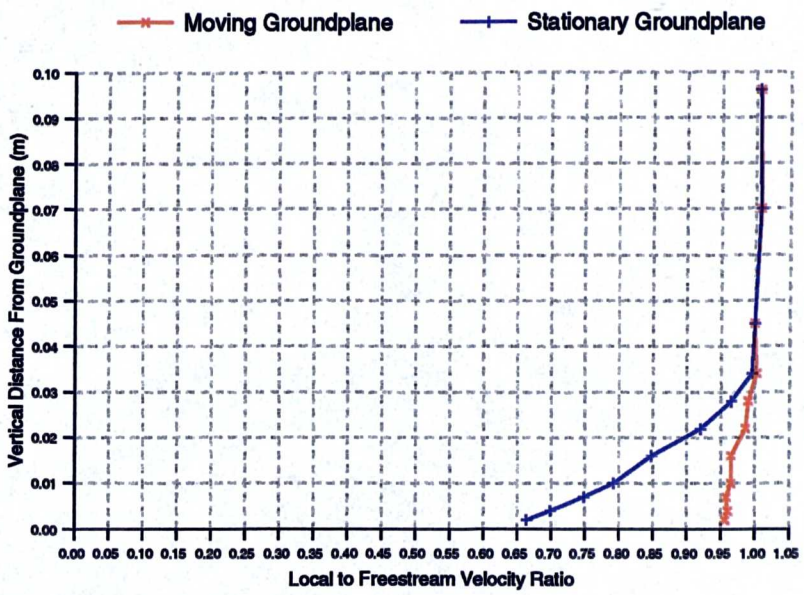

Figure 7.5: Experimental Groundplane Boundary Layer Profiles 0.25m Upstream of the Leading Edge of the Shroud

Fig. 7.5 shows the two profiles. The boundary layer on the stationary groundplane was found to be approximately 0.04m thick.

7.2.2 Force Measurements

Appendix D shows the force data from both sessions. The data is presented both in absolute values and relative to the case of the baseline of $\Delta Y_s = 0$, no front spoiler, moving groundplane, and rotating wheel.

Problems were experienced with the repeatability of the measured forces between the two sessions. Both the absolute forces varied, particularly shroud drag which was found to be up to 20% different in magnitude, as well as, but to a lesser extent, some of the trends with the changes in the configuration of the shroud geometry, or whether the belt was moving or not.

Between the two sessions the MIRA Model Wind Tunnel was closed for a period to allow for a new fan to be installed. As the second session occurred approximately one month after reopening a number of issues concerning the flow inside the working section had still to be quantified. It was subsequently found that the new fan had increased the pressure gradient between the nozzle and collector as well as its motor

introducing some electrical interference problems. The pressure gradient change would have affected the shroud force measurements more than the groundplane influenced wheel and thus the largest differences between the two sessions were found in the shroud drag coefficient C_{Ds}.

To resolve this it was decided that the absolute force measurements from session one were more reliable and, thus, these would be used for the baseline configuration. As more shroud geometry changes had been tested in the second session the relative force coefficients from the baseline case of session two were applied to the baseline from session one to give a derived set of force coefficients, *Table 7.1.* Contour plots of these four datasets are shown from *Fig.7.6* through to *Fig.7.9.*

Moving Groundplane **Stationary Groundplane**

Shroud Lift Coefficient, C_{Ls}

	SPOILER DEPTH (m)						SPOILER DEPTH (m)				
ΔY_s	*0.000*	*0.025*	*0.050*	*0.075*	*0.100*		*0.000*	*0.025*	*0.050*	*0.075*	*0.100*
0.00	0.080	0.095	0.090	0.058	0.021	0.00	0.107	0.136	0.076	0.087	0.045
0.05	0.081	0.107	0.083	0.068	0.032	0.05	0.105	0.139	0.071	0.090	0.054
0.10	0.081	0.113	0.073	0.073	0.042	0.10	0.101	0.147	0.072	0.091	0.059
0.15	0.085	0.126	0.064	0.080	0.047	0.15	0.105	0.154	0.074	0.087	0.059
0.20	0.087	0.131	0.065	0.071	0.062	0.20	0.106	0.154	0.080	0.080	0.069

Shroud Drag Coefficient, C_{Ds}

	SPOILER DEPTH (m)						SPOILER DEPTH (m)				
ΔY_s	*0.000*	*0.025*	*0.050*	*0.075*	*0.100*		*0.000*	*0.025*	*0.050*	*0.075*	*0.100*
0.00	0.311	0.347	0.345	0.311	0.264	0.00	0.331	0.386	0.294	0.326	0.284
0.05	0.309	0.373	0.330	0.325	0.285	0.05	0.330	0.393	0.290	0.333	0.295
0.10	0.307	0.384	0.307	0.337	0.307	0.10	0.328	0.399	0.292	0.329	0.309
0.15	0.314	0.395	0.289	0.338	0.320	0.15	0.336	0.408	0.294	0.316	0.309
0.20	0.328	0.405	0.290	0.318	0.332	0.20	0.346	0.421	0.304	0.307	0.324

Wheel Drag Coefficient, C_{Dw}

	SPOILER DEPTH (m)						SPOILER DEPTH (m)				
ΔY_s	*0.000*	*0.025*	*0.050*	*0.075*	*0.100*		*0.000*	*0.025*	*0.050*	*0.075*	*0.100*
0.00	0.156	0.146	0.138	0.097	0.109	0.00	0.132	0.115	0.111	0.111	0.091
0.05	0.166	0.150	0.143	0.104	0.114	0.05	0.139	0.121	0.113	0.117	0.100
0.10	0.176	0.157	0.145	0.114	0.121	0.10	0.147	0.131	0.118	0.121	0.108
0.15	0.184	0.163	0.145	0.122	0.132	0.15	0.155	0.140	0.125	0.121	0.108
0.20	0.189	0.172	0.150	0.124	0.137	0.20	0.158	0.147	0.132	0.122	0.124

Total Drag Coefficient, C_{Dt}

	SPOILER DEPTH (m)						SPOILER DEPTH (m)				
ΔY_s	*0.000*	*0.025*	*0.050*	*0.075*	*0.100*		*0.000*	*0.025*	*0.050*	*0.075*	*0.100*
0.00	0.467	0.493	0.483	0.408	0.373	0.00	0.462	0.500	0.404	0.436	0.375
0.05	0.475	0.523	0.473	0.428	0.399	0.05	0.469	0.514	0.403	0.450	0.395
0.10	0.483	0.541	0.452	0.450	0.427	0.10	0.474	0.529	0.410	0.450	0.417
0.15	0.498	0.558	0.434	0.460	0.451	0.15	0.490	0.548	0.419	0.436	0.417
0.20	0.517	0.576	0.440	0.442	0.470	0.20	0.503	0.567	0.436	0.429	0.449

Table 7.1: Derived Experimental Wheel and Shroud Force Coefficients From the Two MIRA Sessions

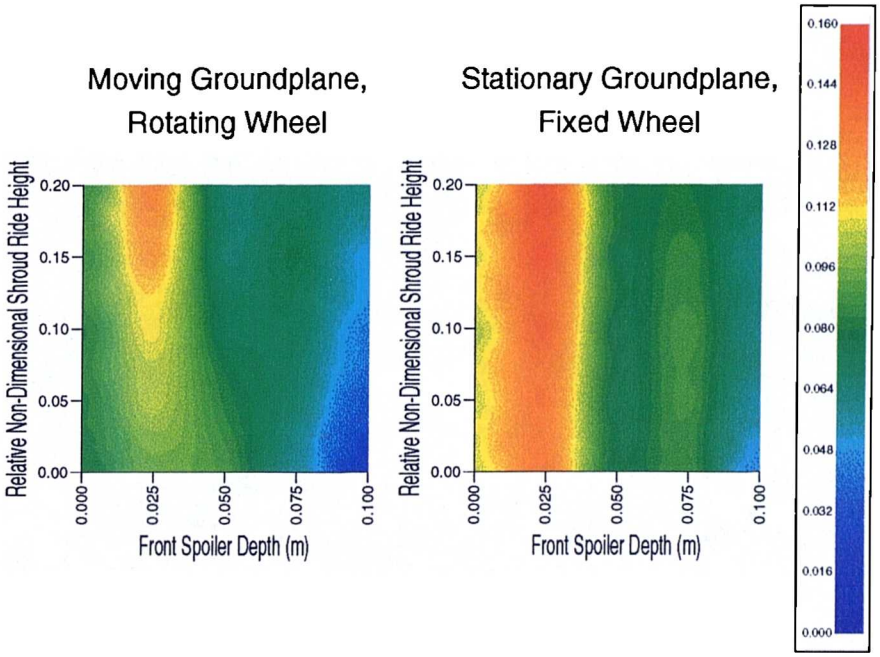

Figure 7.6: The Influence of Ground Condition, Shroud Ride Height, and Front Spoiler Depth on the Derived Experimental Shroud Lift Coefficient

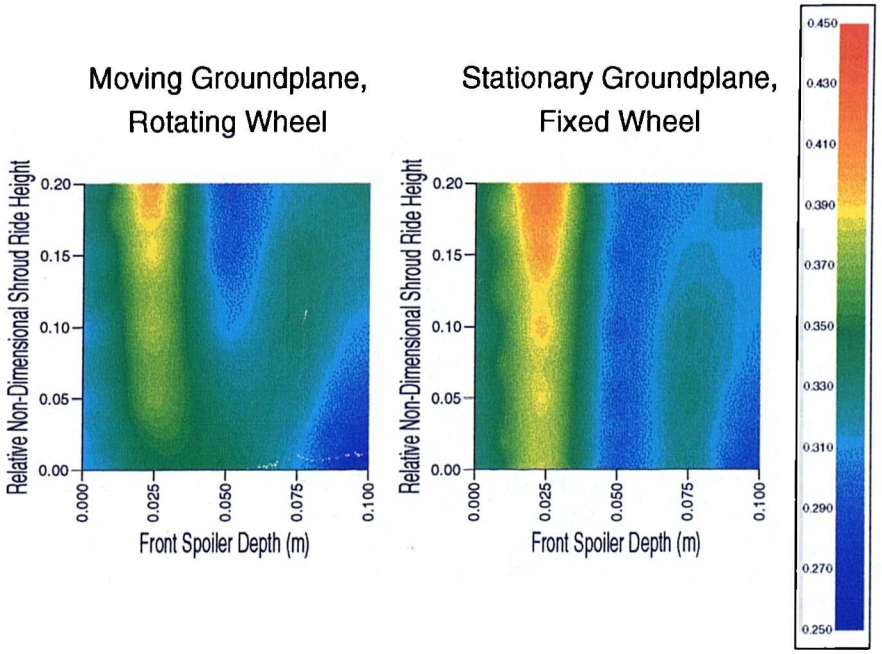

Figure 7.7: The Influence of Ground Condition, Shroud Ride Height, and Front Spoiler Depth on the Derived Experimental Shroud Drag Coefficient

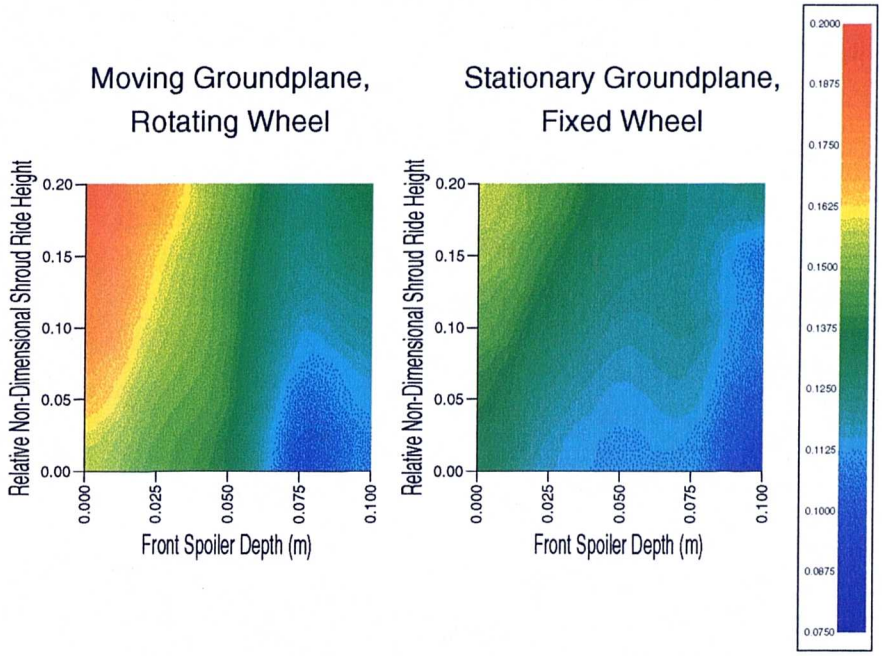

Figure 7.8: The Influence of Ground Condition, Shroud Ride Height, and Front Spoiler Depth on the Derived Experimental Wheel Drag Coefficient

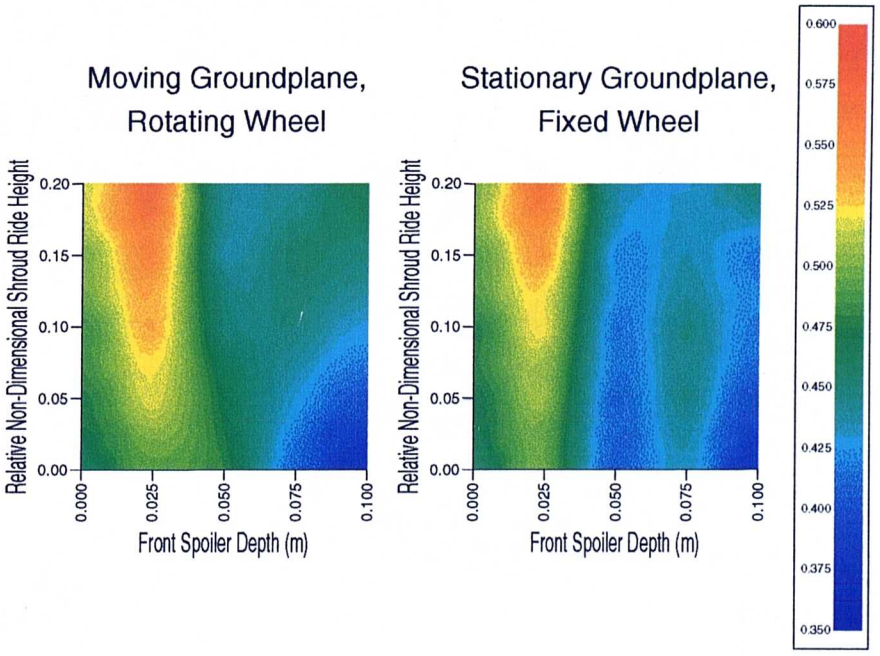

Figure 7.9: The Influence of Ground Condition, Shroud Ride Height, and Front Spoiler Depth on the Derived Experimental Total Drag Coefficient

The use of a stationary groundplane and wheel, instead of a moving groundplane and rotating wheel, increased both shroud lift and shroud drag. This trend was generally independent of both shroud ride height and front spoiler depth. Typically, the increases in C_{Ls} and C_{Ds} were of the order of 0.020. Over the ride height range both force coefficients exhibited maximums when the shroud was fitted with a 0.025m front spoiler. This indicates that shroud leading edge separation effects could be a major influence on the flow inside the wheelhouse cavity. Minimums for both shroud lift and drag coefficient were found for the lowest shroud ride height, the baseline, and the maximum front spoiler depth, 0.100m.

The change in wheel drag with ground condition was contrary to that found by Fackrell, *Ref.[22]*, for an isolated wheel. The stationary wheel produced less drag than the rotating wheel. Again, this was generally independent of the shroud ride height and the front spoiler depth. Increasing the ride height of the shroud increased wheel drag, whilst adding the front spoilers to the shroud generally decreased the wheel drag. The exception was for the rotating wheel and 0.100m spoiler. Unlike for the shroud, no local maximum was found for the 0.025m front spoiler.

For the shroud without spoilers adding $\Delta Y_s = 0.2$ to the baseline ride height increased the rotating wheel drag coefficient by 0.033 from 0.156, an increase of 21.2%, and the stationary wheel drag coefficient by 0.026 from 0.132, an increase of 19.7%. With the shroud at its baseline ride height adding a 0.100m front spoiler decreased the rotating wheel drag coefficient by 0.047, or 30.1%, and the stationary wheel drag coefficient by 0.041, or 31.1%.

However, decreasing wheel drag will be of little consequence if the total drag of the system is increased. The increase in shroud drag found with using the stationary groundplane system instead of the moving groundplane system tended to balance out the decrease in wheel drag. Thus, the total drag was similar for both groundplane conditions. The only exception to this was when the shroud was fitted with a 0.050m spoiler at low ride heights. At this condition the stationary groundplane total drag coefficient was upto 0.079 less than the moving groundplane case. The extent of any separation from the front spoilers, especially at low ride heights, will be affected by any movement of the groundplane and wheel rotation and, thus, whether the flow can re-attach on the lower horizontal front face of the shroud will be an important factor in the flow characteristics within the wheelhouse cavity.

With both the shroud and wheel drag coefficients having minimums with the maximum front spoiler depth and the lowest shroud ride heights, the total drag coefficient

of the system showed the same trend. For the moving groundplane system C_{Dt} varied from a minimum of 0.373 to a maximum of 0.576, and from a minimum of 0.375 to a maximum of 0.567 for the stationary groundplane system. Thus, substantial decreases in total drag coefficient, despite the small reference area (which was approximately 10% that of a small passenger car), were found for simple geometric changes to the shroud for both groundplane / wheel conditions.

7.2.3 Pressure Measurements

Appendix E presents the results of the pressure surveys within the wheelhouse cavity, both in tabular form and as contour plots. For accuracy reasons the experimental data has not been extrapolated to the boundaries of the cavity faces. Also, contours were not generated for the inside of the wheelarch face due to only having six data points in that area.

For the baseline case of moving groundplane, rotating wheel, shroud ride height $\Delta Y_s = 0$, and no front spoiler the measured surface static pressure coefficients varied from -0.126 to 0.299. However, almost all were within the range ± 0.1. This range of pressures is similar to that measured by Fabijanic, *Ref.[29]*, and *Ref.[30]*. The pressure coefficients tended to become more positive going downstream from the front face of the cavity. All of the pressure coefficients on this front face were negative, whilst they were mostly all positive on the rear face. An area of negative pressure coefficient existed near to the top of this rear face on the non-wheelarch side with the area of the highest positive pressures located just below these negative coefficients. The roof of the cavity also experienced mostly all negative pressures apart from three patches; two on the wheelarch side centred approximately 25% and 50% along the cavity, with the third being at the rear of the top face. The side panel was also mostly negative apart from a small patch at the lower rear corner.

Using the same geometric configuration of the shroud above the stationary groundplane system resulted in an overall increase in the pressure coefficients within the wheelhouse cavity. The front face was still totally negative. The almost identical distribution, when compared to the baseline case, indicates that without front spoilers the pressure distribution on this face is more a function of geometry rather than ground movement. Most of the pressures on the roof panel of the cavity were positive, with the transition from negative occurring at approximately 25% of the length of the cavity. On the non-wheelarch side of this face the area of negative pres-

sure extended slightly further downstream as the front half of the side panel also experienced negative pressures. The rest of the pressures on this face were positive apart from two small patches. The maximum pressure coefficients were again found in the lower rear corner of this face. On the rear face of the cavity the pressures again were more positive. Only a very small patch of negative pressure was found, and the positive pressure coefficients on the bottom half of the area measured were greater in magnitude than with the moving groundplane system.

Increasing the ride height of the shroud, without front spoilers fitted, produced only very small changes in the pressure distributions for each of the two groundplane / wheel conditions. The same patterns in the distributions were seen with the major difference being the increase in the extent of the negative pressure coefficients on the rear face, and the front part of the top face, of the wheelhouse cavity for the stationary groundplane system. Thus, it seems any changes in the shroud force coefficients are mainly due to aerodynamic changes outside of the wheelhouse cavity. The changes in the pressure coefficients on the inside of the arch face possibly indicate a change in the flow structure leaving the wheelhouse cavity.

Adding the front spoilers to the leading edge of the shroud produced more significant changes in the wheelhouse cavity pressure distributions due to the change they gave in the upstream flow conditions.

For the baseline ride height and moving groundplane configuration no consistent change was seen. Adding the 0.050m front spoiler, relative to the no front spoiler case, caused more negative pressures, in magnitude, at the bottom of the front face which then became positive at the top of the face. Most of the pressures on the top and rear faces of the cavity became positive and the distributions were more uniform. The lower front corner of the side face experienced lower negative pressures which became positive going downstream and upwards. The pressures on the rear face of the cavity were all positive.

However, adding the 0.100m spoiler changed almost all of the pressures negative again. Within the areas measured on the top and side faces all the coefficients were negative, and only two areas on the front and rear faces experienced small positive pressures.

With the groundplane stationary the trend was more predictable. Adding both combinations of front spoilers reduced the pressures within the wheelhouse cavity and made the distributions more regular. As with the moving groundplane case the

distributions became almost uniform with the 0.100m front spoiler. The differing trends with the 0.050m spoiler accounts for the trend in the shroud force coefficients, and, thus, it seems that reducing the pressure coefficients within the wheelhouse cavity resulted in the observed decreases in shroud drag.

The trends shown in the wheelhouse cavity pressure coefficients, when the ride height of the shroud fitted with front spoilers was increased, became more varied than when no front spoiler was fitted. The flow in the wheelhouse became more shroud ride height sensitive, especially with the moving groundplane system. Increasing the shroud ride height gave, in general, more negative cavity pressure coefficients with the 0.050m front spoiler. However, for the 0.100m spoiler, the increased shroud ride height gave larger areas of positive pressure coefficient, apart from on the lower edge of the front face of the cavity where suction pressure coefficients of the order of -0.25 were measured.

Another trend, independent of ground condition and ride height, was the influence that the front spoilers had on the pressures on the front lower edge of the side panel of the wheelhouse cavity. Increasing the depth of the front spoilers consistently decreased the pressure coefficients in this area. Thus, the increased separation behind the front spoilers affected the flow pattern, and thus the way the flow can enter or leave the cavity, in this area adjacent to the front of the wheel.

7.3 Summary

From this chapter it can be summarized that:

1. An experimental programme has been performed to provide validation data for the CFD shrouded wheel model. Both forces and pressures within the wheelhouse cavity have been measured for changes in wheel rotation / ground movement condition, the ride height of the shroud, and shroud geometric changes through the addition of front spoilers.

2. The influence of ground condition on wheel drag was found to be opposite of that for an isolated wheel. The rotating wheel on a moving groundplane produced more drag that an equivalent stationary wheel on a fixed groundplane.

3. For both groundplane systems it was found that lowering the ride height of the shroud reduced wheel drag. Adding increasing front spoiler depth also decreased wheel drag.

4. The separation behind the front shroud spoiler was influenced by the movement of the groundplane, and the cavity pressures highlighted critical differences in the wheelhouse flowfield with a 0.050m front spoiler.

5. Decreasing the pressures within the wheelhouse cavity correlated with a decrease in the drag of the shroud containing the cavity.

Chapter 8

The Shrouded Wheel CFD Solutions

As an optimum set of numerical parameters for FLUENT/UNS had been determined with the isolated wheel study the main influence on the quality of the shrouded wheel CFD solutions would be the mesh. Due to the complexity of the geometry of the shroud, a mesh consisting of only hexahedral elements, with the required quality of cell skewness, would have been unfeasible. Also, modifications to the geometry of the shroud, whether front spoiler depth or ride height, would have been difficult to incorporate. Therefore, it was decide to utilize the hybrid mesh capabilities of TGrid and FLUENT/UNS.

8.1 Mesh Topology

8.1.1 Hexahedral Elements

Having obtained good qualitative comparisons with the experimental data of Fackrell, *Ref.[22]*, it was considered important to retain as much of the structure of the hexahedral mesh from the isolated wheel solutions as possible. Thus, the block structure of the mesh adjacent to the wheel surface was retained with only minor modifications which slightly improved overall cell quality. It was mapped to the new wheel surface geometry and reflected in its plane of symmetry as both sides of the wheel had to be modelled due to the asymmetric nature of the shroud.

It was also decided to retain hexahedral elements for the farfield of the computational domain as this meant only using a realistic number of elements whilst retaining a refined mesh next to the groundplane for the two-layer turbulence model closure. Therefore, to introduce a space in the hexahedral elements for the shroud, a cuboid volume, or an 'internal box', was introduced that would, at this stage, contain no volume mesh. This required small changes to the mesh block structure next to the groundplane which meant that the mesh wrapped around the wheel contact patch. This also removed some relatively high aspect ratio cells from this area which would help resolve any crossflows around the wheel.

Fig.8.1 shows the structure of the surface mesh on the wheel and groundplane.

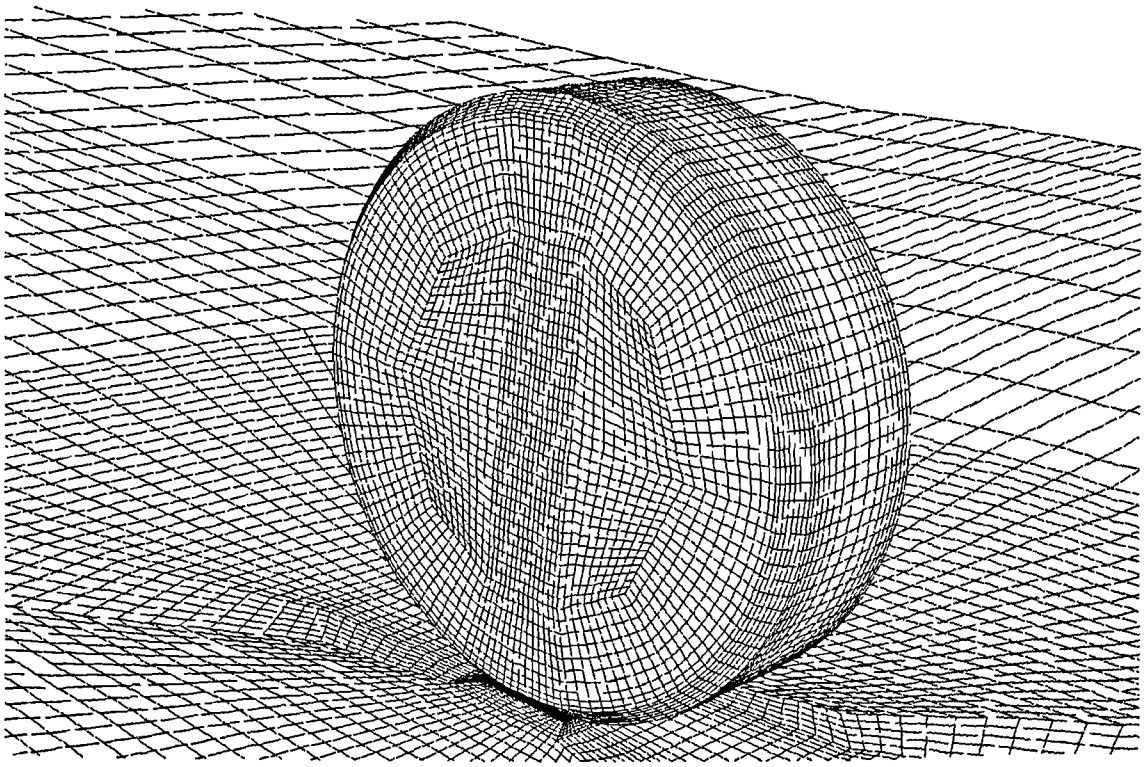

Figure 8.1: The Quadrilateral Element Surface Mesh for the Shrouded Wheel and Groundplane

Whilst both the non-dimensional distance, in terms of numbers of wheel radii, from the centre of the wheel to the side and roof of the computational domain, and the downstream location of the fluid outlet from the domain, remained the same, the distance upstream of the inlet relative to the wheel was increased from ten to twelve

wheel radii. This was to match the thickness of the predicted stationary groundplane computational boundary layer with the experimental data, *Fig.7.5.*

8.1.2 Shroud Surface Mesh

From measurements taken during the two wind tunnel sessions a geometrical representation of the shroud was built in ICEM DDN, *Fig.7.1.* This accurately reflected the experimental geometry apart from an omitted notch in the side wall of the wheelhouse cavity which accommodated the wheel support system at low shroud ride heights. In P-Cube a series of approximately forty inter-connected faces was overlaid onto this geometry for generation of the unstructured triangular surface mesh, *Fig.8.2.* For the baseline shroud configuration this consisted of 19,498 elements. Adding the 0.100m front spoiler to the shroud increased the surface mesh size by a further 9288 elements.

Attention was paid to obtaining as much mesh resolution as possible in the areas of the wheelhouse cavity and on the underneath of the shroud. This meant that the surface mesh on top of the shroud was relatively coarse in comparison. The structure of the mesh faces was constructed so that any sharp edges, for example, on the lower edges of the wheelhouse cavity and wheelarch, and on the lower front edge of the shroud, had a consistent, and as small an edge length as possible to help resolve any fixed flow separations that would exist in the flow field. However, due to skewness requirements and mesh generation restrictions, these elements still had to be approximately equilateral and, therefore, their centres were still of the order of a couple of millimetres away from the actual geometrical edge.

Whilst changes in shroud ride height could be made during the final hybrid volume mesh generation process, the addition of spoilers to the front of the shroud meant that a new surface mesh had to be created for each spoiler depth. The structure of the interconnecting mesh faces in P-Cube was designed so that these changes would retain as much of the baseline mesh between each geometry configuration as possible to maximize consistency.

8.1.3 Hybrid Volume Mesh

Both the hexahedral wheel / groundplane / farfield volume mesh and the unstructured shroud surface mesh were merged on reading into TGrid with Fluent's tfilter

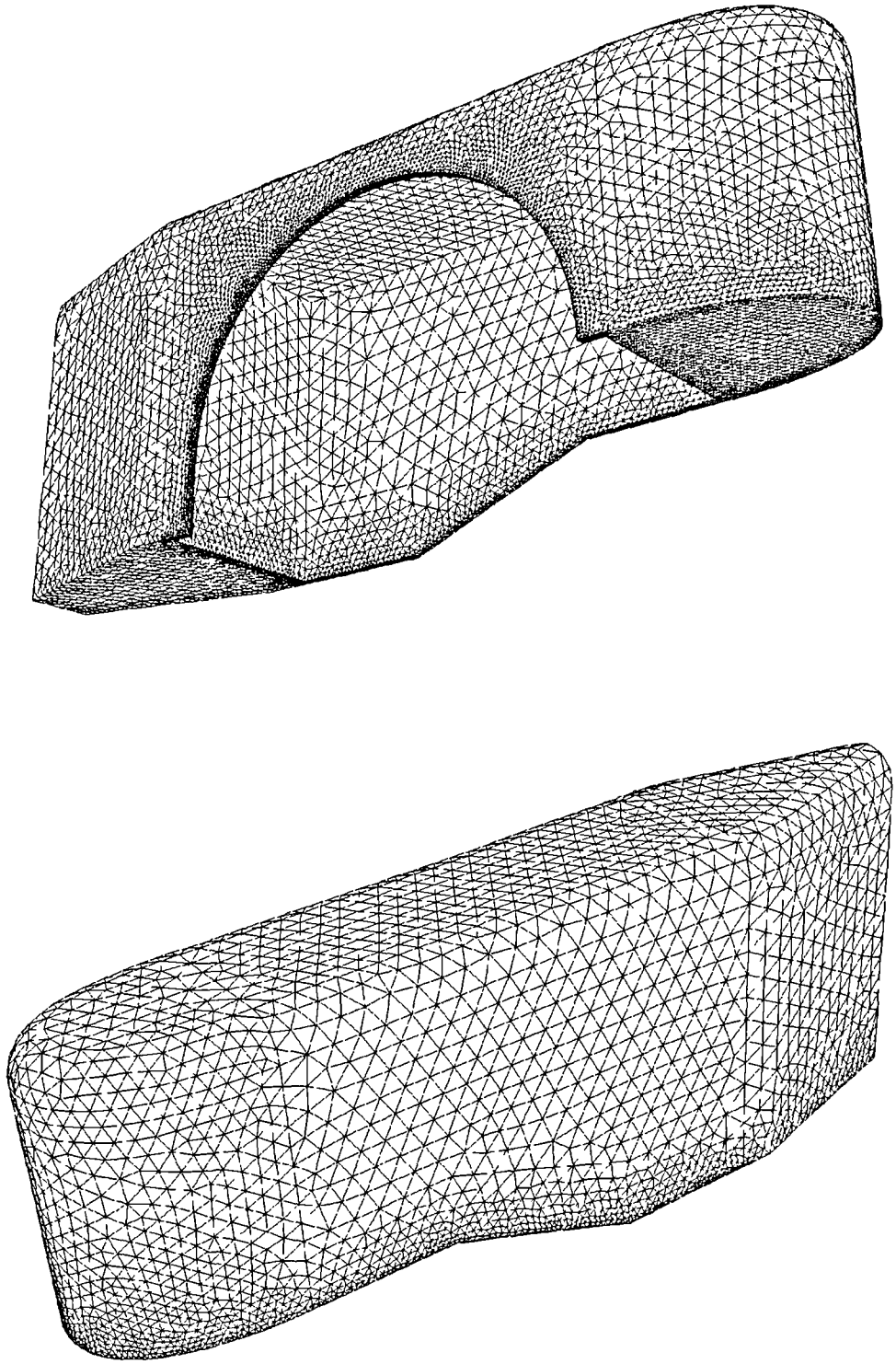

Figure 8.2: The Unstructured Surface Mesh for the Shroud Without a Front Spoiler

routine. This single mesh then formed the basis of the final hybrid volume mesh. *Fig.8.3* shows a combined surface mesh for the wheel, groundplane, and shroud with the 0.100m front spoiler fitted.

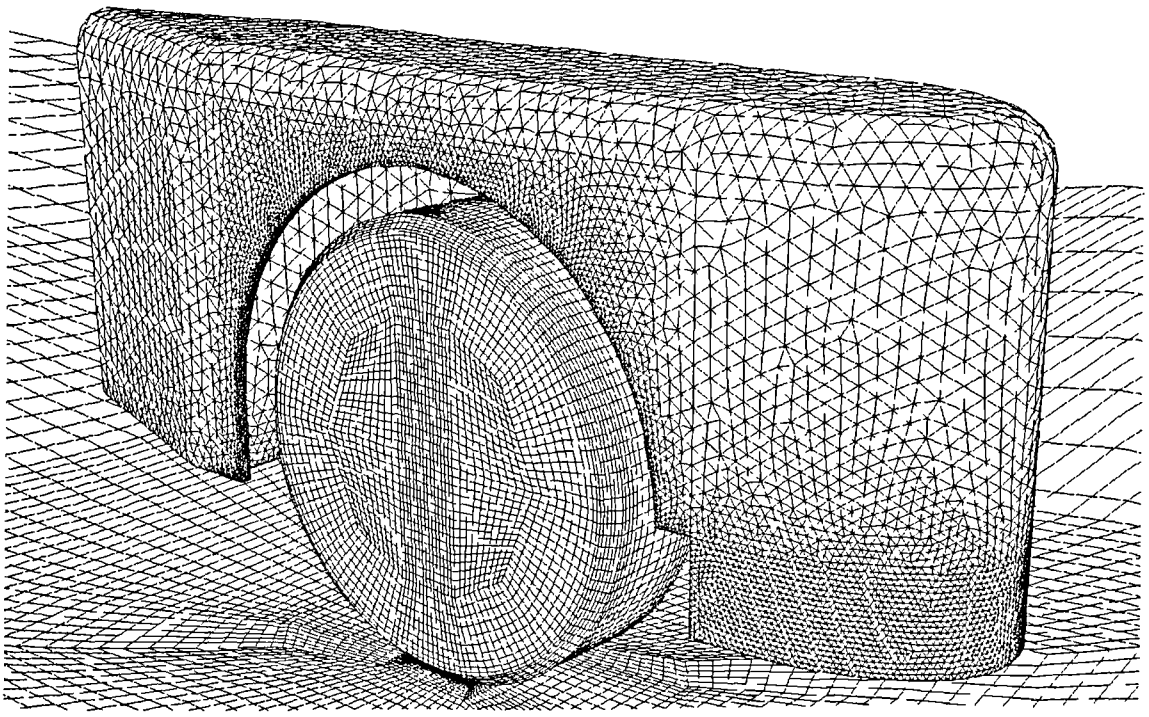

Figure 8.3: Surface Mesh for the Shrouded Wheel, Groundplane, and Shroud Fitted with the 0.100m Front Spoiler

Pyramidal elements were first grown from the quadrilateral faces of the 'internal box' of the hexahedral mesh in which the shroud was located. After experimentation the centroid method was chosen with a height parameter of 0.65. This was found to provide the best compromise of cell skewness, both in the pyramidal elements and the subsequently generated tetrahedral cells, with continuity of cell centre distances between the different sections of the mesh.

Prism layers were then grown from the triangular surface mesh of the shroud. The growth parameters were set to best satisfy the requirements of the two-layer near wall turbulent closure approach and the total number of cells. The first ten layers were set to be orthogonal to the surface of the shroud to further improve the quality of the mesh in the lower parts of the predicted boundary layers. This would help in the simulation of the location of any points of separation.

Finally, a sub-domain was defined which consisted of the triangular faces of the pyramidal elements and the prism layer cap, i.e. the outer layer of triangular faces of the prism cells. These defined an enclosed volume in which a tetrahedral volume mesh was generated. This was then further refined in the area within the wheelhouse cavity and behind the wheel below the lower rear face of the shroud. The aim was to gain better resolution of the expected complex flow structures in this area.

A slice of the final hybrid volume mesh in a plane of constant X through the centre of the wheel is shown in *Fig.8.4*. Each type of element is coloured differently:

Cyan:	Hexahedral Elements
Blue:	Shroud Prism Layers
Green:	Pyramidal Elements
Red:	Tetrahedral Elements

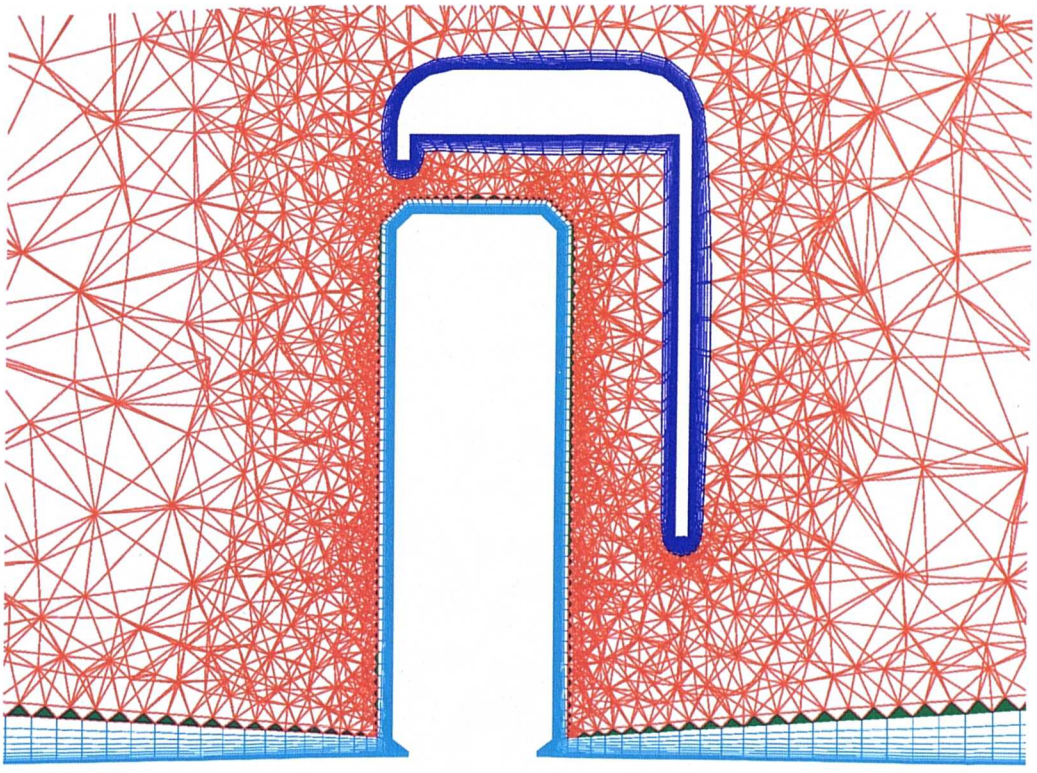

Figure 8.4: Hybrid Volume Mesh Cut in the Plane of Constant X Through the Centre of the Wheel Showing the Locations of the Different Types of Elements Used

The prism layer capability of TGrid also provided a quick method of increasing the distance between the start of the computational domain and the shrouded wheel to further increase the stationary groundplane boundary layer thickness from that

measured experimentally. The faces of the inlet boundary were extruded in the negative X direction, i.e. upstream, in steps equating to the approximate length of the first set of elements next to the inlet in the baseline mesh. This length was set to preserve continuity in cell centre distances. The inlet was extended to distances of eighteen and twenty four wheel radii, which equated to increases in approximate stationary groundplane boundary layer thickness of 0.02m and 0.04m respectively 0.25m upstream of the nose of the shroud.

8.2 The Influence of Total Volume Mesh Size

It was decided that all the initial solution development should be processed on the SGI Octane. This, therefore, limited the total mesh size to approximately 900,000 elements for processing in parallel within the 1Gb RAM. Initial meshes had between ten and fifteen layers of prisms on the shroud, which was considered minimal for the requirements of boundary layer resolution with the turbulence model. However, this still meant the the mesh adjacent to the wheel and groundplane had to be coarsened by increasing the cell height growth rate away from the wall boundaries compared to the 538,350 element isolated wheel mesh.

Once tetrahedral element skewness had been reduced to acceptable limits in the proximity of the wheel and shroud, the computed solutions, both for the rotating wheel, moving groundplane and the stationary wheel, stationary groundplane configurations, produced irregular oscillations in the histories of wheel and shroud drag coefficient with increasing number of iterations. After a number of attempts to remove these oscillations through adjustments in the first cell height, and the exponential growth rate away from the wheel, groundplane, and shroud surfaces it was concluded that the mesh adjacent to these wall boundaries was not sufficiently refined.

Boundary layer resolution was restored back to levels equivalent to those in the 538,350 element isolated wheel mesh. As well as modifying the mesh next to the wheel and groundplane the number of prism layers grown from the surface mesh of the shroud was increased to thirty, again with ten orthogonal layers. After further numerical investigations the first cell height was set to $7.5 \times 10^{-6}m$ with an exponential growth rate of 0.2125. This gave a final volume mesh size for the baseline shroud configuration of 1,544,324 elements; an increase in over 50% just for the extra resolution next to the wall boundaries.

As well as this volume mesh size making pre- and post-processing very difficult due to the local memory restrictions, iteration of the solution had to be performed in parallel over the Cranfield network using the Octane and the Cranfield Computer Centre's batch farm facilities of DEC Alpha machines. Some initial solutions were also run using Rover's computing facilities. Despite complicating the solution procedure, it was found that the extra mesh resolution greatly reduced the magnitude of the oscillations in the computed force data as well as making them more sinusoidal, *Fig.8.5.* In a couple of cases the solutions converged to give stable force coefficient histories. It seemed that most of the boundary layer mesh dependencies in the solutions had been removed, and that the oscillations were almost regular in nature indicated that the predicted flowfields would display periodicity if the solver was run in a time dependent format. All the data presented in this thesis for the shrouded wheel solutions are from cases stopped at an approximate mid-point in these oscillations.

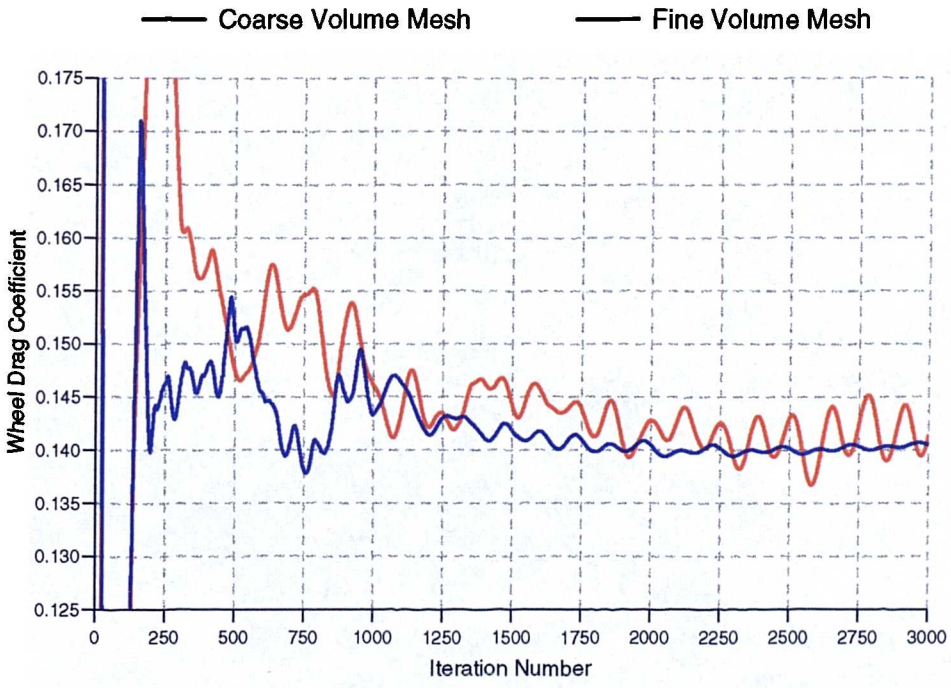

Figure 8.5: The Influence of Volume Mesh Size on the Convergence of Wheel Drag Coefficient for the Baseline Shroud Configuration and Fixed Wheel Stationary Groundplane

Unfortunately, the available computer resources did not allow a further increase in volume mesh size, or an unsteady solver configuration to be used for these ini-

tial cases. Therefore, this mesh configuration became the basis for the analysis of shrouded wheel flows.

When the maximum depth front shroud spoiler was added a further 300,000 elements were introduced into the volume mesh due to the requirements for a fine surface mesh on the spoiler.

8.3 Validation Results

Presented in the remainder of this chapter is an analysis of the quality of the CFD shrouded wheel solutions in relation to the experimental data. The aerodynamic analysis of the flowfields is located in Chapter 9.

Ten calculations were performed that simulated conditions tested in the wind tunnel when both force and pressure measurements were taken. For both fixed and moving groundplane configurations, flow simulations for the baseline geometry, two shroud shroud ride heights, $\Delta Y_s = 0.1$ and $\Delta Y_s = 0.2$, and the 0.050m and 0.100m front spoiler depths were all run. The 0.025m and 0.075m front spoiler depths were also run for force coefficient comparisons.

8.3.1 Force Coefficients

Table 8.1 shows the comparison of the absolute force coefficients from the comparable cases, whilst *Table 8.2* shows the comparison of the changes in the experimental and computational force coefficients relative to the case of the baseline shroud geometry above a moving groundplane / rotating wheel.

For this baseline case the comparisons were encouraging. Both the drag coefficients were over-predicted, but were within 10% of the experimental values. The more proven mesh geometry around the wheel and groundplane resulted in the wheel drag coefficient, C_{Dw}, being 0.009, or 5.8%, in error. The worst force coefficient comparison was for shroud lift, C_{Lw}, which was over-predicted by 0.050, or 62.5%. The coarse mesh on the upper parts of the outer surface of the shroud will be a contributory factor to this difference. However, it is possible that the interactions with the moving groundplane underneath the nose of the shroud were not predicted with enough accuracy.

Moving Groundplane, Rotating Wheel

	Experimental				Computational				Percentage Error			
	C_{Ls}	C_{Ds}	C_{Dw}	C_{Dt}	C_{Ls}	C_{Ds}	C_{Dw}	C_{Dt}	C_{Ls}	C_{Ds}	C_{Dw}	C_{Dt}
Baseline Configuration												
	0.080	0.311	0.156	0.467	0.130	0.340	0.165	0.505	62.5	9.3	5.8	8.1
Shroud Ride Height Increments, ΔY_s												
0.1	0.081	0.307	0.176	0.483	0.117	0.355	0.170	0.525	44.4	15.6	-3.4	8.7
0.2	0.087	0.328	0.189	0.517	0.094	0.367	0.186	0.554	8.0	11.9	-1.6	7.2
Front Spoiler Depth (m)												
0.025	0.095	0.347	0.146	0.493	0.116	0.417	0.151	0.568	22.1	20.2	3.4	15.2
0.050	0.090	0.345	0.138	0.483	0.131	0.443	0.135	0.578	45.5	28.4	-2.2	19.7
0.075	0.058	0.311	0.097	0.408	0.086	0.359	0.150	0.509	48.3	15.4	54.6	24.7
0.100	0.021	0.264	0.109	0.373	0.141	0.440	0.117	0.557	571.4	66.7	7.3	49.3

Stationary Groundplane, Fixed Wheel

	Experimental				Computational				Percentage Error			
	C_{Ls}	C_{Ds}	C_{Dw}	C_{Dt}	C_{Ls}	C_{Ds}	C_{Dw}	C_{Dt}	C_{Ls}	C_{Ds}	C_{Dw}	C_{Dt}
Baseline Configuration												
	0.107	0.331	0.132	0.462	0.125	0.343	0.143	0.485	16.8	3.6	8.3	5.0
Shroud Ride Height Increments, ΔY_s												
0.1	0.101	0.328	0.147	0.474	0.108	0.346	0.160	0.506	6.9	5.5	8.8	6.8
0.2	0.106	0.346	0.158	0.503	0.083	0.352	0.185	0.537	-21.7	1.7	17.1	6.8
Front Spoiler Depth (m)												
0.025	0.136	0.386	0.115	0.500	0.133	0.414	0.140	0.554	-2.2	7.3	21.8	10.8
0.050	0.076	0.294	0.111	0.404	0.117	0.370	0.149	0.518	53.9	25.9	34.2	28.2
0.075	0.087	0.326	0.111	0.436	0.052	0.302	0.118	0.420	-40.2	-7.4	6.3	-3.7
0.100	0.045	0.284	0.091	0.375	0.025	0.276	0.091	0.367	-44.4	-2.8	0.0	-2.1

Table 8.1: Comparison of the Numerical Absolute Wheel and Shroud Force Coefficients with the Derived Experimental Data

Moving Groundplane, Rotating Wheel

	Experimental				Computational				Difference			
	C_{Ls}	C_{Ds}	C_{Dw}	C_{Dt}	C_{Ls}	C_{Ds}	C_{Dw}	C_{Dt}	C_{Ls}	C_{Ds}	C_{Dw}	C_{Dt}
Baseline Configuration												
	-	-	-	-	-	-	-	-	-	-	-	-
Shroud Ride Height Increments, ΔY_s												
0.1	0.001	-0.004	0.020	0.016	-0.013	0.015	0.005	0.020	-0.014	0.019	-0.015	0.004
0.2	0.007	0.017	0.033	0.050	-0.036	0.027	0.021	0.049	-0.043	0.010	-0.012	-0.001
Front Spoiler Depth (m)												
0.025	0.015	0.036	-0.010	0.026	-0.014	0.077	-0.014	0.063	-0.029	0.041	-0.004	0.037
0.050	0.010	0.034	-0.018	0.016	0.001	0.103	-0.030	0.073	-0.009	0.069	-0.012	0.057
0.075	-0.022	0.000	-0.059	-0.059	-0.044	0.019	-0.015	0.004	-0.022	0.019	0.044	0.063
0.100	-0.059	-0.047	-0.047	-0.094	0.011	0.100	-0.048	0.052	0.070	0.147	-0.001	0.146

Stationary Groundplane, Fixed Wheel

	Experimental				Computational				Difference			
	C_{Ls}	C_{Ds}	C_{Dw}	C_{Dt}	C_{Ls}	C_{Ds}	C_{Dw}	C_{Dt}	C_{Ls}	C_{Ds}	C_{Dw}	C_{Dt}
Baseline Configuration												
	0.027	0.020	-0.024	-0.005	-0.005	0.003	-0.022	-0.020	-0.032	-0.017	0.002	-0.015
Shroud Ride Height Increments, ΔY_s												
0.1	0.021	0.017	-0.009	0.007	-0.022	0.006	-0.005	0.001	-0.043	-0.011	0.004	-0.006
0.2	0.026	0.035	0.002	0.036	-0.047	0.012	0.020	0.032	-0.073	-0.023	0.018	-0.004
Front Spoiler Depth (m)												
0.025	0.056	0.075	-0.041	0.033	0.003	0.074	-0.025	0.049	-0.053	-0.001	0.016	0.016
0.050	-0.004	-0.017	-0.045	-0.063	-0.013	0.030	-0.016	0.013	-0.009	0.047	0.029	0.076
0.075	0.007	0.015	-0.045	-0.031	-0.078	-0.038	-0.047	0.085	-0.085	-0.053	-0.002	0.116
0.100	-0.035	-0.027	-0.065	-0.092	-0.105	-0.064	-0.074	0.138	-0.070	-0.037	-0.009	0.230

Table 8.2: Comparison of the Numerical Wheel and Shroud Force Coefficients with the Derived Experimental Data Relative to the Baseline Shroud Configuration with Moving Ground and Rotating Wheel

The solution for the same shroud geometry above the stationary groundplane configuration gave a reduced error in the predicted shroud lift coefficient of 16.8%, or just 0.018. With the flow over the top of the shroud unlikely to have changed significantly with the change in groundplane simulation it seems that the prediction of the flow under the shroud is improved with the stationary groundplane, especially as the predicted and experimental groundplane boundary layer thicknesses were comparable. This improvement in correlation is also seen in the shroud drag coefficient, which was just 3.6% in error. However, the prediction in the wheel drag was worse than in the rotating wheel case. C_{Dw} was over-predicted by 0.011, or 8.3%, from the experimental value of 0.132.

The movement of the groundplane will increase the massflow drawn under the nose of the shroud. Despite the fine surface mesh in this area the use of triangular elements meant that the closest cell centres will still have been two millimetres away from the geometric edge. Thus, the actual volume mesh resolution of the complex flow structures in this area of fixed separation was probably inadequate. As the front spoilers were added in this area, decreasing the distance between this lower front edge to the groundplane, and, thus, increasing their interaction, the comparisons with the experimental data became worse. The progressive decrease in shroud lift with increasing front spoiler depth, particularly with the moving groundplane, was not adequately simulated.

The simulation of any separation bubble behind these front spoilers will depend on the accuracy of the prediction of the flow around the leading edge. This will then affect the prediction of the flow structure within the downstream wheelhouse cavity. The experimental force data showed a critical difference between the two groundplane configurations when the 0.050m front spoiler was fitted. A lower total drag coefficient was found with the stationary groundplane. It is possible that the length of any separation bubble became greater than the length of the lower front face of the shroud. CFD models, for example, of the flow over a backward facing step, generally have difficulty predicting the length of separation bubbles. The only two significant errors found in the predicted wheel drag coefficients were with the 0.075m spoiler above the moving groundplane, and with the 0.050m spoiler above the stationary groundplane, i.e. in this critical flow regime.

Thus, it seems that the CFD model does not accurately predict the flow separation from the front lower edge of the shroud. However, the lack of experimental pressure data in this area means that verification of this is difficult.

As the ride height of the shroud was increased the interaction of the shroud with the wheel and groundplane would become less. The rotating wheel drag predictions became within 2% of the experimental data as the influence of the groundplane on the flow around this front edge of the shroud became less important. With the stationary groundplane the fixed wheel drag coefficient was increasingly over-predicted with increased shroud ride height.

A solution to this problem was not available with the memory limits of the available hardware, i.e. increased surface mesh refinement, or with the surface and volume mesh generator technology of Geomesh. It would have been possible to get cell centres closer to the lower leading edge of the shroud by using high aspect ratio quadrilateral faces in this area. Even restricting these aspect ratios to ten would enable local cell centres to have been placed approximately a third of a millimetre away from the geometric edge without significantly increasing the volume mesh size. The same hybrid mesh generation techniques within TGrid could still have been used with an additional set of pyramidal elements being introduced where required.

8.3.2 Wheelhouse Cavity Pressure Coefficients

Appendix F presents contour plots of the predicted surface static pressure coefficient distributions on the five internal faces of the wheelhouse cavity for all the configurations run. In the following section referenced figures from Appendices E & F are duplicated in the main text for clarity.

As the comparison of computational with experimental force data has highlighted issues with the accuracy of the solutions, errors should be apparent in some of the pressure distributions, especially in the magnitude of the coefficients. Analysis will be made of the structure and trends shown in the CFD pressure results, and how these compare to experiment.

For the baseline shroud geometry above the moving groundplane / rotating wheel the comparisons of the two sets of pressure distributions, *Fig.8.6* and *Fig.8.7*, show that the CFD predicted coefficients are generally higher than the experimental ones. Whilst almost all of the predicted pressures on the front face of the wheelhouse cavity were negative they were typically one contour level, or 0.04, more positive in magnitude. The area of lowest pressure on the wheelarch side of this face was predicted. On the roof of the cavity three areas of high pressure were predicted, as measured experimentally. The two areas on the wheelarch side of the face were,

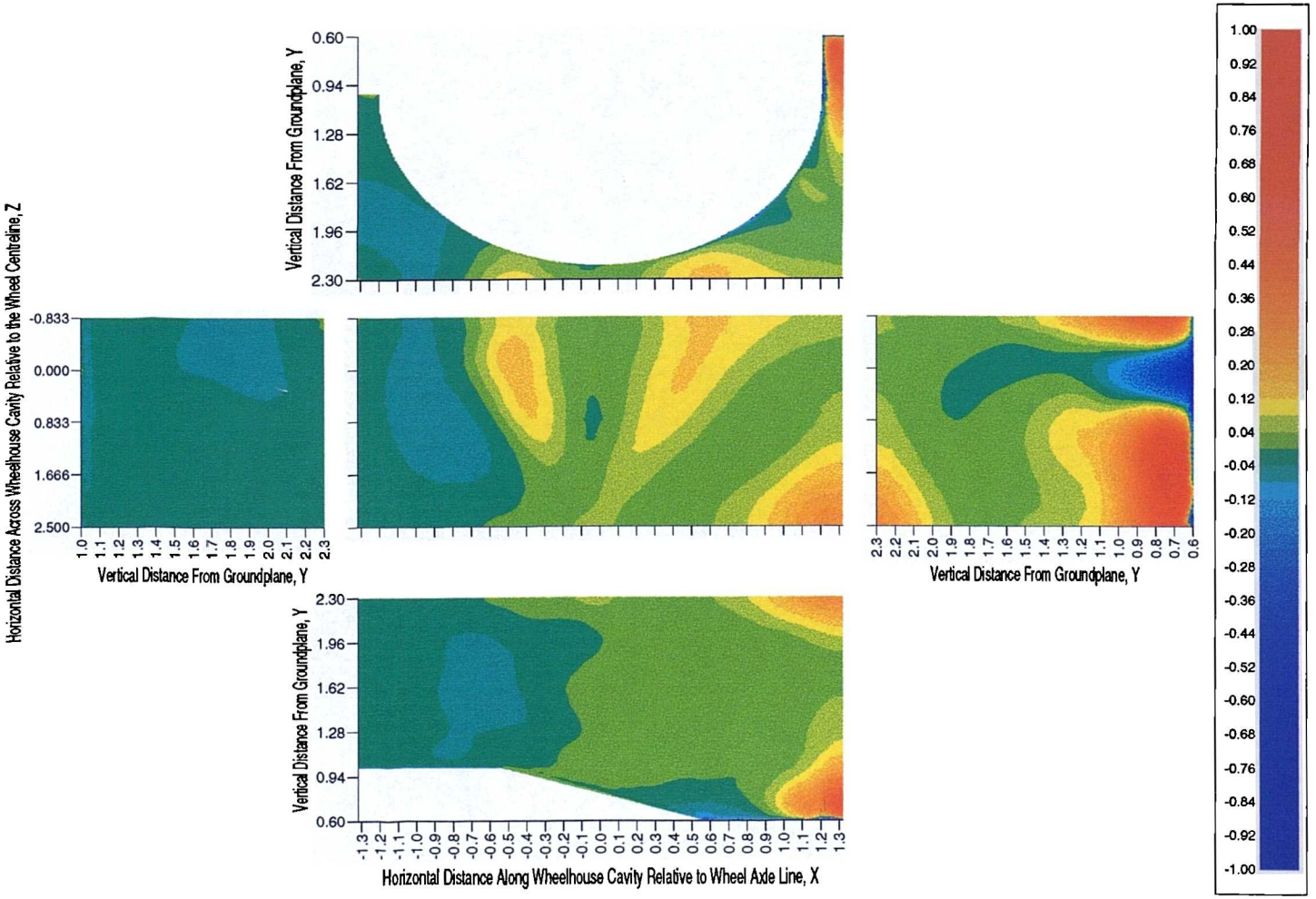

Figure 8.6: Computational Wheelhouse Cavity Pressure Coefficient Distribution - No Front Spoiler, Front Ride Height, $Y_f = 1.0$, Rear Ride Height, $Y_r = 0.6$, Moving Groundplane

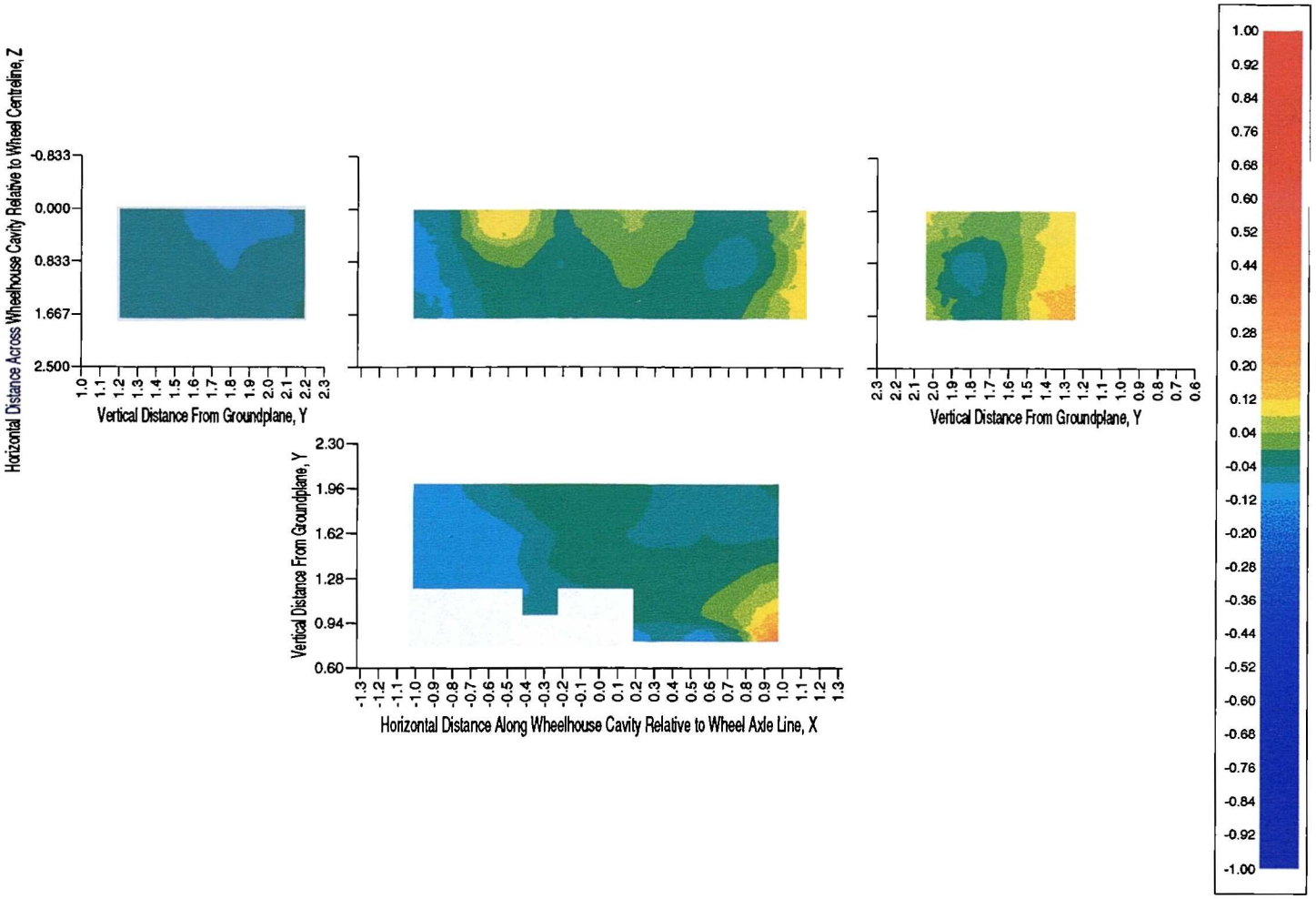

Figure 8.7: Experimental Wheelhouse Cavity Pressure Coefficient Distribution - No Front Spoiler, Front Ride Height, $Y_f = 1.0$, Rear Ride Height, $Y_r = 0.6$, Moving Groundplane

however, too far downstream. Due to the higher predicted pressures, approximately the rear two-thirds of this face experienced positive pressure coefficients. However, the structure of the distribution was encouraging. The high pressure coefficients on the lowest rear corner of the side face were also predicted, along with the area of comparatively low pressures immediately upstream. Despite this, the area of low pressures on the front lower part of this face was not predicted. The area of low pressure on the rear face was present in the CFD solutions, although it was located more to the wheelarch side of the cavity, and extended down to the bottom of this face. Outside of this area the positive pressures on the lower parts of this rear face were predicted. The CFD distributions showed coefficients above 0.5 in magnitude, although outside areas that were pressure tapped in the experiment.

In summary, the structure of the predicted pressure distributions from this baseline model was qualitatively accurate, although the magnitude of the pressure coefficients were generally too large. This supports the idea that the structure of the flow separating, and re-attaching, from the front lower edge of the shroud, was the main cause of the discrepancies from the experimental data, and not the structure, and density, of the mesh within the wheelhouse cavity.

Comparing the fixed groundplane wheelhouse cavity pressures in the baseline shroud geometry, *Fig.8.8* and *Fig.8.9*, gave an overall improvement in the correlation of the magnitude of the coefficients. The main exception was again on the front face of the cavity. Two large areas of slightly positive pressures were predicted on this face which were not measured experimentally. These more positive predicted coefficients extended onto the roof and side faces of the cavity. However, for the rear half of the cavity the general magnitude of the predicted pressures was to within 0.1 of experiment. At the top of the rear face the small area of low pressure was not predicted, but, similar to the rotating wheel solution, two regions of high pressure at the bottom of this rear face were predicted either side of an area of low pressure.

Very similar trends were found in the comparisons of the four shroud ride height cases. Thus, despite the improvements in the correlation of the shroud drag coefficient, the discrepancies in the wheelhouse cavity pressure distributions show that both forces and surface pressures are required for the detailed validation of a CFD model.

The problems with the separation from the front of the shroud are highlighted further in the comparisons of the wheelhouse cavity pressure coefficients for the

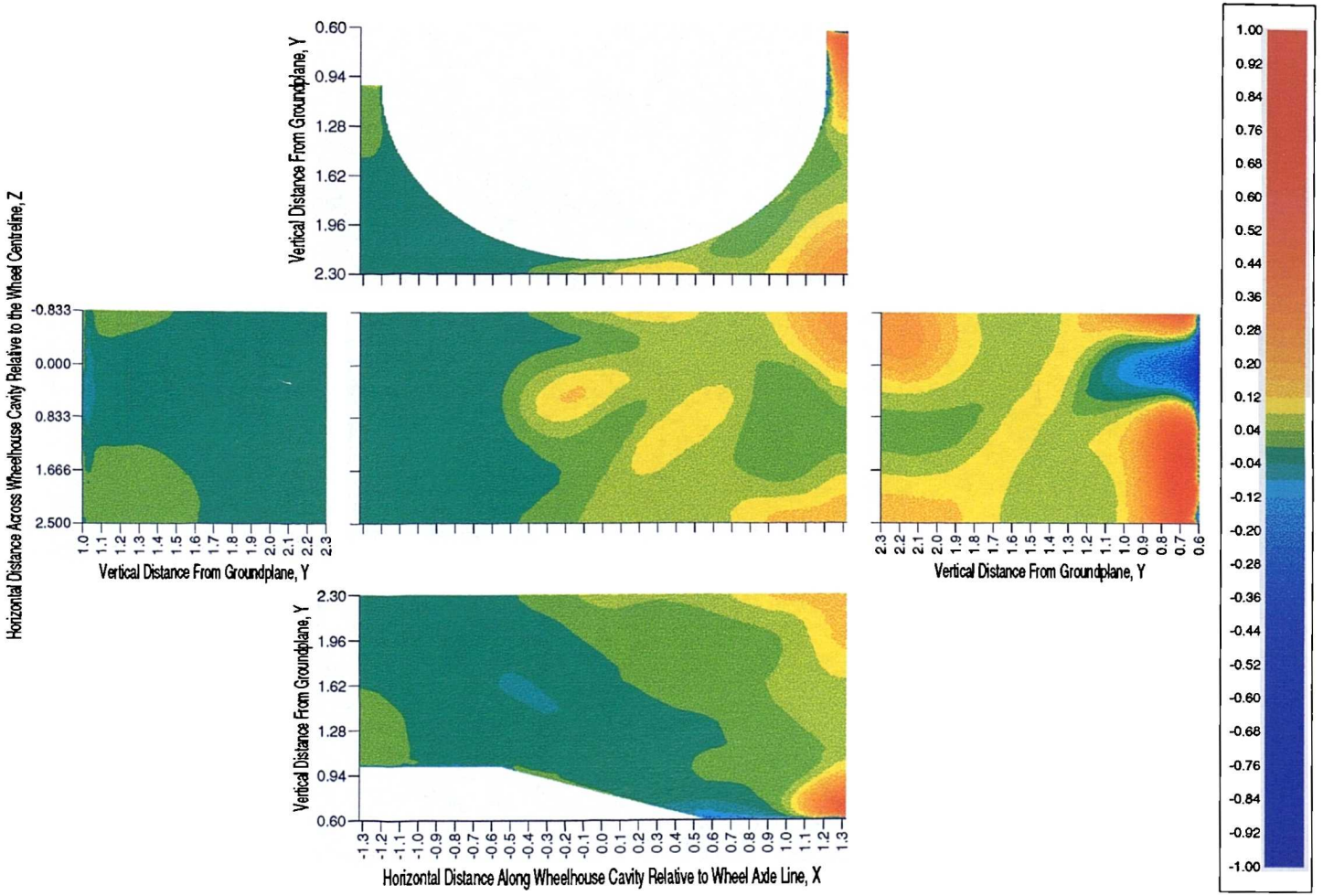

Figure 8.8: Computational Wheelhouse Cavity Pressure Coefficient Distribution - No Front Spoiler, Front Ride Height, $Y_f = 1.0$, Rear Ride Height, $Y_r = 0.6$, Stationary Groundplane

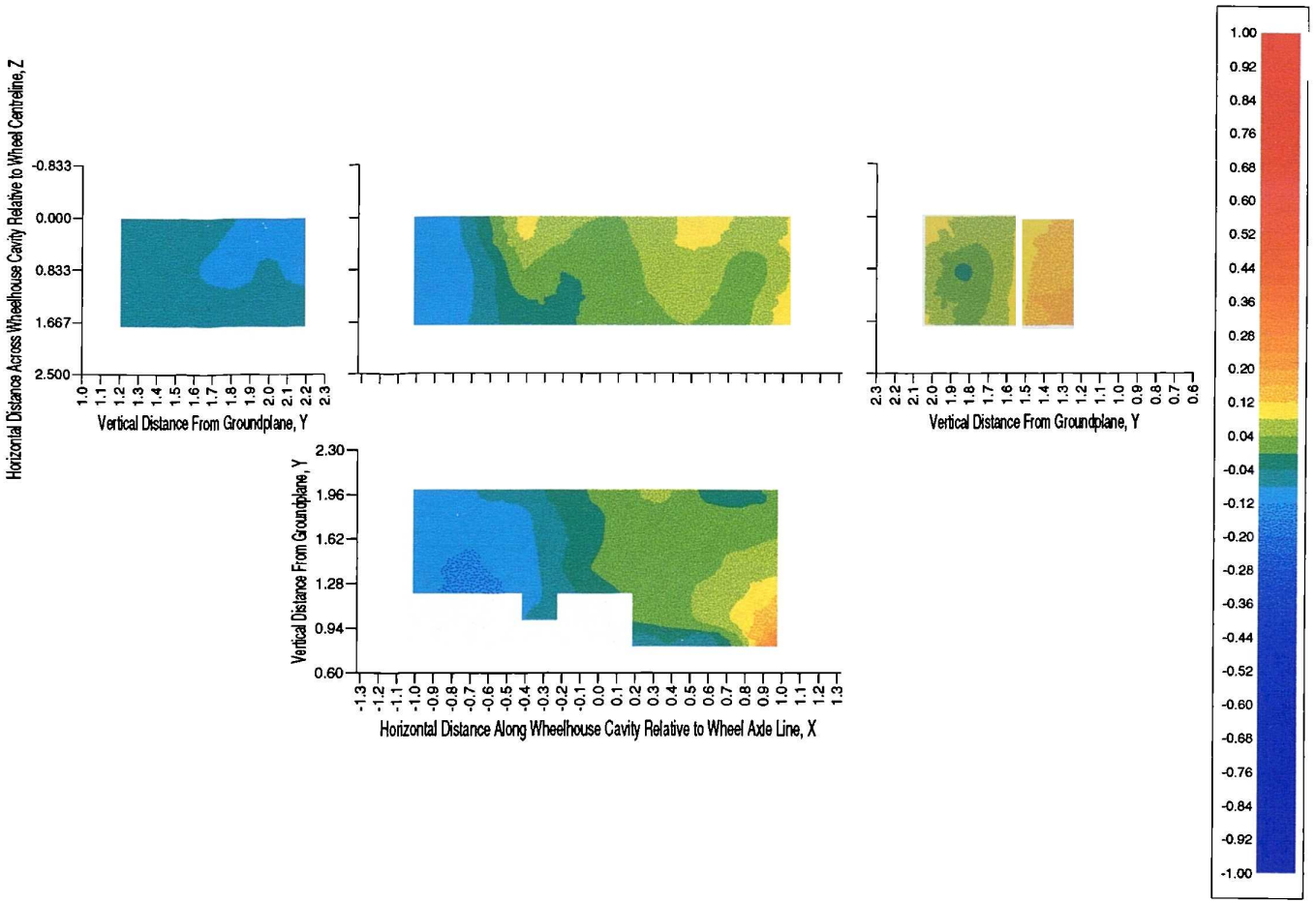

Figure 8.9: Experimental Wheelhouse Cavity Pressure Coefficient Distribution - No Front Spoiler, Front Ride Height, $Y_f = 1.0$, Rear Ride Height, $Y_r = 0.6$, Stationary Groundplane

four front spoiler cases. Only the 0.100m front spoiler stationary groundplane case showed comparable distributions, *Fig.8.10* and *Fig.8.11.* The comparisons for the three other cases were poor. Generally the magnitude of the pressure coefficients were greatly over-predicted, especially for the 0.100m front spoiler case above the moving groundplane. This reflects the over-prediction of the shroud lift and drag coefficients.

However, comparing the trends in the computational shroud drag coefficients and the wheelhouse pressure coefficients gives support to the theory that lowering the pressure in the wheelhouse cavity reduced the drag of the shroud. For the four front spoiler cases above the stationary wheel and groundplane the increased front spoiler depth resulted in decreased surface pressure coefficients in the rear half of the cavity, which correlated to a decrease in the predicted shroud drag.

8.4 Summary

From this chapter it can be summarized that:

1. A hybrid mesh topology has been developed for shrouded wheel calculations which incorporated much of the proven isolated wheel hexahedral mesh topology. A volume was incorporated into this new hexahedral wheel / groundplane / farfield mesh which allowed an unstructured asymmetric shroud surface mesh to be easily added. The space between the two meshes was then filled with prismatic, pyramidal, and tetrahedral elements. The predicted flowfields were compared to experimental data obtained from two MIRA wind tunnel sessions.

2. For almost all the cases the model correctly predicted that for this shroud geometry the rotating wheel on a moving groundplane generated more drag than the equivalent stationary wheel on a stationary groundplane.

3. The fixed separation of the flow under the front of the shroud was poorly predicted. This was thought to be due to the unstructured surface elements having cell centres too far away from the actual geometric edge.

4. In the solutions a correlation was found between a reduction in the magnitude of the surface pressures in the rear half of the wheelhouse cavity and a reduction in the shroud drag.

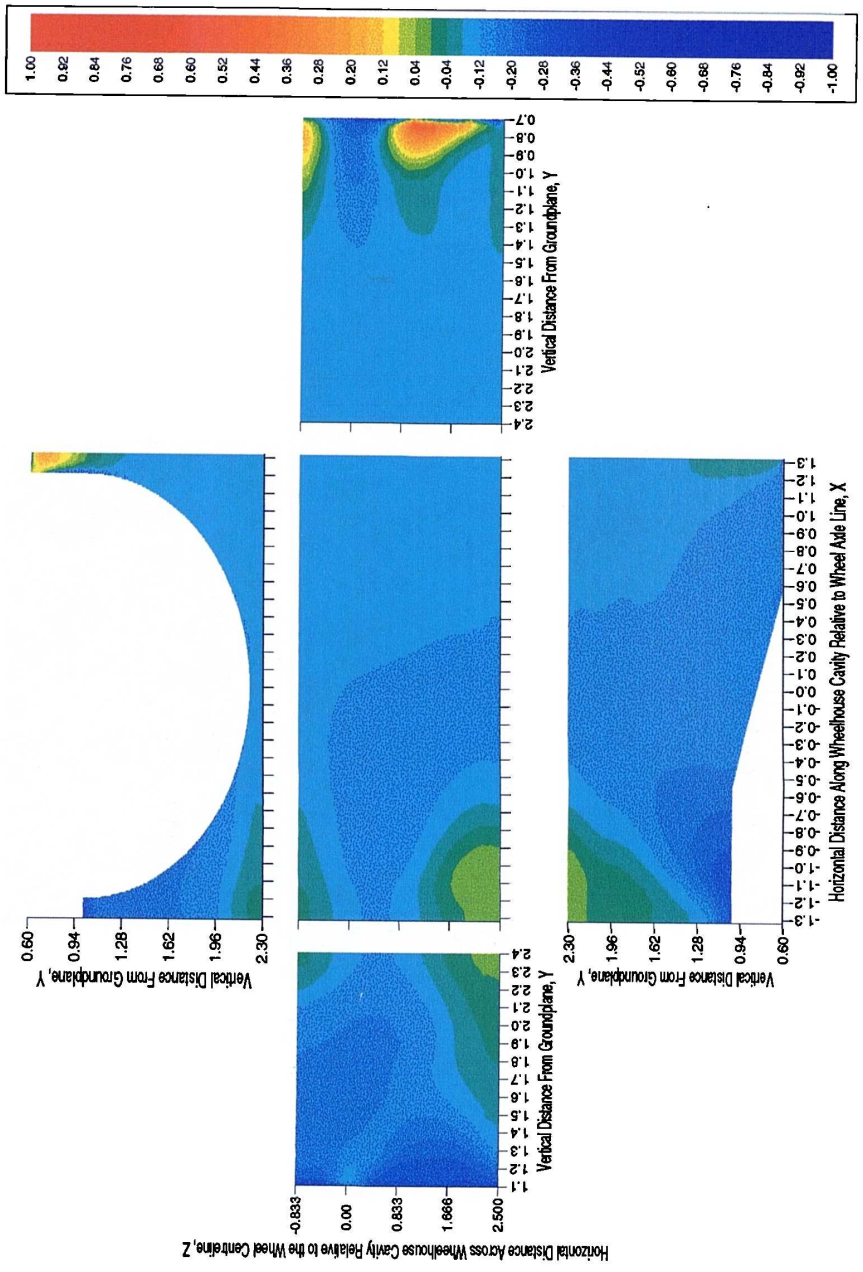

Figure 8.10: Computational Wheelhouse Cavity Pressure Coefficient Distribution - 0.100m Front Spoiler, Front Ride Height, $Y_f = 1.0$, Rear Ride Height, $Y_r = 0.6$, Stationary Groundplane

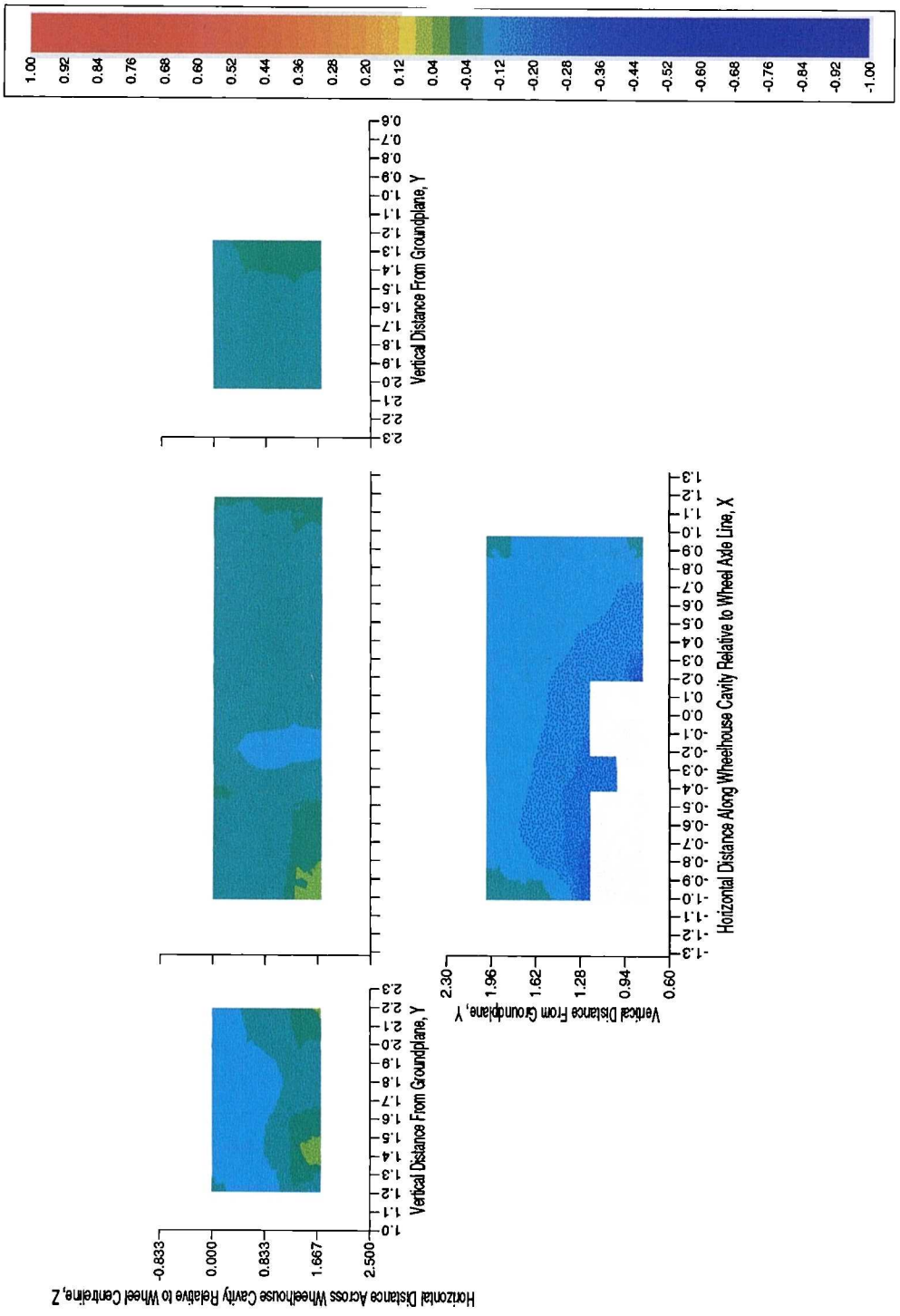

Figure 8.11: Experimental Wheelhouse Cavity Pressure Coefficient Distribution - 0.100m Front Spoiler, Front Ride Height, $Y_f = 1.0$, Rear Ride Height, $Y_r = 0.6$, Stationary Groundplane

Chapter 9

Analysis of the Aerodynamic Characteristics of Shrouded Wheels

As with the analysis of the flowfield around an isolated wheel, the, at best, qualitative agreement with experimental data of the shrouded wheel solutions means that only large scale predicted flow features can be analyzed with any degree of confidence. Comparisons with experimental flow visualization gave further support to this analysis. As the best comparisons were for the wheel drag coefficients, attention will be given to the localized flow around the wheel. Also, the flow features associated with some of the issues relating to the quality of the solutions will be highlighted.

Due to the size of the volume meshes and the local memory limitations on the SGI Octane, post-processing of the shrouded wheel solutions had to use the parallel version of FLUENT/UNS. As a consequence, pathline analysis of the flowfield was unavailable. The very three-dimensional nature of the flowfield means that graphical presentation of the results through simple planar flow variable contours is unfeasible. Thus, initially, a brief description of the solutions for the two different groundplane conditions with the baseline shroud geometry will be presented.

9.1 General Description of the Predicted Baseline Flowfield

For the moving groundplane / rotating wheel solution a separation bubble was predicted on the lower front horizontal face of the shroud. Despite the symmetric nature of this part of the shroud, the blockage of the wheel meant that the length of the bubble was shorter on the wheelarch side of the shroud. The attached flow then separated from the rear edge of this face into the wheelhouse cavity. On the non-wheelarch side this produced a free shear layer which passed downstream by the side of the wheel, *Fig.9.1.* The flow was then deflected under the back of the shroud by the rear face of the cavity, which resulted in the high pressures in this area of the wheelhouse cavity, *Fig.8.6.*

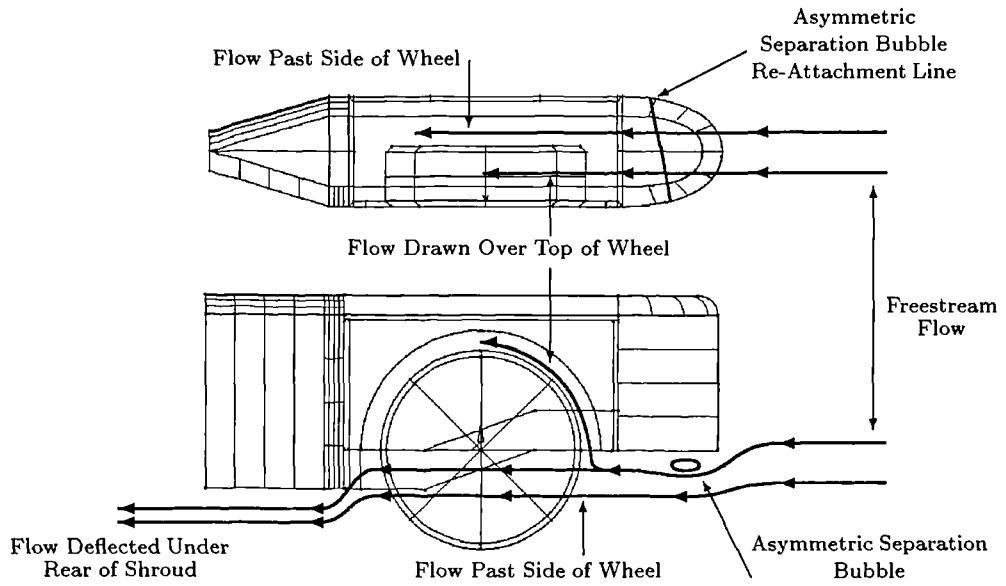

Figure 9.1: Schematic of the Predicted Flow Around a Shrouded Wheel

On the wheelarch side, some of the flow separating from the front lower face of the shroud was deflected around either side of the wheel, but most was drawn into the wheelhouse cavity above the wheel. This, therefore, opposed the direction of the rotation of the wheel, as in the isolated wheel solutions. In the upper front part of the wheelhouse cavity a region of separated recirculating flow was predicted. The pressure differential between the interior and the exterior of the wheelhouse cavity resulted in most of the flow that was drawn up towards the top of the wheel exiting

the cavity through the wheelarch. A vortex formed from this exiting flow, the origin of which was located at approximately 225° on the outside of the shroud.

At the front of the contact patch pressure coefficients greater than unity were again predicted, *Fig.9.2.* This figure is duplicated, again for clarity, from Appendix G, where computational wheel surface pressure distributions are presented for all the simulations. Fackrell's 'jetting' phenomena is, therefore, independent of the geometry of the wheel. The flow from this region was deflected down either side of the wheel and entrained into the vortex structures formed from the flow near to the groundplane being deflected around the edge of the wheel. However, the presence of the shroud resulted in an asymmetric development downstream. The vortex on the wheelarch side of the wheel remained close to the wheel, whilst the vortex on the other side of the wheel spread out, and became more diffusive further upstream.

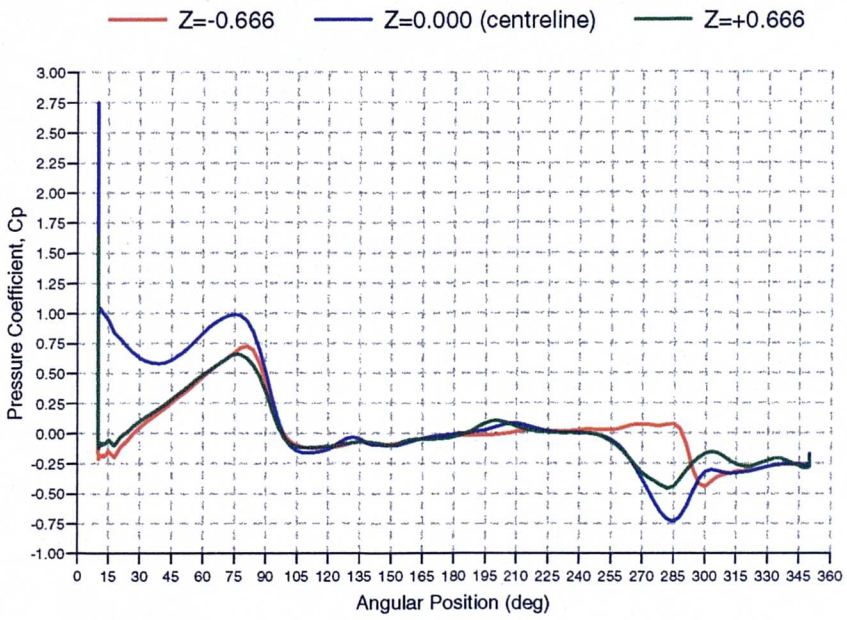

Figure 9.2: Computational Wheel Surface Pressure Coefficient Distributions - No Front Spoiler, Front Ride Height, Y_f = 1.0, Rear Ride Height, Y_r = 0.6, Moving Groundplane

For the stationary wheel, stationary groundplane simulation a similar asymmetric separation was predicted on the front lower face of the shroud. More flow was drawn into the upper parts of the wheelhouse cavity, relative to the rotating wheel case, and a conventional boundary layer structure formed on the 'tread' area of the wheel surface. On the centreline of the wheel this boundary layer remained attached

until approximately 190°. This flow again exited the wheelhouse cavity through the wheelarch. The vortical structure on the side of the shroud formed earlier though, at 210°, than the rotating wheel case, and, thus, the vortex passed higher down the side of the shroud.

A vortex either side of the wheel was again predicted. The stationary groundplane meant that they rapidly became diffused. In both cases these vortices at the side of the wheel were much smaller in size than those predicted in the isolated wheel cases.

9.2 The Predicted Separation of the Flow from the Lower Leading Edge of the Shroud

It was stated in Section 8.3.1 that there could exist a critical shroud front spoiler depth beyond which the separated flow behind the spoiler would prevent flow re-attachment on the front lower face of the shroud. *Fig.9.3* shows fixed length velocity vectors on the plane of the centreline of the wheel for the stationary groundplane cases when the shroud was fitted either with no front spoiler or the 0.1m front spoiler.

The difference in the separation patterns behind the front spoiler can clearly be seen. Whilst the flow re-attaches without the front spoiler, a large recirculation was predicted behind the 0.1m front spoiler. Consequently, the flow drawn into the wheelhouse cavity was reduced as the separation bubble filled the gap between the wheel and the lower front face of the shroud.

This shows the importance of the prediction of the separation region from the front lower edge of the shroud, and that, whilst unstructured surface and volume meshes are relatively quick to generate, their use in areas of complex flows with fixed separation points must be carefully considered.

9.3 The Influence of the Ride Height of the Shroud

Raising the ride height of the shroud was found to increase the drag coefficient of both the wheel and shroud. The experimental wheelhouse pressure coefficients

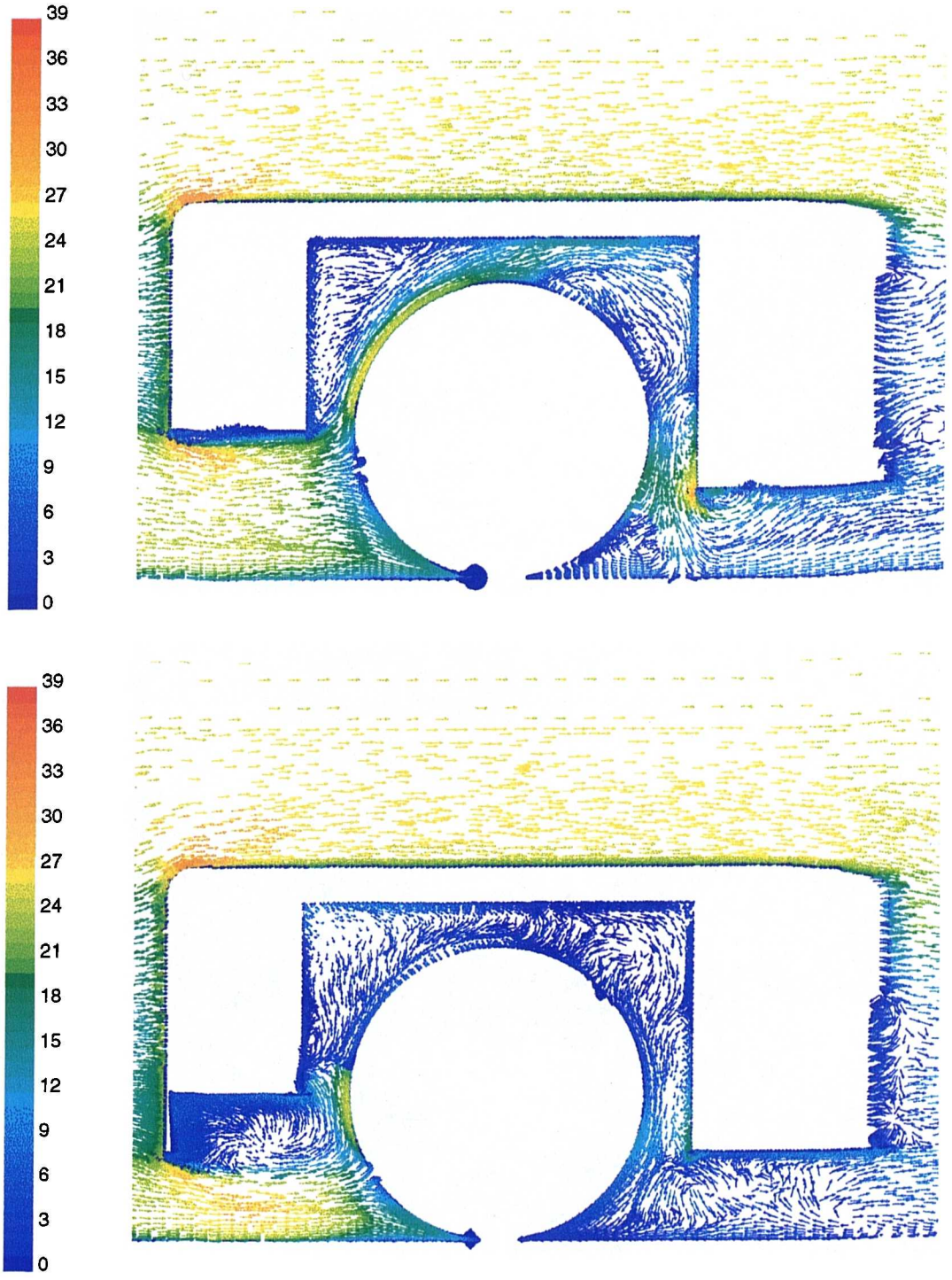

Figure 9.3: Fixed Length Velocity Vectors, Coloured by Velocity Magnitude, Showing the Influence of the Shroud Front Spoiler on the Flow Around a Stationary Shrouded Wheel on the Plane of the Wheel Centreline

suggested that this was due to a change in the structure of the flow leaving the wheelhouse cavity, Section 7.2.3.

It was found computationally that increasing the shroud ride height increased the angular position of the flow leaving the wheelhouse cavity, and, thus, the start of the formation of the vortex on the outside of the shroud was further around the wheelarch. The strength of this vortex was also reduced. The increased ride height meant that more of the front of the wheel was exposed to the flow beneath the shroud. The stagnation point on the surface of the wheel was predicted at an increased angular position with increasing shroud ride height. For the stationary wheel the separation point of the flow from the wheel surface was, therefore, delayed, giving the change in flow structure leaving the wheelhouse cavity. A similar trend was found in the three rotating wheel cases, with the increased shroud ride height delaying the angular position of the flow 'separating' from the attached wheel boundary layer.

9.4 Vortical Flow Structures Within the Wheelhouse Cavity

In the predicted surface static pressure coefficients on the internal faces of the wheelhouse cavity an area of low pressure was found on the rear face in all of the cases. Similar experimental regions of low pressure were also measured in some of the comparative cases. The pressure gradient between the interior and exterior of the wheelhouse cavity resulted in the flow from the top of the shrouded wheel leaving the cavity through the wheelarch. This pressure gradient also resulted in some of the flow that passes down the side of the wheel within the wheelhouse cavity exiting through the wheelarch in the angular region 225^o to 270^o.

Fig.9.4 shows fixed length velocity vectors for the baseline shroud geometry, rotating wheel case on the horizontal plane through the centre of the wheel, Y=1.0. As the flow leaving the wheelhouse cavity passed around the rear of the wheel it induced a vertical vortex structure behind the wheel. This accounts for the area of low pressure on the rear face of the wheelhouse cavity. The flow entrained in this vortex leaves the bottom of the rear of the cavity and was deflected downstream along the rear lower face of the shroud.

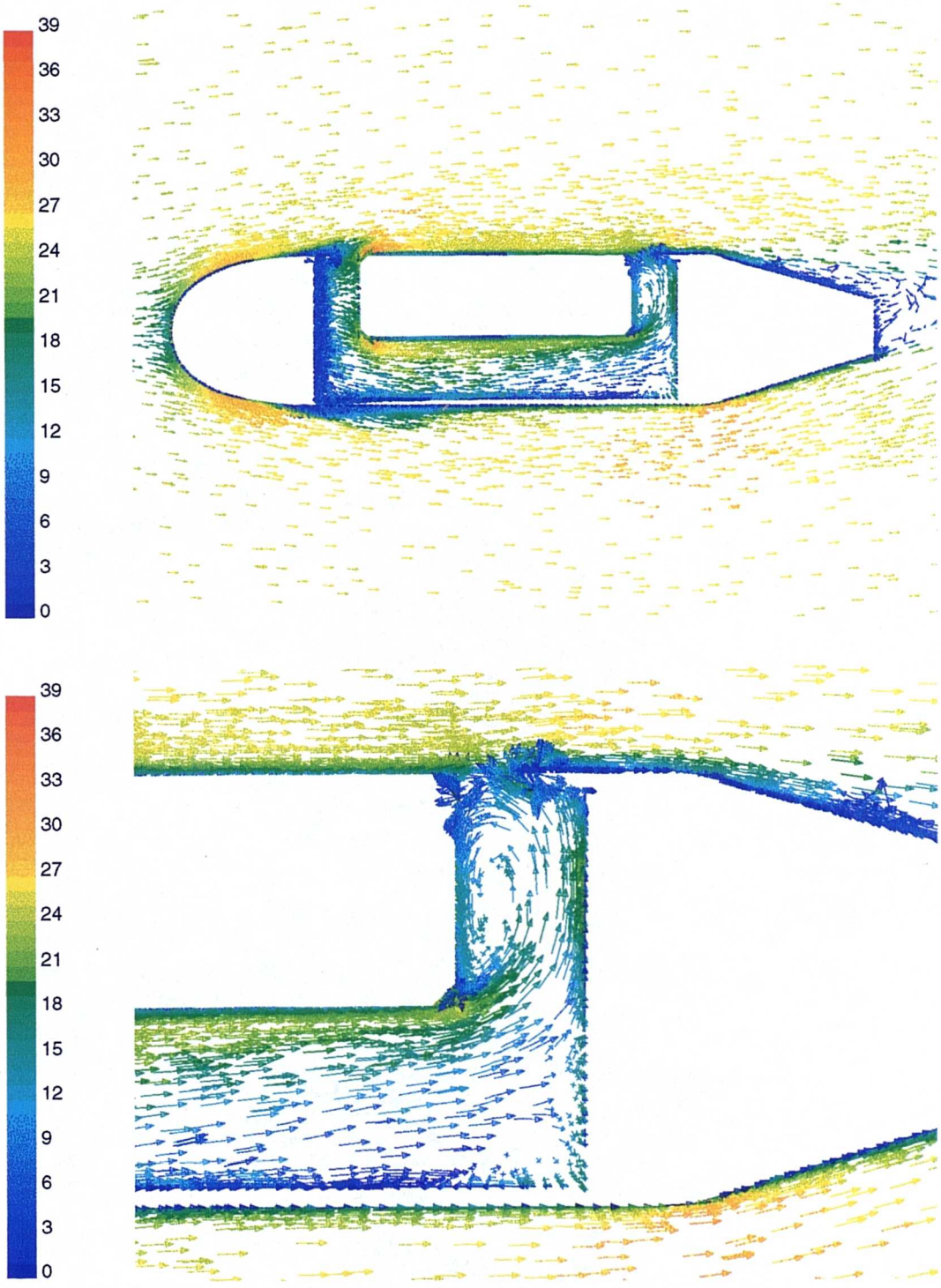

Figure 9.4: Fixed Length Velocity Vectors, Coloured by Velocity Magnitude, Showing the Predicted Vortex Behind the Shrouded Wheel on the Horizontal Plane Through the Centre of the Wheel (Baseline Shroud Geometry, Rotating Wheel, Moving Groundplane)

9.5 The Flowfield Adjacent to the Groundplane

The structure of the flow just above the groundplane was visualized experimentally using wool tufts attached to thin support wires stretched laterally across the belt, with the groundplane both moving and stationary. The change in ground condition induced a significant change in the flow direction in front of the wheel. The lateral flow component in this area was greater with the stationary groundplane than for the moving groundplane.

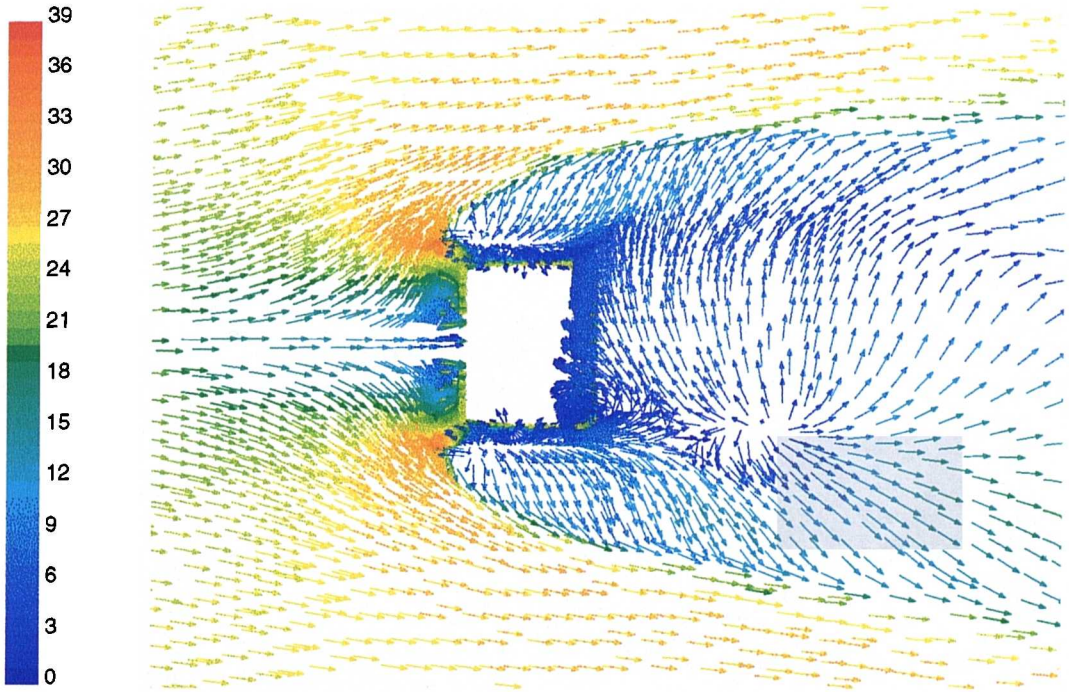

Figure 9.5: Fixed Length Velocity Vectors, Coloured by Velocity Magnitude, Showing the Flow Structure Adjacent to the Groundplane for the Rotating Shrouded Wheel Solution with the Baseline Shroud Geometry

Fig.9.5 and *Fig.9.6* show the predicted fixed length velocity vectors from the two baseline geometry solutions 0.005m above the groundplane. The view looks vertically down onto the groundplane, and, thus, the wheelarch side of the shroud is at the top of the plots. The increased lateral deflection of the flow in front of the contact patch area for the stationary groundplane case was predicted. The moving groundplane forced the flow closer in towards the contact patch region before it was deflected around either side of the wheel.

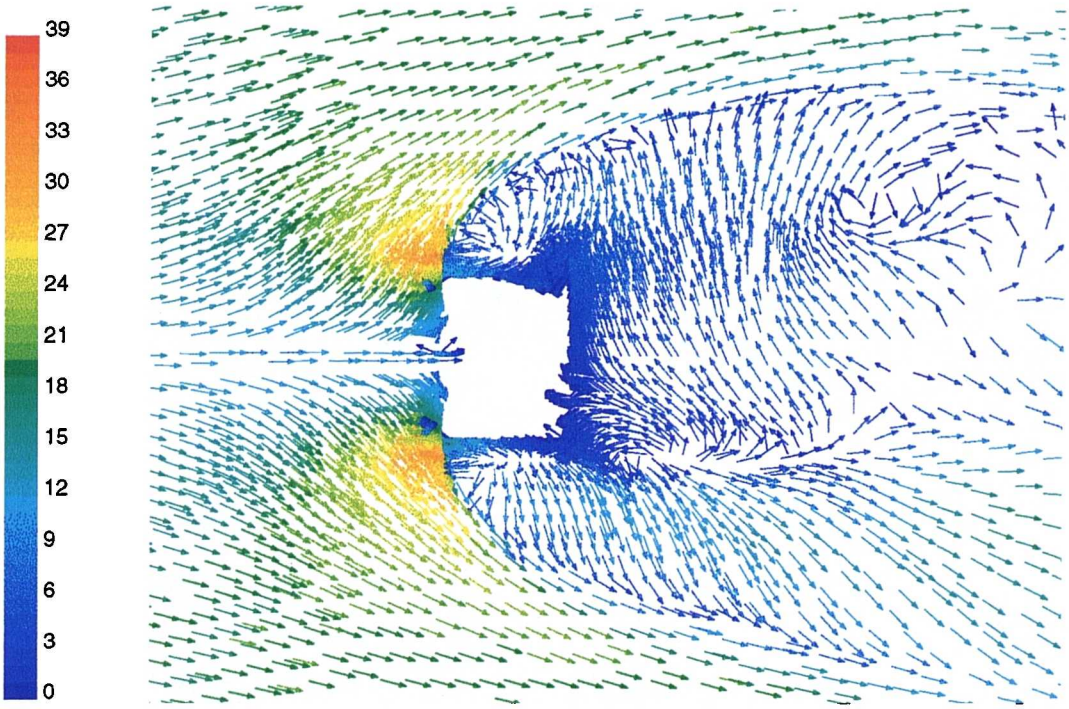

Figure 9.6: Fixed Length Velocity Vectors, Coloured by Velocity Magnitude, Showing the Flow Structure Adjacent to the Groundplane for the Stationary Shrouded Wheel Solution with the Baseline Shroud Geometry

A wider wake behind the wheel in the stationary groundplane case is also clearly predicted.

Behind the wheel, in both cases, the asymmetry of the wake is clearly seen. This is despite the non yawed freestream flow. The flow behind the wheel near to the groundplane is drawn towards the wheelarch side of the shroud. This feature of the wake was also seen experimentally.

9.6 The Shrouded Wheel Surface Static Pressure Coefficient Distributions

Appendix G presents predicted wheel surface static pressure coefficient distributions on three planes, Z=0 (centreline) and Z=$\pm$0.666, for all the shrouded wheel computations.

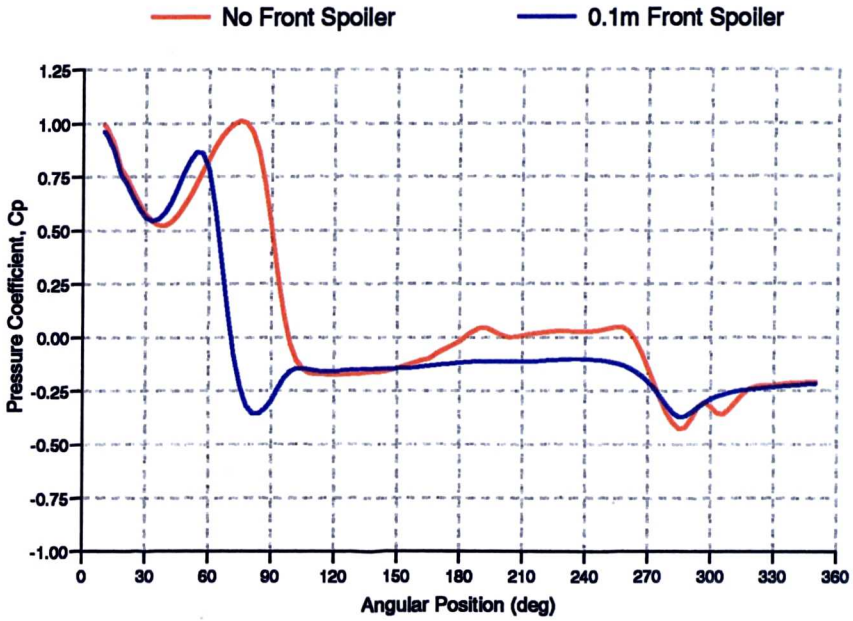

Figure 9.8: The Influence of Shroud Front Spoiler Depth on the Predicted Centreline Surface Static Pressure Coefficient Distribution on a Stationary Shrouded Wheel

wheelhouse cavity. The higher suctions on the rear of the rotating wheel will be a major factor in its higher drag coefficient. Also, it seems the vortex behind the wheel is stronger when the wheel was rotating than when it was stationary. In both cases, the centreline pressure coefficients on the rear of the wheel, near to the groundplane, were almost constant, and of magnitude -0.25.

The use of a 0.1m front spoiler on the shroud was found to reduce the predicted drag coefficient of the stationary wheel by 0.052. This was in good agreement of the experimental reduction in the drag coefficient of 0.041. *Fig.9.8* shows the differences in the wheel centreline pressure distributions for these two cases.

Adding the front spoiler decreased the pressures on the front of the wheel, which would contribute to the drag reduction. The front spoiler shielded the front of the wheel from the flow under the front of the shroud so that a stagnation point did not form. The pressure gradient from the pressure peak to the suction peak at the top of the wheel was similar in both cases. The pressure coefficients between 120° and 150°, were approximately constant in both cases at -0.15. The lower pressure at the rear of the wheelhouse cavity were also reflected in the wheel surface pressures between 160° and 260°.

9.7 The Influence of Varying Stationary Groundplane Boundary Layer Thickness

The prism layer capability of TGrid was used to extend the distance between the computational domain inlet and the wheel. This enabled the effects of the stationary groundplane boundary layer thickness to be studied for the baseline shroud geometry. The experimental stationary boundary layer thickness, 0.25m upstream of the leading edge of the shroud, of 0.04m was increased to 0.06m and 0.08m.

Table 9.1 shows the change in the shrouded wheel drag coefficient, C_{Dw}. It was found that doubling the stationary groundplane boundary layer thickness reduced C_{Dw} by 0.010 from 0.143, a reduction of 7%. The first 0.02m increase in boundary layer thickness gave 50% more reduction in wheel drag than the second incremental increase. Thus, it seems that the reductions in C_{Dw} would become increasingly smaller with further increases in the thickness of the stationary groundplane boundary layer.

Groundplane Boundary Layer Thickness (m)	Wheel Drag Coefficient C_{Dw}
0.04	0.143
0.06	0.137
0.08	0.133

Table 9.1: The Influence of Stationary Groundplane Boundary Layer Thickness, 0.25m Upstream of the Leading Edge of the Shroud, on the Shrouded Wheel Drag Coefficient

Fig.9.9 shows the wheel centreline pressure distributions for the three cases. The reduction in the wheel drag coefficient resulted from a decrease in the surface pressures on the front of the wheel at 40°, and an increase in the pressures on the rear of the wheel at 310°.

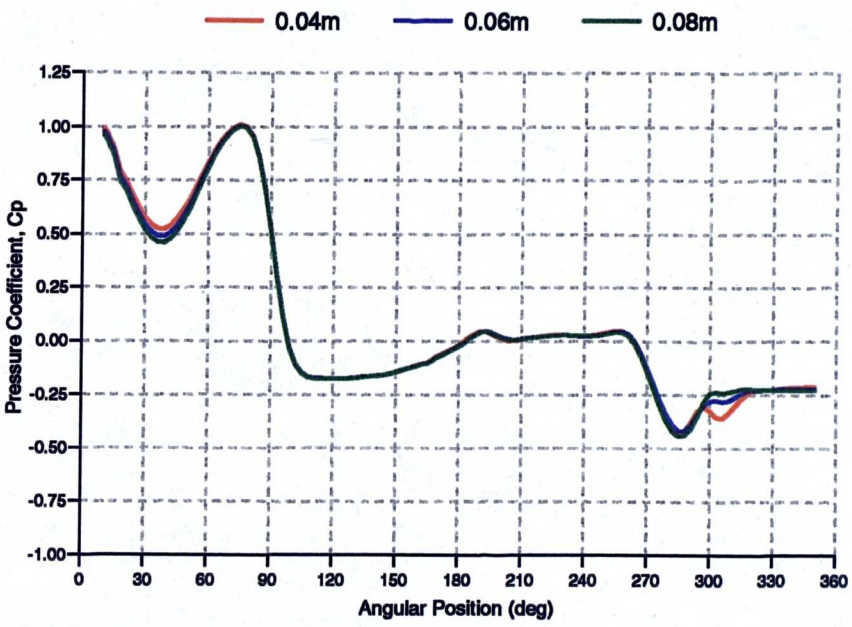

Figure 9.9: The Influence of Groundplane Boundary Layer Thickness on the Predicted Centreline Surface Static Pressure Coefficient Distribution on a Stationary Shrouded Wheel

9.8 Summary

From this chapter it can be summarized that:

1. The large scale flow structures predicted in the shrouded wheel solutions have been analyzed. These include asymmetric flow separation from the lower leading edge of the shroud, and flow entering the wheelhouse cavity on top of the wheel. The pressure differential between the interior and the exterior of the wheelhouse cavity resulted in the flow from the top of the wheel exiting the cavity through the wheelarch, and forming a vortex on the outside of the shroud.

2. For the rotating wheel simulations pressure coefficients greater than unity were predicted at the front of the contact patch. Thus, Fackrell's 'jetting' phenomena is independent of the geometry of the wheel.

3. Increasing the depth of the spoiler fitted to the front lower leading edge of the shroud increased the length of the separation bubble formed behind it. A critical spoiler depth existed, beyond which the flow could not re-attach, which then inhibited massflow entering the wheelhouse cavity.

4. A vortex structure was predicted behind the wheel within the wheelhouse cavity, which was stronger when the wheel was rotating compared to when the wheel was stationary.

5. Increasing the stationary groundplane boundary layer thickness was found to reduce the drag coefficient of the stationary shrouded wheel. Analysis of the wheel surface pressure distributions showed that this reduction was due to pressure changes on the lower half of the wheel.

Chapter 10

Conclusions and Recommendations

10.1 Conclusions

A steady state 3D Navier-Stokes CFD model to study the aerodynamic characteristics of automobile wheels has been developed. It was validated with experimental data. Both a rotating wheel on a moving groundplane and a stationary wheel on a stationary groundplane were considered. Initial 2D circular cylinder studies aided the development of strategies for boundary conditions and mesh topology. This was extended into 3D with the modelling of an isolated wheel. Existing experimental data was used for validation of an extensive investigation into the effects of numerical parameters, in particular the turbulence model. Finally, the effects of enclosing the wheel within an asymmetric shroud were analyzed with both CFD and a parallel experimental programme.

From this research it can be concluded that:

1. Computational Fluid Dynamics can accurately predict that a rotating isolated wheel on a moving groundplane generates less lift and drag than the equivalent stationary wheel on a stationary groundplane.

2. The use of the RNG k-ϵ turbulence model gave improved isolated wheel solutions compared to the equivalent ones with the standard k-ϵ model. However, this was at the expense of extra solution instability. The use of a full boundary

layer closure, compared to the use of wall functions, improved, in particular, the structure of the wake behind the wheel.

3. It is important to move the computational farfield boundaries as far away from the object of interest as possible. However, for automotive solutions, this conflicts with the requirement of matching the thickness of stationary groundplane boundary layers.

4. The success of any fully turbulent CFD simulation is highly dependent on the accurate setting of the range of y^+ values for the wall boundaries.

5. The optimum isolated rotating wheel solution corroborated the postulation of a 'jetting' phenomena at the front of the contact patch of the rotating wheel. This accounted for the pressure coefficients greater than unity in this region.

6. Both the rotating and stationary final isolated wheel solutions provided evidence of a weak vortex shed from the top of the wheel which was entrained vertically downwards into the main groundplane vortex structure.

7. The influence of ground condition on shrouded wheel drag was found to be opposite of that for an isolated wheel. The rotating wheel on a moving groundplane produced more drag that an equivalent stationary wheel on a fixed groundplane.

8. For both moving and stationary groundplane systems it was found that lowering the ride height of a shroud reduced shrouded wheel drag. Adding increasing depth of spoilers to the front of the shroud also decreased shrouded wheel drag.

9. Decreasing the pressures within the rear half of the wheelhouse cavity correlated with a decrease in the drag of the shroud containing the cavity.

10. Increasing the stationary groundplane boundary layer thickness was found to reduce the drag coefficient of the stationary shrouded wheel.

10.2 Recommendations

This research programme represents a relatively small step towards the complete understanding of the aerodynamic characteristics of automobile wheels. The following points form recommendations, both for the direction of possible further work, and in the application of experimental and computational techniques.

1. The shape of the wheels used in this study were simple generic ones. The geometry of the wheels should be made more realistic. In terms of the validation of the isolated wheel model, the correct wheel edge profile needs to be modelled. This then could be used to further refine the numerical techniques for modelling wheel flows. For example, the effects of using a Reynolds Stress turbulence model could be evaluated. The central hub could also be added as a first step to modelling the flow through the wheel, which would be required for a brake cooling study.

2. For wheels installed on an actual passenger car, it has been shown that the local freestream flow is at an significant yaw angle. The effects of a yawed freestream should be modelled, first with an isolated wheel, and then with a shrouded wheel.

3. The analysis of the predicted flowfields around an isolated wheel highlighted flow angularity that would be difficult to measure experimentally with a pressure probe without significant error. Experimental data of the structure of the wake, not just the position its edge, would be invaluable for the validation of a CFD model. To minimize experimental errors, a 3-axis hot-wire system, or a laser anemometry technique, should be used.

4. Such experimental wake measurements would allow the validation of an time dependent CFD model. This would need to be solved without a symmetry plane to allow for wake interactions.

5. The effects of using hybrid meshes, both surface and volume, need to be further evaluated. For the shrouded wheel solutions, a quadrilateral shroud surface mesh in the areas of fixed separation would allow cell centres to be placed closer to geometric corners, without a large penalty in volume mesh size, which should give better resolution of the complex separation flow structures. To help validate the model in such area, further pressure data, closer to the geometric

edges, would be required in the wheelhouse cavity, and on the lower front edge. This would require the use of flush tappings.

6. In simulations of complex flow structures with full boundary layer turbulence model closure, it can be difficult to maintain the y^+ values within the small range required. With an exponential growth rate of cell height away from the wall boundaries, it should be possible at stages throughout the iteration process, but within the solver routine, to recalculate the first cell height and growth rate to optimize automatically the range of y^+ values.

Chapter 11

Non Technical Study: The Provision and Management of Compute Resources for CFD

11.1 Introduction

The use of Computational Fluid Dynamics is becoming increasingly common in the major automotive companies, both for research into conceptual ideas and, as confidence in it increases, actual product development. Whilst it has had most influence on internal flow issues, such as engine cooling, where detailed flow measurements and visualization are difficult to obtain, it is now also being used for external aerodynamics.

This research project formed part of Rover Group's investigations into using CFD as a tool for development of the external aerodynamics of its vehicles. Despite a number of problems with the final shrouded wheel model, especially in terms of the absolute force coefficients, it has shown good relative results and highlighted a number of numerical issues and aerodynamic properties of wheel flows that warrant further investigation.

Whilst currently only a complementary tool to wind tunnel testing there is no doubt that as both numerical techniques and computer technology develop CFD will play an ever increasing role in product development. However, its current and potential future use is limited due to poor provision and management of scarce high perfor-

mance computer resources.

Throughout the course of this research the provision of sufficient computer resources, both in terms of memory limits and time to convergence, was always a problem. For the shrouded wheel calculations this was the determining factor for the final mesh size which consequently affected the quality of the solutions. The size of mesh used for a solution should always be governed by the flow features to be resolved and not computer limitations.

For CFD to form an important part of the design process solution run times, relative to those experienced during this project, would have to be reduced dramatically. This chapter documents the study undertaken as part of the Total Technology programme and looks at the provision and management of computer resources for CFD within the design environment. Five possible solutions are considered. The use of a dedicated multi-processor system for CFD calculations will be compared to the use of existing resources as a virtual parallel machine, the hiring of computer resources, as well as outsourcing part or all of the solution procedure to external consultancies or other departments within the group of companies.

11.2 The Computer Resources Required to Give Viable CFD Solution Times

Consider a CFD solution typical of those outlined in the final stages of this research; a parallel commercial solver optimized for UNIX operating systems, 1.5 million cells, and full boundary layer closure of a two equation turbulence model. This would require of the order of 1.5Gb of 32-bit RAM so that the solution can be processed entirely in physical memory.

Also consider the dual processor Silicon Graphics Octane machine used for most of the calculations in this research. If it was fitted with enough memory to process this typical 1.5 million cell solution then the time per iteration would have been approximately eight CPU minutes (i.e. fifteen iterations per hour) assuming 100% speedup on the dual processor machine. Say this solution takes 1500 iterations before the convergence criterion was satisfied. Therefore, the time for the iteration part of the solution would be just over four days.

Clearly, if CFD is to be used within the design environment, with its ever decreasing

lead times to market, then this time to convergence must be reduced. Such a component level analysis should be able to be solved overnight. Solutions for larger assemblies, such as a detailed full vehicle model where the mesh size could be of the order of ten million cells, would typically need to be solved within the time-span of a weekend to make commercial sense.

With the 1.5 million cell component case what level of processing power would be required, assuming there is enough physical memory, to reduce iteration time to convergence down to twelve hours? These twelve hours, plus the time to read and write solution files, would equate to an overnight run. Again assuming an equivalent processor speed to the Octane and linear speed-up with increasing number of processors, a 16 node machine would be required. A machine capable of delivering this level of performance, for example a Silicon Graphics Origin 2000, would have cost approximately a quarter of a million pounds at the end of 1998. Whilst computing power per pound is increasing all the time so too is the complexity of CFD models, either numerically or through increased volume mesh size, and, consequently, to obtain an adequate CFD processing capability a large financial outlay would be required. This would form a substantial proportion of an I.T. or aerodynamics annual budget. Are there any viable alternatives?

11.3 Computer Hardware Requirements for the CFD Solution Procedure

A detailed analysis of the procedure to obtain a solution with FLUENT/UNS was given in Chapter 3. What are the minimum hardware requirements to complete the four stages of pre-processing, definition of initial solution parameters, iteration of the solution, and post-processing of the computed flowfield?

Pre-processing should take place on a local workstation and the CPU timescales of each individual task mean that only a single processor should be required, although a twin processor system would give much increased user flexibility. Presuming an unstructured volume mesh is to be used TGrid 3.0 would require approximately 0.5Gb of RAM to generate and store the 1.5 million cell volume mesh. This is a typical configuration for a high end desktop CAD workstation.

For setting up the initial solution extra system resources would be required; for the 1.5 million cell case approximately 1.25Gb RAM and a similar amount of swap space.

These requirements scale approximately linearly with increasing volume mesh size. Partitioning these meshes for parallel processing can also utilize large periods of CPU time which makes other tasks, such as CAD, extremely slow. Thus, for large simulations local desktop system limits are generally too small unless an expensive dedicated high-end server is used as a desktop machine for each CFD user.

If a dedicated high performance computer resource is available then solution set-up can take place using a single processor on that machine, either interactively across the network or via a script if a job control system exists forbidding large periods of X-resource application usage. Should such a machine not be available then this will have to take place locally using swap space as a supplement to the physical memory, and a script. This generally would have to take place overnight as the workstation would be unsuitable for any other concurrent tasks. An alternative would be to run the set-up script as part of the solver process on the virtual parallel machine. FLUENT/UNS has the facility to partition a mesh automatically when reading into a parallel solver. However, this generally leads to an uneven and inefficient partition, relative to those generated manually in the serial solver, which would give longer times to convergence.

Running the solution generally requires little user involvement apart from monitoring and interpreting convergence progress. Thus, the time for completion is a function of the computer resources available.

Solution post-processing would take place on the local workstation. Again local resource limitations can be a major issue for large volume meshes. For analysis with the tools available in FLUENT/UNS the complete solution dataset has to be loaded into memory. This requires approximately 1Mb of RAM for every one thousand cells in 3D, and thus 1.5Gb for the 1.5 million cell solution. Parallel processing is generally not an option due to some of the routines only being available for a serial, or single CPU, process. Read time for the data files is also much longer in parallel than it is in serial. Alternatively a separate post-processing package, such as Ensight or Fieldview, could be used which have reduced memory requirements.

Presuming that enough local system resources are available to meet the needs of pre- and post-processing then the main issue is how to set-up and iterate the solutions through to convergence in the aforementioned time periods. Whilst it is clear that having a dedicated multi-processor machine would be the most practical way of providing the required resources is it the best solution for the entire company?

11.4 The Virtual Parallel Machine

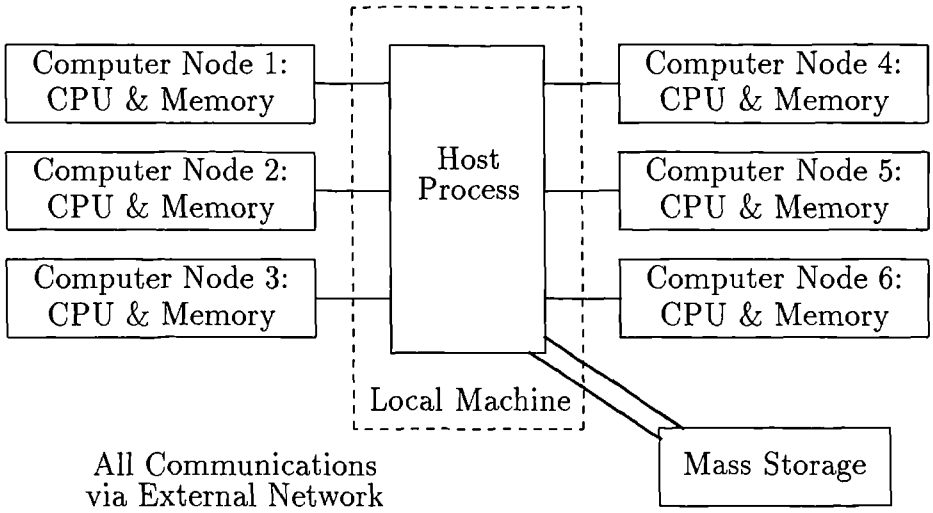

Figure 11.1: Schematic of the Architecture of a Distributed Memory Virtual Parallel Machine

Large modern engineering companies will invariably have many powerful desktop workstations. These usually will be located in different departments, such as design or structural analysis, and networked to one or more central servers for provision of user file space and software installation. This form of resource is known as a distributed computer system. Most of the applications that are used on these machines would be interactive ones, such as CAD, and consequently the CPUs are idle for most evenings and weekends. A virtual parallel machine is the term given to when these distributed workstations are used together as a multi-processor machine with communications between the various computer nodes via the external network, *Fig.11.1.* This is opposed to a dedicated multi-processor machine where all the memory and CPUs exist physically within the one machine, *Fig.11.2.*

Presuming that the CFD code to be used can utilize the distributed memory architecture of the virtual parallel machine (some are only available for dedicated multi-processor platforms) what are the strengths and weaknesses of both systems? Which method of providing computer power for CFD will provide enough system resources for the group whilst having minimal impact on the rest of the company through both budget constraints and overall system performance?

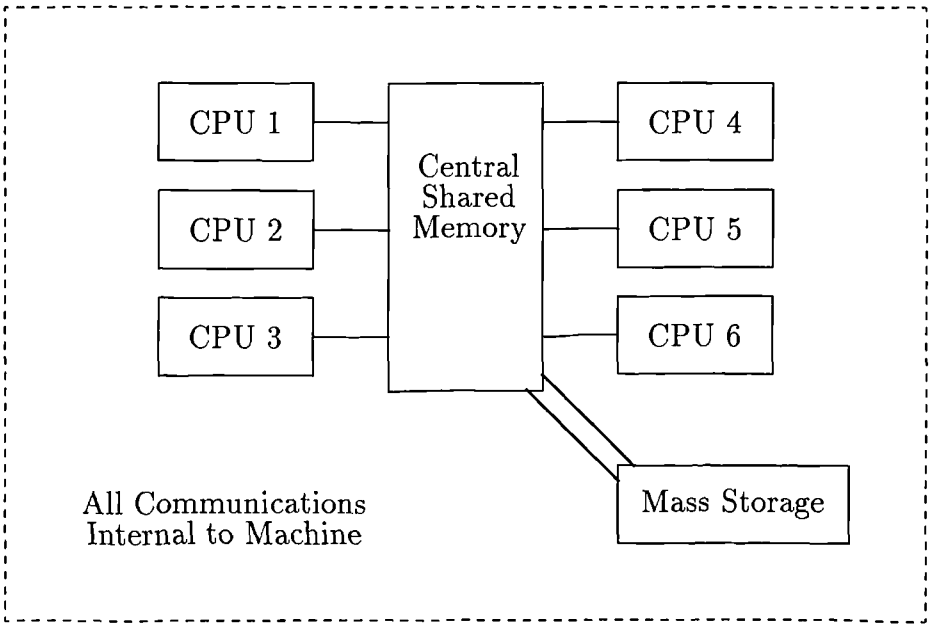

Figure 11.2: Schematic of the Architecture of a Shared Memory Dedicated Multi-Processor Computer

Both these options require an investment in in-house computer resources whether or not the hardware would be solely for CFD use. What if the company wanted to have a CFD capability but could not find the resources to invest in a dedicated machine, and the existing computer resources were not suitable to use and unviable to upgrade. Other options do exist. The entire CFD process could be contracted out to a specialized consultancy, computer hardware could be hired to avoid a large capital expenditure on a system, or if there existed computer resources within any other existing member companies in a group then would CPU time be available on those machines. For example, would Rover Group's parent company BMW allow a login and make resources available on their computer systems?

11.5 The Relative Performance of Dedicated and Virtual Parallel Machines

Consider dedicated and virtual parallel machines of equivalent specification in terms of the amount, and specification, of processors and memory. The two main issues impacting the performance of the two machines will the availability of, and communications speeds between, the computer nodes.

A dedicated multi-processor machine is theoretically available 24 hours per day / 7 days per week. If this machine is for CFD use only then if a job takes longer to complete than expected, or crashes through solution divergence for example, it only affects the CFD group and not other users of the system. With the virtual parallel machine either scenario would at least slow the individual workstations down or, at worst, make them unusable. This would be considered unacceptable and measures would have to be put in place to ensure the system was ready for interactive 'day-time' users. Having the dedicated machine available during the day also makes it much easier for the CFD engineer to develop new models and test solutions interactively before batch running. These batch runs can then be left until convergence is reached instead of manually stopping and restarting them when the system is required by other users.

The time for each iteration will also be much more variable on a virtual parallel machine. Running a computation in parallel essentially means the solution domain is split down into a number of sections, or partitions, and run individually on different machines. At various time throughout the iteration cycle information will have to be passed between the individual computer nodes. Computation will not be able to continue until all this message passing is complete. This could amount to tens of megabytes of data per iteration. Therefore the speed of, and load on, the external network will have a major influence on the wall clock time to solution. For example, if the network was very quiet the time per iteration could be at least 75% that of when the network was saturated. Also, the time to distribute the initial data from file around the system will be affected. Whilst network speed and capacity can always be upgraded, and 100Mbit[1] should be the minimum specification, communication performance will never be as dependable, or as quick, as that from a dedicated multi-processor machine where internal bandwidth can exceed 10Gbit.

However, network improvements would cost only a fraction of that of the dedicated multi-processor machine and would benefit all the users. Also, any subsequent upgrades, such as to faster processors, would improve the productivity of both groups of users. The monies invested in a single dedicated machine would have limited other uses if the CFD group experienced a period of having no large calculations to run. During this period the system would still require administration which often requires specialist training. Also, if there is a system failure the whole machine generally becomes unavailable. If one of the workstations forming the virtual system goes

[1]For a 32-bit operating system 8bits equals 1byte of information. Therefore a 100Mbit network has the capacity of transferring almost 12Mb of data per second

down there should be enough resources remaining to allow computation to continue, albeit at a slower rate.

Some of the weaknesses of the virtual machine can be compensated for by the use of extra software. For example, FLUENT5, the current unstructured code from Fluent Incorporated which superseded FLUENT/UNS 4.2, is integrated with Platform Computing's LSF suite of codes which allow the loadings on a network of workstations to be managed centrally. Both single node and parallel applications, whether interactive or run as a batch job, are submitted to the system, continually analyzed and processed on the best computer nodes available. The whole system will appear more like a single multi-processor machine.

The use of LSF, or other equivalent software, should allow:

1. The migration of computer processes between nodes in a cluster to ensure optimum load balancing, and therefore minimum possible time per iteration.
2. Compensation for varying specifications of machines, such as CPU clock speed, within a cluster of nodes.
3. Spotchecking of jobs should the system require attention or is required by large numbers of 'day-time' users. The job can then be started from the halt point when resources are free again instead of at the last save.

In summary, the purchase of a dedicated multi-processor machine, when compared to a virtual parallel machine, for CFD would dramatically increase the productivity of the group and reduce their impact on the rest of the computer users. However, such machines are expensive, of limited use to other users, and alternative methods of setting-up and iterating solutions are available. Is the initial monetary saving worth the potential costs to a company though?

11.6 Risk and Strategic Analyses

Analysis of the two types of multi-processor architecture has so far concentrated on their benefits for the CFD group. Is the expenditure on the provision of dedicated in-house resources the best solution for the whole company?

Suppose that the company using CFD decides not to buy the dedicated 16 node

multi-processor machine it requires, thus saving an outlay of a quarter of a million pounds. Consider the four other options and their short term financial implications:

1. *The Virtual Parallel Machine*
   Say the company decides instead to use a virtual parallel machine comprising of 25 design workstations and spends approximately £50,000 on network upgrades and a load management system. If it considers that this system won't adversely affect the productivity of the CFD group, relative to that if it had the dedicated hardware, then it will see a £200,000 saving.

2. *The Hiring of Computer Resources*
   Companies exist who purchase computer hardware in bulk and then hire it out for set periods of time. However, these tend to concentrate on low-end single processor desktop systems and the hire costs can easily add up to more than the actual purchase price of the equipment in a few months, despite there being minimal initial costs. The warranty terms would be advantageous though, as immediate replacement of failed components is usually standard.

3. *The Use of CFD Consultancies*
   Consultancies can be employed to either just run solutions or complete the whole analysis process. Whilst this would avoid employment costs and headcount increases a degree of flexibility throughout the course of a project would be lost due to the work being completed off-site with its consequent communication problems. Thus the management time for a project will be greater than if it was conducted in-house. Contract costs for large projects would probably be more than having in-house skills. Company legal costs would also increase due to the need for complex confidentiality agreements for design work.

   Also, if it was required to look at a solution subsequent to the completion of the contract, say to look at a flow variable not presented in the final report, then the consultancy firm would have to be contracted again due to the lack of local facilities and expertise. Thus, costs for a project would grow and the lead times for a design would probably be increased by a large amount.

4. *Resource Sharing Within a Group of Companies*
   Suppose sufficient computer resources were available within another member company of a group. Then this could be used to provide CFD iteration capacity if a login and a secure data transfer link could be provided at what would equate to a very small capital expenditure. Resource allocation could be set

through a queueing system to prevent system saturation by a single group of users. The cost of providing and maintaining the data link would be minimal compared to the actual purchase of hardware.

The effectiveness of this is highly dependent on the data transfer rate of the link between the two companies. The compressed binary files for a large simulation can easily become 250Mb per save, and enough bandwidth must be provided to transfer files quickly. Reducing the iteration time to convergence is not beneficial if it takes an overnight period to transfer the files between sites. Any instability in the file transfer procedure could also become extremely costly in terms of a project not meeting a tight deadline. Also, depending on company policy, a charge may be incurred per second of CPU usage which could easily absorb any initial cost savings.

All these four options considerably reduce the initial financial outlay for establishing a CFD capability. Does the short-term saving translate into a long term financial gain though? For example, how much of this saving will be lost due to unexpected expenditures as a result of the CFD calculations affecting the other users.

11.6.1 Backups

Most user files will be stored in central filespace on the main server. However, there are some applications, such as the structural analysis pre- and post-processor PATRAN, which benefit, in terms of speed, from local workstation filespace for databases. These local files should be archived as part of the main system backup routine and as a consequence will have to be read over the network overnight.

This network traffic will therefore conflict with the CFD processes if a virtual parallel machine is being used for CFD calculations. The increased network load from the CFD will not only slow down the backup process down but will also increase the risk of a network problem, for example, through saturation. If such a problem occurs, and if this causes the backup to miss the local files, should they need to be restored before the next archive takes place then two possible problems exist. The system administrator will have to go back to the previous complete backup and, as work is progressing with these files, it is likely that an significantly older version existed on backup or it didn't exist at all. If either scenario is true then the work will have to be done again. This would probably put the project behind its schedule which could incur large penalty payments as well as the cost of the extra man hours to redo the

work. These could easily remove a large part of the £200,000 initial saving.

Any files located on hired computer resources would probably not be fully configured into the main system backup routines. Either they would be have to treated separately by the department using the resource or backed up over the network as a temporarily mounted filesystem. Thus, the risk of losing work if a problem occurs increases and it takes extra system administration time to organize the backups than if the company owned the hardware and it was fully integrated onto the main system. Also, transferring all the files from the machine once the hire period had finished would take up administrator time.

Having the files located outside the company, whether at a consultancy or on the filesystems of another company within the group, would mean that the main backup issues would be their concern and only once the final files are brought in-house would backup become a requirement. As the data would probably be located on a main filesystem they would be covered by the main backup routines.

11.6.2 System Downtime

To upgrade the network and install the extra load monitoring software for the virtual parallel machine would require periods when the computer network would be unavailable. It is likely that this would have to be done during periods outside normal 'day-time' working hours, probably during a weekend or bank holiday. Although the main financial costs of this will be included in the upgrade cost of £50,000 it is often that employment policy will state that extra holiday will have to be given to employees working during these periods. The costs of providing cover for these holidays could become significant. Alternatively, companies such as Platform Computing, will install and configure their software on site at a typical cost of hundreds of pounds per employee visit. The other three methods of providing computer resources would probably only require minimal periods, if any, of main system downtime.

11.6.3 System Monitoring

Should a system problem occur during the CFD iteration process on the virtual parallel machine then man-hours will be required to sort out the problem before interactive users require the system. Therefore it is likely that extra computer administration support will be required out of normal working hours. Whilst this

has an associated employment cost it is likely that this will be much smaller than the costs to a company of having the users of the 25 workstations idle for the first hour of the day whilst any overnight problems are resolved.

Any hired computer hardware installed on a system will require some initial monitoring of its stability and to verify that it is not conflicting with any other resource within the company. Running solutions outside the company would have no implications on the existing system administration routines.

11.6.4 Overtime Hours

If computer system problems do occur as a result of the CFD virtual machine, or other computer resources within the group of companies, and time on a project has to be recovered then overtime costs will generally apply. When all the company employment costs are added together this could easy come to over £50 per man-hour. At £50 per hour for a twenty five man team it takes only 160 hours of group overtime to absorb the total £200,000 initial cost savings. Any contract with a consultancy would probably state a delivery date for the final results and any financial implications on man hours of a project being behind schedule would therefore impact on their profit margin and not the overall cost of the contract.

11.6.5 Summary

The benefits of a number of ways of providing computer capacity for CFD calculations have been discussed. Relative to the purchase of dedicated hardware these methods all save some, if not all, of the initial expenditure. However, this saving could easily be lost through unexpected additional and unplanned support and personnel costs throughout the financial year. This, together with the increased productivity of the CFD group through having a dedicated resource, means that this is the best facility to set-up and iterate CFD solutions with.

11.7 Other Potential Benefits of the Use of CFD

What if the extra cost of a dedicated CFD multi-processor machine could be met from other budgets or sources. BMW are currently using the issue of aerodynamic

crosswind sensitivity in one of its television advertising campaigns. Would the promotion of the use of CFD technology in the design process promote the market image of a range of vehicles? Could this attract younger car buyers to a range without deterring the existing purchasers of these models? If so, then the investment in the CFD hardware and software would be justified through increased market share. Also, some of the marketing budget could possibly be used for hardware and software costs instead of it having to be spent for a consultancy to do the CFD work before the marketing campaign.

The purchase costs of a large machine could also be reduced by agreeing to let the manufacturer use the fact that the company is using its hardware products in their advertising campaigns as well. This is often used in areas such as Formula 1 racing where an association with a winning team can give significant marketing leverage.

11.8 Conclusions

A study has be done of the relative merits of five ways of providing enough hardware resources for set-up and iteration through to convergence of large CFD cases. The purchase of a dedicated multi-processor machine has been compared to the use of existing workstation resources in parallel during periods of non-interactive use, both in terms of CFD performance and the impact on the rest of the users of the main computer system. The hiring of computer resources, the use of CFD consultancies, and resource sharing within a group of companies, have been shown to be good ways of providing extra CFD capacity for short-term surges in workload but their use would be unjustifiable as the main computer resource due to the inflexibility in working practises that they would bring to the CFD and aerodynamics groups. Whilst the virtual parallel machine would bring major cost savings to the company, and give network upgrade benefits to most users, the initial financial savings could be absorbed by extra unexpected costs due to system problems caused by the extra network load of the message passing during solution iteration. This, coupled with the fact that a CFD group would very probably be much more productive with its own hardware, means that if a company is serious that Computational Fluid Dynamics is going to form an important part in its product development cycles then a dedicated multi-processor machine is the only way to provide enough system resources.

Bibliography

[1] Hucho.W-H, editor. *Aerodynamics of Road Vehicles.* SAE International, fourth edition, 1998.

[2] Hackett.J.E. et al. On the Influence of Ground Movement and Wheel Rotation in Tests on Modern Car Shapes. Technical Report 870245, SAE, 1987.

[3] Cogotti.A. A Parametric Study on the Ground Effect of a Simplified Car Model. Technical Report 980031, SAE, 1998.

[4] Mercker.E. et al. On the Aerodynamic Interference Due to the Rolling Wheels of Passenger Cars. Technical Report 910311, SAE, 1991.

[5] Howell.J. and Hickman.D. The Influence of Ground Simulation on the Aerodynamics of a Simple Car Model. Technical Report 970134, SAE, 1997.

[6] Le Good.G.M. *Aerodynamic Characteristics of Passenger Cars: Comparison Between Wind Tunnel and Track Derived Data.* PhD thesis, Cranfield University, 1994.

[7] Mercker.E. et al. Experimental Investigation on the Influence of Various Ground Simulation Techniques on a Passenger Car. In *Proceedings of the Royal Aeronautical Society Vehicle Aerodynamics Conference*, 1994.

[8] Mueller.R. et al. Moving Belt with Distributed Suction in the Porsche Model Wind Tunnel. Technical Report 1999-01-0650, SAE, 1999.

[9] Wickern.G. et al. Rotating Wheels - Their Impact on Wind Tunnel Test Techniques and on Vehicle Drag Results. Technical Report 970133, SAE, 1997.

[10] Coiro.D.P. et al. Experiments and Numerical Investigation on a Multi-Component Airfoil Employed in a Racing Car Wing. Technical Report 970411, SAE, 1997.

[11] Batchelor.G.K. *An Introduction to Fluid Dynamics.* Cambridge University Press, 1967.

[12] Hajiloo.A. et al. Limited Mesh Refinement Study of the Aerodynamic Flow Field Around a Car-Like Shape: Computational Verses Experimental Fluid Dynamics. Technical Report 960677, SAE, 1996.

[13] Ramnefors.M. et al. Accuracy of Drag Predictions on Cars using CFD - Effect of Grid Refinement and Turbulence Models. Technical Report 960681, SAE, 1996.

[14] Axelsson.N. et al. Accuracy in Computational Aerodynamics Part 1: Stagnation Pressure. Technical Report 980037, SAE, 1998.

[15] Perzon.S. et al. Accuracy in Computational Aerodynamics Part 2: Base Pressure. Technical Report 980038, SAE, 1998.

[16] Dhaubhadel.M.N. Review: CFD Applications in the Automotive Industry. *Journal of Fluids Engineering*, 118(4):647–653, December 1996.

[17] Morelli.A. Aerodynamic Effects of an Automobile Wheel. Technical Report Trans 47/69, MIRA, 1969.

[18] Morelli.A. Aerodymanic Actions on an Automobile Wheel. In Sabor-Rylski.A.J., editor, *Road Vehicle Aerodynamics - Proceedings of the First Symposium on Road Vehicle Aerodynamics, City University*, 1970.

[19] Stapleford.W.R. and Carr.G.W. Aerodynamic Characteristics of Exposed Rotating Wheels. Technical Report 1970/2, MIRA, 1970.

[20] Fackrell.J.E. and Harvey.J.K. The Flow Field and Pressure Distribution of an Isolated Road Wheel. In Stephens.H.S., editor, *Advances in Road Vehicle Aerodynamics*. BHRA Fluid Engineering, 1973.

[21] Fackrell.J.E. and Harvey.J.K. The Aerodynamics of an Isolated Road Wheel. In Pershing.B., editor, *Proceedings of the Second AIAA Symposium of Aerodynamics of Sports and Competion Automobiles*, 1975.

[22] Fackrell.J.E. *The Aerodynamic Characteristics of an Isolated Wheel Rotating in Contact with the Ground.* PhD thesis, Imperial College, University of London, 1974.

[23] Cogotti.A. Aerodynamic Characteristics of Car Wheels. In *Technological Advances in Vehicle Design Series, SP3 - Impact of Aerodynamics on Vehicle Design*, pages 173–196. International Journal of Vehicle Design, 1983.

[24] Bearman.P.W. et al. The Effect of a Moving Floor on Wind Tunnel Simulation of Road Vehicles. Technical Report 880245, SAE, 1988.

[25] Hilhorst.R. and Giachi.M. An Experimental Study on Drag Evaluation Referred to the Geometry of the Formula One Racing Car Tires. In *Proceedings of the Royal Aeronautical Society Vehicle Aerodynamics Conference*, 1994.

[26] Schiefer.U. et al. Two Different Approaches to a Better Simulation of Road Conditions in the Wind Tunnel. In *Proceedings of the MIRA International Conference on Vehicle Aerodynamics*, 1996.

[27] Skea.A.F. et al. The use of CFD to Predict the Air Flow Around a Rotating Wheel. In *Proceedings of the MIRA International Conference on Vehicle Aerodynamics*, 1998.

[28] Oswald.L.J. and Browne.A.L. The Airflow Field Aound an Operating Tire and its Effect on Tire Power Loss. Technical Report 810166, SAE, 1981.

[29] Fabijanic.J. An Experimental Investigation of Wheel-Well Flows. Technical Report 960901, SAE, 1996.

[30] Fabijanic.J. and George.A.R. An Experimental Investigation of the Aerodynamics of Automobile Wheel Wells. Technical Report 962475, AIAA, 1996.

[31] Imaizumi.T. and Yoshida.Y. The Aerodynamic Effect of Rotating Wheels. *JSAE Review*, 12(4):64–66, 1991.

[32] Pfadenhauer.M. et al. On the Influenece of Wheels and Tyres on the Aerodynamic Drag of Vehicles. In *Proceedings of the MIRA International Conference on Vehicle Aerodynamics*, 1996.

[33] Wiedemann.J. The Influence of Ground Simulation and Wheel Rotation on Aerodynamic Drag Optimization - Potential for Reducing Fuel Consumption. Technical Report 960672, SAE, 1996.

[34] Piccioni.C.F. et al. Numerical Investigation on the Fender of a Motorcycle. Technical Report 970412, SAE, 1997.

[35] Turkiyyah.G. et al. Fast Vortex Methods for Predicting Wind-Induced Pressures on Buildings. *Journal of Wind Engineering and Industrial Aerodynamics*, 58(1-2):51–81, 1995.

[36] Axon.L.J. A Computational Model of the Flow Over a Two-Dimensional Cylinder in Contact With a Plane Surface. Master's thesis, Cranfield University, 1995.

[37] Fluent Europe. *FLUENT/UNS 4.2 USER'S GUIDE*, 1997.

[38] Fluent Europe. *GEOMESH 3.0 USER'S GUIDE*, 1996.

[39] Fluent Europe. *TGrid 3.0 USER'S GUIDE*, 1997.

[40] Jones.W.P. and Launder.B.E. The Prediction of Laminarization with a Two-Equation Turbulence Model. *International Journal of Heat and Mass Transfer*, 15:301–314, January - June 1972.

[41] Launder.B.E. and Spalding.D.B. *Lectures in Mathematical Models of Turbulence.* Academic Press, 1972.

[42] Yakhot.V. and Orszag.S.A. Renormalization Group Analysis of Turbulence: I. Basic Theory. *Journal of Scientific Computing*, 1(1):1–51, 1986.

[43] Launder.B.E. and Spalding.D.B. The Numerical Computation of Turbulent Flows. *Computer Methods in Applied Mechanics and Engineering*, 3:268–289, 1974.

[44] Patankar.S.V. *Numerical Heat Transfer and Fluid Flow.* Hemisphere Publishing Corporation, 1980.

[45] Vandoormaal.J.P. and Raithby.G.D. Enhancements of the SIMPLE Method for Predicting Incompressible Fluid Flows. *Numerical Heat Transfer*, 7(2):147–163, 1984.

[46] Zdravkovich.M.M. *Flow Around Circular Cylinders*, volume 1: Fundamentals. Oxford University Press, 1997.

[47] Prandtl.L. and Tietjens.O.G. *Applied Hydro- and Aero- Mechanics.* McGraw-Hill, 1934.

[48] Wulfsohn.D. and Upadhyaya.S.K. Determination of Dynamic Three-Dimensional Soil-Tyre Contact Profile. *Journal of Terramechanics*, 29(4/5):433–464, 1992.

[49] Upadhyaya.S.K. and Wulfsohn.D. Relationship Between Tire Deflection Characteristics and 2-D Tire Contact Area. *Transactions of the American Society of Agricultural Engineers*, 33(1):25–30, January-February 1990.

[50] Bearman.P.W. and Zdravkovich.M.M. Flow Around a Circular Cylinder Near a Plane Boundary. *Journal of Fluid Mechanics*, 89(1):33–47, 1978.

[51] Closed-Test-Section Wind Tunnel Blockage Corrections for Road Vehicles, 1996. SAE SP-1176.

Appendix A

Publications

During the course of this research the following papers have been published.

1. Lee Axon, Kevin Garry, Jeff Howell
   An Evaluation of CFD for Modelling the Flow Around Stationary and Rotating Wheels
   SAE 980032

   Also Reprinted in

   (a) Developments in Vehicle Aerodynamics, SAE SP-1318, SAE International, 1998

   (b) SAE 1998 Transactions

2. Lee Axon, Kevin Garry, Jeff Howell
   The Influence of Ground Condition on the Flow Around a Wheel Located Within a Wheelhouse Cavity
   SAE 1999-01-0806

   Also Reprinted in

   (a) Vehicle Aerodynamics and Wind Noise, SAE SP-1441, SAE International, 1999

Appendix B

Two Dimensional Experimental Data

In this appendix surface static pressure coefficient distributions are presented from the experimental programme, described in Section 4.3.2, to provide validation data for the model of the flow over a two-dimensional cylinder resting on an infinite groundplane.

Distributions are presented for both the cylinder surface, in ten degree intervals, and along the groundplane downstream of the cylinder. The plane of all the pressure tapping locations was approximately half way between the floor and roof of the working section of the tunnel. All the positional data is relative to the contact point between the cylinder surface and the tunnel wall in this plane. The angular orientation is such that 90° is then facing upstream.

B.1 Cylinder Surface Static Pressure Coefficients

Angular Position (deg)	Pressure Coefficient C_P		
	$Re_D = 2.0 \times 10^5$	$Re_D = 3.0 \times 10^5$	$Re_D = 4.0 \times 10^5$
9	0.823	0.826	0.820
19	0.830	0.839	0.846
29	0.814	0.817	0.822
39	0.768	0.771	0.781
49	0.724	0.718	0.725
59	0.654	0.685	0.675
69	0.641	0.664	0.659
79	0.588	0.608	0.616
89	0.453	0.506	0.542
99	0.220	0.310	0.320
109	-0.134	-0.085	-0.044
119	-0.637	-0.557	-0.550
129	-1.172	-1.133	-1.095
139	-1.736	-1.687	-1.616
149	-2.127	-2.080	-2.018
159	-2.378	-2.382	-2.253
169	-2.297	-2.306	-2.175
179	-1.948	-1.916	-1.743
189	-1.217	-1.248	-1.063
199	-0.802	-0.843	-0.808
209	-0.714	-0.765	-0.731
219	-0.687	-0.717	-0.703
229	-0.648	-0.698	-0.666
239	-0.645	-0.660	-0.665
249	-0.616	-0.655	-0.645
259	-0.618	-0.641	-0.639
269	-0.617	-0.641	-0.634
279	-0.614	-0.633	-0.633
289	-0.593	-0.621	-0.626
299	-0.594	-0.612	-0.618
309	-0.581	-0.599	-0.599
319	-0.568	-0.597	-0.591
329	-0.567	-0.588	-0.578
339	-0.563	-0.568	-0.570
349	-0.555	-0.562	-0.568

Table B.1: The Influence of Reynolds Number on the Cylinder Surface Static Pressure Coefficients

B.2 Groundplane Static Pressure Coefficients

Distance Downstream From Contact Point (m)	Pressure Coefficient C_P		
	$Re_D = 2.0 \times 10^5$	$Re_D = 3.0 \times 10^5$	$Re_D = 4.0 \times 10^5$
0.25	-0.616	-0.658	-0.644
0.50	-0.632	-0.657	-0.670
0.75	-0.593	-0.579	-0.615
1.00	-0.331	-0.345	-0.393
1.25	-0.133	-0.155	-0.207
1.50	0.006	-0.036	-0.071
1.75	0.031	0.018	0.012
2.00	0.056	0.044	0.035
2.25	0.049	0.043	0.044
2.50	0.041	0.039	0.035
2.75	0.039	0.039	0.044
3.00	0.038	0.038	0.040

Table B.2: The Influence of Reynolds Number on the Groundplane Surface Static Pressure Coefficients

Appendix C

Summary of Computational Forces from the 3D Isolated Wheel Cases

In this appendix the lift and drag coefficients from all the three dimensional isolated wheel CFD calculations to assess the influence of solver numerics are presented together with the reference data from Fackrell, *Ref.[22].*

The freestream velocity of 18.6m/s resulted in a Reynolds number, Re_D, of approximately 530,000 based on the wheel diameter of 0.415m. All the CFD force coefficients are based on a frontal reference area of the round edged profile wheel used in the calculations, equal to $0.05115m^2$ for half the wheel.

For cases based on the wall function meshes the solutions were stopped after 2000 iterations, and after 3000 iterations for the full boundary layer resolution two-layer meshes.

The convergence of the solutions at this point is also considered. In terms of the histories of the isolated wheel lift and drag coefficients with the iteration number the solutions converged in three manners. Either the force coefficients were stable, unstable with irregular oscillations, or oscillating periodically. In this case the stated force coefficients are the values at the mid-point of the oscillations. The magnitudes of the oscillations are also stated. If the solutions were unstable just the coefficients at the end of the calculation are stated.

C.1 Fackrell and Harvey

	Stationary	Rotating
C_{Lw}	0.76	0.44
C_{Dw}	0.77	0.58

Table C.1: Rotating and Stationary Force Characteristics for Wheel B2, $Re_D = 5.3 \times 10^5$, (Fackrell)

C.2 The Influence of the Numerical Schemes

All the calculations used the RNG k-ϵ turbulence model with non-equilibrium wall functions. The initial configuration used the SIMPLEC algorithm, instead of SIMPLE, without both the PRESTO and implicit body force options.

C.2.1 Stationary Wheel, Stationary Groundplane

Numerical Options Used	C_{Lw}	C_{Dw}	Stable?
SIMPLEC	0.647	0.718	Yes
SIMPLE	0.647	0.717	Yes
SIMPLEC & PRESTO	0.631	0.704	Yes
SIMPLEC & Implicit Body Forces	0.647	0.718	Yes

Table C.2: The Influence of Numerical Schemes for the RNG k-ϵ Turbulent CFD Solution of an Stationary Isolated Wheel on a Stationary Groundplane with Non-Equilibrium Wall Functions

C.3 The Influence of the Turbulence Model: Laminar Calculations

All laminar calculations were based on the two-layer turbulent closure meshes for full boundary layer resolution.

C.3.1 Rotating Wheel, Moving Groundplane

Volume Mesh Size	C_{Lw}	C_{Dw}	Stable?
248349	0.338	0.652	No
392836	0.435	0.644	No
538350	0.500	0.686	No
686870	0.373	0.689	No

Table C.3: The Influence of Mesh Size and Turbulent Closure Method for the Laminar CFD Solution of an Rotating Isolated Wheel on a Moving Groundplane

C.3.2 Stationary Wheel, Stationary Groundplane

Volume Mesh Size	C_{Lw}	C_{Dw}	Stable?
248349	0.566	0.608	No
392836	0.417	0.614	No
538350	0.601	0.704	No
686870	0.535	0.617	No

Table C.4: The Influence of Mesh Size and Turbulent Closure Method for the Laminar CFD Solution of an Stationary Isolated Wheel on a Stationary Groundplane

C.4 The Influence of the Turbulence Model: K-ϵ Calculations

C.4.1 Rotating Wheel, Moving Groundplane

Volume Mesh Size	Closure Condition	C_{Lw}	C_{Dw}	Stable?
248349	Standard Wall Function	0.519	0.759	Yes
	Non-Equilibrium Wall Function	0.502	0.738	Yes
	Two-layer	0.511	0.763	Yes
392836	Two-layer	0.513	0.766	Yes
538350	Two-layer	0.513	0.764	Yes
686870	Two-layer	0.527	0.708	1.

Table C.5: The Influence of Mesh Size and Turbulent Closure Method for the CFD Solution of an Rotating Isolated Wheel on a Moving Groundplane with the k-ϵ Turbulence Model

C.4.2 Stationary Wheel, Stationary Groundplane

Volume Mesh Size	Closure Condition	C_{Lw}	C_{Dw}	Stable?
248349	Standard Wall Function	0.588	0.815	Yes
	Non-Equilibrium Wall Function	0.577	0.798	Yes
	Two-layer	0.582	0.812	Yes
392836	Two-layer	0.585	0.811	Yes
538350	Two-layer	0.586	0.811	Yes
686870	Two-layer	0.596	0.772	2.

Table C.6: The Influence of Mesh Size and Turbulent Closure Method for the CFD Solution of an Stationary Isolated Wheel on a Stationary Groundplane with the k-ϵ Turbulence Model

Convergence Notes

1. & 2. The force coefficients were still slowly decreasing after 3000 iterations

C.5 The Influence of the Turbulence Model: RNG K-ϵ Calculations

C.5.1 Rotating Wheel, Moving Groundplane

Volume Mesh Size	Closure Condition	C_{Lw}	C_{Dw}	Stable?
248349	Standard Wall Function	0.403	0.560	3.
	Non-Equilibrium Wall Function	0.430	0.591	4.
	Two-layer	0.501	0.635	5.
392836	Two-layer	0.466	0.592	Yes
538350	Two-layer	0.462	0.588	Yes
686870	Two-layer	0.535	0.596	6.

Table C.7: The Influence of Mesh Size and Turbulent Closure Method for the CFD Solution of an Rotating Isolated Wheel on a Moving Groundplane with the RNG k-ϵ Turbulence Model

C.5.2 Stationary Wheel, Stationary Groundplane

Volume Mesh Size	Closure Condition	C_{Lw}	C_{Dw}	Stable?
248349	Standard Wall Function	0.642	0.735	Yes
	Non-Equilibrium Wall Function	0.647	0.718	Yes
	Two-layer	0.620	0.728	7.
392836	Two-layer	0.633	0.713	Yes
538350	Two-layer	0.632	0.707	Yes
686870	Two-layer	0.647	0.704	8.

Table C.8: The Influence of Mesh Size and Turbulent Closure Method for the CFD Solution of an Stationary Isolated Wheel on a Stationary Groundplane with the RNG k-ϵ Turbulence Model

Convergence Notes

3. Regular Oscillations of ± 0.004 in C_{Lw} and ± 0.002 in C_{Dw}
4. Regular Oscillations of ± 0.025 in C_{Lw} and ± 0.010 in C_{Dw}
5. Regular Oscillations of ± 0.039 in C_{Lw} and ± 0.023 in C_{Dw}
6. The force coefficients were still slowly decreasing after 3000 iterations
7. Regular Oscillations of ± 0.035 in C_{Lw} and ± 0.025 in C_{Dw}
8. The force coefficients were still slowly decreasing after 3000 iterations

C.6 The Influence of the Symmetry Plane

C.6.1 Rotating Wheel, Moving Groundplane

	C_{Lw}	C_{Dw}	Stable?
With Symmetry Plane, 538350 cells	0.462	0.588	Yes
Without Symmetry Plane, 1076700 cells	0.467	0.593	Yes

Table C.9: The Influence of a Symmetry Plane for the Two-Layer RNG k-ϵ Turbulent CFD Solution of an Rotating Isolated Wheel on a Moving Groundplane

Appendix D

Experimental Shrouded Wheel & Cavity Force Data

In this appendix experimental force coefficient data for shroud lift C_{Ls}, shroud drag C_{Ds}, wheel drag C_{Dw}, and total drag C_{Dt}, from the two MIRA Model Wind Tunnel sessions described in Chapter 7 are presented both as absolute data, and also as relative forces to the baseline case of $\Delta Y_s = 0$, no front spoiler, moving groundplane, and rotating wheel.

The freestream velocity of 25m/s resulted in a Reynolds number, Re_D, of approximately 850,000 based on the wheel diameter of 0.5m. All the coefficients are corrected for blockage using Mercker's open jet correction and are based on a frontal reference area of the model, A_T, of $0.15526m^2$.

D.1 First MIRA Session

Moving Groundplane

Shroud Lift Coefficient, C_{Ls}

		SPOILER DEPTH (m)		
		0.00	*0.05*	*0.10*
ΔY_s	*0.0*	0.080	0.097	0.019
	0.1	0.082	0.083	0.051
	0.2	0.091	0.058	0.070

Shroud Drag Coefficient, C_{Ds}

		SPOILER DEPTH (m)		
		0.00	*0.05*	*0.10*
ΔY_s	*0.0*	0.311	0.347	0.261
	0.1	0.299	0.319	0.299
	0.2	0.314	0.274	0.335

Wheel Drag Coefficient, C_{Dw}

		SPOILER DEPTH (m)		
		0.00	*0.05*	*0.10*
ΔY_s	*0.0*	0.156	0.136	0.114
	0.1	0.169	0.142	0.129
	0.2	0.193	0.157	0.141

Total Drag Coefficient, C_{Dt}

		SPOILER DEPTH (m)		
		0.00	*0.05*	*0.10*
ΔY_s	*0.0*	0.467	0.483	0.374
	0.1	0.468	0.461	0.429
	0.2	0.506	0.431	0.475

Stationary Groundplane

Shroud Lift Coefficient, C_{Ls}

		SPOILER DEPTH (m)		
		0.00	*0.05*	*0.10*
ΔY_s	0.0	0.101	0.093	0.034
	0.1	0.102	0.075	0.057
	0.2	0.099	0.077	0.073

Shroud Drag Coefficient, C_{Ds}

		SPOILER DEPTH (m)		
		0.00	*0.05*	*0.10*
ΔY_s	0.0	0.326	0.311	0.258
	0.1	0.324	0.286	0.302
	0.2	0.339	0.293	0.336

Wheel Drag Coefficient, C_{Dw}

		SPOILER DEPTH (m)		
		0.00	*0.05*	*0.10*
ΔY_s	0.0	0.129	0.118	0.097
	0.1	0.146	0.117	0.114
	0.2	0.160	0.131	0.131

Total Drag Coefficient, C_{Dt}

		SPOILER DEPTH (m)		
		0.00	*0.05*	*0.10*
ΔY_s	0.0	0.455	0.429	0.355
	0.1	0.471	0.403	0.416
	0.2	0.499	0.424	0.467

Table D.1: Absolute Experimental Wheel and Shroud Force Coefficients: First MIRA Session

Moving Groundplane **Stationary Groundplane**

Shroud Lift Coefficient, C_{Ls}

		SPOILER DEPTH (m)		
		0.00	*0.05*	*0.10*
ΔY_s	*0.0*	0.000	0.016	-0.061
	0.1	0.002	0.002	-0.029
	0.2	0.010	-0.022	-0.011

		SPOILER DEPTH (m)		
		0.00	*0.05*	*0.10*
ΔY_s	0.0	0.020	0.012	-0.046
	0.1	0.022	-0.005	-0.023
	0.2	0.019	-0.004	-0.007

Shroud Drag Coefficient, C_{Ds}

		SPOILER DEPTH (m)		
		0.00	*0.05*	*0.10*
ΔY_s	*0.0*	0.000	0.036	-0.050
	0.1	-0.012	0.008	-0.012
	0.2	0.003	-0.036	0.024

		SPOILER DEPTH (m)		
		0.00	*0.05*	*0.10*
ΔY_s	0.0	0.015	0.000	-0.053
	0.1	0.014	-0.025	-0.008
	0.2	0.029	-0.018	0.025

Wheel Drag Coefficient, C_{Dw}

		SPOILER DEPTH (m)		
		0.00	*0.05*	*0.10*
ΔY_s	*0.0*	0.000	-0.020	-0.043
	0.1	0.013	-0.014	-0.027
	0.2	0.036	0.000	-0.016

		SPOILER DEPTH (m)		
		0.00	*0.05*	*0.10*
ΔY_s	0.0	-0.027	-0.038	-0.059
	0.1	-0.010	-0.040	-0.043
	0.2	0.003	-0.025	-0.025

Total Drag Coefficient, C_{Dt}

		SPOILER DEPTH (m)		
		0.00	*0.05*	*0.10*
ΔY_s	*0.0*	0.000	0.016	-0.093
	0.1	0.001	-0.006	-0.039
	0.2	0.039	-0.036	0.008

		SPOILER DEPTH (m)		
		0.00	*0.05*	*0.10*
ΔY_s	0.0	-0.012	-0.038	-0.112
	0.1	0.004	-0.064	-0.051
	0.2	0.032	-0.043	0.000

Table D.2: Relative Experimental Wheel and Shroud Force Coefficients: First MIRA Session

D.2 Second MIRA Session

Shroud Lift Coefficient, C_{Ls}

		SPOILER DEPTH (m)				
		0.000	*0.025*	*0.050*	*0.075*	*0.100*
ΔY_s	*0.00*	0.069	0.083	0.078	0.046	0.009
	0.05	0.069	0.095	0.072	0.056	0.020
	0.10	0.069	0.102	0.061	0.062	0.030
	0.15	0.074	0.114	0.053	0.068	0.036
	0.20	0.076	0.119	0.054	0.060	0.051

Shroud Drag Coefficient, C_{Ds}

		SPOILER DEPTH (m)				
		0.000	*0.025*	*0.050*	*0.075*	*0.100*
ΔY_s	*0.00*	0.267	0.303	0.301	0.267	0.220
	0.05	0.265	0.329	0.286	0.281	0.241
	0.10	0.263	0.340	0.263	0.293	0.263
	0.15	0.270	0.351	0.245	0.295	0.276
	0.20	0.284	0.361	0.246	0.274	0.288

Wheel Drag Coefficient, C_{Dw}

		SPOILER DEPTH (m)				
		0.000	*0.025*	*0.050*	*0.075*	*0.100*
ΔY_s	*0.00*	0.152	0.142	0.134	0.093	0.105
	0.05	0.162	0.146	0.139	0.099	0.110
	0.10	0.172	0.152	0.140	0.109	0.116
	0.15	0.180	0.158	0.141	0.117	0.127
	0.20	0.185	0.167	0.146	0.120	0.133

Total Drag Coefficient, C_{Dt}

		SPOILER DEPTH (m)				
		0.000	*0.025*	*0.050*	*0.075*	*0.100*
ΔY_s	*0.00*	0.419	0.444	0.435	0.360	0.325
	0.05	0.427	0.475	0.425	0.380	0.351
	0.10	0.435	0.493	0.403	0.402	0.379
	0.15	0.450	0.509	0.386	0.412	0.403
	0.20	0.469	0.528	0.392	0.394	0.421

Table D.3: Absolute Experimental Wheel and Shroud Force Coefficients: Second MIRA Session, Moving Groundplane

Shroud Lift Coefficient, C_{Ls}

		SPOILER DEPTH (m)				
		0.000	*0.025*	*0.050*	*0.075*	*0.100*
ΔY_s	*0.00*	0.095	0.124	0.065	0.076	0.034
	0.05	0.093	0.128	0.060	0.079	0.042
	0.10	0.090	0.136	0.061	0.080	0.047
	0.15	0.094	0.142	0.063	0.076	0.047
	0.20	0.094	0.142	0.069	0.069	0.058

Shroud Drag Coefficient, C_{Ds}

		SPOILER DEPTH (m)				
		0.000	*0.025*	*0.050*	*0.075*	*0.100*
ΔY_s	*0.00*	0.287	0.342	0.250	0.282	0.240
	0.05	0.286	0.349	0.246	0.289	0.252
	0.10	0.283	0.355	0.248	0.285	0.265
	0.15	0.292	0.364	0.250	0.272	0.265
	0.20	0.302	0.377	0.260	0.263	0.281

Wheel Drag Coefficient, C_{Dw}

		SPOILER DEPTH (m)				
		0.000	*0.025*	*0.050*	*0.075*	*0.100*
ΔY_s	*0.00*	0.127	0.110	0.106	0.106	0.087
	0.05	0.135	0.117	0.109	0.113	0.095
	0.10	0.143	0.126	0.114	0.116	0.104
	0.15	0.150	0.136	0.120	0.116	0.104
	0.20	0.153	0.142	0.128	0.117	0.120

Total Drag Coefficient, C_{Dt}

		SPOILER DEPTH (m)				
		0.000	*0.025*	*0.050*	*0.075*	*0.100*
ΔY_s	*0.00*	0.414	0.452	0.356	0.388	0.327
	0.05	0.421	0.465	0.354	0.401	0.347
	0.10	0.426	0.481	0.362	0.402	0.368
	0.15	0.442	0.500	0.371	0.388	0.368
	0.20	0.455	0.519	0.388	0.381	0.400

Table D.4: Absolute Experimental Wheel and Shroud Force Coefficients: Second MIRA Session, Stationary Groundplane

Shroud Lift Coefficient, C_{Ls}

		SPOILER DEPTH (m)				
		0.000	*0.025*	*0.050*	*0.075*	*0.100*
ΔY_s	*0.00*	0.000	0.014	0.009	-0.023	-0.060
	0.05	0.000	0.026	0.003	-0.013	-0.049
	0.10	0.000	0.033	-0.008	-0.007	-0.038
	0.15	0.005	0.046	-0.016	-0.001	-0.033
	0.20	0.007	0.050	-0.015	-0.009	-0.018

Shroud Drag Coefficient, C_{Ds}

		SPOILER DEPTH (m)				
		0.000	*0.025*	*0.050*	*0.075*	*0.100*
ΔY_s	*0.00*	0.000	0.036	0.034	0.000	-0.047
	0.05	-0.002	0.062	0.019	0.014	-0.026
	0.10	-0.004	0.073	-0.004	0.026	-0.004
	0.15	0.003	0.084	-0.022	0.027	0.009
	0.20	0.017	0.094	-0.021	0.007	0.021

Wheel Drag Coefficient, C_{Dw}

		SPOILER DEPTH (m)				
		0.000	*0.025*	*0.050*	*0.075*	*0.100*
ΔY_s	*0.00*	0.000	-0.010	-0.018	-0.059	-0.047
	0.05	0.010	-0.006	-0.013	-0.053	-0.042
	0.10	0.020	0.000	-0.012	-0.043	-0.036
	0.15	0.028	0.006	-0.011	-0.035	-0.025
	0.20	0.033	0.015	-0.006	-0.032	-0.019

Total Drag Coefficient, C_{Dt}

		SPOILER DEPTH (m)				
		0.000	*0.025*	*0.050*	*0.075*	*0.100*
ΔY_s	*0.00*	0.000	0.025	0.016	-0.059	-0.094
	0.05	0.008	0.056	0.006	-0.039	-0.068
	0.10	0.016	0.074	-0.015	-0.017	-0.040
	0.15	0.031	0.091	-0.033	-0.007	-0.016
	0.20	0.050	0.109	-0.027	-0.025	0.002

Table D.5: Relative Experimental Wheel and Shroud Force Coefficients: Second MIRA Session, Moving Groundplane

Shroud Lift Coefficient, C_{Ls}

		SPOILER DEPTH (m)				
		0.000	*0.025*	*0.050*	*0.075*	*0.100*
ΔY_s	*0.00*	0.026	0.056	-0.004	0.007	-0.035
	0.05	0.024	0.059	-0.009	0.010	-0.027
	0.10	0.021	0.067	-0.008	0.011	-0.021
	0.15	0.025	0.073	-0.006	0.007	-0.021
	0.20	0.026	0.073	0.000	0.000	-0.011

Shroud Drag Coefficient, C_{Ds}

		SPOILER DEPTH (m)				
		0.000	*0.025*	*0.050*	*0.075*	*0.100*
ΔY_s	*0.00*	0.020	0.075	-0.017	0.015	-0.027
	0.05	0.019	0.082	-0.021	0.022	-0.015
	0.10	0.016	0.088	-0.019	0.018	-0.002
	0.15	0.025	0.097	-0.017	0.005	-0.002
	0.20	0.035	0.110	-0.007	-0.004	0.014

Wheel Drag Coefficient, C_{Dw}

		SPOILER DEPTH (m)				
		0.000	*0.025*	*0.050*	*0.075*	*0.100*
ΔY_s	*0.00*	-0.025	-0.042	-0.046	-0.046	-0.065
	0.05	-0.017	-0.035	-0.043	-0.039	-0.057
	0.10	-0.009	-0.026	-0.038	-0.036	-0.048
	0.15	-0.002	-0.016	-0.032	-0.036	-0.048
	0.20	0.001	-0.010	-0.024	-0.034	-0.032

Total Drag Coefficient, C_{Dt}

		SPOILER DEPTH (m)				
		0.000	*0.025*	*0.050*	*0.075*	*0.100*
ΔY_s	*0.00*	-0.005	0.033	-0.063	-0.031	-0.092
	0.05	0.002	0.047	-0.065	-0.017	-0.072
	0.10	0.007	0.062	-0.057	-0.017	-0.050
	0.15	0.023	0.081	-0.048	-0.031	-0.050
	0.20	0.036	0.100	-0.031	-0.038	-0.019

Table D.6: Relative Experimental Wheel and Shroud Force Coefficients: Second MIRA Session, Stationary Groundplane

Appendix E

Experimental Wheelhouse Pressure Distributions

In this appendix experimental surface static pressure coefficient distributions on the five planar internal wheelhouse cavity faces from the first MIRA Model Wind Tunnel session, Chapter 7, are presented, in both tabular form and as contour plots. All the pressure coefficients are referenced to the freestream velocity of 25m/s.

The contour plots were produced using the data plotting package Gsharp which is distributed by AVS/UNIRAS. As just six data points were recorded on the wheelarch face, contours are only presented for the four other faces. The mapping of the faces to the plot areas is shown in *Fig.E.1.* The contours are only generated within the area of the face for which pressures were measured, i.e. the data has not been extrapolated to the boundary edges of the faces. Accuracy is also limited due to the coarse distributions of data points, particularly on the rear face.

The discontinuity in the colourmap was intentionally incorporated to help distinguish between areas of positive and negative pressure coefficient.

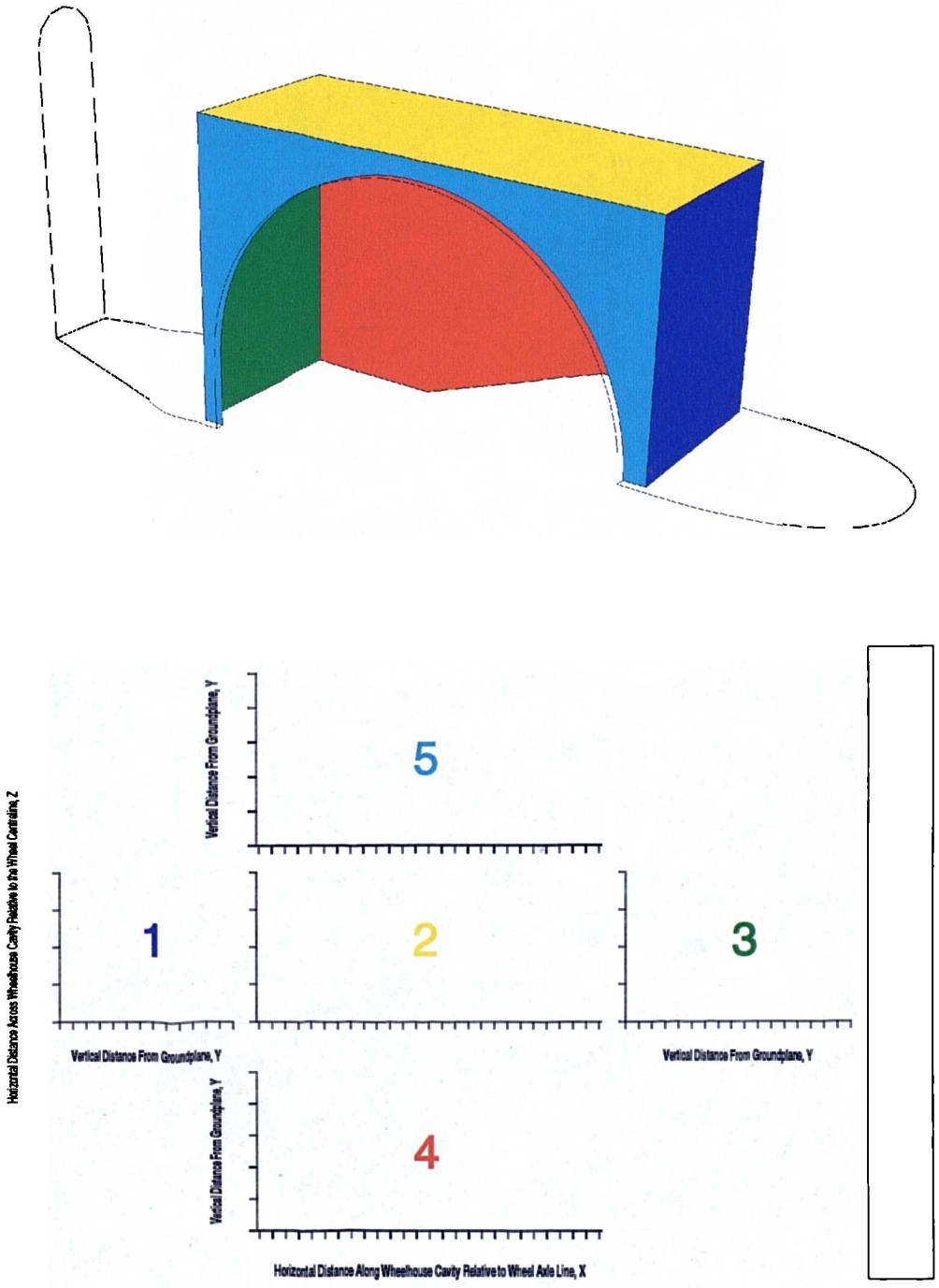

Figure E.1: The Mapping of the Five Internal Faces of the Wheelhouse Cavity on the Pressure Distribution Contour Plots

E.1 0.000m Front Spoiler

E.1.1 Front Ride Height, $Y_f = 1.0$, Rear Ride Height, $Y_r = 0.6$, Moving Groundplane

Front Face, $X = -1.320$

Y/Z	*0.000*	*0.867*	*1.733*
2.20	-0.047	-0.047	-0.034
2.00	-0.098	-0.066	-0.064
1.80	-0.103	-0.083	-0.071
1.60	-0.085	-0.063	-0.061
1.40	-0.069	-0.058	-0.057
1.20	-0.053	-0.056	-0.058

Top Face, $Y = 2.300$

X/Z	*0.000*	*0.867*	*1.733*
-1.02	-0.078	-0.099	-0.056
-0.82	-0.042	-0.071	-0.084
-0.62	0.122	-0.007	-0.040
-0.42	0.105	0.003	-0.025
-0.22	-0.006	-0.044	-0.018
-0.02	0.038	-0.015	-0.010
0.18	0.046	0.017	-0.009
0.38	0.035	-0.012	-0.026
0.58	-0.011	-0.044	-0.035
0.78	-0.021	-0.072	0.003
0.98	0.020	0.011	0.075
1.18	0.116	0.143	0.104

Rear Face, $X = 1.320$

Y/Z	*0.000*	*0.867*	*1.733*
2.04	0.086	0.038	0.053
1.84	0.051	-0.082	-0.019
1.64	0.018	-0.013	-0.002
1.44	0.067	0.076	0.105
1.24	0.104	0.104	0.158

Arch, $Z = -0.833$

Y/X	*-1.02*	*-0.82*	*0.82*	*1.02*
2.00	-0.121	-0.103	-0.126	-0.002
1.80	-0.108			-0.012

Side Panel, $Z = 2.500$

Y/X	*-1.02*	*-0.82*	*-0.62*	*-0.42*	*-0.22*	*-0.02*	*0.18*	*0.38*	*0.58*	*0.78*	*0.98*
2.00	-0.085	-0.095	-0.044	-0.033	-0.010	-0.003	-0.019	-0.055	-0.058	-0.062	-0.022
1.80	-0.099	-0.108	-0.078	-0.044	-0.010	-0.006	-0.031	-0.054	-0.060	-0.056	-0.049
1.60	-0.100	-0.121	-0.117	-0.081	-0.035	-0.019	-0.044	-0.049	-0.039	-0.050	-0.042
1.40	-0.090	-0.113	-0.104	-0.076	-0.024	-0.017	-0.034	-0.028	-0.040	-0.018	0.002
1.20	-0.095	-0.111	-0.115	-0.087	-0.053	-0.038	-0.025	-0.026	-0.010	0.017	0.075
1.00				-0.069	-0.042		-0.020	-0.028	0.005	0.057	0.132
0.80							-0.111	-0.070	-0.117	-0.009	0.299

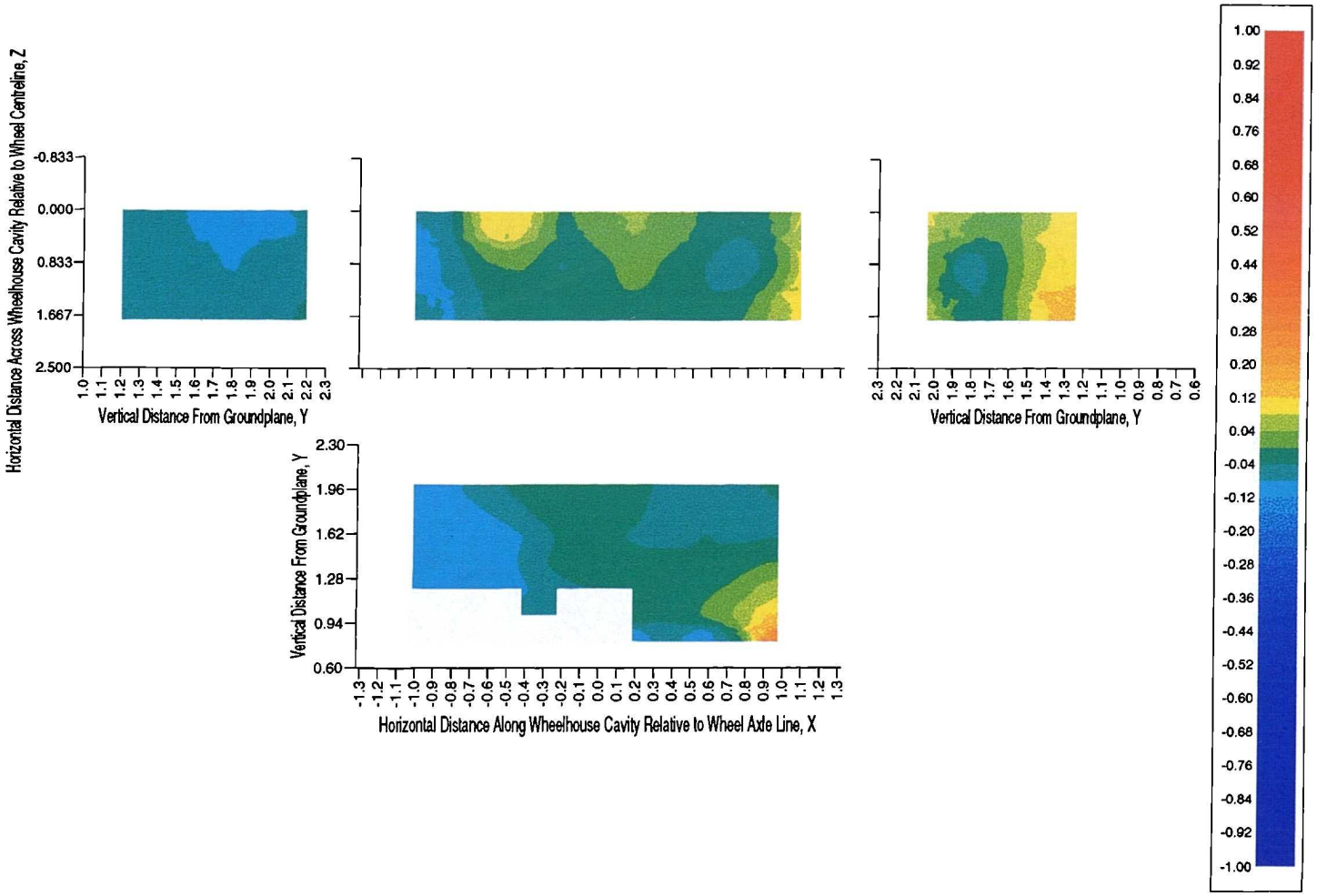

Figure E.2: Experimental Wheelhouse Cavity Pressure Coefficient Distribution - No Front Spoiler, Front Ride Height, $Y_f = 1.0$, Rear Ride Height, $Y_r = 0.6$, Moving Groundplane

E.1.2 Front Ride Height, $Y_f = 1.0$, Rear Ride Height, $Y_r = 0.6$, Stationary Groundplane

Front Face, $X = -1.320$

Y/Z	*0.000*	*0.867*	*1.733*
2.20	-0.086	-0.090	-0.059
2.00	-0.087	-0.083	-0.064
1.80	-0.084	-0.092	-0.063
1.60	-0.069	-0.067	-0.060
1.40	-0.061	-0.064	-0.057
1.20	-0.052	-0.061	-0.049

Top Face, $Y = 2.300$

X/Z	*0.000*	*0.867*	*1.733*
-1.02	-0.090	-0.106	-0.084
-0.82	-0.101	-0.106	-0.102
-0.62	-0.006	-0.065	-0.056
-0.42	0.098	0.041	-0.016
-0.22	0.058	0.000	-0.009
-0.02	0.041	0.004	0.011
0.18	0.043	0.031	0.025
0.38	0.076	0.068	0.038
0.58	0.104	0.066	0.036
0.78	0.077	0.012	0.031
0.98	0.071	0.053	0.094
1.18	0.131	0.143	0.115

Rear Face, $X = 1.320$

Y/Z	*0.000*	*0.867*	*1.733*
2.04	0.111	0.061	0.084
1.84	0.073	-0.017	0.034
1.64	0.061	0.052	0.059
1.44	0.106	0.131	0.150
1.24	0.134	0.154	0.178

Arch, $Z = -0.833$

Y/X	*-1.02*	*-0.82*	*0.82*	*1.02*
2.00	-0.098	-0.117	-0.056	0.052
1.80	-0.089			0.029

Side Panel, $Z = 2.500$

Y/X	*-1.02*	*-0.82*	*-0.62*	*-0.42*	*-0.22*	*-0.02*	*0.18*	*0.38*	*0.58*	*0.78*	*0.98*
2.00	-0.091	-0.103	-0.071	-0.065	-0.019	0.006	0.040	0.045	-0.009	-0.035	0.013
1.80	-0.095	-0.104	-0.102	-0.092	-0.041	-0.009	0.021	0.033	0.018	0.013	0.030
1.60	-0.093	-0.115	-0.119	-0.094	-0.053	-0.007	0.019	0.028	0.040	0.031	0.042
1.40	-0.089	-0.127	-0.120	-0.110	-0.044	0.005	0.025	0.036	0.028	0.057	0.069
1.20	-0.098	-0.129	-0.131	-0.109	-0.059	-0.025	0.007	0.022	0.050	0.074	0.121
1.00				-0.083	-0.038		0.002	0.016	0.049	0.098	0.163
0.80							-0.090	-0.042	-0.085	0.024	0.297

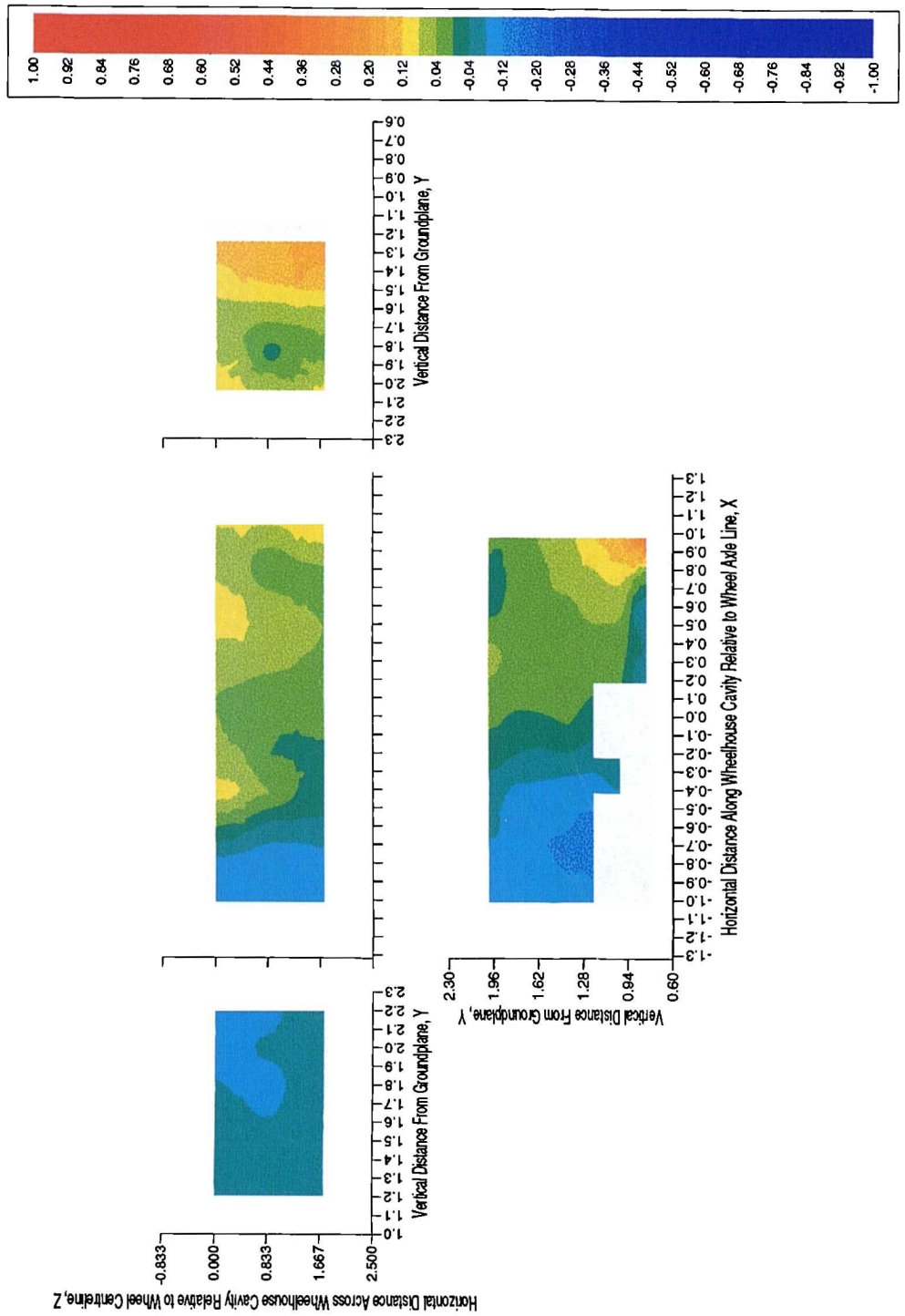

Figure E.3: Experimental Wheelhouse Cavity Pressure Coefficient Distribution - No Front Spoiler, Front Ride Height, $Y_f = 1.0$, Rear Ride Height, $Y_r = 0.6$, Stationary Groundplane

E.1.3 Front Ride Height, $Y_f = 1.1$, Rear Ride Height, $Y_r = 0.7$, Moving Groundplane

Front Face, $X = -1.320$

Y/Z	*0.000*	*0.867*	*1.733*
2.30	-0.050	-0.041	-0.034
2.10	-0.096	-0.068	-0.067
1.90	-0.106	-0.095	-0.082
1.70	-0.084	-0.072	-0.075
1.50	-0.074	-0.069	-0.075
1.30	-0.056	-0.063	-0.076

Top Face, $Y = 2.400$

X/Z	*0.000*	*0.867*	*1.733*
-1.02	-0.093	-0.109	-0.056
-0.82	-0.094	-0.088	-0.100
-0.62	0.049	-0.011	-0.045
-0.42	0.126	0.019	-0.034
-0.22	-0.039	-0.072	-0.050
-0.02	-0.038	-0.051	-0.038
0.18	0.027	0.011	-0.025
0.38	0.049	-0.008	-0.043
0.58	0.015	-0.049	-0.059
0.78	-0.017	-0.098	-0.031
0.98	0.014	-0.006	0.054
1.18	0.119	0.138	0.081

Rear Face, $X = 1.320$

Y/Z	*0.000*	*0.867*	*1.733*
2.14	0.088	0.020	0.039
1.94	0.042	-0.104	-0.028
1.74	0.008	-0.032	0.001
1.54	0.068	0.083	0.155
1.34	0.101	0.179	0.268

Arch, $Z = -0.833$

Y/X	*-1.02*	*-0.82*	*0.82*	*1.02*
2.10	-0.139	-0.126	-0.134	-0.010
1.90	-0.123			-0.024

Side Panel, $Z = 2.500$

Y/X	*-1.02*	*-0.82*	*-0.62*	*-0.42*	*-0.22*	*-0.02*	*0.18*	*0.38*	*0.58*	*0.78*	*0.98*
2.10	-0.096	-0.108	-0.062	-0.053	-0.041	-0.031	-0.026	-0.063	-0.087	-0.081	-0.033
1.90	-0.111	-0.125	-0.101	-0.055	-0.023	-0.016	-0.027	-0.052	-0.067	-0.058	-0.049
1.70	-0.114	-0.137	-0.132	-0.094	-0.041	-0.022	-0.042	-0.047	-0.047	-0.054	-0.049
1.50	-0.109	-0.130	-0.124	-0.088	-0.034	-0.025	-0.038	-0.034	-0.045	-0.028	0.001
1.30	-0.111	-0.122	-0.133	-0.102	-0.060	-0.026	-0.034	-0.036	-0.017	0.021	0.106
1.10				-0.083	-0.062		-0.090	-0.047	0.016	0.092	0.171
0.90							-0.202	-0.063	-0.090	0.050	0.219

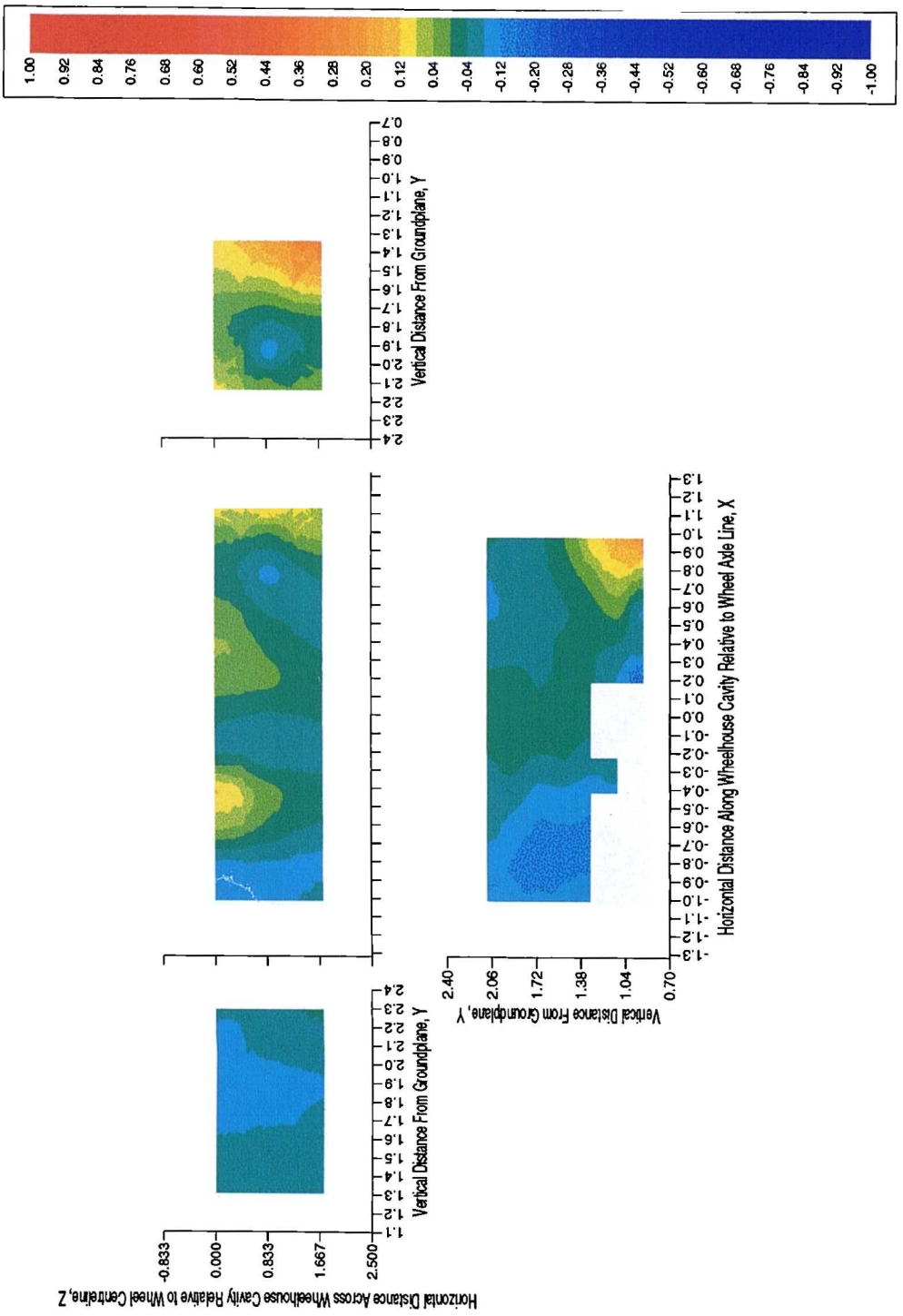

Figure E.4: Experimental Wheelhouse Cavity Pressure Coefficient Distribution - No Front Spoiler, Front Ride Height, $Y_f = 1.1$, Rear Ride Height, $Y_r = 0.7$, Moving Groundplane

E.1.4 Front Ride Height, $Y_f = 1.1$, Rear Ride Height, $Y_r = 0.7$, Stationary Groundplane

Front Face, $X = -1.320$

Y/Z	*0.000*	*0.867*	*1.733*
2.30	-0.096	-0.103	-0.067
2.10	-0.096	-0.093	-0.069
1.90	-0.095	-0.105	-0.073
1.70	-0.082	-0.085	-0.075
1.50	-0.076	-0.083	-0.075
1.30	-0.069	-0.079	-0.069

Top Face, $Y = 2.400$

X/Z	*0.000*	*0.867*	*1.733*
-1.02	-0.102	-0.120	-0.094
-0.82	-0.129	-0.125	-0.131
-0.62	-0.112	-0.118	-0.090
-0.42	0.016	0.013	-0.041
-0.22	0.071	0.033	-0.005
-0.02	0.071	0.019	0.013
0.18	0.071	0.043	0.027
0.38	0.102	0.073	0.031
0.58	0.118	0.069	0.033
0.78	0.095	0.004	0.020
0.98	0.085	0.052	0.093
1.18	0.156	0.171	0.123

Rear Face, $X = 1.320$

Y/Z	*0.000*	*0.867*	*1.733*
2.14	0.132	0.073	0.087
1.94	0.087	-0.041	0.030
1.74	0.061	0.032	0.069
1.54	0.125	0.169	0.219
1.34	0.157	0.264	0.343

Arch, $Z = -0.833$

Y/X	*-1.02*	*-0.82*	*0.82*	*1.02*
2.10	-0.102	-0.133	-0.043	0.057
1.90	-0.099			0.024

Side Panel, $Z = 2.500$

Y/X	*-1.02*	*-0.82*	*-0.62*	*-0.42*	*-0.22*	*-0.02*	*0.18*	*0.38*	*0.58*	*0.78*	*0.98*
2.10	-0.102	-0.125	-0.095	-0.090	-0.028	0.014	0.050	0.044	-0.017	-0.052	-0.004
1.90	-0.105	-0.120	-0.128	-0.115	-0.055	-0.009	0.035	0.043	0.016	0.013	0.028
1.70	-0.108	-0.132	-0.139	-0.115	-0.066	-0.015	0.020	0.039	0.043	0.032	0.041
1.50	-0.111	-0.142	-0.141	-0.118	-0.050	-0.016	0.016	0.042	0.034	0.044	0.067
1.30	-0.117	-0.142	-0.144	-0.121	-0.059	-0.010	0.011	0.020	0.057	0.078	0.146
1.10				-0.101	-0.066		-0.063	-0.009	0.052	0.118	0.173
0.90							-0.169	-0.030	-0.052	0.070	0.217

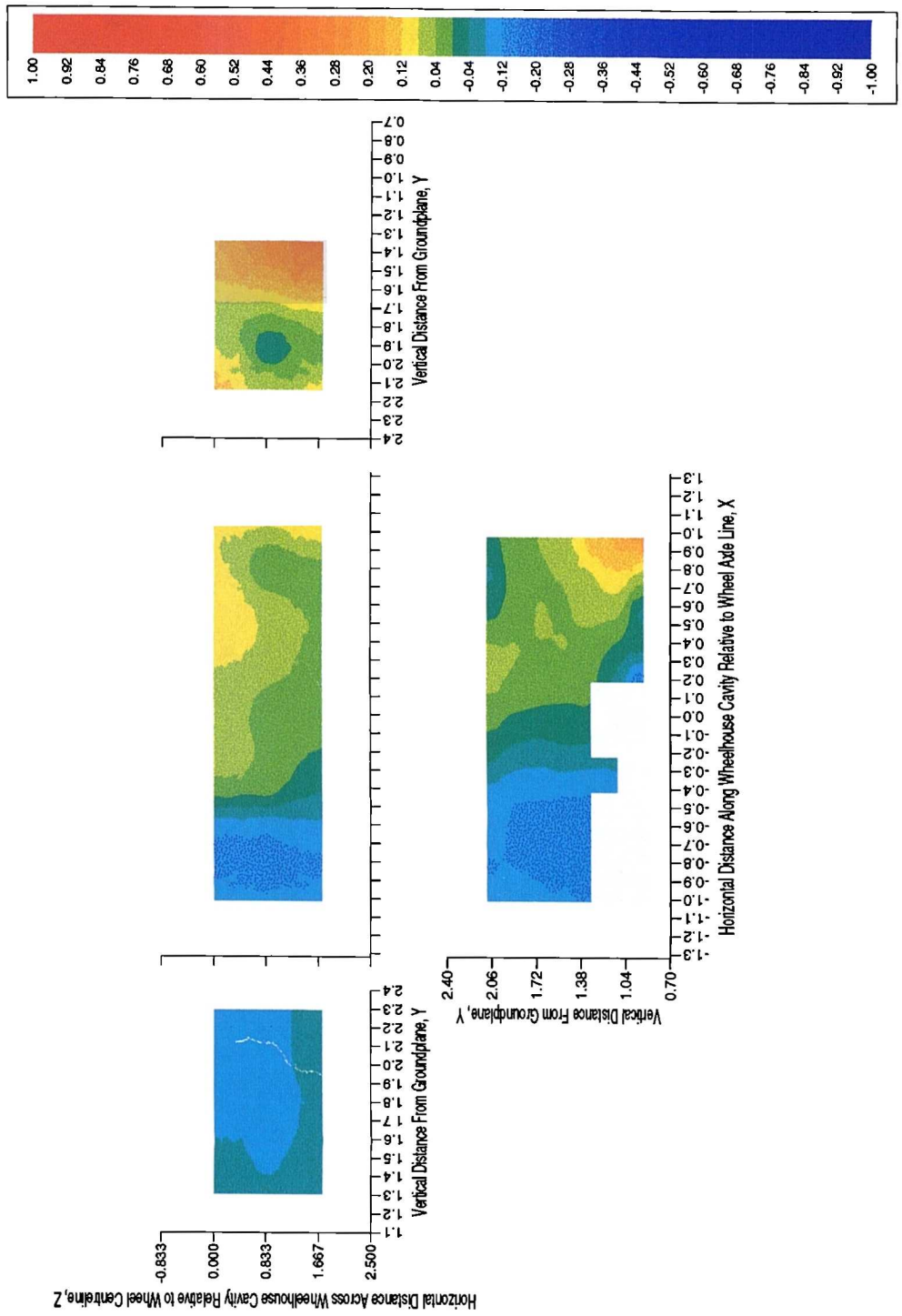

Figure E.5: Experimental Wheelhouse Cavity Pressure Coefficient Distribution - No Front Spoiler, Front Ride Height, $Y_f = 1.1$, Rear Ride Height, $Y_r = 0.7$, Stationary Groundplane

E.1.5 Front Ride Height, $Y_f = 1.2$, Rear Ride Height, $Y_r = 0.8$, Moving Groundplane

Front Face, $X = -1.320$

Y/Z	*0.000*	*0.867*	*1.733*
2.40	-0.054	-0.039	-0.024
2.20	-0.095	-0.068	-0.055
2.00	-0.100	-0.096	-0.075
1.90	-0.083	-0.079	-0.081
1.60	-0.062	-0.072	-0.088
1.40	-0.052	-0.065	-0.084

Top Face, $Y = 2.500$

X/Z	*0.000*	*0.867*	*1.733*
-1.02	-0.106	-0.105	-0.069
-0.82	-0.127	-0.107	-0.102
-0.62	0.001	-0.034	-0.049
-0.42	0.132	0.044	-0.025
-0.22	0.040	-0.046	-0.040
-0.02	-0.025	-0.053	-0.037
0.18	0.028	0.023	-0.009
0.38	0.074	0.022	-0.027
0.58	0.039	-0.022	-0.047
0.78	0.013	-0.077	-0.014
0.98	0.041	0.004	0.087
1.18	0.139	0.155	0.127

Rear Face, $X = 1.320$

Y/Z	*0.000*	*0.867*	*1.733*
2.24	0.107	0.035	0.056
2.04	0.060	-0.111	-0.025
1.84	0.020	-0.026	-0.005
1.64	0.079	0.088	0.146
1.44	0.127	0.207	0.340

Arch, $Z = -0.833$

Y/X	*-1.02*	*-0.82*	*0.82*	*1.02*
2.20	-0.142	-0.140	-0.068	0.016
2.00	-0.124			-0.020

Side Panel, $Z = 2.500$

Y/X	*-1.02*	*-0.82*	*-0.62*	*-0.42*	*-0.22*	*-0.02*	*0.18*	*0.38*	*0.58*	*0.78*	*0.98*
2.20	-0.098	-0.118	-0.080	-0.056	-0.053	-0.041	-0.027	-0.073	-0.107	-0.092	-0.026
2.00	-0.114	-0.127	-0.120	-0.063	-0.024	-0.017	-0.017	-0.046	-0.075	-0.058	-0.044
1.80	-0.117	-0.142	-0.147	-0.088	-0.031	-0.002	-0.017	-0.035	-0.034	-0.047	-0.034
1.60	-0.114	-0.138	-0.134	-0.090	-0.026	-0.003	-0.019	-0.023	-0.039	-0.011	0.005
1.40	-0.115	-0.138	-0.145	-0.114	-0.059	-0.010	-0.003	-0.011	0.003	0.023	0.094
1.20				-0.095	-0.091		-0.047	-0.028	0.022	0.090	0.189
1.00							-0.271	-0.069	-0.082	0.044	0.253

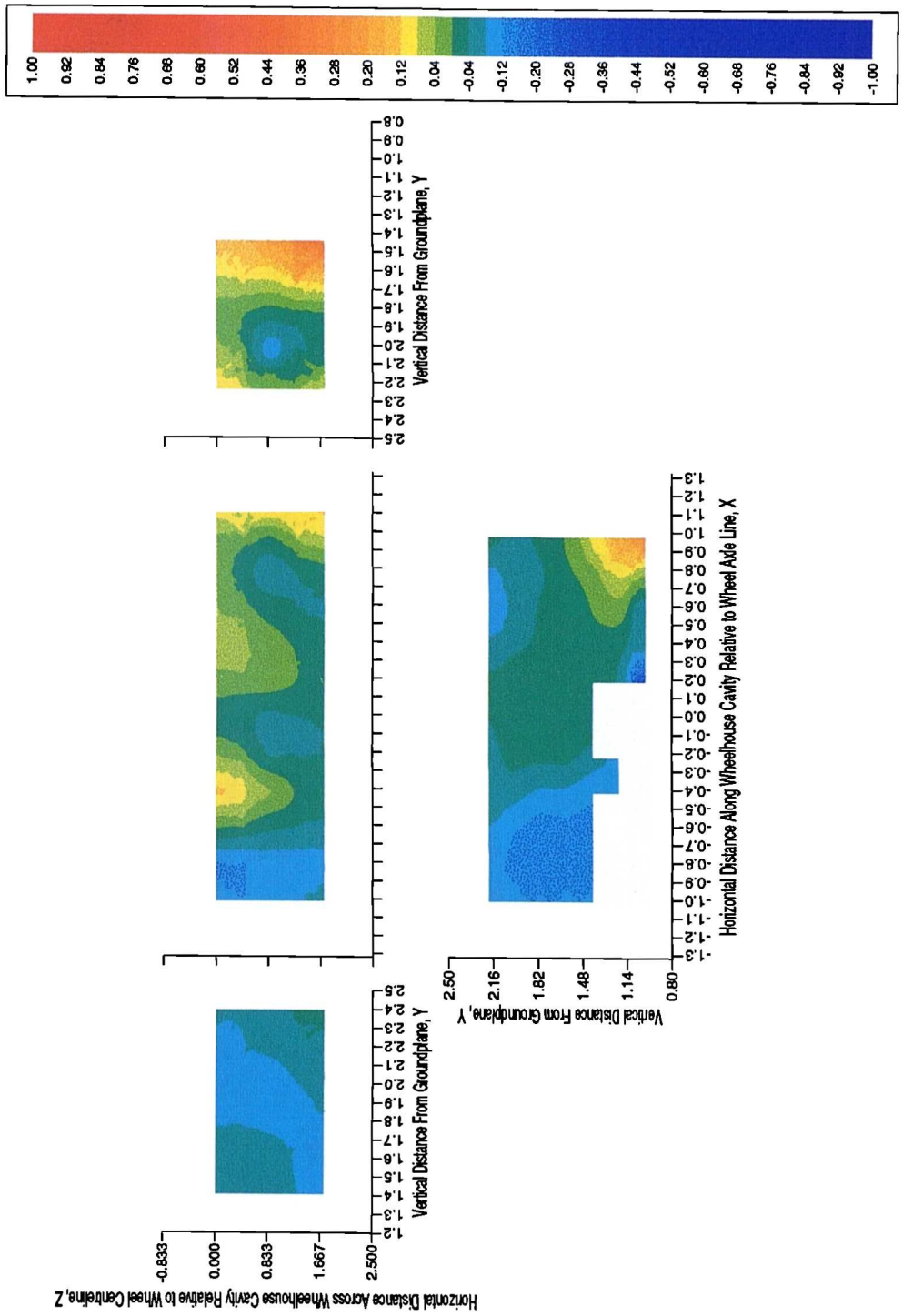

Figure E.6: Experimental Wheelhouse Cavity Pressure Coefficient Distribution - No Front Spoiler, Front Ride Height, $Y_f = 1.2$, Rear Ride Height, $Y_r = 0.8$, Moving Groundplane

E.1.6 Front Ride Height, $Y_f = 1.2$, Rear Ride Height, $Y_r = 0.8$, Stationary Groundplane

Front Face, $X = -1.320$

Y/Z	*0.000*	*0.867*	*1.733*
2.40	-0.088	-0.094	-0.060
2.20	-0.090	-0.086	-0.060
2.00	-0.090	-0.100	-0.067
1.80	-0.082	-0.085	-0.080
1.60	-0.072	-0.083	-0.080
1.40	-0.067	-0.083	-0.066

Top Face, $Y = 2.500$

X/Z	*0.000*	*0.867*	*1.733*
-1.02	-0.100	-0.113	-0.098
-0.82	-0.119	-0.125	-0.129
-0.62	-0.138	-0.138	-0.108
-0.42	-0.087	-0.067	-0.067
-0.22	0.021	0.037	-0.012
-0.02	0.090	0.051	0.025
0.18	0.101	0.065	0.041
0.38	0.122	0.076	0.034
0.58	0.130	0.069	0.029
0.78	0.111	0.016	0.048
0.98	0.110	0.071	0.130
1.18	0.183	0.199	0.165

Rear Face, $X = 1.320$

Y/Z	*0.000*	*0.867*	*1.733*
2.24	0.148	0.086	0.109
2.04	0.105	-0.047	0.033
1.84	0.064	0.021	0.057
1.64	0.121	0.158	0.217
1.44	0.172	0.277	0.404

Arch, $Z = -0.833$

Y/X	*-1.02*	*-0.82*	*0.82*	*1.02*
2.20	-0.090	-0.131	-0.014	0.073
2.00	-0.096			0.037

Side Panel, $Z = 2.500$

Y/X	*-1.02*	*-0.82*	*-0.62*	*-0.42*	*-0.22*	*-0.02*	*0.18*	*0.38*	*0.58*	*0.78*	*0.98*
2.20	-0.101	-0.126	-0.106	-0.111	-0.043	0.011	0.045	0.037	-0.008	-0.016	0.035
2.00	-0.106	-0.120	-0.136	-0.127	-0.068	-0.015	0.035	0.051	0.024	0.023	0.030
1.80	-0.107	-0.133	-0.141	-0.127	-0.077	-0.020	0.023	0.046	0.056	0.044	0.048
1.60	-0.108	-0.144	-0.142	-0.126	-0.064	-0.014	0.018	0.040	0.040	0.050	0.072
1.40	-0.117	-0.137	-0.150	-0.120	-0.065	-0.013	0.013	0.027	0.059	0.078	0.147
1.20				-0.096	-0.092		-0.035	0.000	0.058	0.126	0.207
1.00							-0.243	-0.042	-0.051	0.069	0.250

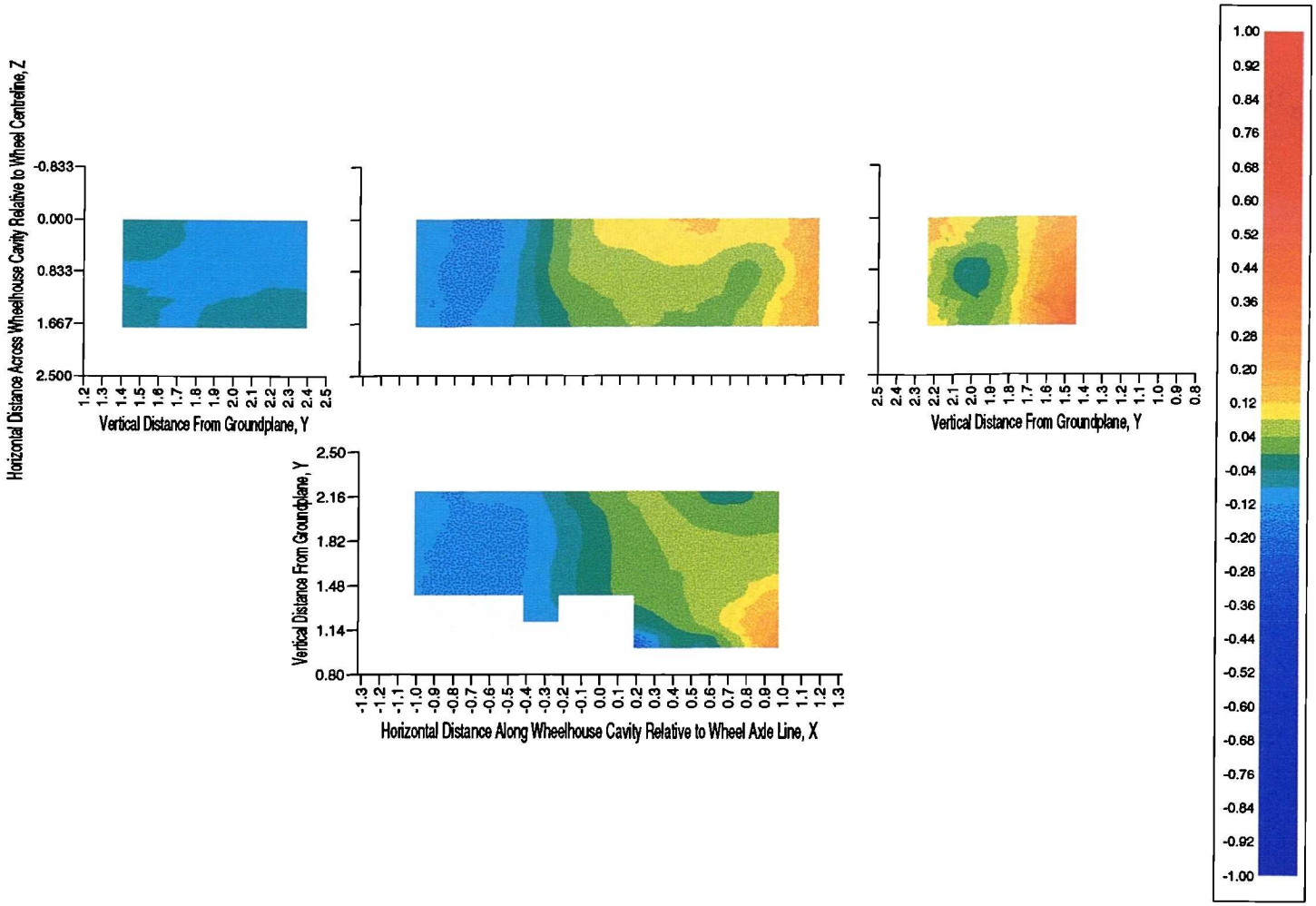

Figure E.7: Experimental Wheelhouse Cavity Pressure Coefficient Distribution - No Front Spoiler, Front Ride Height, $Y_f = 1.2$, Rear Ride Height, $Y_r = 0.8$, Stationary Groundplane

E.2 0.050m Front Spoiler

E.2.1 Front Ride Height, $Y_f = 1.0$, Rear Ride Height, $Y_r = 0.6$, Moving Groundplane

Front Face, $X = -1.320$

Y/Z	*0.000*	*0.867*	*1.733*
2.20	0.082	0.143	0.140
2.00	0.007	0.063	0.083
1.80	-0.021	0.013	0.032
1.60	-0.026	-0.046	-0.048
1.40	-0.128	-0.158	-0.162
1.20	-0.250	-0.217	-0.228

Top Face, $Y = 2.300$

X/Z	*0.000*	*0.867*	*1.733*
-1.02	0.069	0.102	0.097
-0.82	-0.018	0.007	0.018
-0.62	-0.012	-0.016	0.002
-0.42	0.013	0.016	0.002
-0.22	0.017	0.011	0.031
-0.02	0.036	0.046	0.042
0.18	0.039	0.053	0.064
0.38	0.048	0.055	0.069
0.58	0.054	0.061	0.075
0.78	0.067	0.066	0.090
0.98	0.081	0.083	0.093
1.18	0.116	0.116	0.113

Rear Face, $X = 1.320$

Y/Z	*0.000*	*0.867*	*1.733*
2.04	0.112	0.110	0.112
1.84	0.123	0.090	0.107
1.64	0.089	0.083	0.088
1.44	0.087	0.090	0.090
1.24	0.077	0.084	0.080

Arch, $Z = -0.833$

Y/X	*-1.02*	*-0.82*	*0.82*	*1.02*
2.00	-0.019	-0.056	-0.008	0.076
1.80	-0.070			0.063

Side Panel, $Z = 2.500$

Y/X	*-1.02*	*-0.82*	*-0.62*	*-0.42*	*-0.22*	*-0.02*	*0.18*	*0.38*	*0.58*	*0.78*	*0.98*
2.00	0.044	0.008	-0.001	-0.004	0.019	0.027	0.037	0.049	0.057	0.052	0.079
1.80	0.015	-0.024	-0.025	-0.015	0.014	0.029	0.036	0.043	0.048	0.060	0.076
1.60	-0.045	-0.064	-0.058	-0.050	-0.022	0.010	0.023	0.038	0.061	0.057	0.074
1.40	-0.145	-0.144	-0.118	-0.106	-0.060	-0.039	-0.026	0.009	0.023	0.042	0.063
1.20	-0.207	-0.163	-0.130	-0.134	-0.105	-0.060	-0.034	-0.019	0.014	0.026	0.050
1.00				-0.114	-0.110		-0.046	-0.030	-0.006	0.018	0.037
0.80							-0.079	-0.024	-0.027	-0.001	0.054

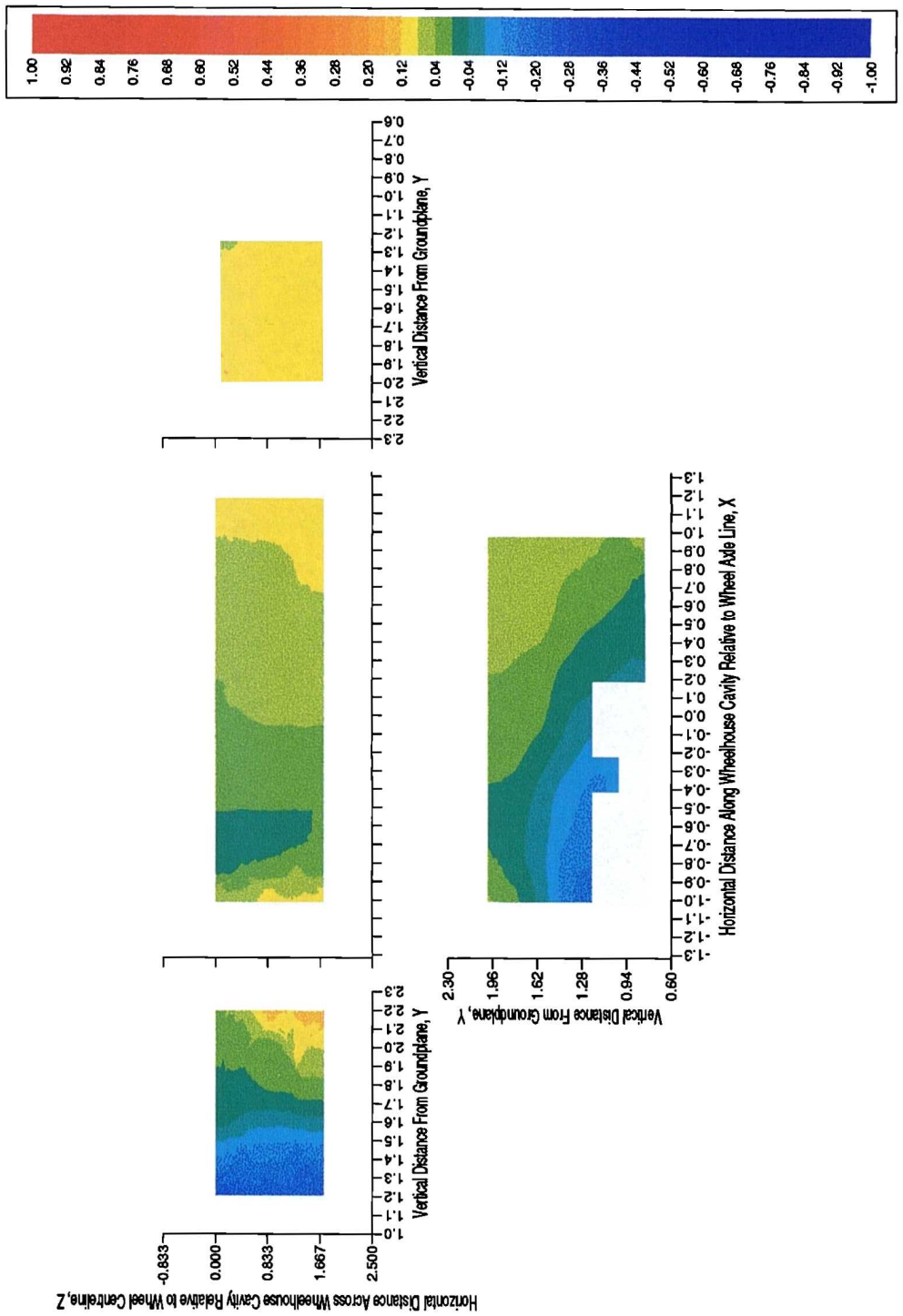

Figure E.8: Experimental Wheelhouse Cavity Pressure Coefficient Distribution - 0.050m Front Spoiler, Front Ride Height, $Y_f = 1.0$, Rear Ride Height, $Y_r = 0.6$, Moving Groundplane

E.2.2 Front Ride Height, $Y_f = 1.0$, Rear Ride Height, $Y_r = 0.6$, Stationary Groundplane

Front Face, $X = -1.320$

Y/Z	*0.000*	*0.867*	*1.733*
2.20	-0.016	0.001	0.047
2.00	-0.068	-0.050	-0.046
1.80	-0.106	-0.085	-0.085
1.60	-0.133	-0.128	-0.137
1.40	-0.187	-0.170	-0.174
1.20	-0.250	-0.223	-0.217

Top Face, $Y = 2.300$

X/Z	*0.000*	*0.867*	*1.733*
-1.02	-0.007	0.028	0.037
-0.82	-0.001	0.067	0.044
-0.62	-0.005	0.001	0.004
-0.42	-0.020	-0.015	-0.023
-0.22	-0.043	-0.054	-0.034
-0.02	-0.026	-0.022	-0.025
0.18	-0.023	-0.016	-0.011
0.38	-0.021	-0.019	-0.011
0.58	-0.013	-0.019	-0.005
0.78	-0.010	-0.018	0.007
0.98	-0.003	0.000	0.018
1.18	0.025	0.026	0.030

Rear Face, $X = 1.320$

Y/Z	*0.000*	*0.867*	*1.733*
2.04	0.018	0.011	0.022
1.84	0.021	-0.003	0.000
1.64	-0.003	-0.012	-0.012
1.44	0.000	0.005	0.008
1.24	-0.002	0.014	0.005

Arch, $Z = -0.833$

Y/X	*-1.02*	*-0.82*	*0.82*	*1.02*
2.00	-0.060	-0.069	-0.076	-0.017
1.80	-0.087			-0.024

Side Panel, $Z = 2.500$

Y/X	*-1.02*	*-0.82*	*-0.62*	*-0.42*	*-0.22*	*-0.02*	*0.18*	*0.38*	*0.58*	*0.78*	*0.98*
2.00	-0.029	-0.022	-0.028	-0.041	-0.035	-0.034	-0.025	-0.018	-0.013	-0.021	0.000
1.80	-0.090	-0.076	-0.084	-0.075	-0.049	-0.036	-0.030	-0.029	-0.022	-0.014	-0.005
1.60	-0.141	-0.130	-0.132	-0.116	-0.089	-0.065	-0.056	-0.038	-0.016	-0.022	-0.009
1.40	-0.173	-0.169	-0.136	-0.124	-0.087	-0.081	-0.076	-0.053	-0.046	-0.041	-0.033
1.20	-0.192	-0.163	-0.141	-0.133	-0.118	-0.091	-0.078	-0.078	-0.051	-0.052	-0.032
1.00				-0.136	-0.133		-0.089	-0.078	-0.069	-0.062	-0.036
0.80							-0.141	-0.089	-0.096	-0.062	0.029

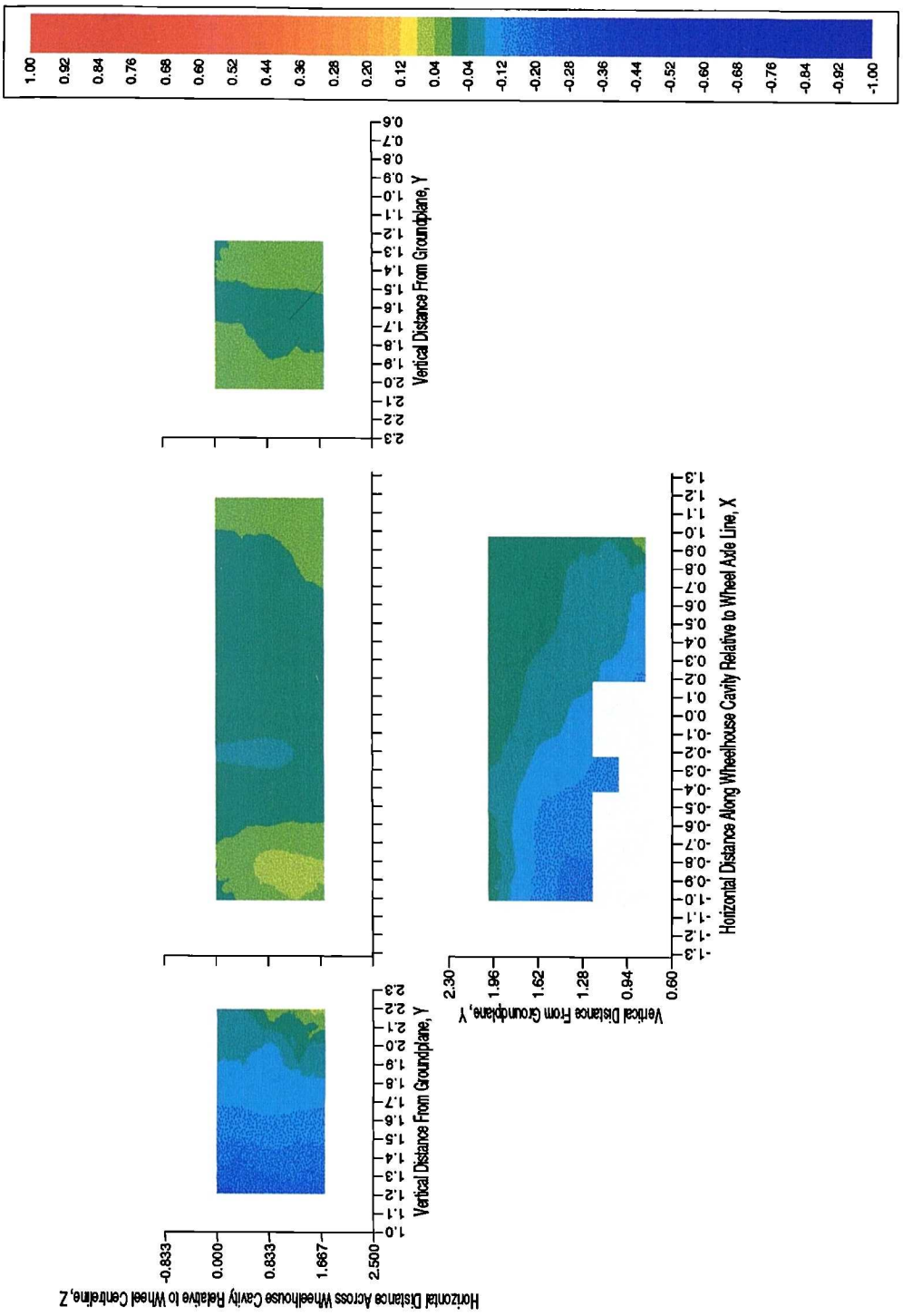

Figure E.9: Experimental Wheelhouse Cavity Pressure Coefficient Distribution - 0.050m Front Spoiler, Front Ride Height, $Y_f = 1.0$, Rear Ride Height, $Y_r = 0.6$, Stationary Groundplane

E.2.3 Front Ride Height, $Y_f = 1.1$, Rear Ride Height, $Y_r = 0.7$, Moving Groundplane

Front Face, $X = -1.320$

Y/Z	*0.000*	*0.867*	*1.733*
2.30	0.022	0.029	0.054
2.10	-0.041	-0.014	-0.016
1.90	-0.076	-0.081	-0.069
1.70	-0.153	-0.142	-0.140
1.50	-0.201	-0.186	-0.185
1.30	-0.239	-0.214	-0.225

Top Face, $Y = 2.400$

X/Z	*0.000*	*0.867*	*1.733*
-1.02	0.042	0.050	0.035
-0.82	0.014	0.032	0.011
-0.62	-0.025	-0.035	-0.022
-0.42	-0.038	-0.034	-0.046
-0.22	-0.027	-0.035	-0.025
-0.02	-0.004	-0.001	-0.015
0.18	-0.011	-0.007	-0.001
0.38	-0.012	-0.013	0.003
0.58	-0.010	-0.014	0.005
0.78	-0.007	-0.024	0.015
0.98	0.018	0.013	0.045
1.18	0.067	0.067	0.068

Rear Face, $X = 1.320$

Y/Z	*0.000*	*0.867*	*1.733*
2.14	0.065	0.041	0.056
1.94	0.064	0.024	0.046
1.74	0.040	0.050	0.055
1.54	0.038	0.047	0.064
1.34	0.017	0.034	0.024

Arch, $Z = -0.833$

Y/X	*-1.02*	*-0.82*	*0.82*	*1.02*
2.10	-0.014	-0.061	-0.068	0.027
1.90	-0.070			0.019

Side Panel, $Z = 2.500$

Y/X	*-1.02*	*-0.82*	*-0.62*	*-0.42*	*-0.22*	*-0.02*	*0.18*	*0.38*	*0.58*	*0.78*	*0.98*
2.10	0.017	-0.006	-0.017	-0.039	-0.027	-0.027	-0.023	-0.016	-0.015	-0.027	0.006
1.90	-0.034	-0.037	-0.054	-0.046	-0.022	-0.016	-0.019	-0.019	-0.022	-0.010	0.005
1.70	-0.103	-0.085	-0.087	-0.070	-0.048	-0.031	-0.033	-0.019	0.002	-0.006	0.011
1.50	-0.171	-0.159	-0.138	-0.123	-0.085	-0.075	-0.066	-0.036	-0.030	-0.006	0.011
1.30	-0.213	-0.193	-0.162	-0.146	-0.125	-0.105	-0.076	-0.063	-0.029	-0.016	0.007
1.10				-0.139	-0.129		-0.084	-0.075	-0.057	-0.044	-0.027
0.90							-0.119	-0.065	-0.076	-0.043	0.034

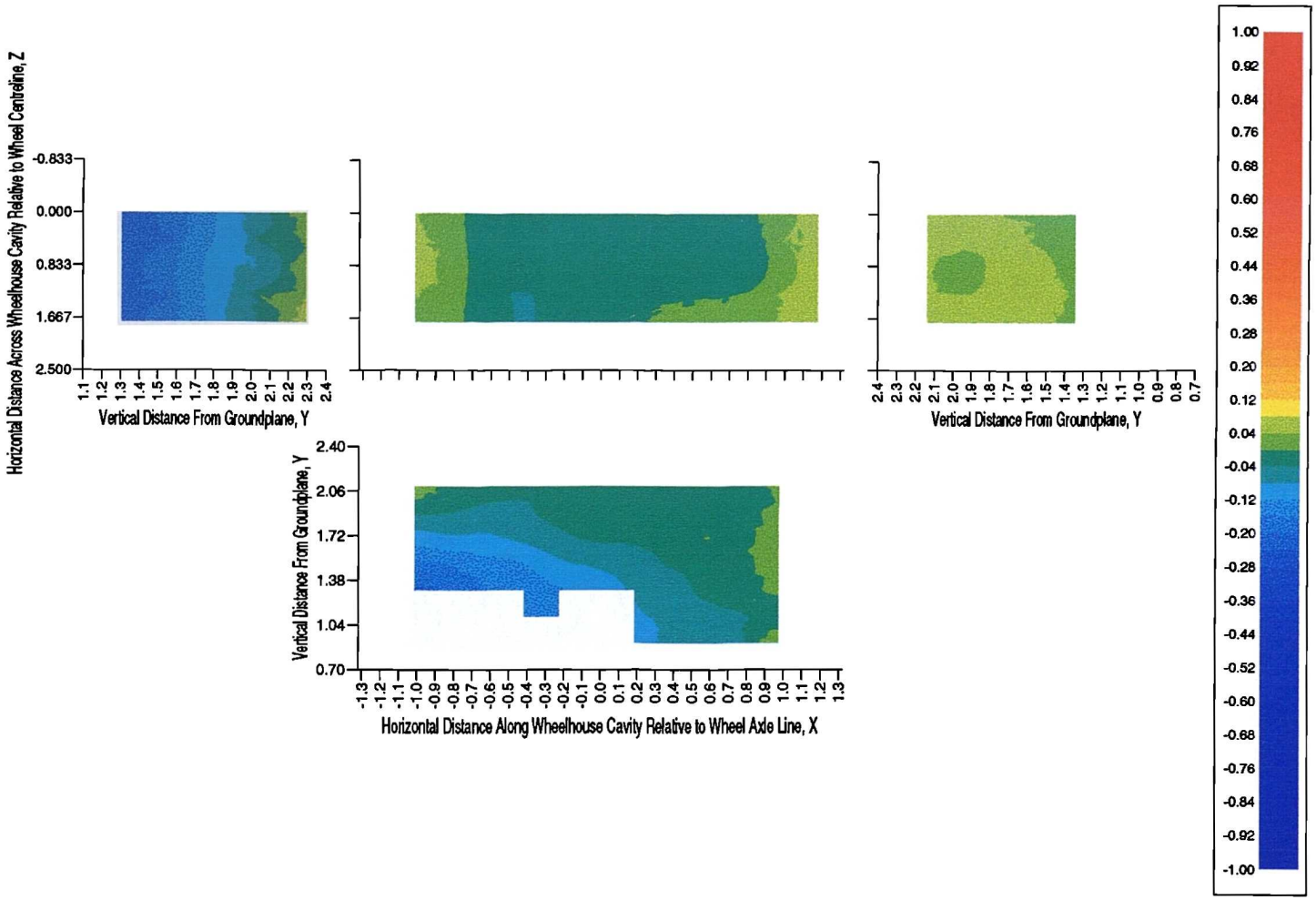

Figure E.10: Experimental Wheelhouse Cavity Pressure Coefficient Distribution - 0.050m Front Spoiler, Front Ride Height, $Y_f = 1.1$, Rear Ride Height, $Y_r = 0.7$, Moving Groundplane

E.2.4 Front Ride Height, $Y_f = 1.1$, Rear Ride Height, $Y_r = 0.7$, Stationary Groundplane

Front Face, $X = -1.320$

Y/Z	*0.000*	*0.867*	*1.733*
2.30	-0.065	-0.059	-0.019
2.10	-0.114	-0.100	-0.091
1.90	-0.140	-0.141	-0.125
1.70	-0.163	-0.151	-0.152
1.50	-0.172	-0.165	-0.176
1.30	-0.195	-0.208	-0.209

Top Face, $Y = 2.400$

X/Z	*0.000*	*0.867*	*1.733*
-1.02	-0.095	-0.100	-0.077
-0.82	-0.069	-0.040	-0.058
-0.62	-0.001	0.017	-0.005
-0.42	0.003	0.009	-0.014
-0.22	-0.053	-0.069	-0.047
-0.02	-0.045	-0.050	-0.047
0.18	-0.043	-0.037	-0.036
0.38	-0.037	-0.042	-0.041
0.58	-0.038	-0.047	-0.046
0.78	-0.035	-0.050	-0.027
0.98	-0.030	-0.027	-0.012
1.18	0.001	0.007	0.006

Rear Face, $X = 1.320$

Y/Z	*0.000*	*0.867*	*1.733*
2.14	-0.007	-0.015	0.000
1.94	-0.001	-0.036	-0.021
1.74	-0.018	-0.022	-0.028
1.54	-0.017	-0.007	0.002
1.34	-0.024	-0.005	-0.024

Arch, $Z = -0.833$

Y/X	*-1.02*	*-0.82*	*0.82*	*1.02*
2.10	-0.133	-0.118	-0.090	-0.032
1.90	-0.154			-0.042

Side Panel, $Z = 2.500$

Y/X	*-1.02*	*-0.82*	*-0.62*	*-0.42*	*-0.22*	*-0.02*	*0.18*	*0.38*	*0.58*	*0.78*	*0.98*
2.10	-0.104	-0.087	-0.055	-0.069	-0.064	-0.064	-0.061	-0.063	-0.065	-0.066	-0.041
1.90	-0.143	-0.119	-0.100	-0.090	-0.073	-0.065	-0.062	-0.058	-0.061	-0.058	-0.051
1.70	-0.168	-0.151	-0.140	-0.128	-0.104	-0.086	-0.083	-0.069	-0.053	-0.060	-0.050
1.50	-0.179	-0.173	-0.153	-0.146	-0.111	-0.107	-0.104	-0.079	-0.074	-0.060	-0.053
1.30	-0.205	-0.189	-0.175	-0.159	-0.140	-0.117	-0.098	-0.091	-0.075	-0.080	-0.065
1.10				-0.163	-0.144		-0.099	-0.095	-0.085	-0.083	-0.052
0.90							-0.152	-0.104	-0.127	-0.083	0.029

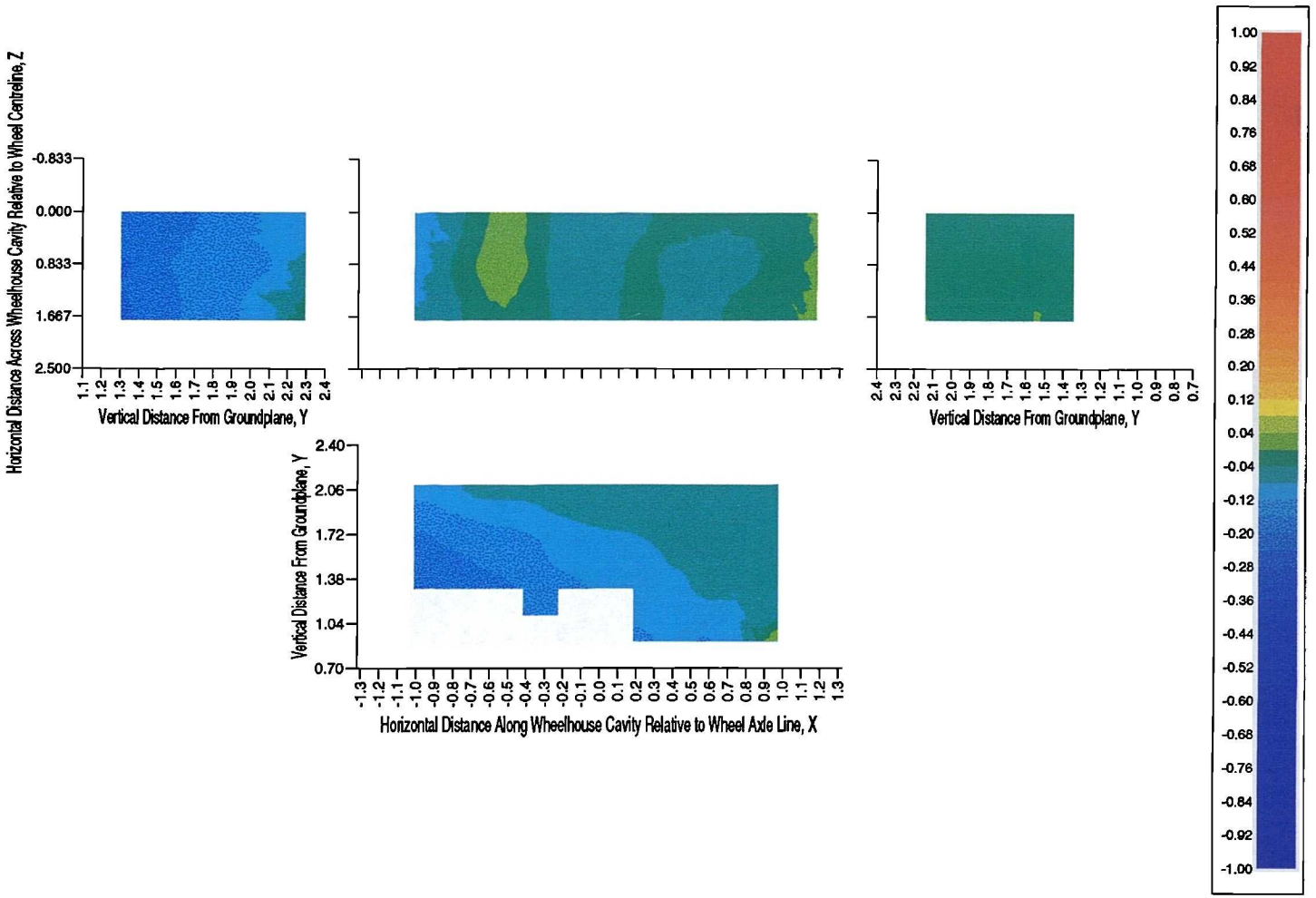

Figure E.11: Experimental Wheelhouse Cavity Pressure Coefficient Distribution - 0.050m Front Spoiler, Front Ride Height, $Y_f = 1.1$, Rear Ride Height, $Y_r = 0.7$, Stationary Groundplane

E.2.5 Front Ride Height, $Y_f = 1.2$, Rear Ride Height, $Y_r = 0.8$, Moving Groundplane

Front Face, $X = -1.320$

Y/Z	*0.000*	*0.867*	*1.733*
2.40	-0.035	-0.018	0.000
2.20	-0.098	-0.067	-0.058
2.00	-0.139	-0.141	-0.117
1.90	-0.141	-0.149	-0.165
1.60	-0.132	-0.154	-0.196
1.40	-0.134	-0.191	-0.229

Top Face, $Y = 2.500$

X/Z	*0.000*	*0.867*	*1.733*
-1.02	-0.070	-0.075	-0.043
-0.82	-0.061	-0.042	-0.039
-0.62	-0.011	-0.009	0.007
-0.42	-0.015	-0.012	-0.008
-0.22	-0.079	-0.086	-0.071
-0.02	-0.060	-0.059	-0.063
0.18	-0.067	-0.058	-0.058
0.38	-0.071	-0.072	-0.062
0.58	-0.076	-0.079	-0.067
0.78	-0.064	-0.081	-0.046
0.98	-0.046	-0.046	-0.017
1.18	-0.007	-0.001	0.000

Rear Face, $X = 1.320$

Y/Z	*0.000*	*0.867*	*1.733*
2.24	-0.015	-0.035	-0.024
2.04	-0.017	-0.061	-0.049
1.84	-0.034	-0.021	-0.037
1.64	-0.018	0.017	0.007
1.44	-0.024	0.025	-0.005

Arch, $Z = -0.833$

Y/X	*-1.02*	*-0.82*	*0.82*	*1.02*
2.20	-0.132	-0.115	-0.101	-0.055
2.00	-0.168			-0.063

Side Panel, $Z = 2.500$

Y/X	*-1.02*	*-0.82*	*-0.62*	*-0.42*	*-0.22*	*-0.02*	*0.18*	*0.38*	*0.58*	*0.78*	*0.98*
2.20	-0.076	-0.073	-0.058	-0.080	-0.075	-0.078	-0.081	-0.080	-0.083	-0.086	-0.058
2.00	-0.123	-0.089	-0.081	-0.093	-0.075	-0.073	-0.081	-0.084	-0.088	-0.083	-0.073
1.80	-0.172	-0.115	-0.096	-0.099	-0.092	-0.081	-0.082	-0.079	-0.070	-0.077	-0.070
1.60	-0.207	-0.174	-0.140	-0.126	-0.100	-0.100	-0.099	-0.083	-0.081	-0.069	-0.056
1.40	-0.237	-0.215	-0.188	-0.161	-0.136	-0.119	-0.109	-0.110	-0.086	-0.073	-0.059
1.20				-0.171	-0.156		-0.138	-0.116	-0.094	-0.080	-0.066
1.00							-0.149	-0.119	-0.113	-0.077	-0.047

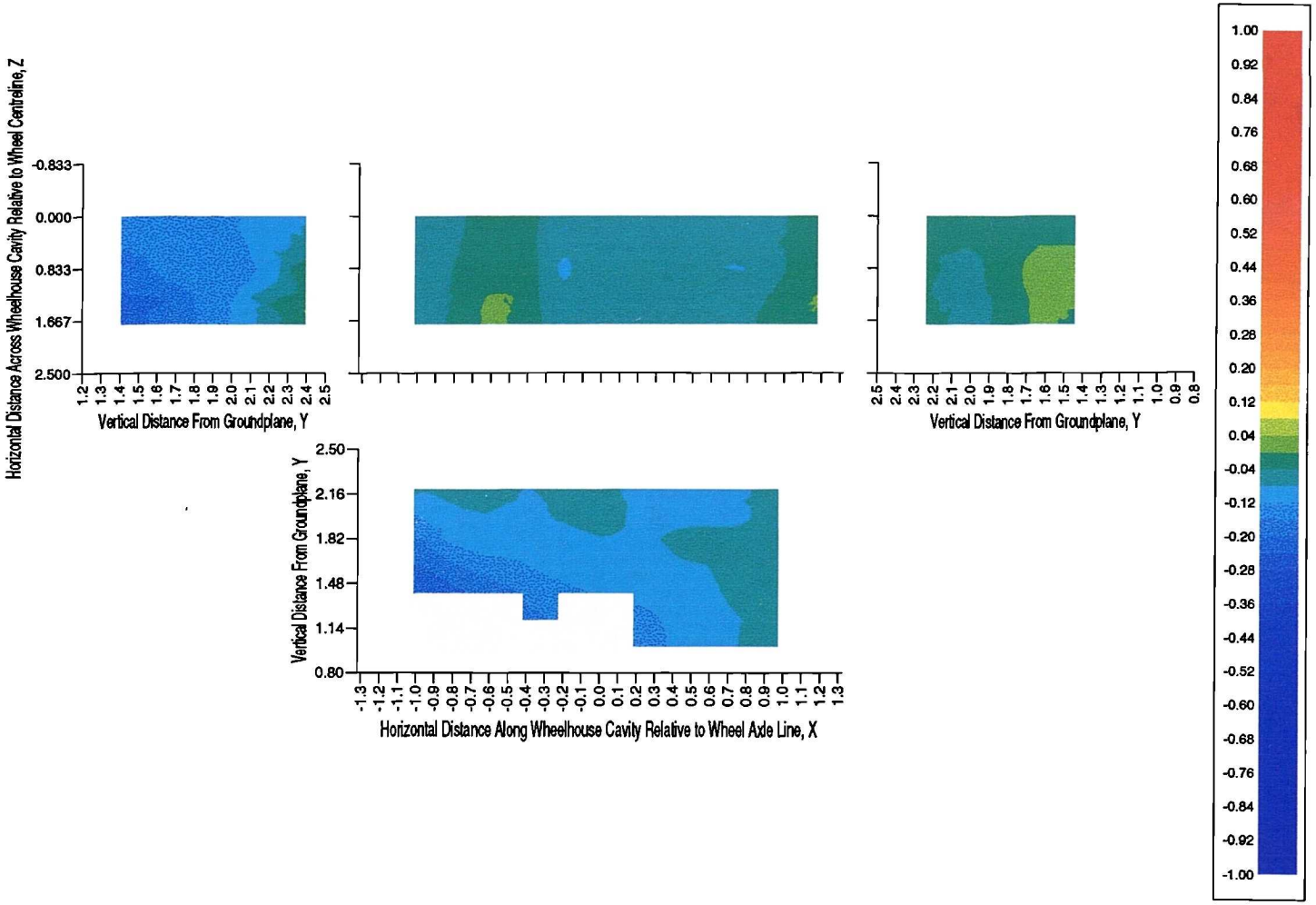

Figure E.12: Experimental Wheelhouse Cavity Pressure Coefficient Distribution - 0.050m Front Spoiler, Front Ride Height, $Y_f = 1.2$, Rear Ride Height, $Y_r = 0.8$, Moving Groundplane

E.2.6 Front Ride Height, $Y_f = 1.2$, Rear Ride Height, $Y_r = 0.8$, Stationary Groundplane

Front Face, $X = -1.320$

Y/Z	*0.000*	*0.867*	*1.733*
2.40	-0.050	-0.023	0.004
2.20	-0.091	-0.078	-0.076
2.00	-0.128	-0.146	-0.131
1.80	-0.134	-0.150	-0.176
1.60	-0.130	-0.160	-0.193
1.40	-0.126	-0.185	-0.219

Top Face, $Y = 2.500$

X/Z	*0.000*	*0.867*	*1.733*
-1.02	-0.082	-0.103	-0.072
-0.82	-0.134	-0.109	-0.098
-0.62	-0.074	-0.013	0.020
-0.42	0.034	0.083	0.061
-0.22	-0.016	-0.024	-0.025
-0.02	-0.030	-0.029	-0.033
0.18	-0.030	-0.017	-0.022
0.38	-0.022	-0.024	-0.023
0.58	-0.013	-0.027	-0.022
0.78	-0.010	-0.034	-0.008
0.98	-0.005	-0.011	0.013
1.18	0.031	0.028	0.030

Rear Face, $X = 1.320$

Y/Z	*0.000*	*0.867*	*1.733*
2.24	0.020	0.002	0.017
2.04	0.028	-0.020	-0.008
1.84	0.011	0.011	0.005
1.64	0.019	0.059	0.048
1.44	-0.002	0.069	0.040

Arch, $Z = -0.833$

Y/X	*-1.02*	*-0.82*	*0.82*	*1.02*
2.20	-0.154	-0.183	-0.068	-0.015
2.00	-0.179			-0.030

Side Panel, $Z = 2.500$

Y/X	*-1.02*	*-0.82*	*-0.62*	*-0.42*	*-0.22*	*-0.02*	*0.18*	*0.38*	*0.58*	*0.78*	*0.98*
2.20	-0.125	-0.117	-0.060	-0.055	-0.047	-0.047	-0.042	-0.038	-0.044	-0.045	-0.022
2.00	-0.158	-0.137	-0.092	-0.080	-0.058	-0.045	-0.043	-0.041	-0.041	-0.038	-0.030
1.80	-0.181	-0.152	-0.129	-0.118	-0.087	-0.066	-0.057	-0.045	-0.035	-0.040	-0.027
1.60	-0.195	-0.178	-0.150	-0.137	-0.104	-0.095	-0.077	-0.052	-0.048	-0.040	-0.027
1.40	-0.223	-0.203	-0.175	-0.155	-0.126	-0.103	-0.083	-0.076	-0.050	-0.039	-0.023
1.20				-0.172	-0.143		-0.111	-0.087	-0.063	-0.046	-0.037
1.00							-0.132	-0.096	-0.088	-0.059	-0.022

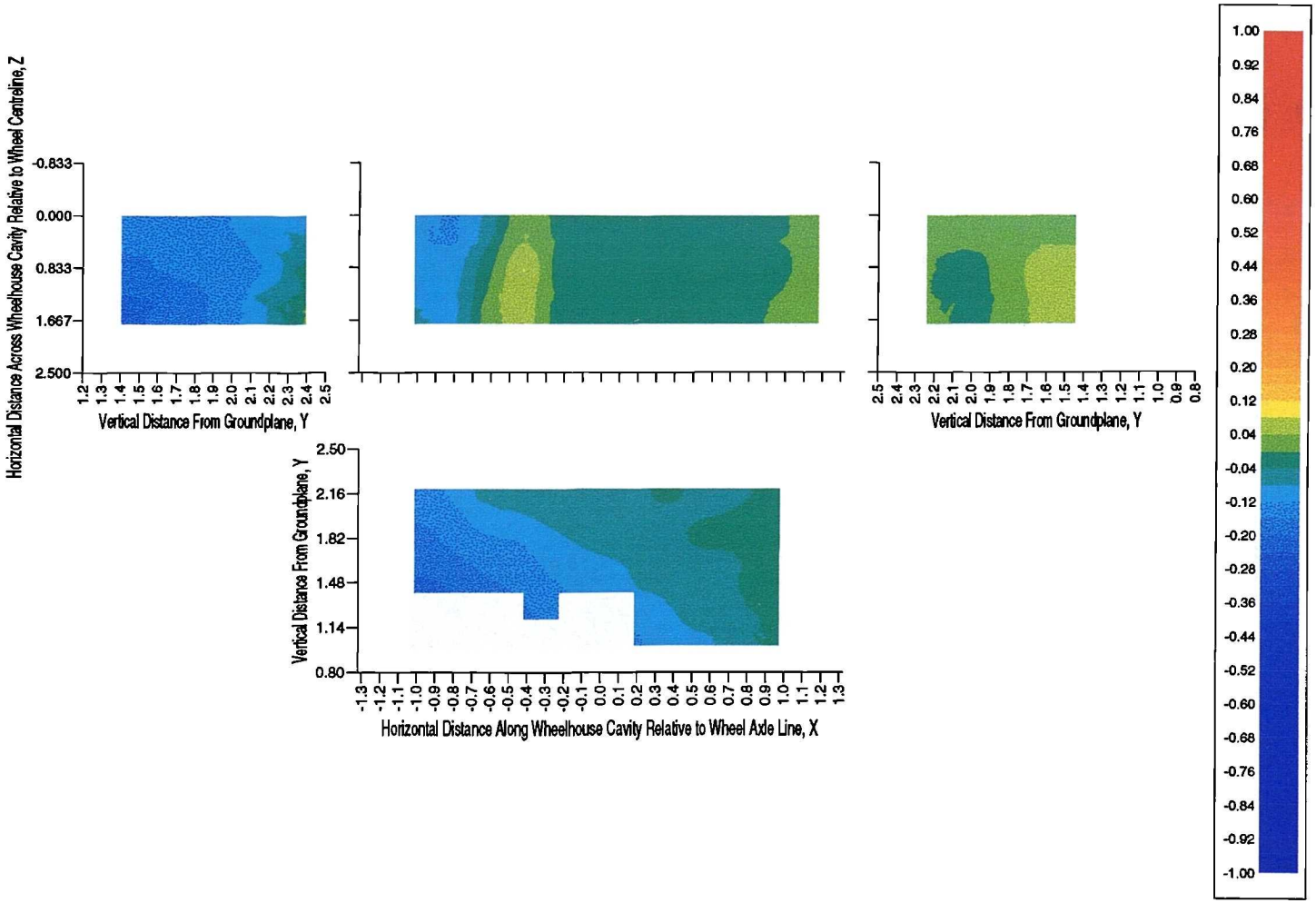

Figure E.13: Experimental Wheelhouse Cavity Pressure Coefficient Distribution - 0.050m Front Spoiler, Front Ride Height, $Y_f = 1.2$, Rear Ride Height, $Y_r = 0.8$, Stationary Groundplane

E.3 0.100m Front Spoiler

E.3.1 Front Ride Height, $Y_f = 1.0$, Rear Ride Height, $Y_r = 0.6$, Moving Groundplane

Front Face, $X = -1.320$

Y/Z	*0.000*	*0.867*	*1.733*
2.20	-0.089	-0.057	-0.042
2.00	-0.120	-0.100	-0.086
1.80	-0.144	-0.145	-0.115
1.60	-0.146	-0.119	-0.090
1.40	-0.133	-0.077	-0.038
1.20	-0.066	-0.002	0.018

Top Face, $Y = 2.300$

X/Z	*0.000*	*0.867*	*1.733*
-1.02	-0.091	-0.100	-0.050
-0.82	-0.117	-0.120	-0.100
-0.62	-0.105	-0.114	-0.102
-0.42	-0.088	-0.083	-0.111
-0.22	-0.084	-0.085	-0.089
-0.02	-0.075	-0.069	-0.080
0.18	-0.081	-0.071	-0.072
0.38	-0.083	-0.080	-0.073
0.58	-0.077	-0.080	-0.076
0.78	-0.073	-0.080	-0.062
0.98	-0.066	-0.065	-0.048
1.18	-0.036	-0.041	-0.035

Rear Face, $X = 1.320$

Y/Z	*0.000*	*0.867*	*1.733*
2.04	-0.042	-0.053	-0.041
1.84	-0.040	-0.071	-0.062
1.64	-0.044	-0.047	-0.058
1.44	-0.039	-0.015	-0.031
1.24	-0.025	0.004	-0.024

Arch, $Z = -0.833$

Y/X	*-1.02*	*-0.82*	*0.82*	*1.02*
2.00	-0.138	-0.154	-0.096	-0.048
1.80	-0.153			-0.054

Side Panel, $Z = 2.500$

Y/X	*-1.02*	*-0.82*	*-0.62*	*-0.42*	*-0.22*	*-0.02*	*0.18*	*0.38*	*0.58*	*0.78*	*0.98*
2.00	-0.115	-0.119	-0.121	-0.151	-0.123	-0.108	-0.094	-0.091	-0.093	-0.096	-0.073
1.80	-0.130	-0.139	-0.139	-0.146	-0.120	-0.102	-0.094	-0.093	-0.094	-0.093	-0.088
1.60	-0.138	-0.146	-0.130	-0.146	-0.130	-0.109	-0.102	-0.093	-0.083	-0.092	-0.085
1.40	-0.141	-0.152	-0.131	-0.149	-0.124	-0.119	-0.108	-0.094	-0.095	-0.105	-0.098
1.20	-0.174	-0.181	-0.175	-0.194	-0.171	-0.148	-0.138	-0.136	-0.113	-0.106	-0.094
1.00				-0.194	-0.205		-0.145	-0.142	-0.126	-0.113	-0.100
0.80							-0.247	-0.156	-0.147	-0.123	-0.090

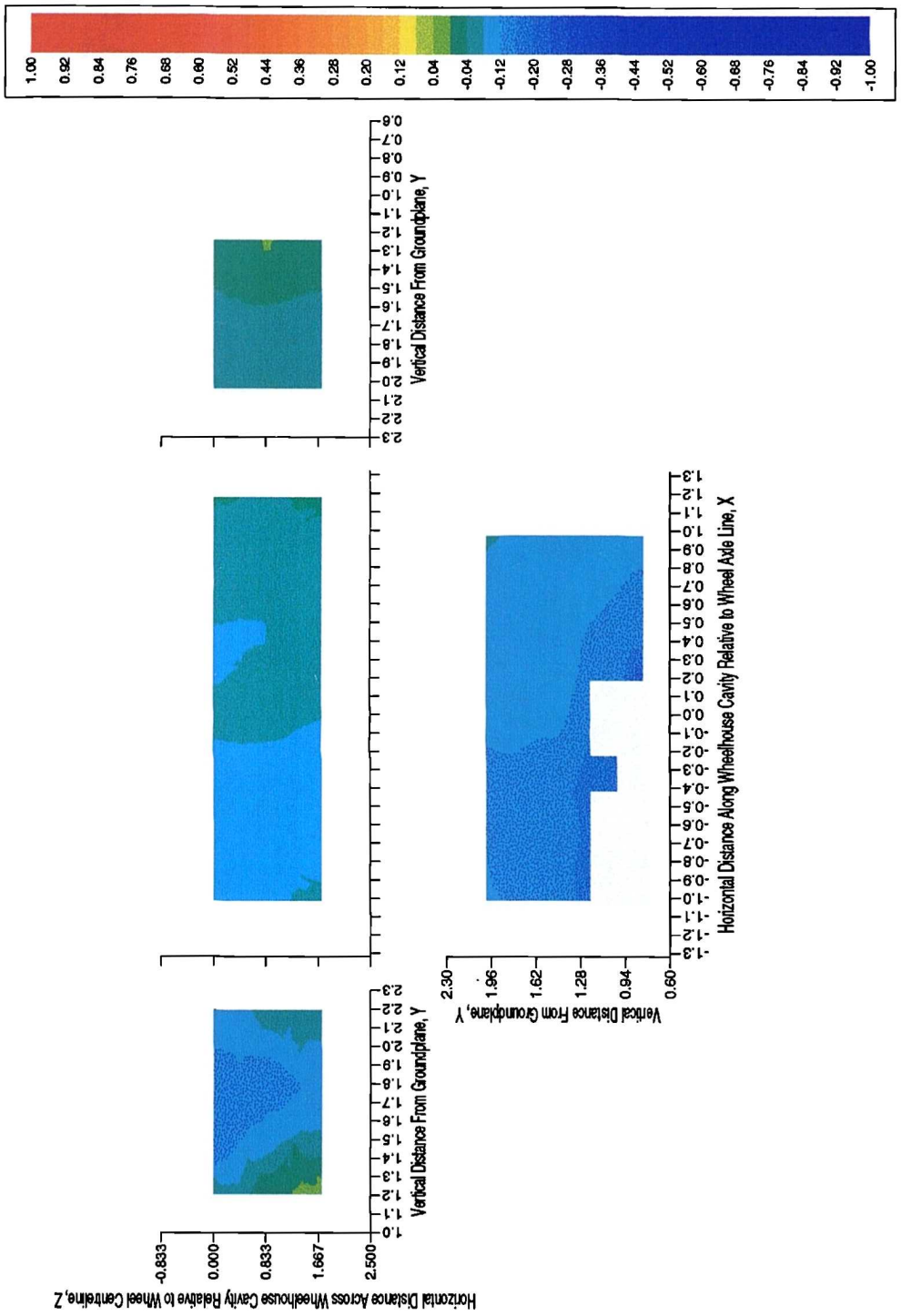

Figure E.14: Experimental Wheelhouse Cavity Pressure Coefficient Distribution - 0.100m Front Spoiler, Front Ride Height, $Y_f = 1.0$, Rear Ride Height, $Y_r = 0.6$, Moving Groundplane

E.3.2 Front Ride Height, $Y_f = 1.0$, Rear Ride Height, $Y_r = 0.6$, Stationary Groundplane

Front Face, $X = -1.320$

Y/Z	*0.000*	*0.867*	*1.733*
2.20	-0.071	-0.071	0.006
2.00	-0.087	-0.072	-0.043
1.80	-0.095	-0.093	-0.067
1.60	-0.094	-0.083	-0.021
1.40	-0.109	-0.079	0.029
1.20	-0.071	-0.101	-0.083

Top Face, $Y = 2.300$

X/Z	*0.000*	*0.867*	*1.733*
-1.02	-0.053	-0.074	0.039
-0.82	-0.064	-0.077	0.004
-0.62	-0.057	-0.079	-0.017
-0.42	-0.036	-0.047	-0.046
-0.22	-0.074	-0.105	-0.083
-0.02	-0.063	-0.065	-0.078
0.18	-0.060	-0.054	-0.063
0.38	-0.059	-0.059	-0.061
0.58	-0.054	*-0.060*	*-0.058*
0.78	-0.058	-0.064	-0.049
0.98	-0.060	-0.055	-0.043
1.18	-0.036	-0.034	-0.031

Rear Face, $X = 1.320$

Y/Z	*0.000*	*0.867*	*1.733*
2.04	-0.044	-0.060	-0.043
1.84	*-0.045*	*-0.075*	*-0.064*
1.64	-0.065	-0.072	-0.071
1.44	-0.053	-0.043	-0.043
1.24	-0.047	-0.010	-0.028

Arch, $Z = -0.833$

Y/X	*-1.02*	*-0.82*	*0.82*	*1.02*
2.00	-0.097	-0.111	-0.104	-0.060
1.80	-0.123			-0.073

Side Panel, $Z = 2.500$

Y/X	*-1.02*	*-0.82*	*-0.62*	*-0.42*	*-0.22*	*-0.02*	*0.18*	*0.38*	*0.58*	*0.78*	*0.98*
2.00	-0.052	-0.081	-0.094	-0.108	-0.103	-0.106	-0.094	-0.086	-0.086	-0.089	-0.071
1.80	-0.057	-0.102	-0.118	-0.109	-0.094	-0.098	-0.093	-0.086	-0.083	-0.080	-0.080
1.60	-0.034	-0.122	-0.132	-0.128	-0.124	-0.113	-0.111	-0.099	-0.081	-0.092	-0.087
1.40	-0.084	-0.162	-0.161	-0.163	-0.137	-0.138	-0.136	-0.114	-0.106	-0.092	-0.085
1.20	-0.247	-0.256	-0.194	-0.183	-0.180	-0.156	-0.134	-0.136	-0.111	-0.109	-0.086
1.00				-0.172	-0.193		-0.137	-0.128	-0.125	-0.115	-0.092
0.80							-0.275	-0.149	-0.148	-0.110	-0.050

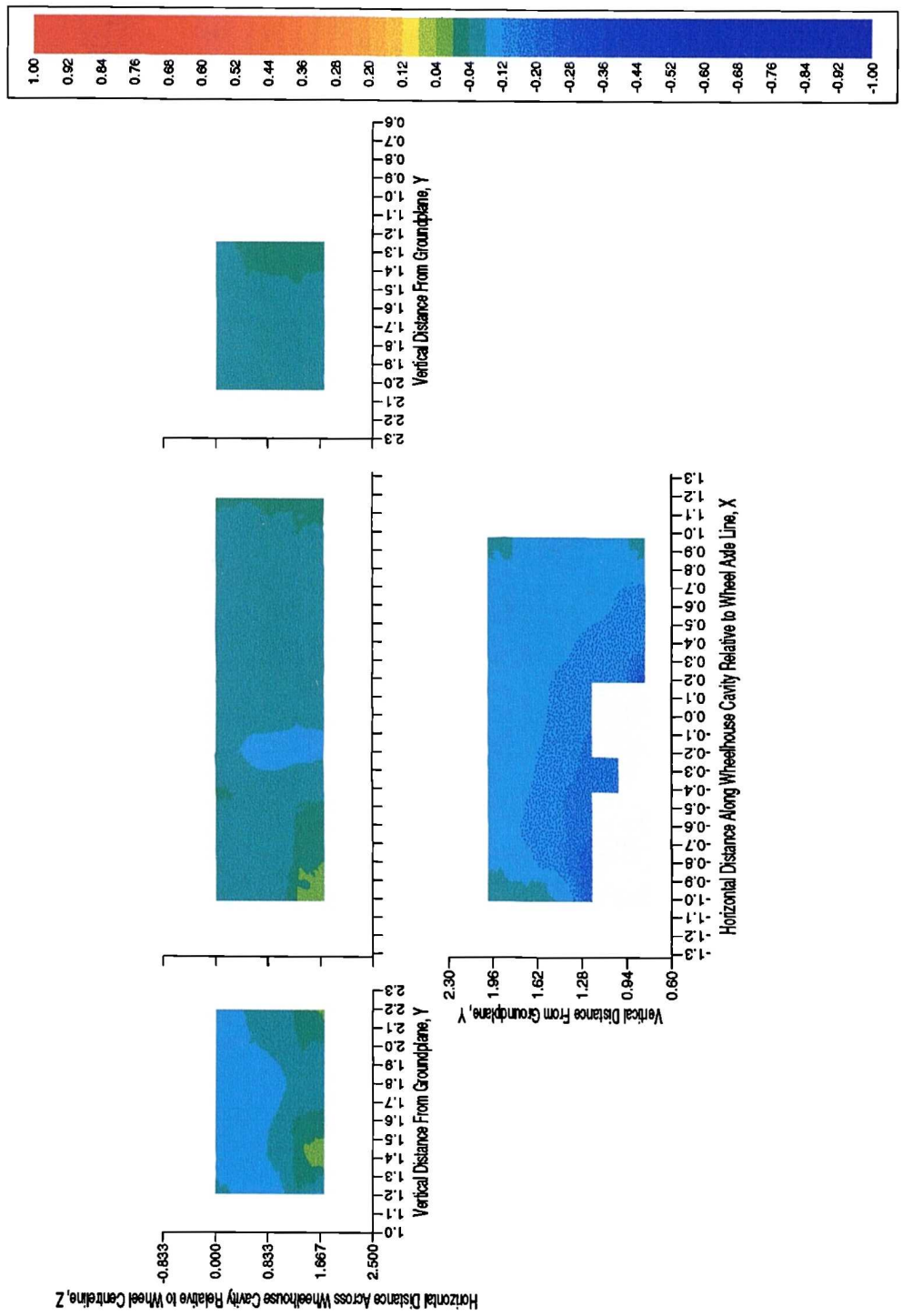

Figure E.15: Experimental Wheelhouse Cavity Pressure Coefficient Distribution - 0.100m Front Spoiler, Front Ride Height, $Y_f = 1.0$, Rear Ride Height, $Y_r = 0.6$, Stationary Groundplane

E.3.3 Front Ride Height, $Y_f = 1.1$, Rear Ride Height, $Y_r = 0.7$, Moving Groundplane

Front Face, $X = -1.320$

Y/Z	*0.000*	*0.867*	*1.733*
2.30	-0.058	-0.005	0.032
2.10	-0.099	-0.059	-0.023
1.90	-0.115	-0.112	-0.059
1.70	-0.122	-0.085	-0.028
1.50	-0.090	-0.031	0.030
1.30	-0.017	-0.080	-0.058

Top Face, $Y = 2.400$

X/Z	*0.000*	*0.867*	*1.733*
-1.02	-0.065	-0.050	0.017
-0.82	-0.100	-0.092	-0.049
-0.62	-0.081	-0.094	-0.065
-0.42	-0.053	-0.062	-0.076
-0.22	-0.055	-0.075	-0.061
-0.02	-0.044	-0.035	-0.044
0.18	-0.039	-0.023	-0.019
0.38	-0.029	-0.021	-0.015
0.58	-0.019	-0.018	-0.018
0.78	-0.014	-0.017	0.000
0.98	-0.013	-0.006	-0.001
1.18	0.011	0.011	0.012

Rear Face, $X = 1.320$

Y/Z	*0.000*	*0.867*	*1.733*
2.14	0.006	0.006	0.017
1.94	0.014	-0.009	0.006
1.74	0.010	0.009	0.022
1.54	0.005	0.007	0.017
1.34	0.000	0.008	-0.012

Arch, $Z = -0.833$

Y/X	*-1.02*	*-0.82*	*0.82*	*1.02*
2.10	-0.101	-0.130	-0.049	0.003
1.90	-0.118			-0.010

Side Panel, $Z = 2.500$

Y/X	*-1.02*	*-0.82*	*-0.62*	*-0.42*	*-0.22*	*-0.02*	*0.18*	*0.38*	*0.58*	*0.78*	*0.98*
2.10	-0.059	-0.075	-0.078	-0.089	-0.069	-0.051	-0.038	-0.023	-0.015	-0.018	0.005
1.90	-0.080	-0.099	-0.099	-0.095	-0.071	-0.056	-0.038	-0.026	-0.020	-0.013	-0.001
1.70	-0.094	-0.117	-0.101	-0.098	-0.081	-0.059	-0.050	-0.034	-0.013	-0.018	-0.003
1.50	-0.098	-0.134	-0.116	-0.125	-0.100	-0.096	-0.086	-0.057	-0.046	-0.051	-0.038
1.30	-0.159	-0.187	-0.168	-0.180	-0.160	-0.136	-0.114	-0.107	-0.077	-0.073	-0.053
1.10				-0.178	-0.182		-0.137	-0.119	-0.098	-0.085	-0.067
0.90							-0.196	-0.113	-0.115	-0.085	-0.022

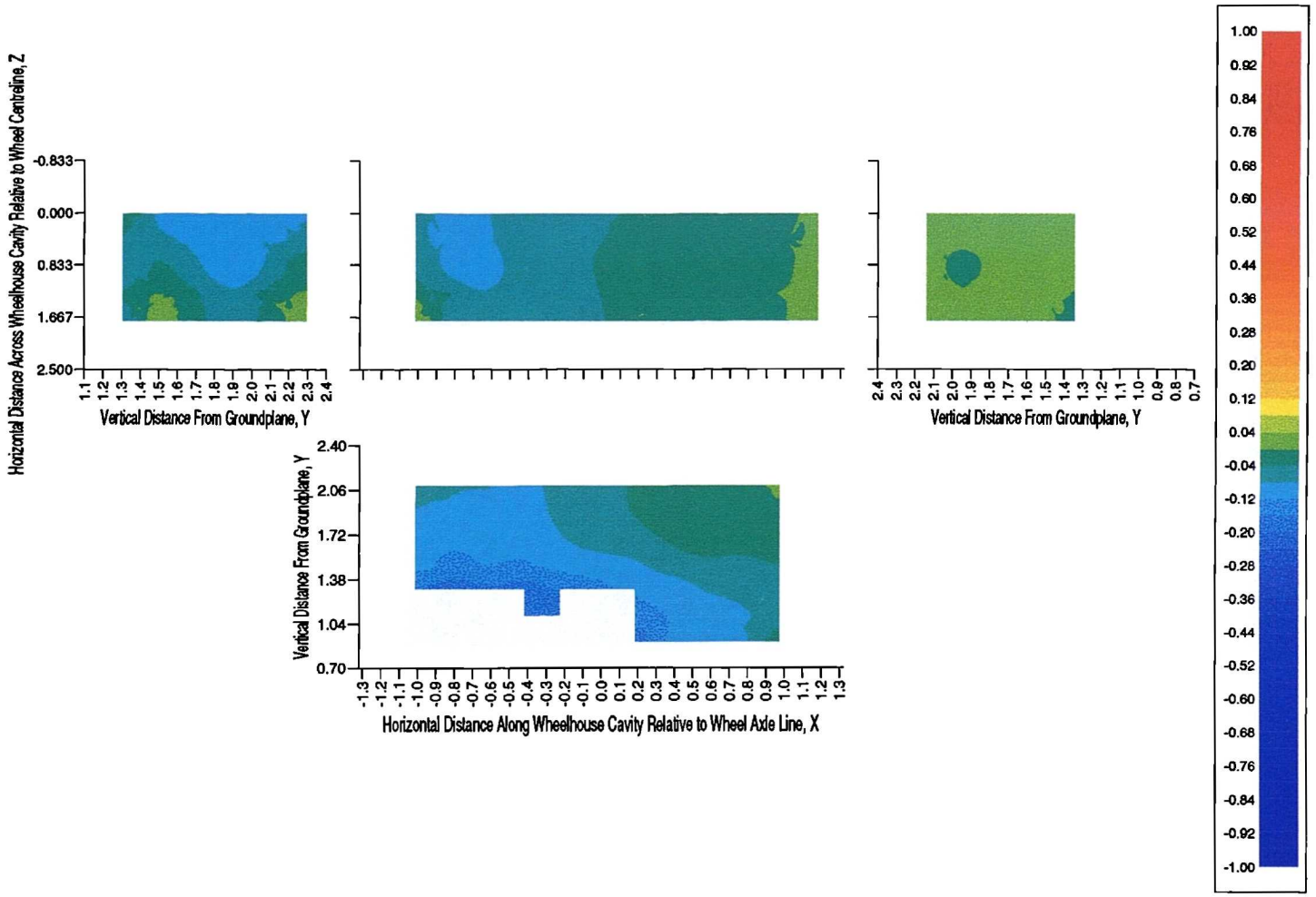

Figure E.16: Experimental Wheelhouse Cavity Pressure Coefficient Distribution - 0.100m Front Spoiler, Front Ride Height, $Y_f = 1.1$, Rear Ride Height, $Y_r = 0.7$, Moving Groundplane

E.3.4 Front Ride Height, $Y_f = 1.1$, Rear Ride Height, $Y_r = 0.7$, Stationary Groundplane

Front Face, $X = -1.320$

Y/Z	*0.000*	*0.867*	*1.733*
2.30	-0.051	-0.037	0.075
2.10	-0.083	-0.050	0.012
1.90	-0.084	-0.078	-0.010
1.70	-0.079	-0.065	0.036
1.50	-0.075	-0.058	-0.020
1.30	-0.046	-0.215	-0.201

Top Face, $Y = 2.400$

X/Z	*0.000*	*0.867*	*1.733*
-1.02	-0.034	-0.040	0.108
-0.82	-0.043	-0.055	0.059
-0.62	-0.027	-0.060	0.018
-0.42	-0.012	-0.026	-0.011
-0.22	-0.040	-0.074	-0.032
-0.02	-0.030	-0.030	-0.033
0.18	-0.029	-0.023	-0.015
0.38	-0.023	-0.022	-0.014
0.58	-0.017	-0.018	-0.009
0.78	-0.007	-0.015	0.009
0.98	-0.007	-0.003	0.006
1.18	0.017	0.015	0.019

Rear Face, $X = 1.320$

Y/Z	*0.000*	*0.867*	*1.733*
2.14	0.015	0.006	0.014
1.94	0.020	-0.009	-0.001
1.74	-0.014	-0.014	-0.021
1.54	-0.010	-0.008	-0.006
1.34	-0.011	0.001	-0.019

Arch, $Z = -0.833$

Y/X	*-1.02*	*-0.82*	*0.82*	*1.02*
2.10	-0.047	-0.066	-0.079	-0.021
1.90	-0.088			-0.033

Side Panel, $Z = 2.500$

Y/X	*-1.02*	*-0.82*	*-0.62*	*-0.42*	*-0.22*	*-0.02*	*0.18*	*0.38*	*0.58*	*0.78*	*0.98*
2.10	0.048	-0.006	-0.040	-0.053	-0.049	-0.050	-0.041	-0.029	-0.024	-0.030	-0.005
1.90	0.056	-0.022	-0.072	-0.071	-0.051	-0.048	-0.046	-0.040	-0.034	-0.026	-0.019
1.70	0.027	-0.070	-0.104	-0.100	-0.094	-0.074	-0.076	-0.058	-0.034	-0.038	-0.023
1.50	-0.123	-0.169	-0.159	-0.154	-0.110	-0.099	-0.095	-0.073	-0.064	-0.063	-0.053
1.30	-0.269	-0.253	-0.181	-0.164	-0.142	-0.133	-0.116	-0.111	-0.092	-0.098	-0.074
1.10				-0.152	-0.153		-0.124	-0.118	-0.107	-0.096	-0.053
0.90							-0.177	-0.111	-0.133	-0.093	0.021

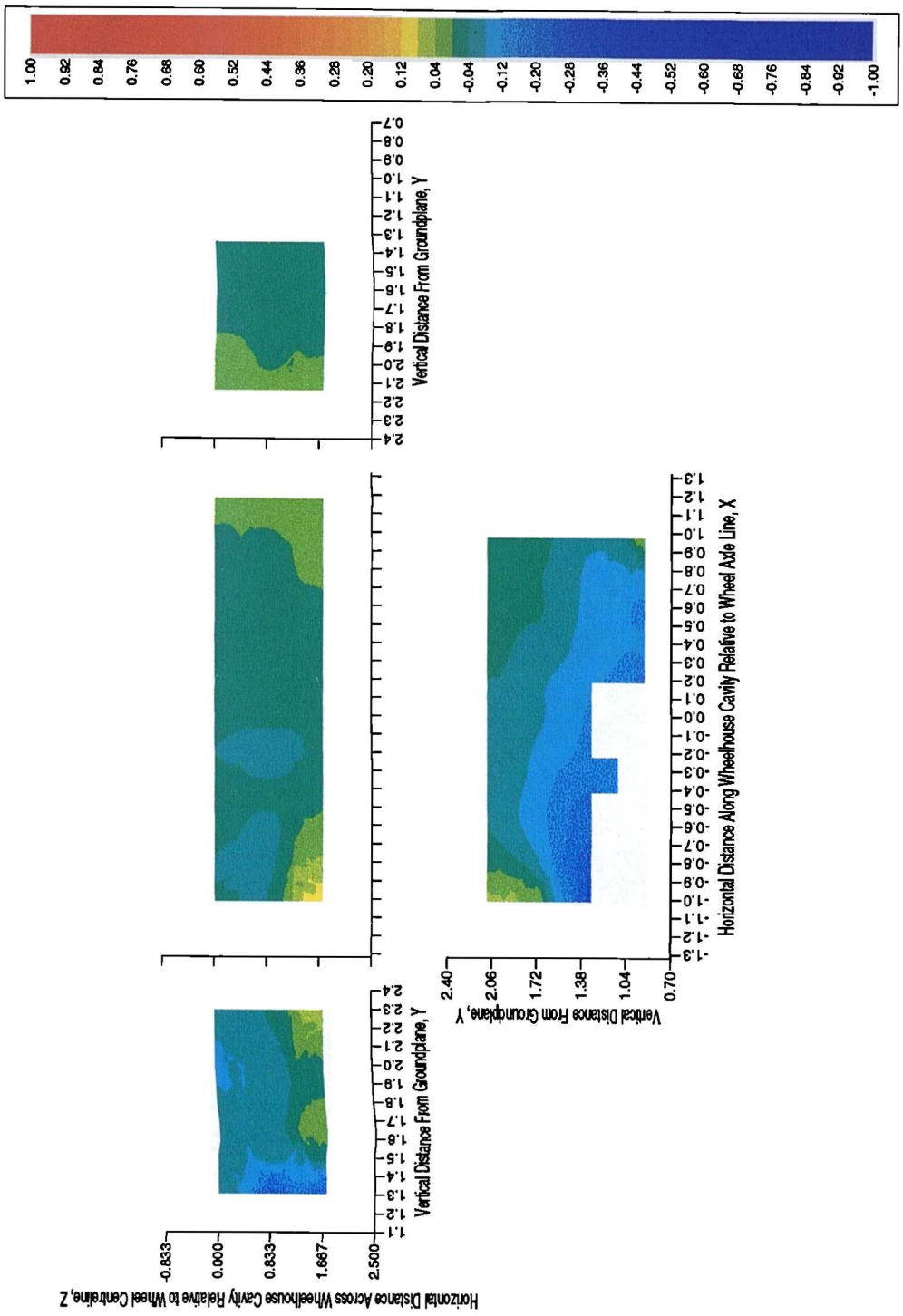

Figure E.17: Experimental Wheelhouse Cavity Pressure Coefficient Distribution - 0.100m Front Spoiler, Front Ride Height, $Y_f = 1.1$, Rear Ride Height, $Y_r = 0.7$, Stationary Groundplane

E.3.5 Front Ride Height, $Y_f = 1.2$, Rear Ride Height, $Y_r = 0.8$, Moving Groundplane

Front Face, $X = -1.320$

Y/Z	*0.000*	*0.867*	*1.733*
2.40	-0.023	0.039	0.086
2.20	-0.069	-0.018	0.024
2.00	-0.096	-0.086	-0.014
1.90	-0.093	-0.056	0.023
1.60	-0.037	-0.013	-0.008
1.40	-0.124	-0.243	-0.210

Top Face, $Y = 2.500$

X/Z	*0.000*	*0.867*	*1.733*
-1.02	-0.036	0.000	0.061
-0.82	-0.085	-0.070	-0.024
-0.62	-0.068	-0.086	-0.056
-0.42	-0.045	-0.055	-0.066
-0.22	-0.030	-0.050	-0.026
-0.02	-0.017	-0.005	-0.007
0.18	-0.014	0.009	0.017
0.38	0.001	0.015	0.026
0.58	0.018	0.023	0.030
0.78	0.021	0.024	0.039
0.98	0.033	0.047	0.056
1.18	0.078	0.077	0.068

Rear Face, $X = 1.320$

Y/Z	*0.000*	*0.867*	*1.733*
2.24	0.070	0.061	0.074
2.04	0.077	0.060	0.064
1.84	0.057	0.078	0.066
1.64	0.044	0.064	0.056
1.44	0.022	0.040	0.025

Arch, $Z = -0.833$

Y/X	*-1.02*	*-0.82*	*0.82*	*1.02*
2.20	-0.077	-0.114	-0.045	0.048
2.00	-0.104			0.032

Side Panel, $Z = 2.500$

Y/X	*-1.02*	*-0.82*	*-0.62*	*-0.42*	*-0.22*	*-0.02*	*0.18*	*0.38*	*0.58*	*0.78*	*0.98*
2.20	-0.022	-0.051	-0.060	-0.059	-0.036	-0.020	-0.003	0.012	0.019	0.014	0.042
2.00	-0.044	-0.084	-0.085	-0.068	-0.039	-0.024	-0.008	0.004	0.009	0.021	0.038
1.80	-0.067	-0.109	-0.099	-0.086	-0.066	-0.042	-0.033	-0.017	0.005	0.010	0.030
1.60	-0.086	-0.124	-0.116	-0.111	-0.081	-0.077	-0.068	-0.041	-0.028	-0.021	0.000
1.40	-0.190	-0.192	-0.163	-0.160	-0.144	-0.127	-0.100	-0.083	-0.045	-0.036	-0.008
1.20				-0.156	-0.150		-0.109	-0.079	-0.058	-0.041	-0.031
1.00							-0.121	-0.077	-0.069	-0.049	-0.035

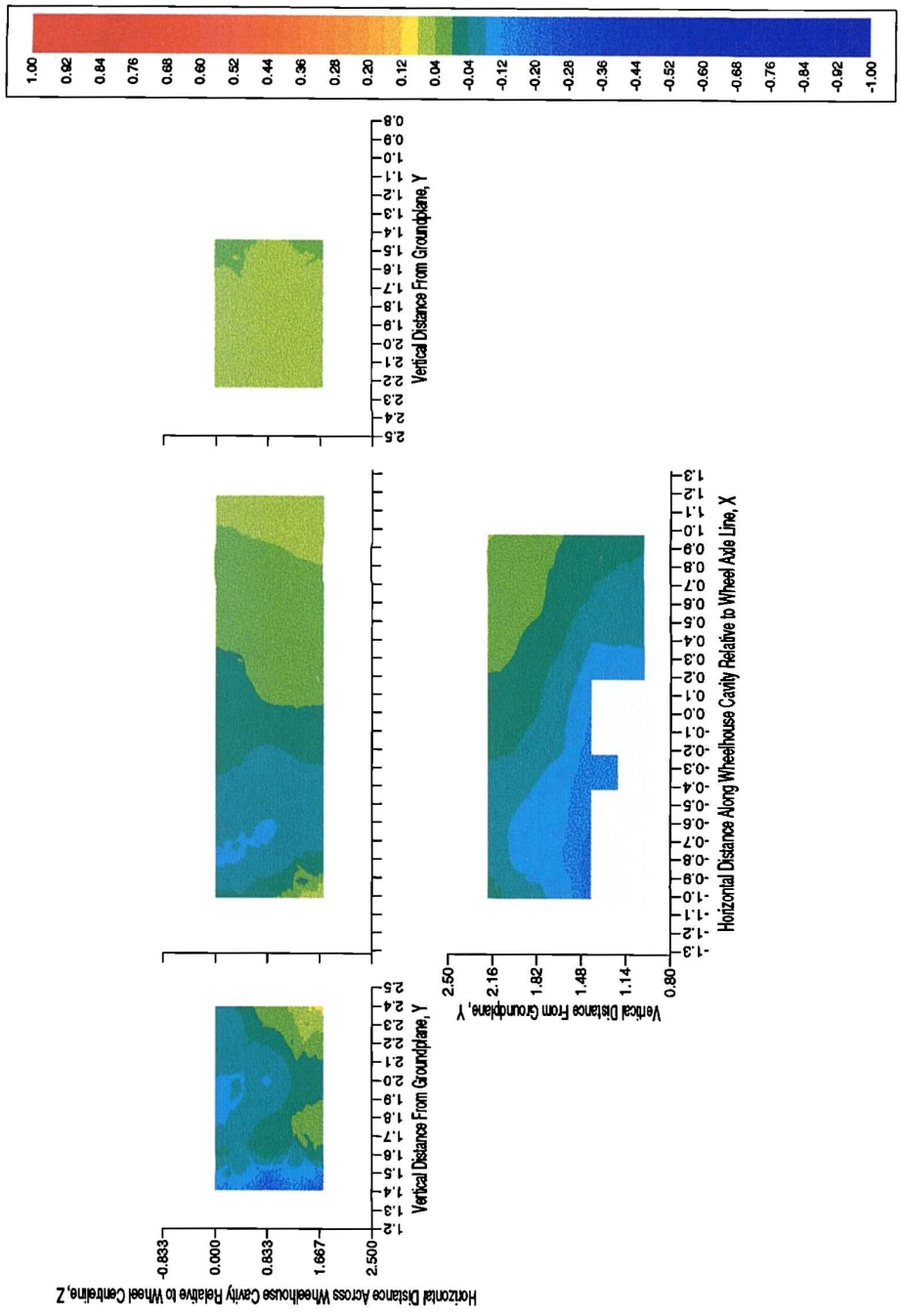

Figure E.18: Experimental Wheelhouse Cavity Pressure Coefficient Distribution - 0.100m Front Spoiler, Front Ride Height, $Y_f = 1.2$, Rear Ride Height, $Y_r = 0.8$, Moving Groundplane

E.3.6 Front Ride Height, $Y_f = 1.2$, Rear Ride Height, $Y_r = 0.8$, Stationary Groundplane

Front Face, $X = -1.320$

Y/Z	*0.000*	*0.867*	*1.733*
2.40	-0.032	0.004	0.107
2.20	-0.095	-0.025	0.046
2.00	-0.085	-0.064	0.032
1.80	-0.078	-0.051	0.038
1.60	-0.041	-0.104	-0.120
1.40	-0.193	-0.298	-0.261

Top Face, $Y = 2.500$

X/Z	*0.000*	*0.867*	*1.733*
-1.02	-0.013	-0.010	0.145
-0.82	-0.028	-0.035	0.098
-0.62	-0.012	-0.061	0.040
-0.42	0.003	-0.028	0.001
-0.22	-0.036	-0.071	-0.020
-0.02	-0.021	-0.027	-0.013
0.18	-0.019	-0.019	0.000
0.38	-0.013	-0.012	0.000
0.58	-0.005	-0.004	0.007
0.78	0.004	0.005	0.021
0.98	0.002	0.007	0.022
1.18	0.035	0.032	0.035

Rear Face, $X = 1.320$

Y/Z	*0.000*	*0.867*	*1.733*
2.24	0.033	0.020	0.030
2.04	0.037	0.018	0.017
1.84	0.021	0.035	0.015
1.64	0.013	0.044	0.034
1.44	-0.011	0.035	0.002

Arch, $Z = -0.833$

Y/X	*-1.02*	*-0.82*	*0.82*	*1.02*
2.20	-0.019	-0.051	-0.074	-0.003
2.00	-0.078			-0.013

Side Panel, $Z = 2.500$

Y/X	*-1.02*	*-0.82*	*-0.62*	*-0.42*	*-0.22*	*-0.02*	*0.18*	*0.38*	*0.58*	*0.78*	*0.98*
2.20	0.111	0.071	0.000	-0.040	-0.036	-0.035	-0.028	-0.013	-0.005	-0.008	0.009
2.00	0.104	0.057	-0.033	-0.067	-0.043	-0.040	-0.039	-0.028	-0.018	-0.010	-0.001
1.80	0.008	-0.046	-0.082	-0.098	-0.098	-0.072	-0.065	-0.047	-0.022	-0.021	-0.009
1.60	-0.167	-0.194	-0.173	-0.176	-0.119	-0.092	-0.080	-0.052	-0.044	-0.045	-0.025
1.40	-0.274	-0.246	-0.196	-0.173	-0.144	-0.124	-0.105	-0.092	-0.066	-0.054	-0.039
1.20				-0.160	-0.150		-0.120	-0.096	-0.083	-0.076	-0.077
1.00							-0.129	-0.101	-0.096	-0.077	-0.050

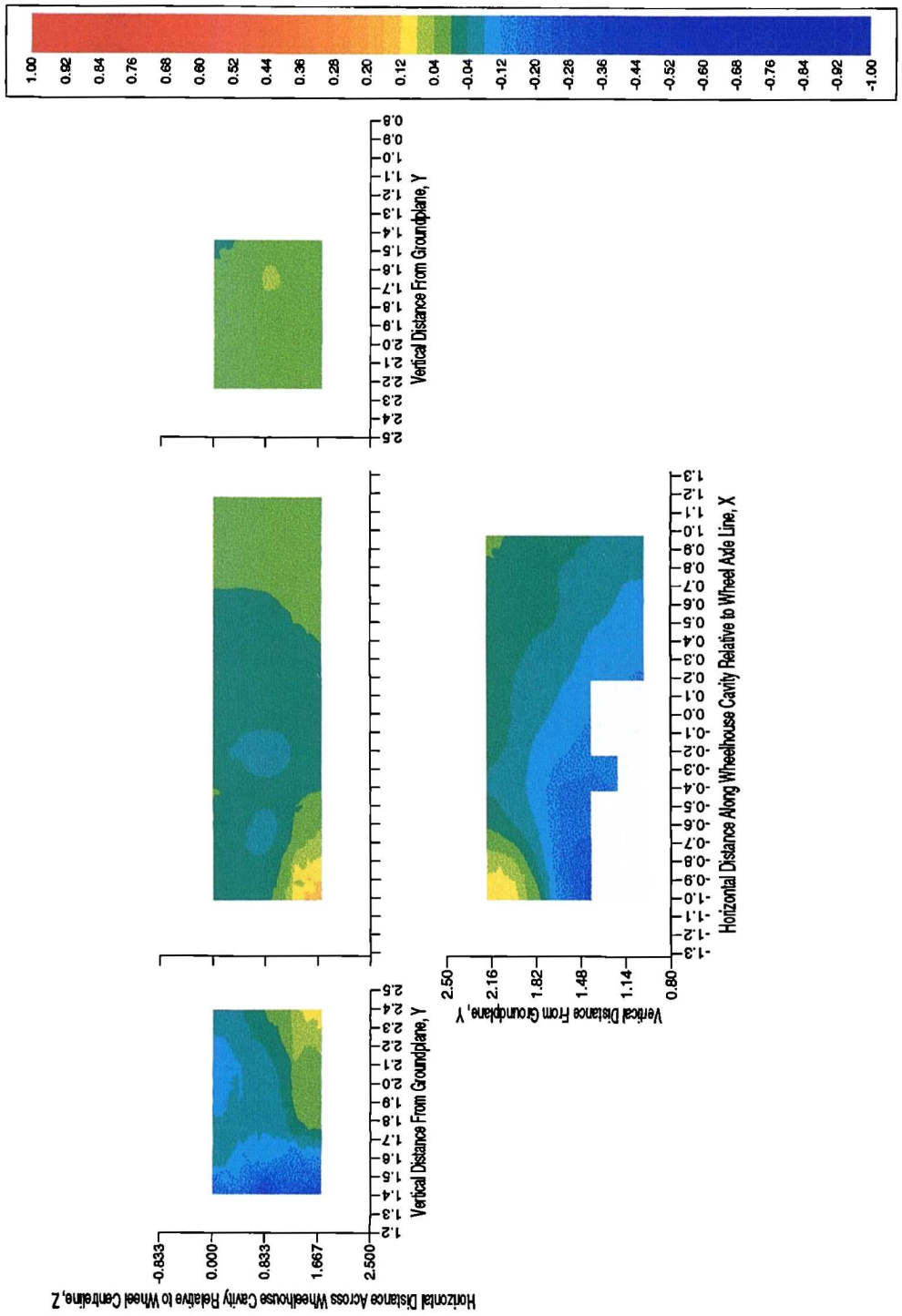

Figure E.19: Experimental Wheelhouse Cavity Pressure Coefficient Distribution - 0.100m Front Spoiler, Front Ride Height, $Y_f = 1.2$, Rear Ride Height, $Y_r = 0.8$, Stationary Groundplane

Appendix F

Computational Wheelhouse Pressure Distributions

In this appendix computational surface static pressure coefficient distributions on the five planar internal wheelhouse cavity faces are presented. All the pressure coefficients are referenced to the freestream velocity of 25m/s.

The contour plots were again produced in Gsharp from ascii solution data exported from FLUENT/UNS, and are mapped according to *Fig.E.1.*

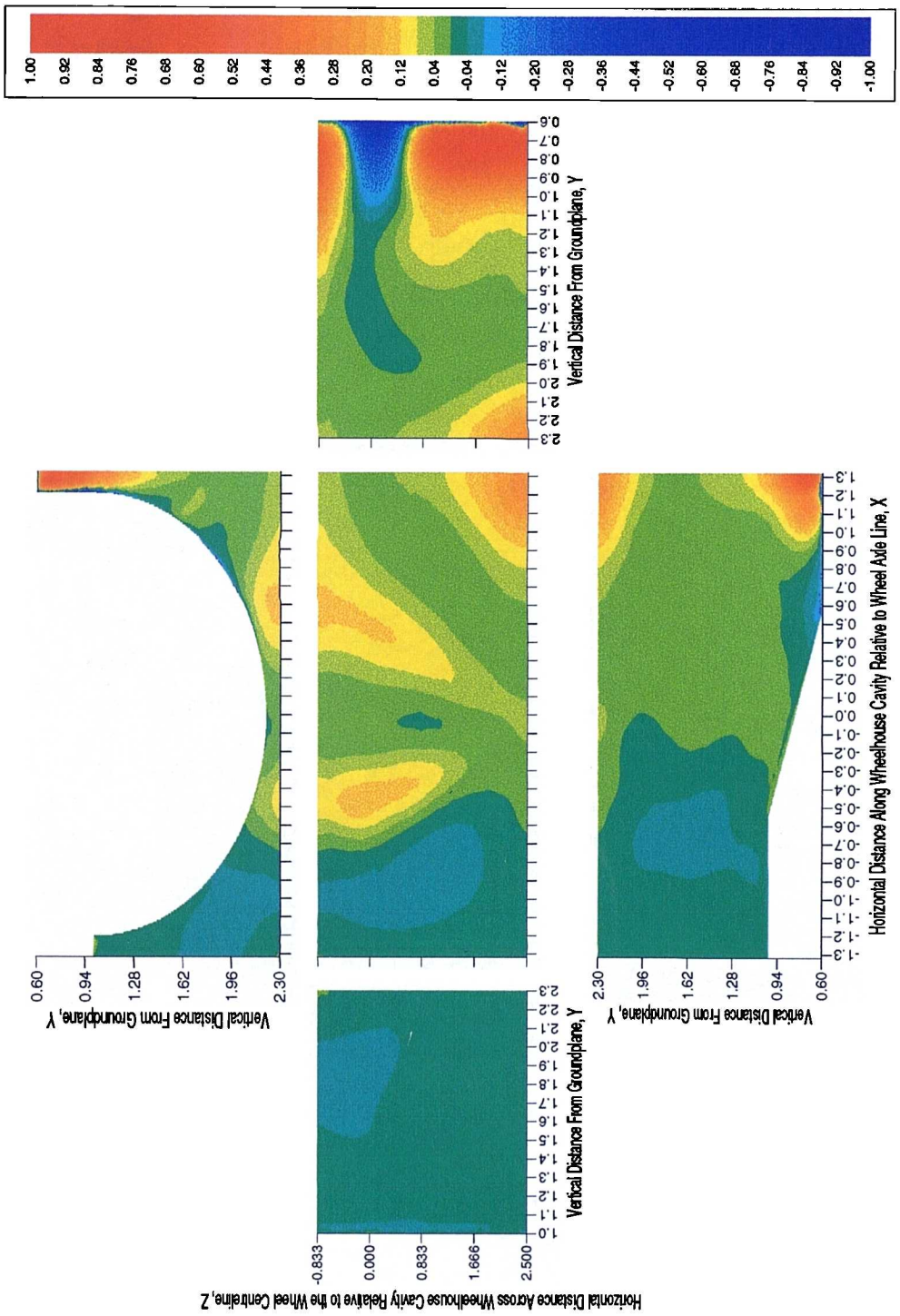

Figure F.1: Computational Wheelhouse Cavity Pressure Coefficient Distribution - No Front Spoiler, Front Ride Height, $Y_f = 1.0$, Rear Ride Height, $Y_r = 0.6$, Moving Groundplane

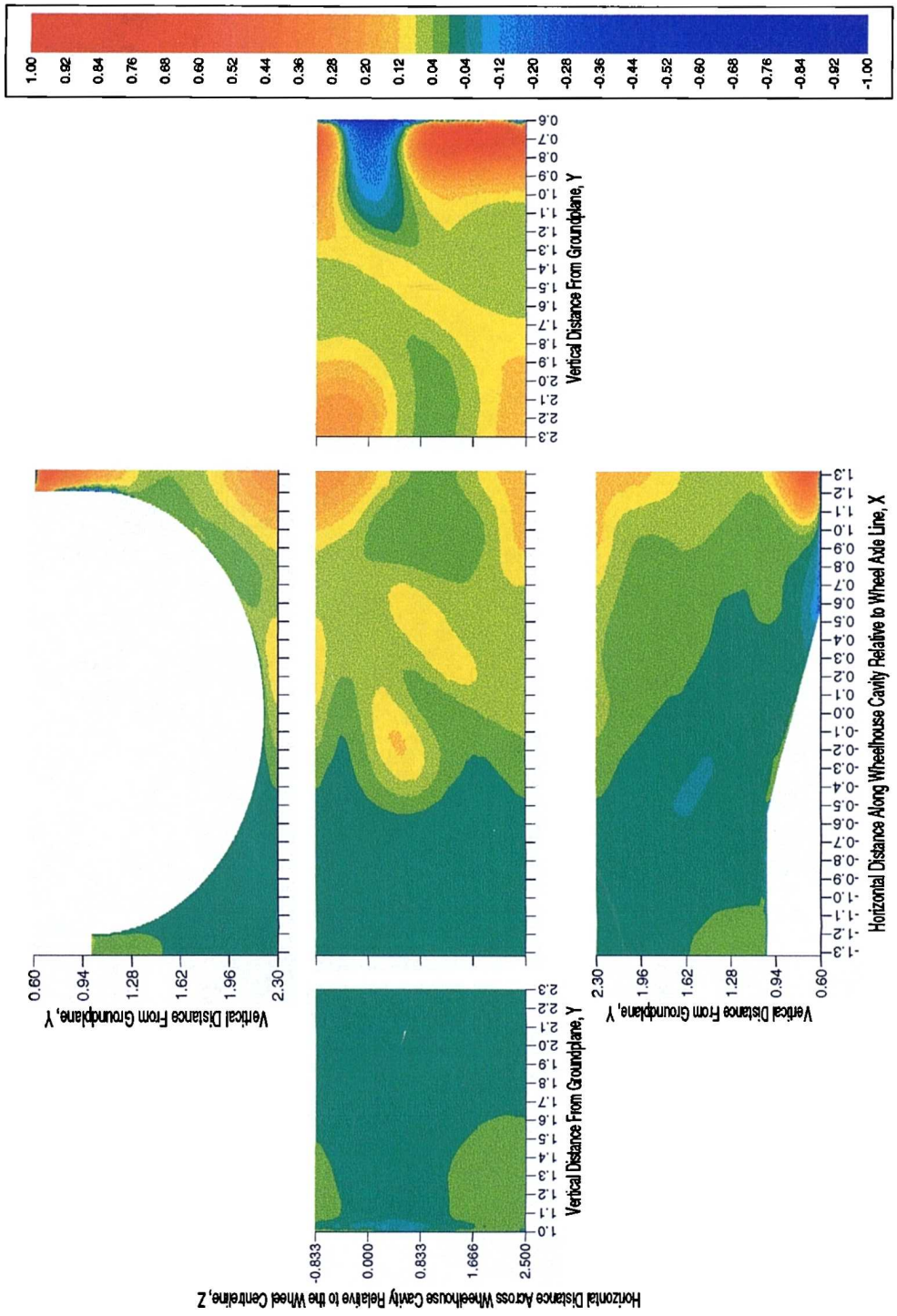

Figure F.2: Computational Wheelhouse Cavity Pressure Coefficient Distribution - No Front Spoiler, Front Ride Height, $Y_f = 1.0$, Rear Ride Height, $Y_r = 0.6$, Stationary Groundplane

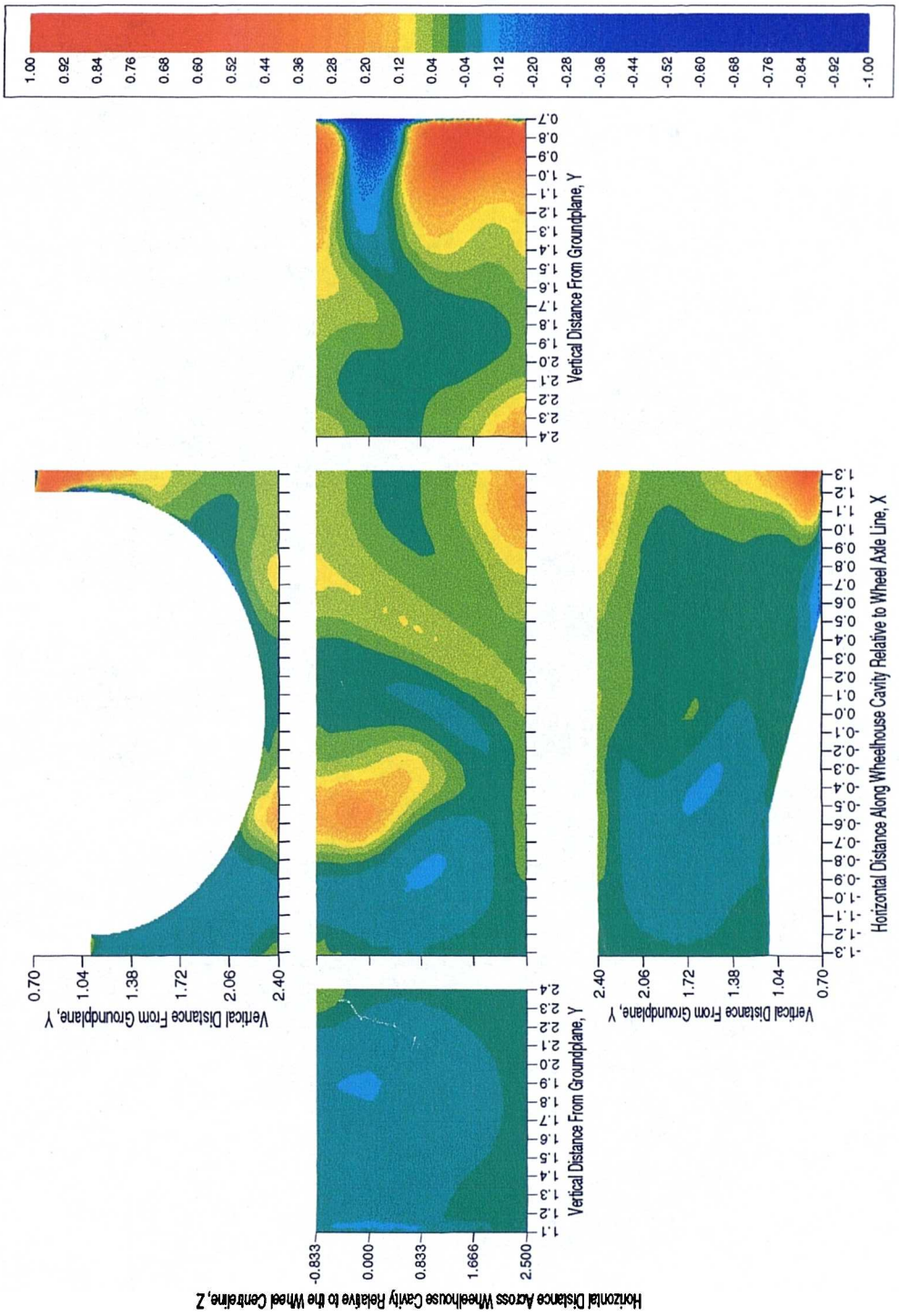

Figure F.3: Computational Wheelhouse Cavity Pressure Coefficient Distribution - No Front Spoiler, Front Ride Height, $Y_f = 1.1$, Rear Ride Height, $Y_r = 0.7$, Moving Groundplane

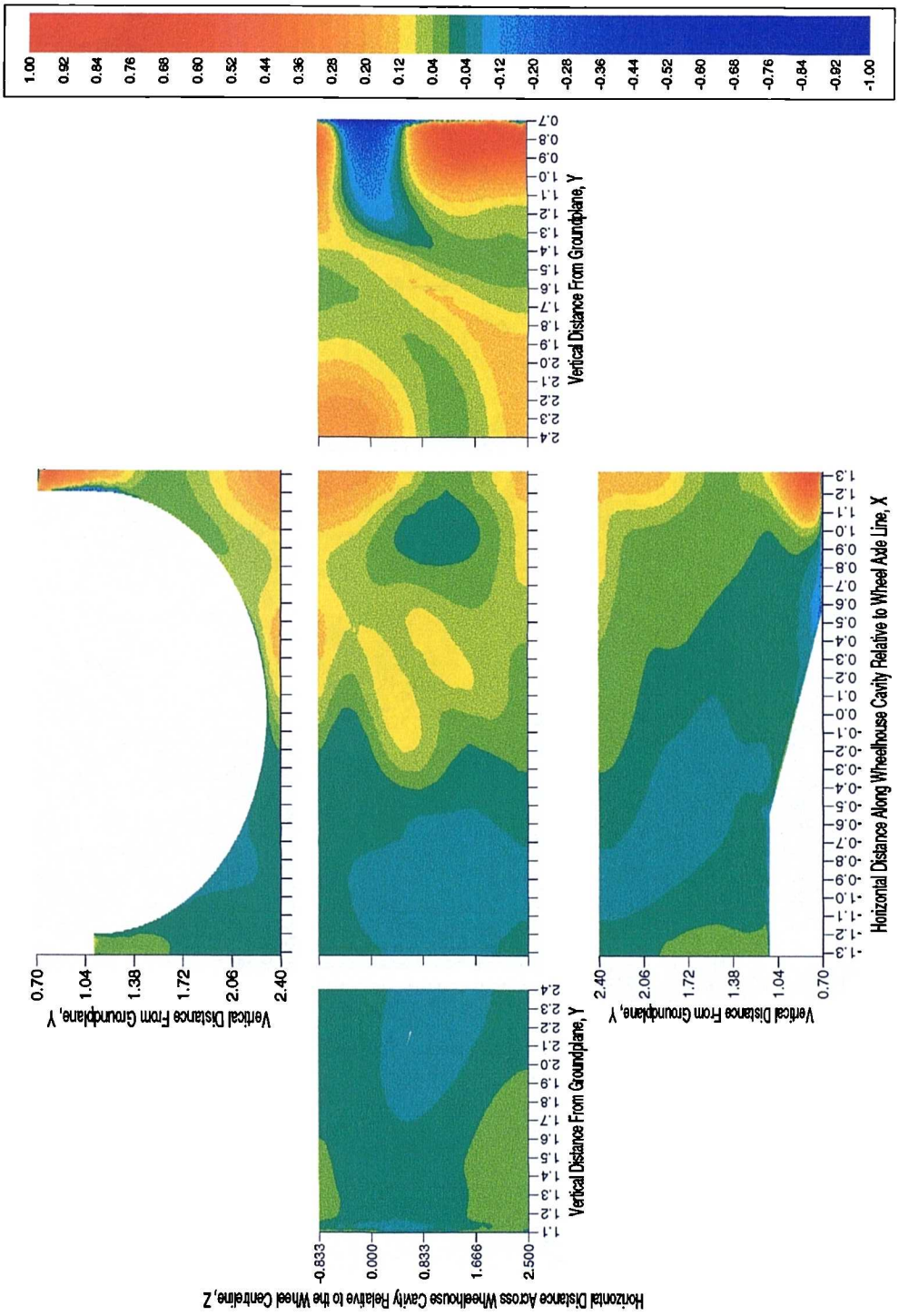

Figure F.4: Computational Wheelhouse Cavity Pressure Coefficient Distribution - No Front Spoiler, Front Ride Height, $Y_f = 1.1$, Rear Ride Height, $Y_r = 0.7$, Stationary Groundplane

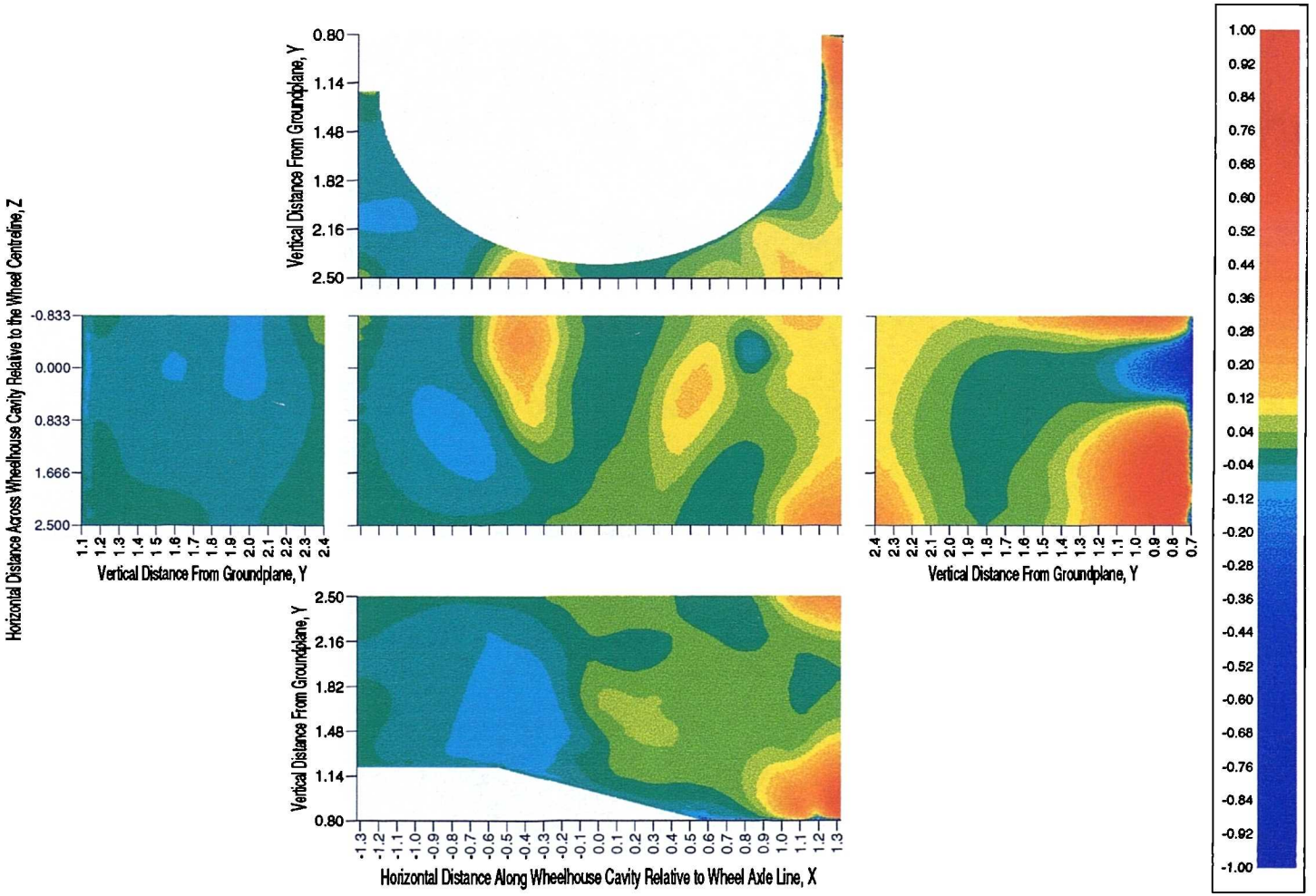

Figure F.5: Computational Wheelhouse Cavity Pressure Coefficient Distribution - No Front Spoiler, Front Ride Height, $Y_f = 1.2$, Rear Ride Height, $Y_r = 0.8$, Moving Groundplane

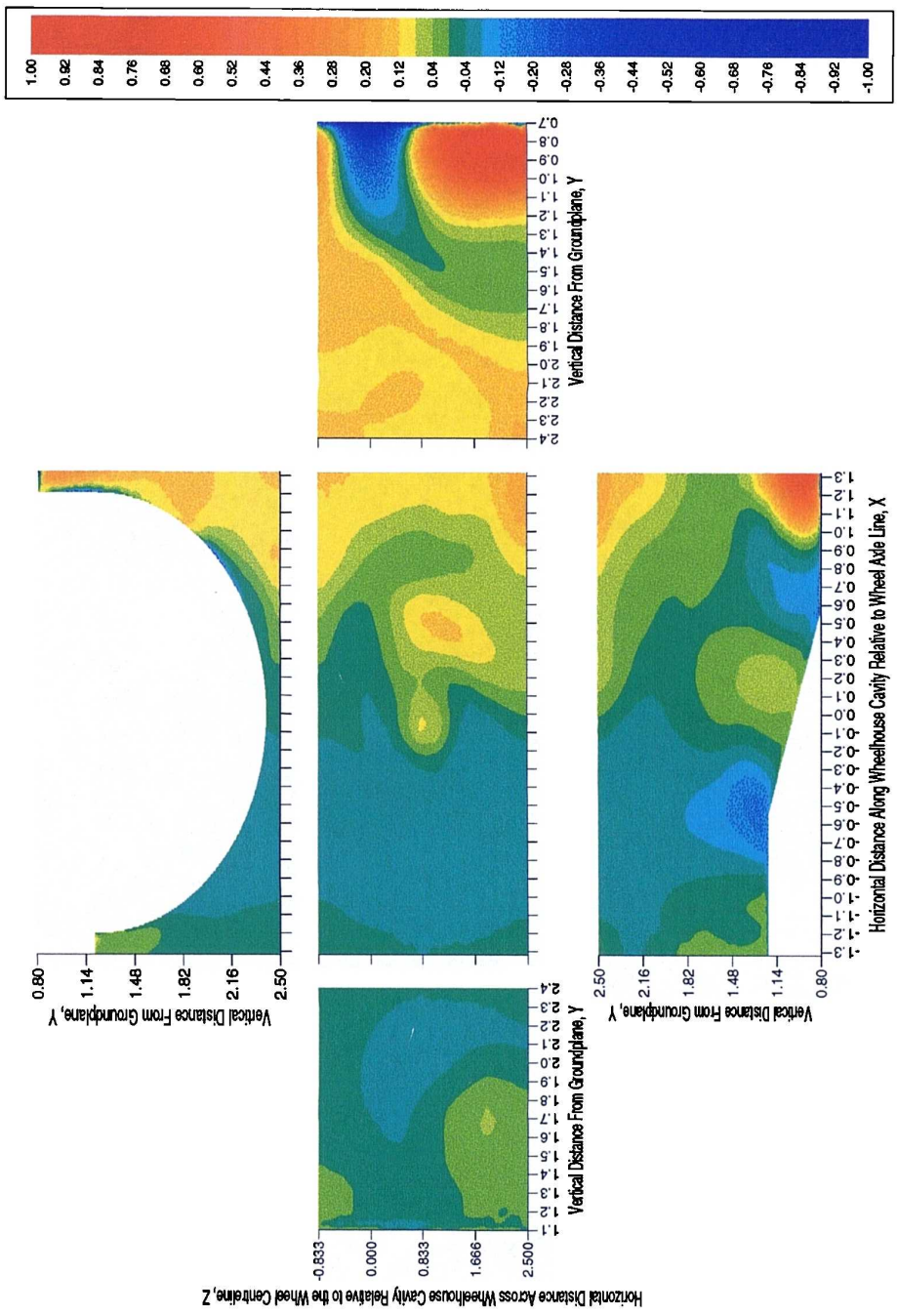

Figure F.6: Computational Wheelhouse Cavity Pressure Coefficient Distribution - No Front Spoiler, Front Ride Height, $Y_f = 1.2$, Rear Ride Height, $Y_r = 0.8$, Stationary Groundplane

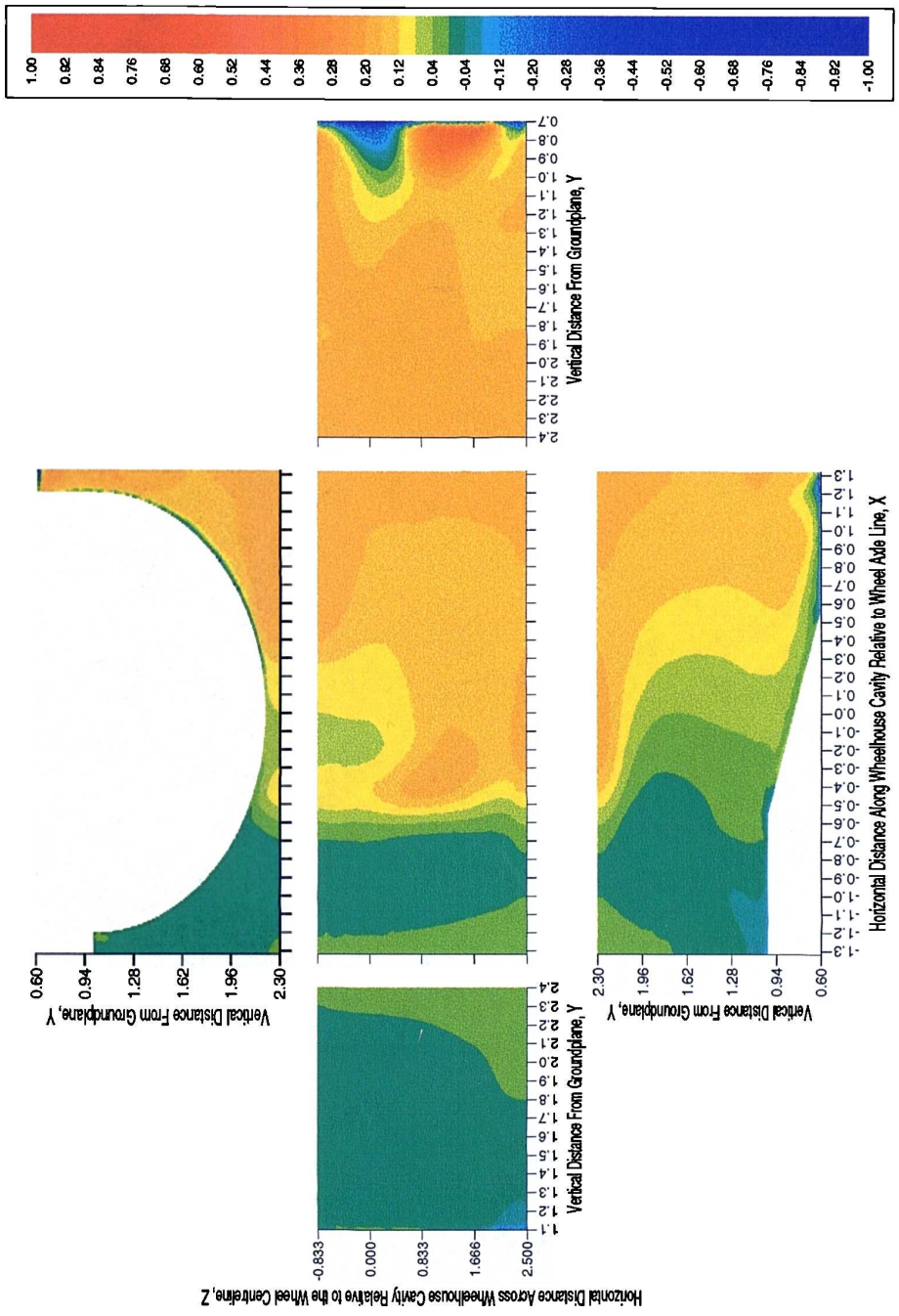

Figure F.7: Computational Wheelhouse Cavity Pressure Coefficient Distribution - 0.025m Front Spoiler, Front Ride Height, $Y_f = 1.0$, Rear Ride Height, $Y_r = 0.6$, Moving Groundplane

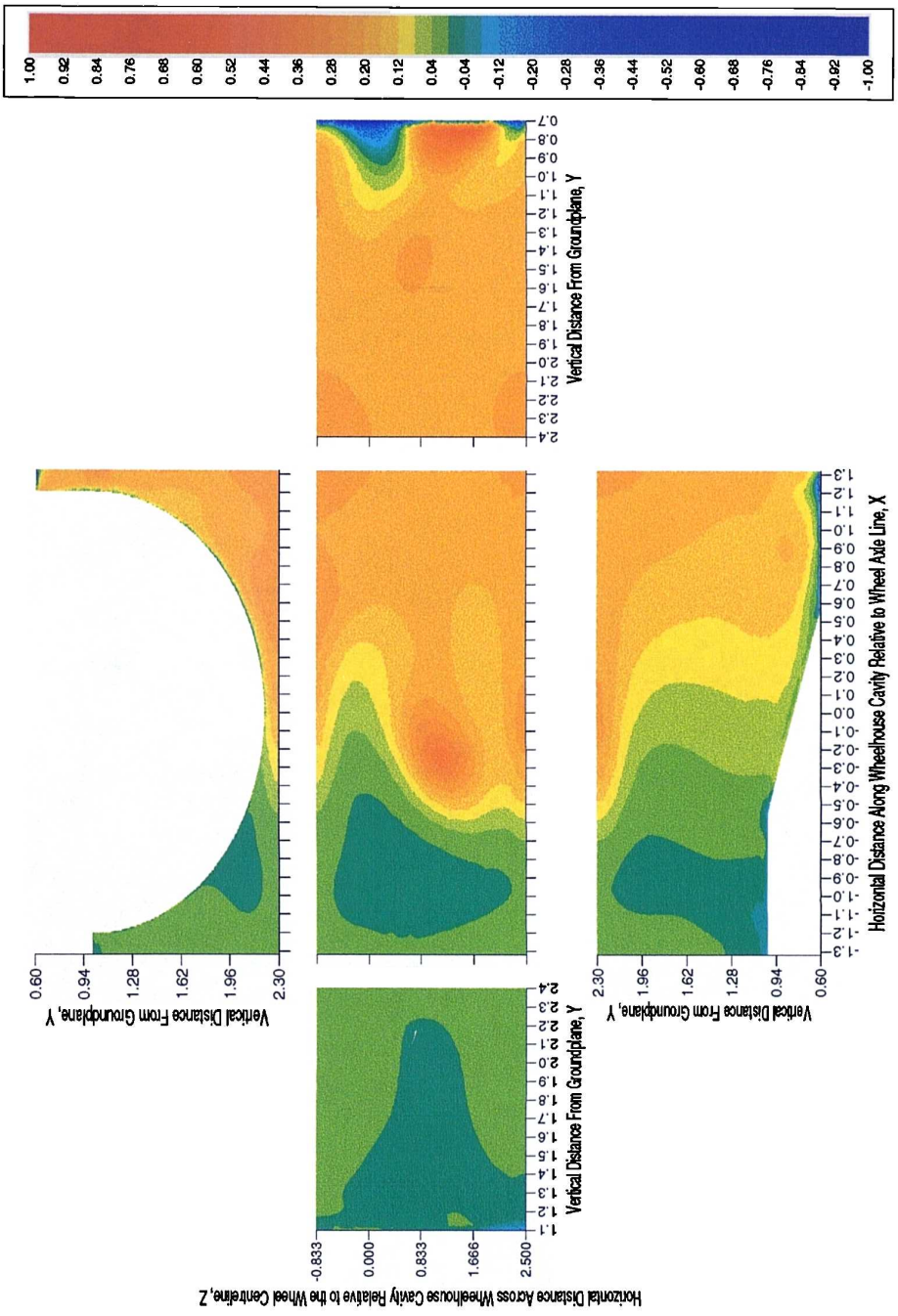

Figure F.8: Computational Wheelhouse Cavity Pressure Coefficient Distribution - 0.025m Front Spoiler, Front Ride Height, $Y_f = 1.0$, Rear Ride Height, $Y_r = 0.6$, Stationary Groundplane

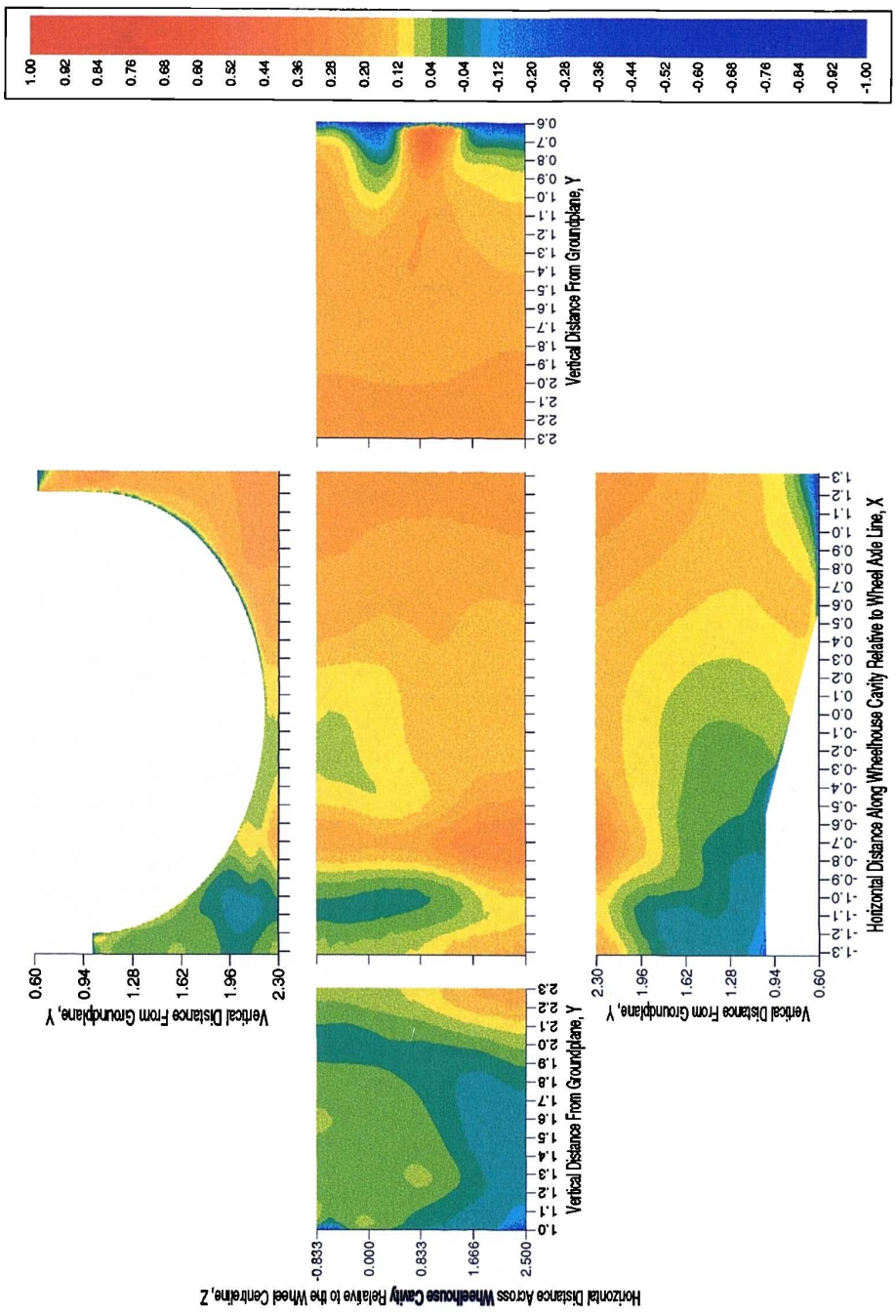

Figure F.9: Computational Wheelhouse Cavity Pressure Coefficient Distribution - 0.050m Front Spoiler, Front Ride Height, $Y_f = 1.0$, Rear Ride Height, $Y_r = 0.6$, Moving Groundplane

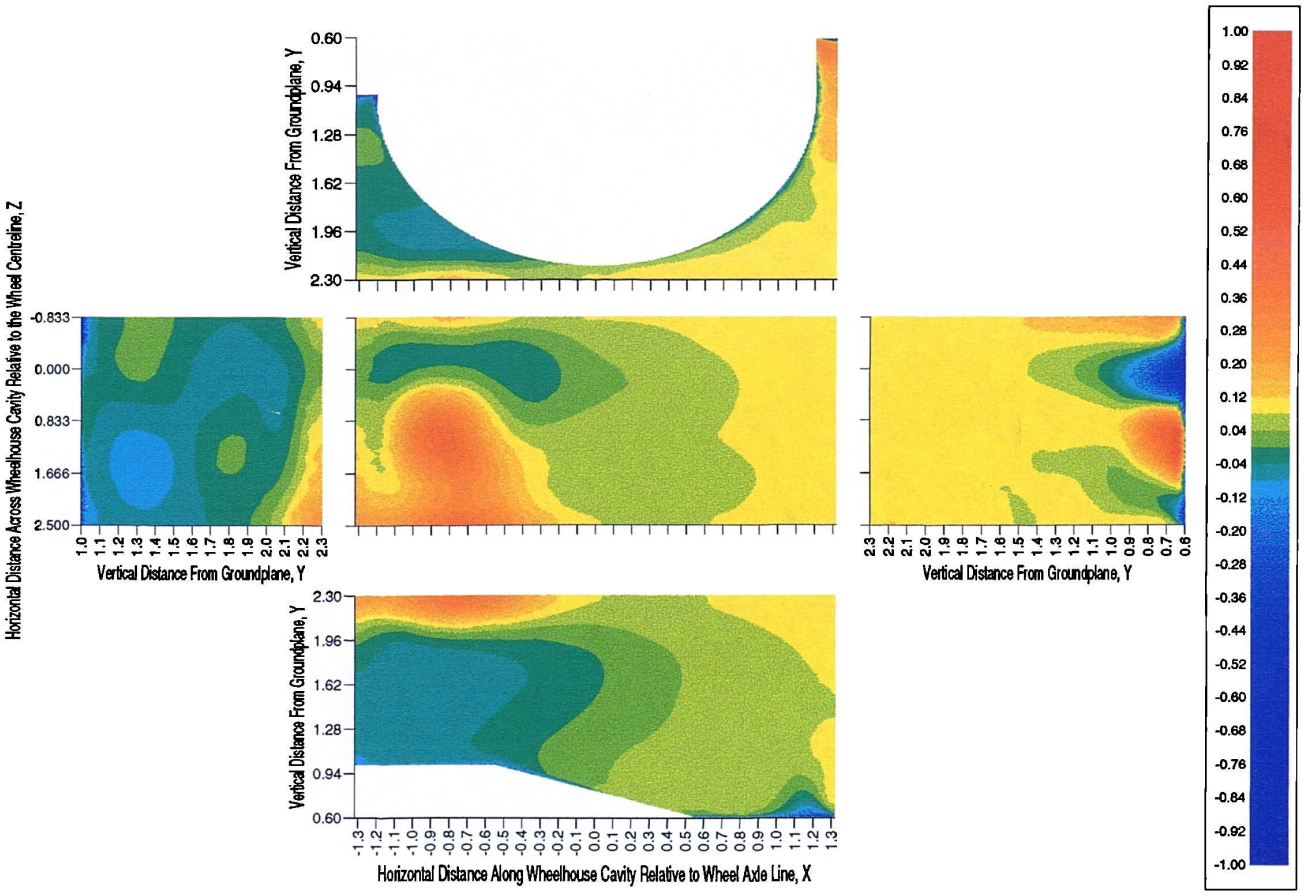

Figure F.10: Computational Wheelhouse Cavity Pressure Coefficient Distribution - 0.050m Front Spoiler, Front Ride Height, Y_f = 1.0, Rear Ride Height, Y_r = 0.6, Stationary Groundplane

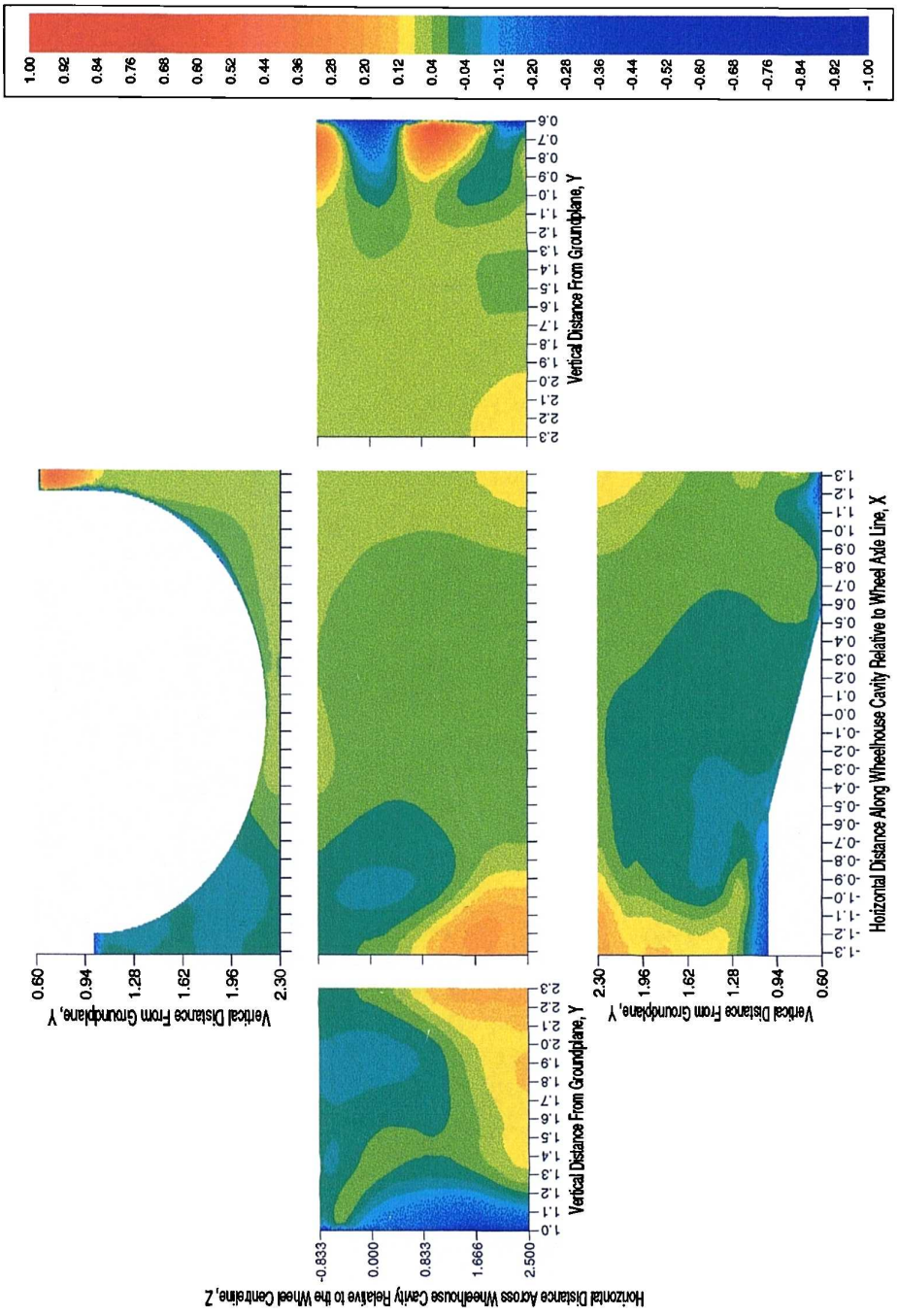

Figure F.11: Computational Wheelhouse Cavity Pressure Coefficient Distribution - 0.075m Front Spoiler, Front Ride Height, Y_f = 1.0, Rear Ride Height, $Y_r = 0.6$, Moving Groundplane

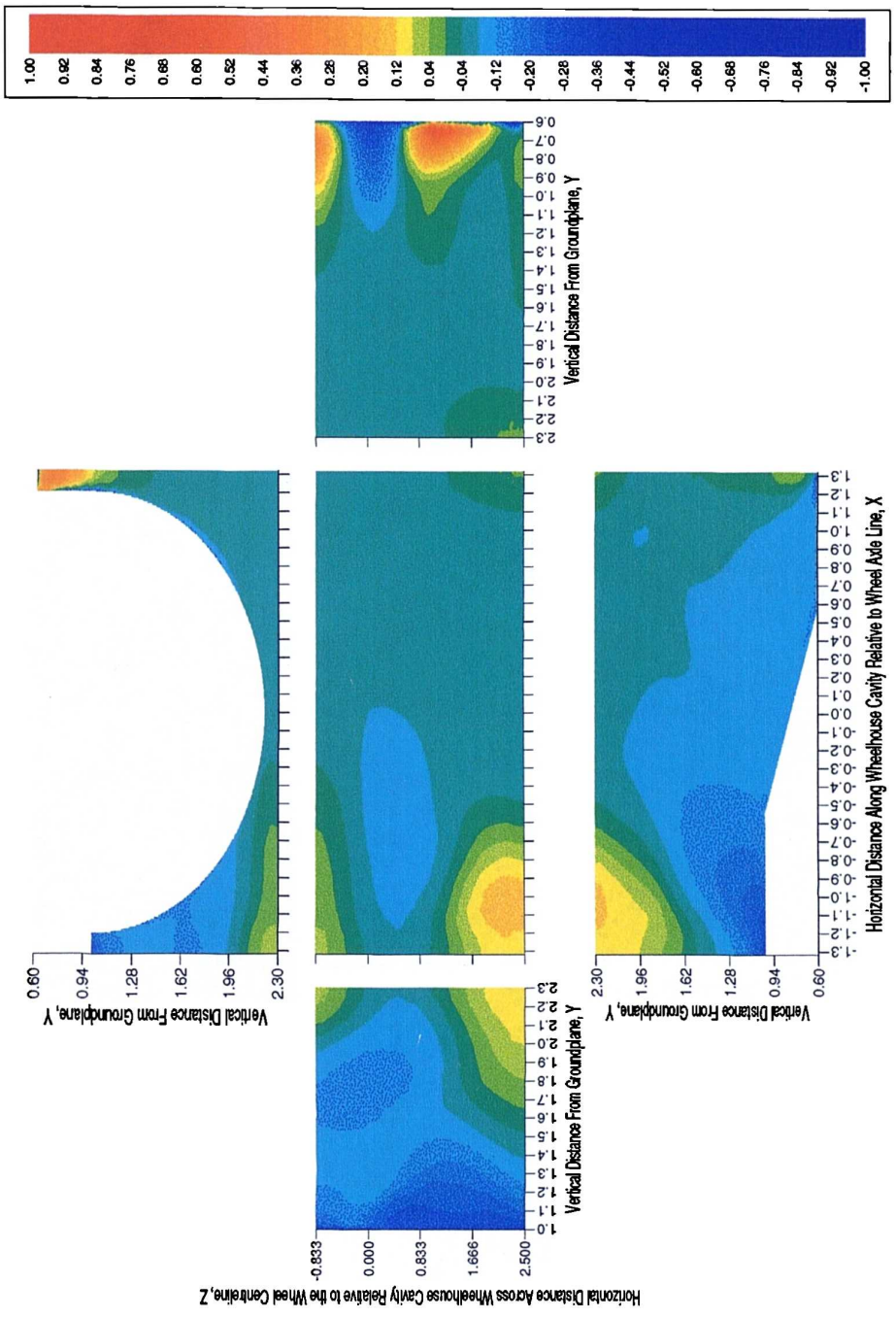

Figure F.12: Computational Wheelhouse Cavity Pressure Coefficient Distribution - 0.075m Front Spoiler, Front Ride Height, Y_f = 1.0, Rear Ride Height, $Y_r = 0.6$, Stationary Groundplane

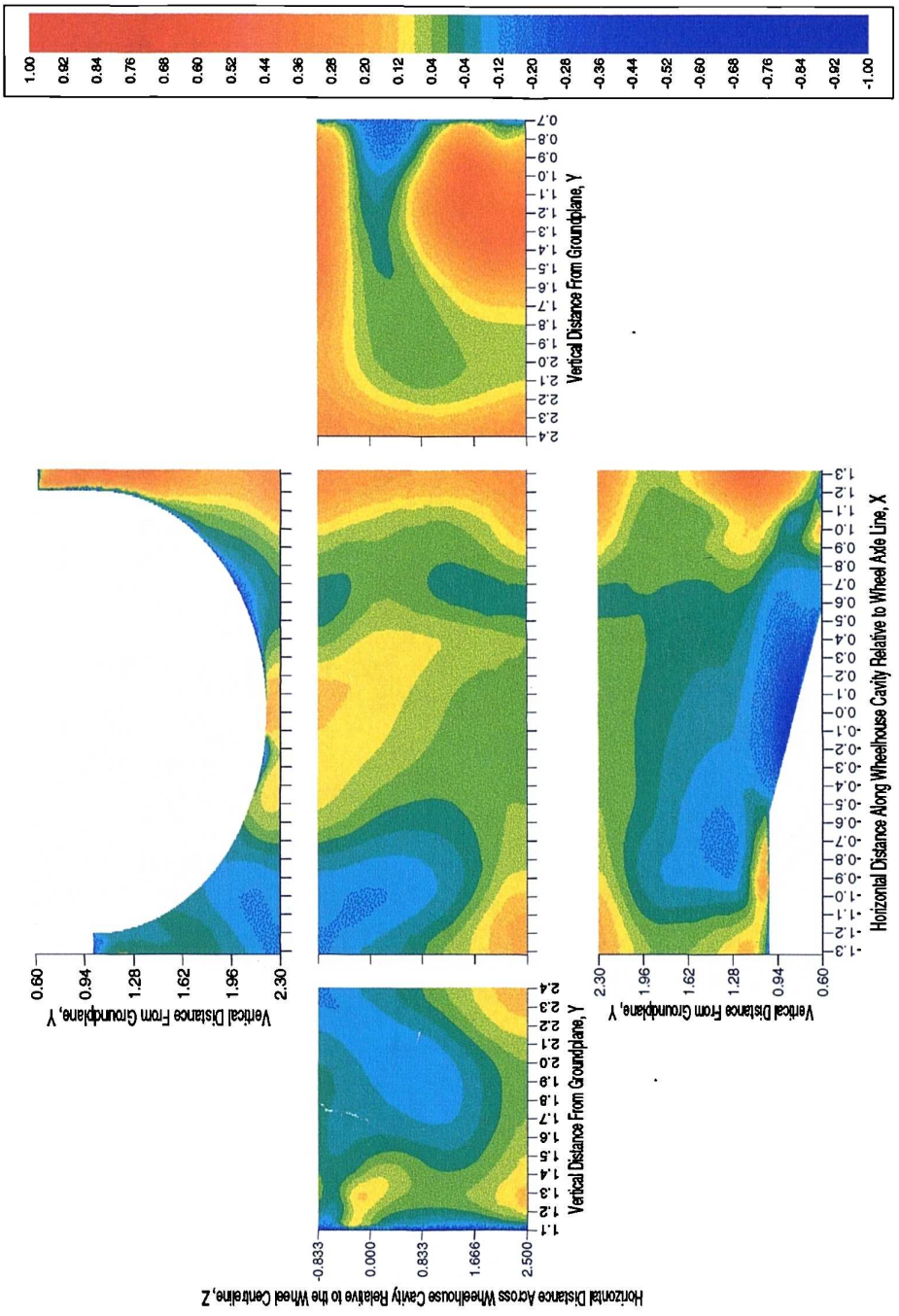

Figure F.13: Computational Wheelhouse Cavity Pressure Coefficient Distribution - 0.100m Front Spoiler, Front Ride Height, Y_f = 1.0, Rear Ride Height, Y_r = 0.6, Moving Groundplane

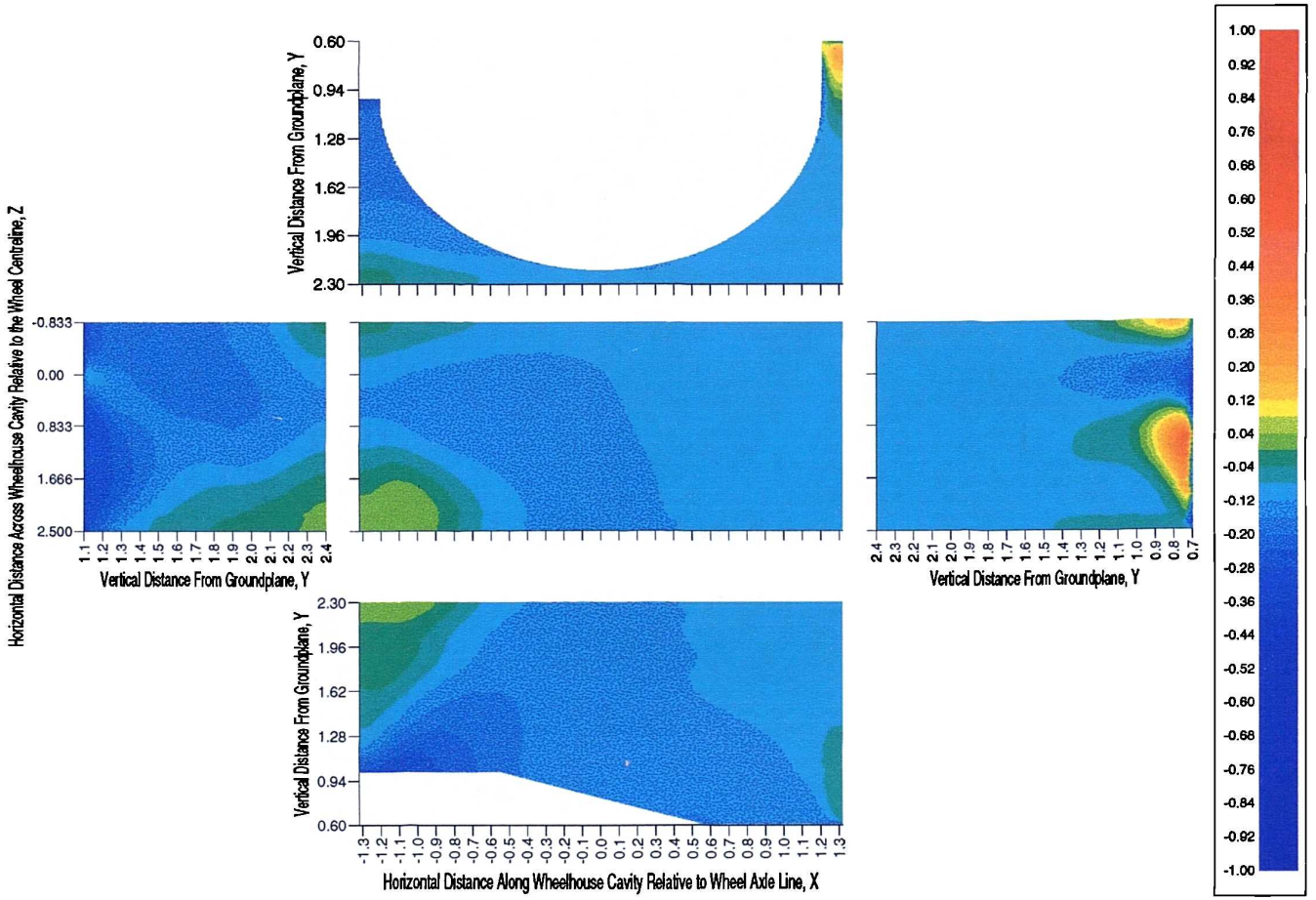

Figure F.14: Computational Wheelhouse Cavity Pressure Coefficient Distribution - 0.100m Front Spoiler, Front Ride Height, Y_f = 1.0, Rear Ride Height, Y_r = 0.6, Stationary Groundplane

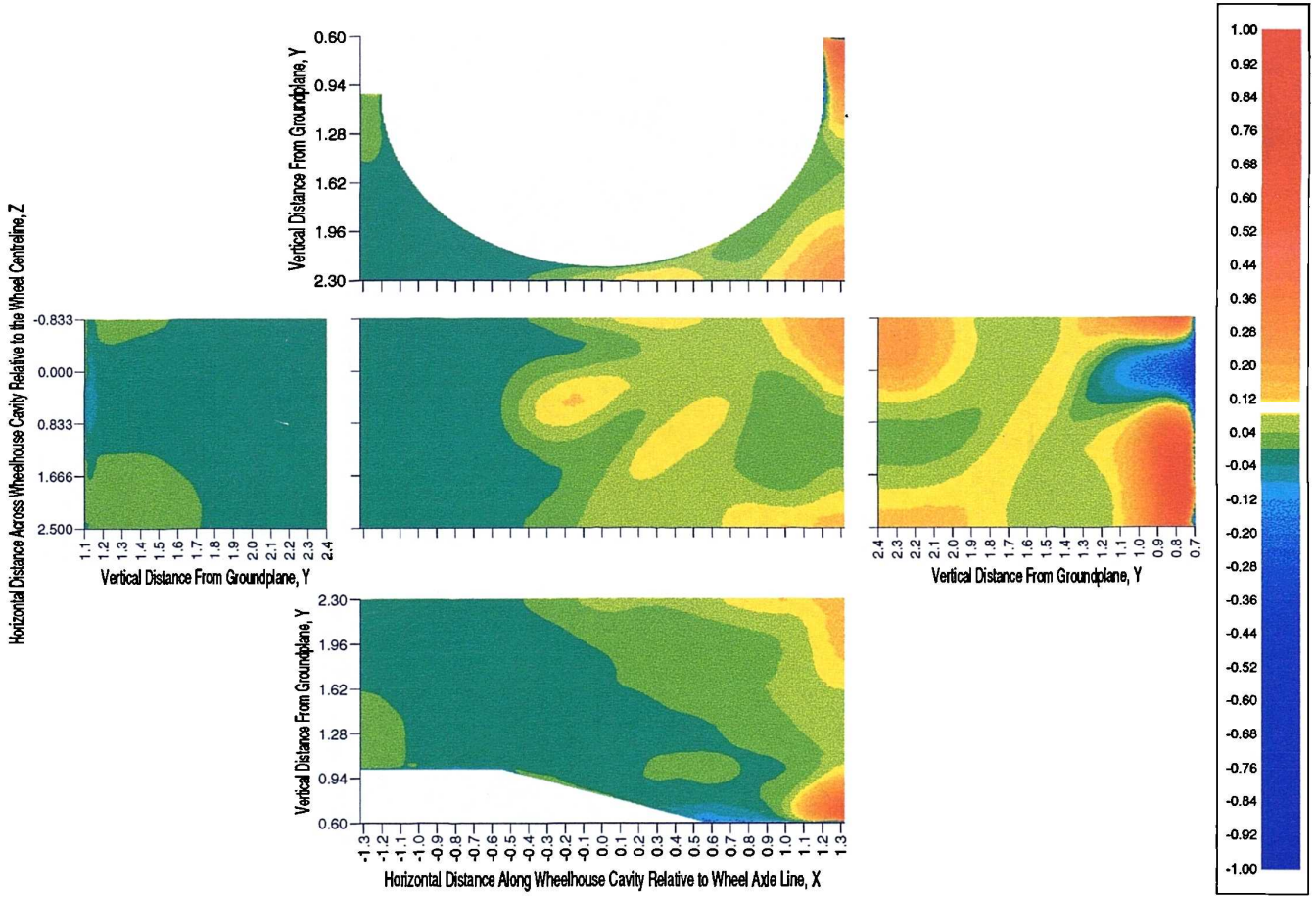

Figure F.15: Computational Wheelhouse Cavity Pressure Coefficient Distribution - No Front Spoiler, Front Ride Height, $Y_f = 1.0$, Rear Ride Height, $Y_r = 0.6$, Stationary Groundplane with 0.06m Boundary Layer Thickness

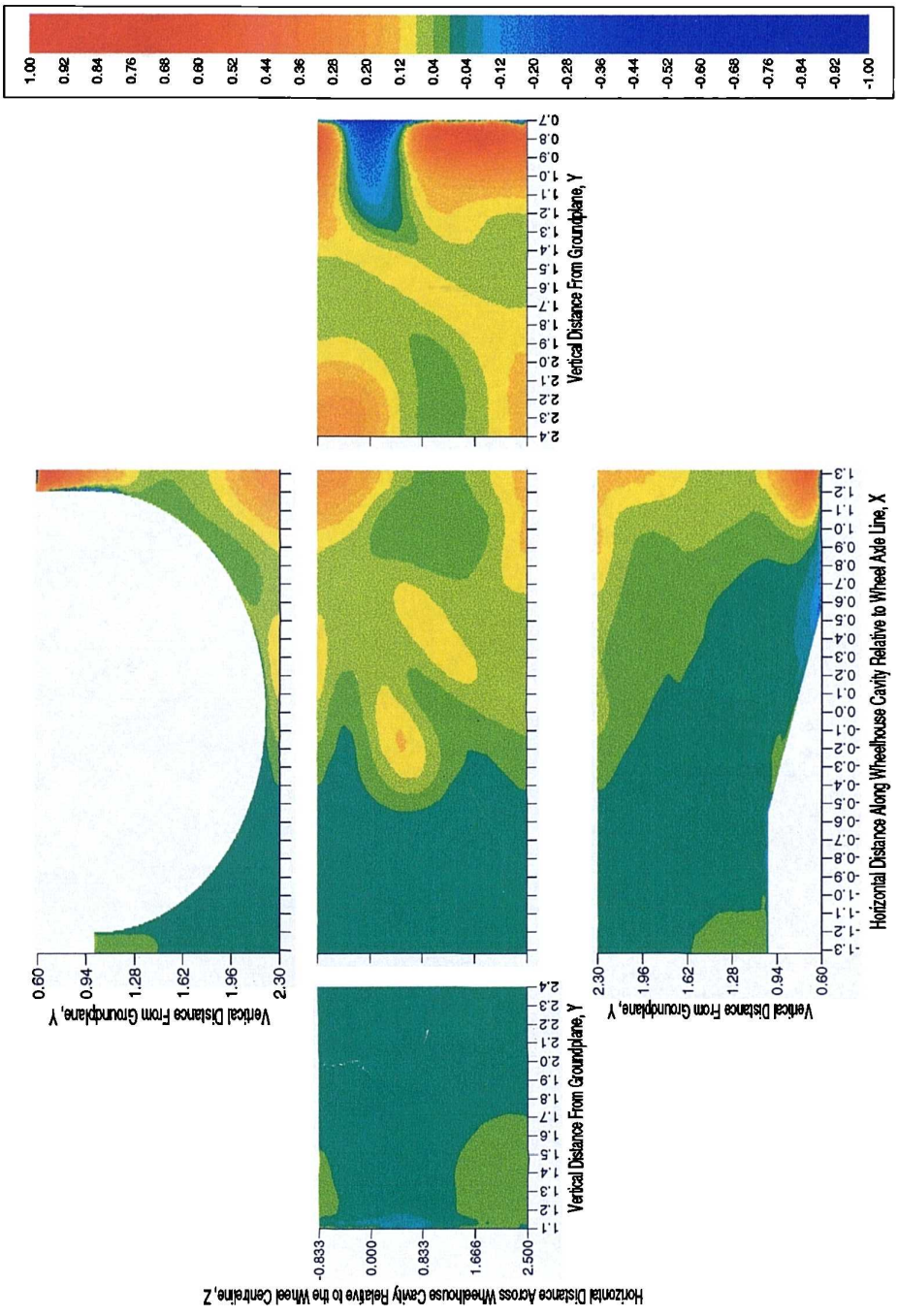

Figure F.16: Computational Wheelhouse Cavity Pressure Coefficient Distribution - No Front Spoiler, Front Ride Height, $Y_f = 1.0$, Rear Ride Height, $Y_r = 0.6$, Stationary Groundplane with 0.08m Boundary Layer Thickness

Appendix G

Computational Wheel Surface Pressure Distributions

In this appendix computational surface static pressure coefficient distributions on three planes, centreline and Z=±0.666, of the shrouded wheel are presented. All the pressure coefficients are referenced to the freestream velocity of 25m/s.

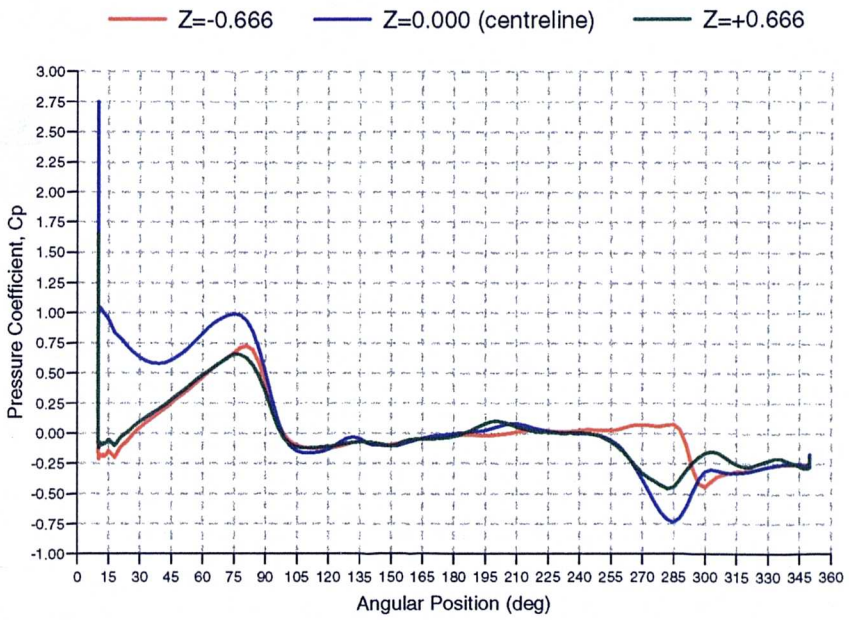

Figure G.1: Computational Wheel Surface Pressure Coefficient Distributions - No Front Spoiler, Front Ride Height, $Y_f = 1.0$, Rear Ride Height, $Y_r = 0.6$, Moving Groundplane

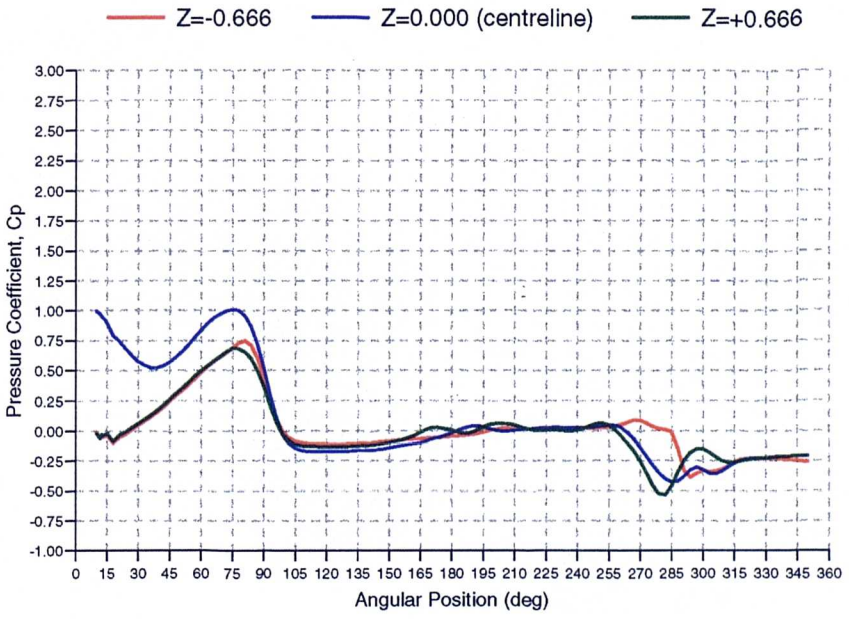

Figure G.2: Computational Wheel Surface Pressure Coefficient Distributions - No Front Spoiler, Front Ride Height, $Y_f = 1.0$, Rear Ride Height, $Y_r = 0.6$, Stationary Groundplane

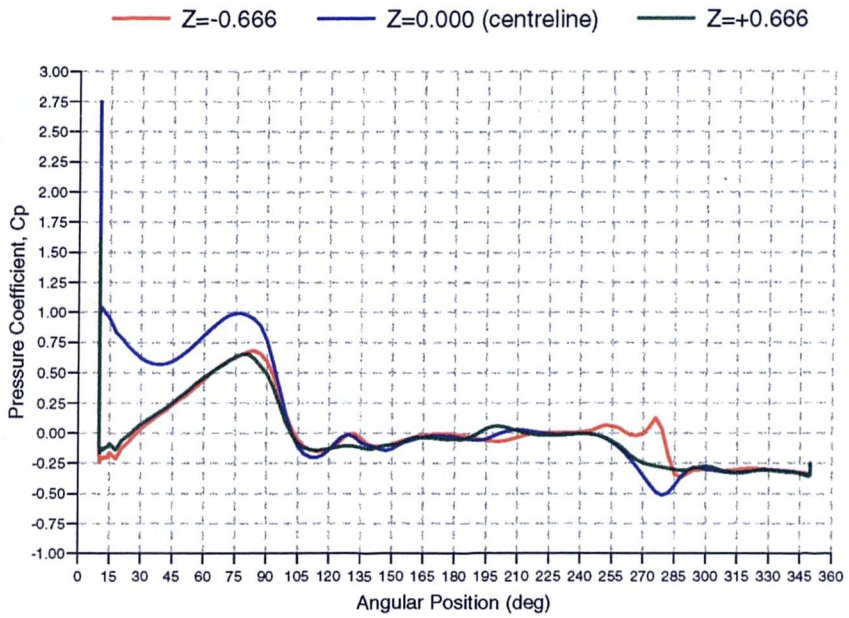

Figure G.3: Computational Wheel Surface Pressure Coefficient Distributions - No Front Spoiler, Front Ride Height, $Y_f = 1.1$, Rear Ride Height, $Y_r = 0.7$, Moving Groundplane

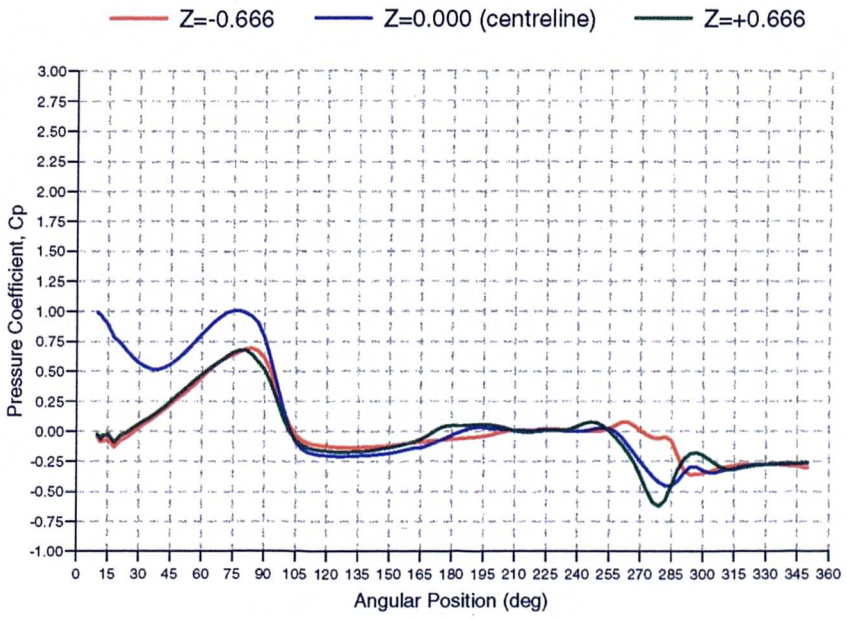

Figure G.4: Computational Wheel Surface Pressure Coefficient Distributions - No Front Spoiler, Front Ride Height, $Y_f = 1.1$, Rear Ride Height, $Y_r = 0.7$, Stationary Groundplane

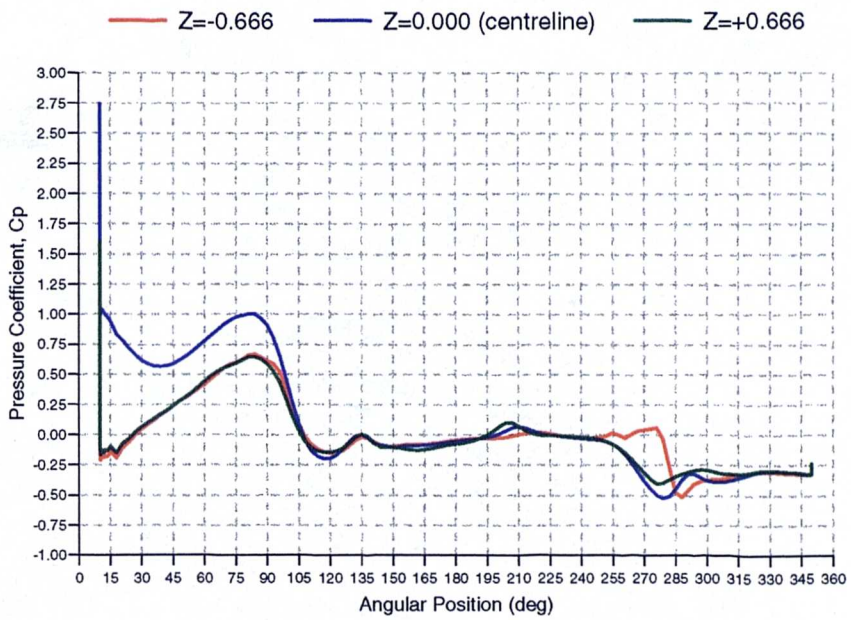

Figure G.5: Computational Wheel Surface Pressure Coefficient Distributions - No Front Spoiler, Front Ride Height, $Y_f = 1.2$, Rear Ride Height, $Y_r = 0.8$, Moving Groundplane

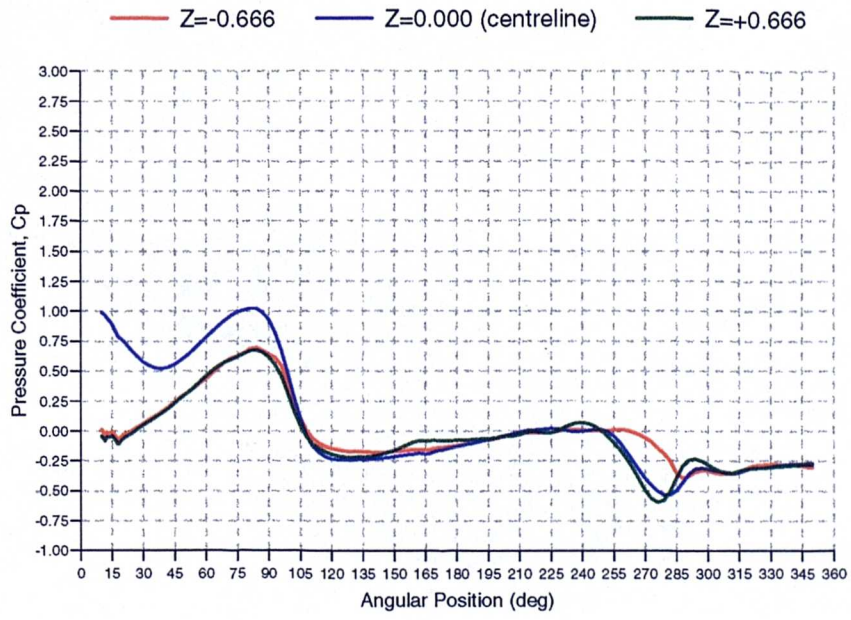

Figure G.6: Computational Wheel Surface Pressure Coefficient Distributions - No Front Spoiler, Front Ride Height, $Y_f = 1.2$, Rear Ride Height, $Y_r = 0.8$, Stationary Groundplane

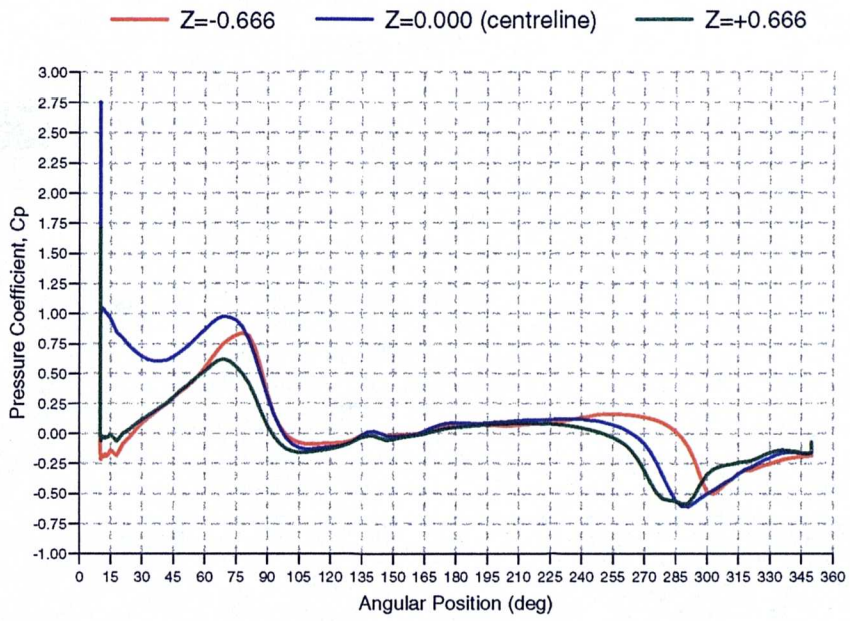

Figure G.7: Computational Wheel Surface Pressure Coefficient Distributions - 0.025m Front Spoiler, Front Ride Height, $Y_f = 1.0$, Rear Ride Height, $Y_r = 0.6$, Moving Groundplane

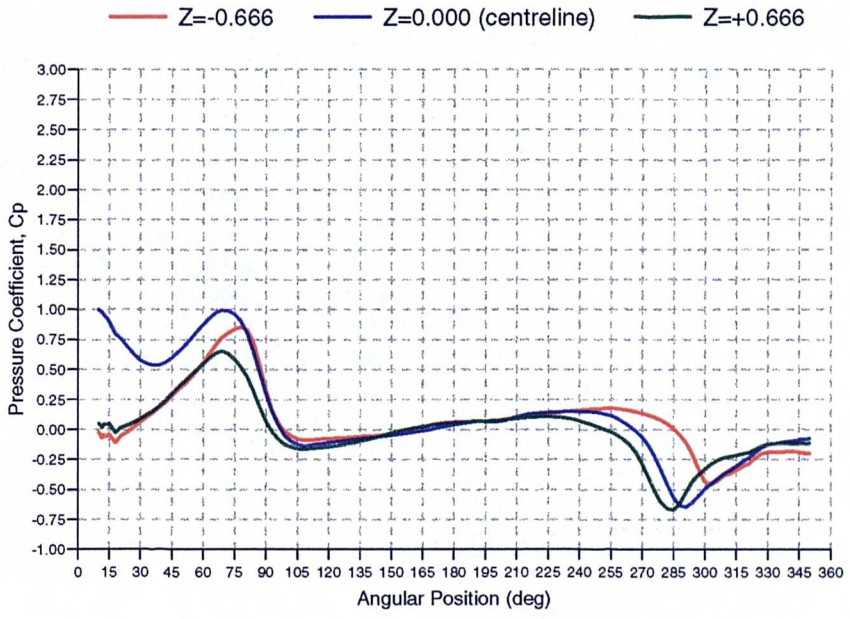

Figure G.8: Computational Wheel Surface Pressure Coefficient Distributions - 0.025m Front Spoiler, Front Ride Height, $Y_f = 1.0$, Rear Ride Height, $Y_r = 0.6$, Stationary Groundplane

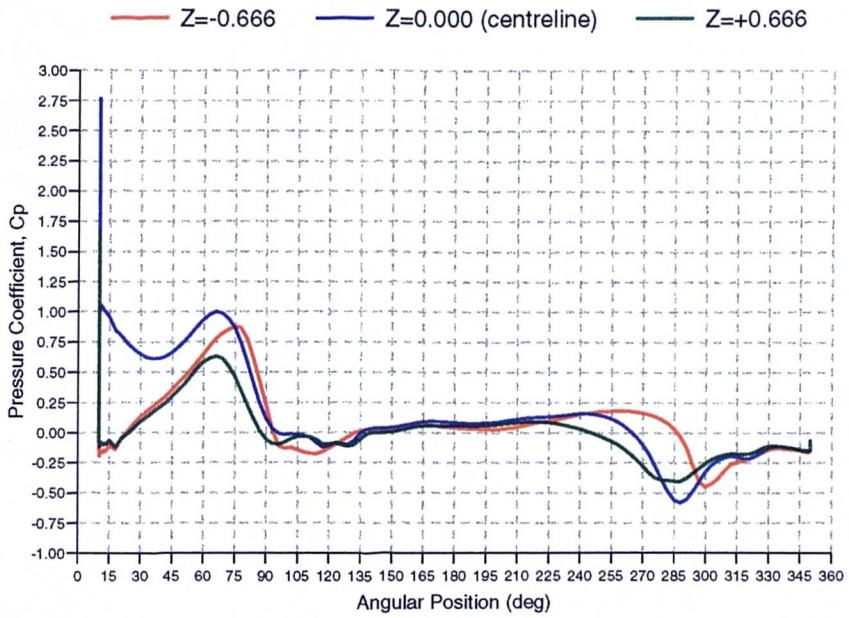

Figure G.9: Computational Wheel Surface Pressure Coefficient Distributions - 0.050m Front Spoiler, Front Ride Height, Y_f = 1.0, Rear Ride Height, Y_r = 0.6, Moving Groundplane

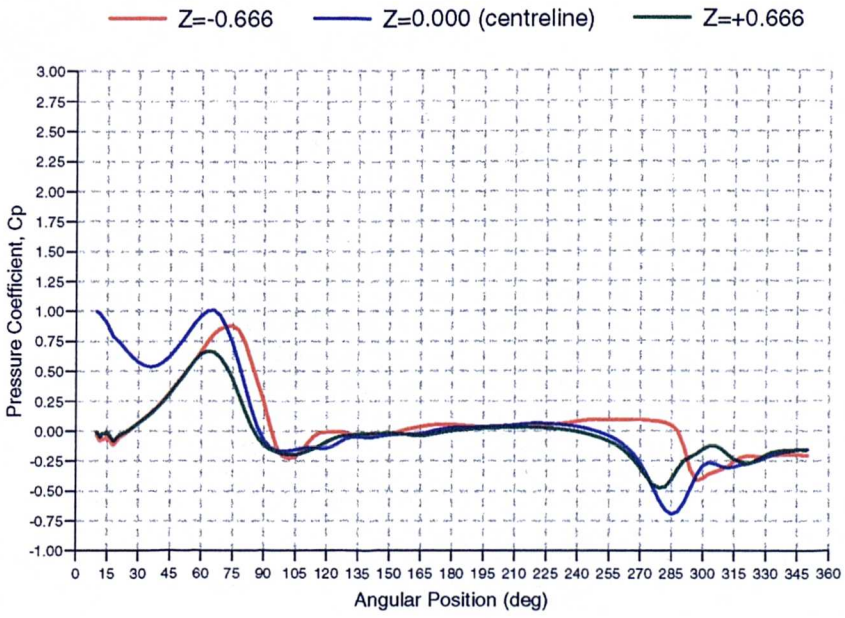

Figure G.10: Computational Wheel Surface Pressure Coefficient Distributions - 0.050m Front Spoiler, Front Ride Height, Y_f = 1.0, Rear Ride Height, Y_r = 0.6, Stationary Groundplane

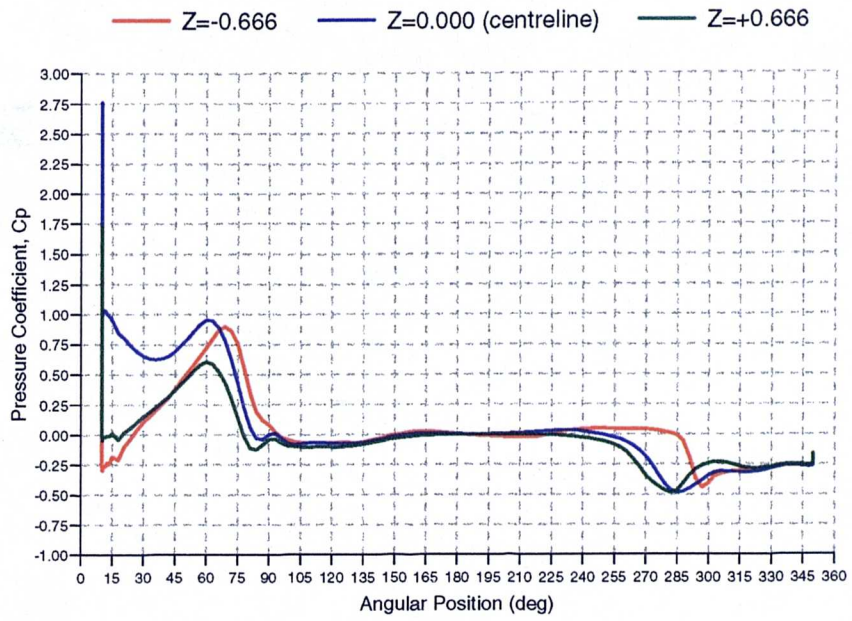

Figure G.11: Computational Wheel Surface Pressure Coefficient Distributions - 0.075m Front Spoiler, Front Ride Height, Y_f = 1.0, Rear Ride Height, Y_r = 0.6, Moving Groundplane

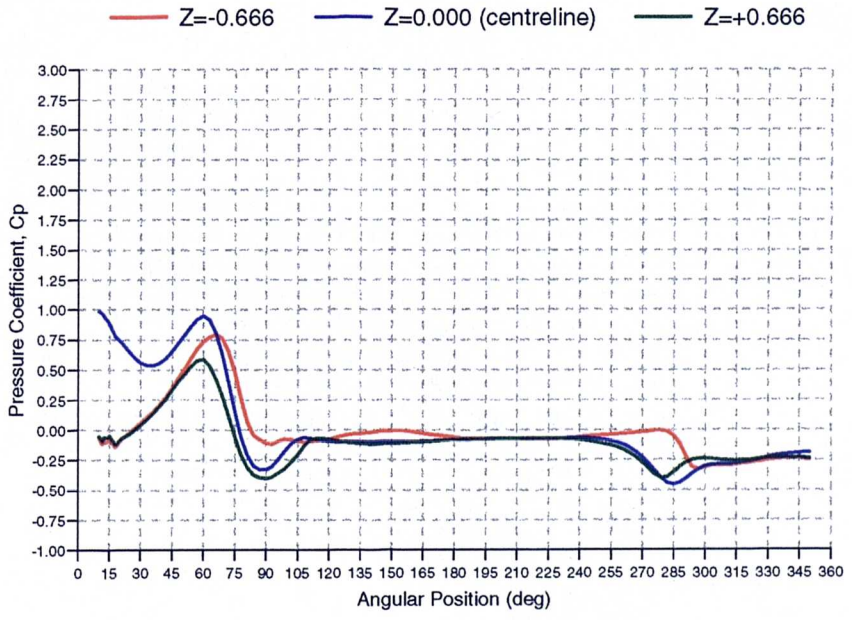

Figure G.12: Computational Wheel Surface Pressure Coefficient Distributions - 0.075m Front Spoiler, Front Ride Height, Y_f = 1.0, Rear Ride Height, Y_r = 0.6, Stationary Groundplane

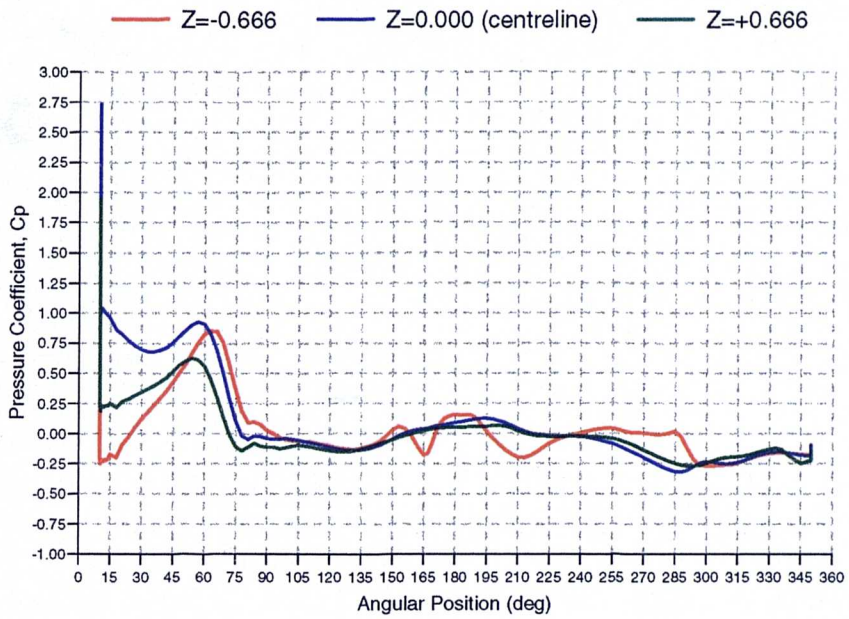

Figure G.13: Computational Wheel Surface Pressure Coefficient Distributions - 0.100m Front Spoiler, Front Ride Height, $Y_f = 1.0$, Rear Ride Height, $Y_r = 0.6$, Moving Groundplane

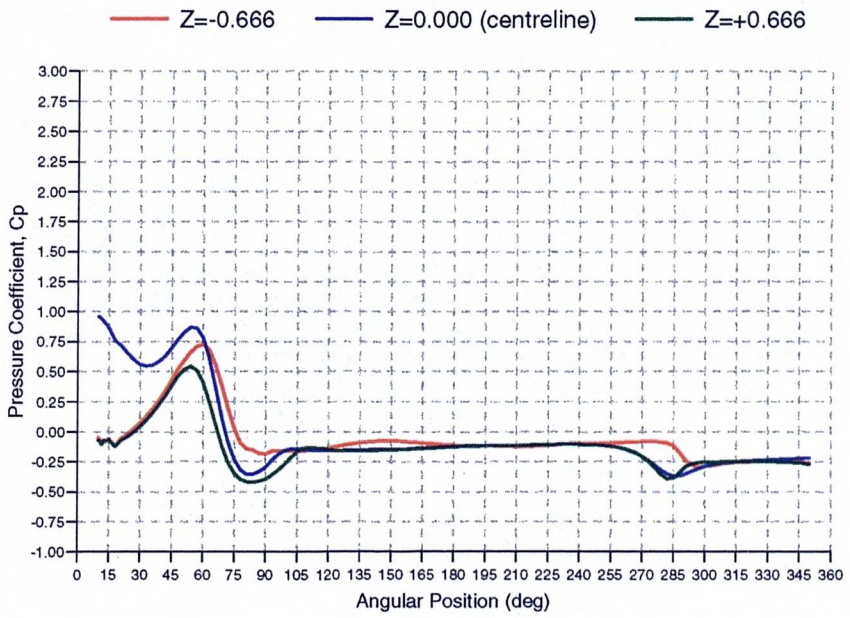

Figure G.14: Computational Wheel Surface Pressure Coefficient Distributions - 0.100m Front Spoiler, Front Ride Height, $Y_f = 1.0$, Rear Ride Height, $Y_r = 0.6$, Stationary Groundplane

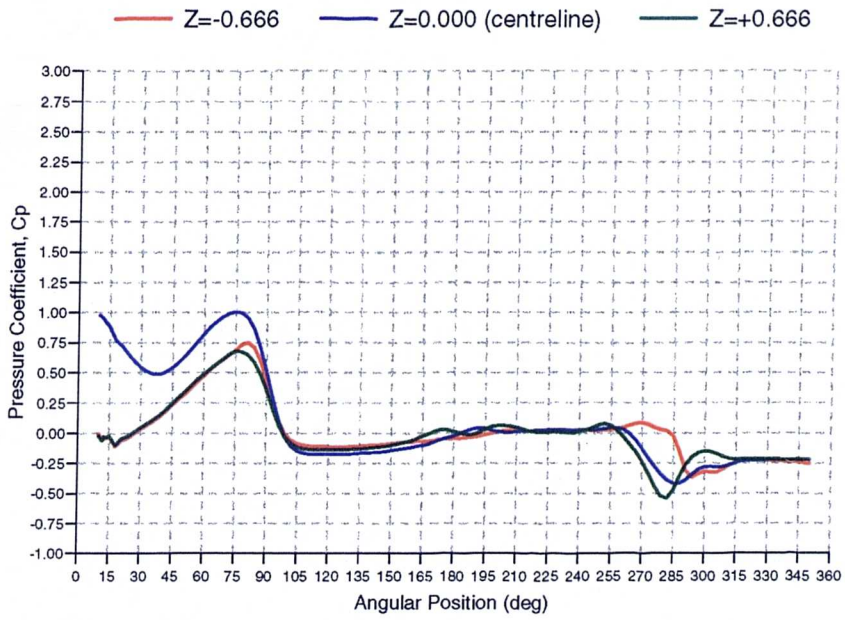

Figure G.15: Computational Wheel Surface Pressure Coefficient Distributions - No Front Spoiler, Front Ride Height, $Y_f = 1.0$, Rear Ride Height, $Y_r = 0.6$, Stationary Groundplane with 0.06m Boundary Layer Thickness

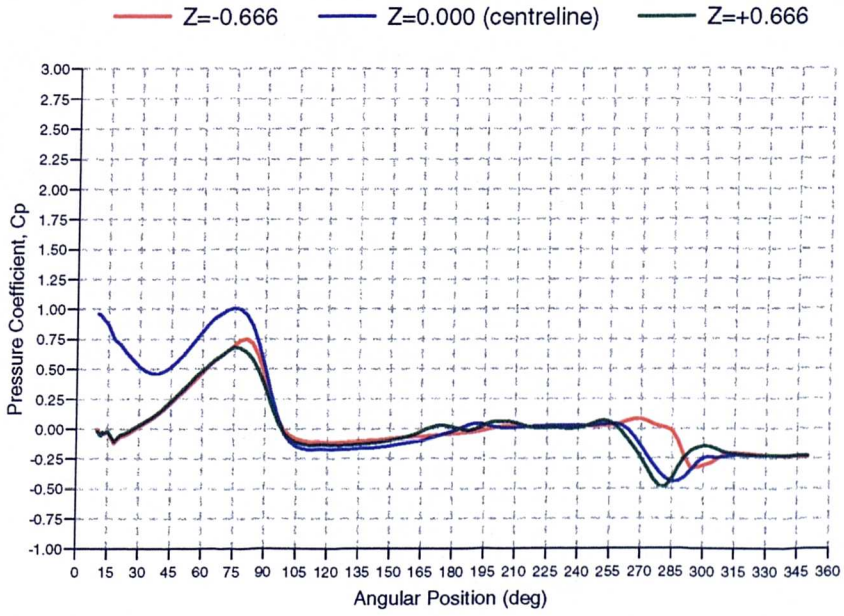

Figure G.16: Computational Wheel Surface Pressure Coefficient Distributions - No Front Spoiler, Front Ride Height, $Y_f = 1.0$, Rear Ride Height, $Y_r = 0.6$, Stationary Groundplane with 0.08m Boundary Layer Thickness